POSTGLACIAL VARIATIONS IN THE LEVEL OF THE SEA: IMPLICATIONS FOR CLIMATE DYNAMICS AND SOLID-EARTH GEOPHYSICS

W. R. Peltier
Department of Physics
University of Toronto
Toronto, Ontario, Canada

Abstract. Throughout the latter half of the Pleistocene epoch of Earth history, beginning ~900 kyr ago, the climate system has been dominated by an intense oscillation between full glacial and interglacial conditions. During each glacial stage, global sea level fell by ~120 m on average, as extensive ice sheets formed and thickened on the surfaces of the continents at high northern (primarily) and southern latitudes. Within each cycle this glaciation phase lasted ~90 kyr and was followed by a much more rapid deglaciation event which terminated after ~10 kyr and which returned the system to the interglacial state. The period of the canonical glacial cycle has remained very close to 100 kyr since its inception in mid-Pleistocene time. Because of the magnitude of the mass that was redistributed over the surface of the Earth during each such glacial cycle and because of the viscoelastic nature of the rheology of the planetary mantle, these shifts in surface mass load induced variations in the shape of the planet that have been indelibly transcribed into the geological record of sea level variability. Indeed, the geological, geophysical, and even astronomical signatures of this process, which is continuing today, are now being measured with unprecedented precision using the methods of space geodesy and have thereby begun to provide important new scientific insight and understanding, both of the interior of the solid Earth and of the climate system variability with which the ice ages themselves are associated. In this article my purpose is to bring together, in a single review, an assessment of where we currently stand scientifically with regard to understanding both of these aspects of the ice ages. Although the discussion will not address in any detail the fascinating issue of ice age climate, since this topic is sufficiently complex of itself to require a detailed review of its own, I will nevertheless attempt to briefly summarize the current state of understanding of the physical processes that are responsible for the occurrence of the ice age cycle, by way of providing a more complete context in which to appreciate the main lines of argument that will be developed.

CONTENTS

1. INTRODUCTION

Since the focus of this article is to be on issues concerned primarily with the level of the sea relative to the surface of the solid Earth, it will be useful at the outset to introduce a number of concepts, and related nomenclature, that are conventionally employed in such discussion. It will be important for the purpose of analyzing the various physical mechanisms that may cause variations of relative sea level to distinguish between those which are eustatic and those which are isostatic. By *eustatic sea level variations* I mean those which occur as a consequence of a change in the mass of water in the global ocean, whereas by *isostatic sea level variations* I imply changes in relative sea level (rsl) that are caused by a change in the local radius of the solid Earth. Since sea level is usually measured with respect to the surface of the solid Earth, it will be clear that such measurements are inherently ambiguous; that is, it is not possible to determine whether the origin of an observed variation is eustatic or isostatic using such measurements. Since

8755-1209/98/98RG-02638$15.00

Reviews of Geophysics, 36,4 / *November 1998*
pages 603–689
Paper number 98RG02638

the late Pleistocene cycle of glaciation and deglaciation involves both eustatic and isostatic effects, their distinct impacts on relative sea level at a given location can be disentangled only on the basis of theory or on the basis of simultaneous direct measurement of one or the other of the two individual elements that contribute to the observed relative variation of level: namely, the local radius of the solid Earth or the absolute level of the surface of the sea (the *geoid*) relative to the center of mass of the planet (the geocenter).

Throughout this article, I will discuss the process of glacial isostatic adjustment (GIA) whereby, owing to the addition (removal) of glacial ice onto (from) the surface of the continents, the shape of the planet is itself distorted. Since the hydrological cycle may be reasonably assumed to remain closed during such surface mass load redistribution, it will be clear that geophysically plausible glaciation events must be mass conserving in that the mass of ice, which for climatological reasons appears on the continents, must be balanced by a loss of water from the oceans and thus a lowering of sea level (and vice versa). Although it will not prove possible herein, for want of space, to do any significant justice to the history of the development of our understanding of the glacial isostatic adjustment process, it will be important to know that such history is, in fact, voluminous and to realize why geophysical science has come to see that the understanding of this process constitutes a fundamental underpinning of the subject that is now referred to as "geodynamics."

The first scientific investigation of the glacial isostatic adjustment process of which I am aware (excepting that of Hjarne, mentioned by *Devoy* [1987]) was that conducted in the Swedish fishing village of Lövgrunde which is located on a small island in the Baltic Sea ~200 km north of Stockholm. In the bay around which this village is constructed, there is a large rock near the shore which was, throughout the seventeenth century, employed by the local fishermen for sealing. Early in the eighteenth century, in the year 1731, the fishermen, having noticed that the rock had emerged sufficiently above sea level that the seals were no longer able to scale it, became increasingly alarmed. Seeking an explanation, they contacted the scientist Celsius, then living in Stockholm, and he visited Lövgrunde in the same year to investigate. At that time a mark was cut in the rock to indicate the level of the sea and the date was also inscribed. Subsequent to this, and at intervals of ~100 years, new marks were successively cut in the same stone to mark the new level of the sea and the date, and this rock still sits in the bay that fronts the village of Lövgrunde. Photographs of this village and of "Celsius rock" are presented in Plate 1, taken in fall 1996 on a visit there that was led by my colleague M. Eckman, who is seen on the ladder that he employed to scale the rock to the height of Celsius' mark. This mark is now found several meters above the present level of the sea. Celsius' preferred explanation as quoted by *Devoy* [1987, p. 2] for the apparent fall of level of the Baltic Sea, referring to commentary of Newton on planetary desiccation, was that the amount of water in the global ocean was diminishing due to "evaporation and the amount of water used by plants to form Humus." Celsius' explanation was therefore a eustatic explanation.

Our modern understanding of the falling sea levels in the Baltic region as being dominated by an isostatic response to deglaciation was not achieved until the mid-nineteenth century when *MacLaren* [1842, p. 353], having read the recently published book of *Agassiz* [1840] on glacial theory, wrote "if we suppose the region from the 35th parallel to the North Pole to be invested with a coat of ice thick enough to reach the summits of the Jura, . . . it is evident that the abstraction of such a quantity of water from the ocean would immediately affect its depth." Working in the similarly glaciated region of Scotland, *Jamieson* [1865, 1882] was apparently the first to suggest that the removal of a large quantity of ice from the surface of the solid Earth could lead to an uplift of the crust, and *Jamieson* [1842, p. 178] wrote "It has occurred to me that the enormous weight of ice thrown upon the land may have something to do with this (land level) depression" and thus apparently invented the concept of glacial isostasy. The concept of isostasy itself (Gr. isostasios, "in equipoise") was of course earlier introduced by *Pratt* [1855], *Airy* [1855], and *Dutton* [1889] [cf. *Holmes*, 1965]. The interested reader will find the more complete review of this history provided by *Devoy* [1987] especially informative.

From a modern solid-Earth geophysical perspective, the phenomenon of GIA has come to assume a position of considerable importance. Solely on the basis of the observation that the uplift of the crust in regions that were once ice covered is continuing at present, thousands of years after the last remnants of late glacial ice have disappeared from the landscape, we may conclude that the rheology of the planetary mantle is not perfectly elastic. If it were, then the deformation of the solid Earth would have ceased with the cessation of melting. On such long timescales the planetary mantle must then be capable of deforming as a viscous fluid. Since this is precisely the rheological behavior required in order that the phenomenon of plate tectonics be explicable in

Plate 1. (opposite) (top) Fishing village of Lövgrunde in the Baltic Sea off the coast of Sweden. Several of the small buildings are boat houses originally constructed in the nineteenth century but which have become inaccessible to the sea due to the postglacial rebound of the crust that is ongoing throughout the Fennoscandia region. (bottom) The author on Celsius rock in the bay at Lövgrunde together with his colleague M. Eckman, who is standing on the ladder at the height of the mark made by Celsius to denote the mean level of the sea in the year 1731. Clearly, Celsius' mark is now more than 3 m above the present level of the sea (in which the foot of the ladder is immersed). This photograph was taken by S. Crane of the BBC in connection with filming of a segment entitled "Journey to the Centre of the Earth" of the series entitled "Earth Story."

terms of a thermally driven convective circulation in the mantle, there is clearly a fundamental link in the logical edifice of geodynamics between the processes of glacial isostatic adjustment and mantle convection. Since observations of the former process may be employed to directly measure the viscosity that is required to build a theory of the latter, this link is extremely strong indeed. As I discuss at length in section 4, it has, in fact, proven possible in the past several years to demonstrate that the radial variation of viscosity that is required to reconcile the totality of the GIA data that are presently available is not inconsistent with the radial profile that has been independently inferred on the basis of observations related to the convection process itself. This is a rather profound result since it suggests that sublithospheric mantle rheology could well be essentially Newtonian rather than *non-Newtonian*.

From a paleoclimatological perspective the development of an extremely realistic global theory of the GIA process has also begun to enable very detailed calculations of climatologically important Earth system properties to be realized. Perhaps foremost among these concerns the thickness of glacial ice that must have existed over the known centers of continental glaciation at Last Glacial Maximum (LGM). As I discuss in detail in section 5, very significant advances have recently been achieved in the development of observational constraints upon this important property of the full glacial state that may be successfully brought to bear through use of the global theory. Of equal significance to the issue of ice amount at LGM is the question of the impact on the geographical distribution of land and sea that was caused by the lowering of sea level due to ice sheet growth. In certain regions of the globe, such as the Bering Strait, the English Channel, and the Indonesian Archipelago, vast land bridges were created by the fall of sea level, and these have proven to be especially important to the understanding of human migration patterns, most especially concerning the first habitation of the North and South American continents. These land bridges and the great tracts of continental shelf that were also exposed at LGM became important sources of the increasing atmospheric load of terrigenous dust that is known to have been characteristic of the full-glacial state. Also discussed in section 5, and constituting additional material of considerable climatological significance, are the question of the impact upon the *thermohaline circulation of the oceans* of the geographic partitioning of LGM ice sheet mass, the question of the impact of the last deglaciation event of the current ice age upon modern measurements of the rate of global sea level rise that appears to be a robust feature of the climate system at present, and finally, the issue of the feedback of the ice age cycle of glaciation and deglaciation upon the *orbital insolation anomaly* regime whose variations are generally believed to be responsible for the ice age cycle itself.

In section 2 I will first set the stage for these analyses of the solid-Earth geophysical and climatological implications of glacial-cycle-induced variations in the level of the sea by providing an overview of the observational data upon which our understanding is currently based. Section 3 provides a complete review of the derivation and structure of the so-called "sea level equation" that my students and I at Toronto have continued to develop as the primary theoretical vehicle for the interpretation of these observations. Section 6 focuses upon recent progress in developing an acceptable theory of ice age occurrence, while a statement of conclusions along with a discussion of important outstanding issues is given in section 7. It is hoped that the glossary will be helpful to the reader for whom the ideas discussed herein are unfamiliar.

2. GEOLOGICAL, GEOPHYSICAL, AND ASTRONOMICAL OBSERVATIONS

The primary set of data that may be invoked to constrain the variations of relative sea level that have occurred in response to the glaciation-deglaciation process consists of records from a variety of different geological archives. These include radiocarbon-dated histories of the radial displacement of the shoreline, relative to the present level of the sea, in which the carbon-dated material may consist of mollusc shells or driftwood or even whale bone. Of similar importance are radiocarbon or U/Th dated coral sequences from the tropics or subtropics where conditions amenable to the growth of coral exist. Finally, and certainly the most subtle measure of the history of the globally averaged (in some sense) changes of sea level, there is the information recorded as oxygen isotope stratigraphies in deep-sea sedimentary cores. In the following, I will first provide an overview of these different types of geological records and then will focus successively on the solid-Earth geophysical and astronomical signatures of the ice age cycle that have continued to play such an important role in our understanding of both the planetary interior and the long timescale climate variability that continues to occur on its surface.

2.1. Geological Recordings of Relative Sea Level History

Of the three sources of geological information mentioned above, by far the most voluminous consists of the postglacial (Holocene) records that have been collected since approximately 1960 when the ^{14}C method of radioactive age determination [*Libby*, 1952] first came to be widely applied to the problem of reconstructing sea level history. In employing this method to determine the age of a particular indicator of relative sea level, there are of course a variety of corrections that one must apply to the raw age in order to determine sidereal age. Since the ^{14}C clock depends upon ^{14}C abundance and since the production rate varies with the changing strength of

Earth's magnetic field due to its modulation of cosmic ray flux, the map from ^{14}C age to sidereal age is not linear but rather exhibits a number of well-developed plateaux. For the *Holocene period*, which we might reasonably assume to constitute the last 10 kyr of Earth history, this map may be considered to be well known on the basis of the tree ring calibration [e.g., *Stuiver et al.*, 1986]. In the rather recent past [*Fairbanks*, 1989; *Bard et al.*, 1990] this calibration was successfully extended to ~35 kyr B.P. (before present) by simultaneously dating a collection of coral samples from the Island of Barbados in the Caribbean, using both the ^{14}C method and the U/Th method [*Edwards*, 1988]. Since the U/Th method applied to corals has been shown to give an age that is essentially sidereal and since the discrepancy between the ^{14}C age of an LGM sample and the U/Th age is very nearly 3 kyr, it is clear that as one reaches back into this full glacial period (LGM occurred at ~21 sidereal kyr B.P.), the error between ^{14}C age and sidereal age becomes highly significant. Also significant when the ^{14}C method is employed to determine the age of marine specimens is the so-called "reservoir correction," which is of order 450 years and which is required to account for the fact that the ocean with which the sample equilibrates is typically 450 years older than the sample itself. Rather than counting β decays as in the original *^{14}C dating* method of *Libby* [1952], ^{14}C dating is now often performed using accelerator mass spectrometry (AMS) whereby the atoms of ^{14}C in the sample may be counted directly [*Litherland*, 1980], a technique through which it is now possible to determine the age of samples that are much smaller than could previously be dated using the conventional method. The standard calibration procedure that is now conventionally employed to convert ^{14}C age to sidereal age is that described by *Stuiver and Reimer* [1993].

There currently exists an extremely large collection of ^{14}C dated records of relative sea level history, the most extensive archive of which I am aware being that which has been developed in my own group at the University of Toronto. There are currently 577 distinct time series in this archive which are based upon 5397 distinct ^{14}C dated samples. A preliminary "reconnaissance" version of this collection was presented by *Tushingham and Peltier* [1992], but this has been considerably refined and enlarged since that time. Figure 1 presents the locations of the points on the Earth's surface from which individual time series are available, and it is clear that their distribution provides global coverage. The circles and triangles indicate the sites that were ice-covered at LGM and those that were ice free, respectively. At the former sites, which include those from Canada, from Fennoscandia (centered on the Baltic Sea), and from the Barents and Kara Seas, Scotland, Antarctica, and Patagonia, sea level is usually falling due to the glacial isostatic rebound of the Earth's crust. Beyond the ice sheet margins the spatial variations of relative sea level are also extreme, and these variations will be discussed in detail below.

By way of providing specific examples of the nature of these variations and of the data that determine them, Figure 2 is a photograph of a flight of raised beaches at a site called Richmond Gulf, which is located on the southeast coast of Hudson Bay (Canada), near the center of postglacial rebound where present-day rates of relative sea level fall approach 1.2 cm yr^{-1}. The data from the southeast Hudson Bay region and from the equivalent "center of rebound" location in Fennoscandia, Angerman River, are shown on Figures 3a and 3b, respectively, in which individual points are based upon ^{14}C measurements on collected samples but for which sample age is in sidereal years determined by employing the *Stuiver and Reimer* [1993] calibration. For the southeast Hudson Bay location the observations are primarily based upon age measurements on shell samples (all unreworked and found in growth position). Those based upon the species *Mytilus edulis*, an intertidal species which therefore provides good control on the actual location of sea level, provide the most reliable information.

The complete collection of ^{14}C data employed to construct the southeast Hudson Bay relative sea level curve is provided in Table 1 since these data have been in danger of being lost to posterity and have not previously been collected in one place. The rsl curve for southeast Hudson Bay is, in fact, a composite record based upon samples collected over a broad spatial area enclosed between 76.5° and 79°W longitude and 51.5° and 56.5°N latitude. That it is not unreasonable to combine the individual data sets from all sites in this area follows from the fact that the entire region was deglaciated essentially simultaneously at ~7.9 kyr ago (on the ^{14}C timescale). Furthermore, the *marine limit* in this region is found everywhere at ~270 m above mean sea level. This data point is plotted as a solid circle on Figure 3a and is undoubtedly the most accurately determined sea level datum in the entire southeast Hudson Bay data set. The data points denoted by asterisks on Figure 3a and in Table 1 were culled on the basis of geomorphological arguments and were not employed in further analyses. Figure 3c shows one of the individual data sets from which the southeast Hudson Bay composite record has been constructed, namely, that of *Hardy* [1976] based upon shell samples collected from the east coast of James Bay. Also shown on Figures 3a–3c are best fit exponential curves to the individual data sets (shown as solid lines) of the form $\text{rsl}(t) = A\ [e^{(t-t_p)/T} - 1]$ in which t is age, t_p is the present time, T is a characteristic relaxation time for the rsl curve in question, and A is its amplitude. The parameters A and T for each curve are determined using a Monte Carlo procedure, in which the elevation errors were assumed to be ±0.5 m for elevation <10 m, ±5% for elevations between 10 and 50 m, and ±2.5 m for elevations greater than 50 m, and these parameters are shown on each plate for the different

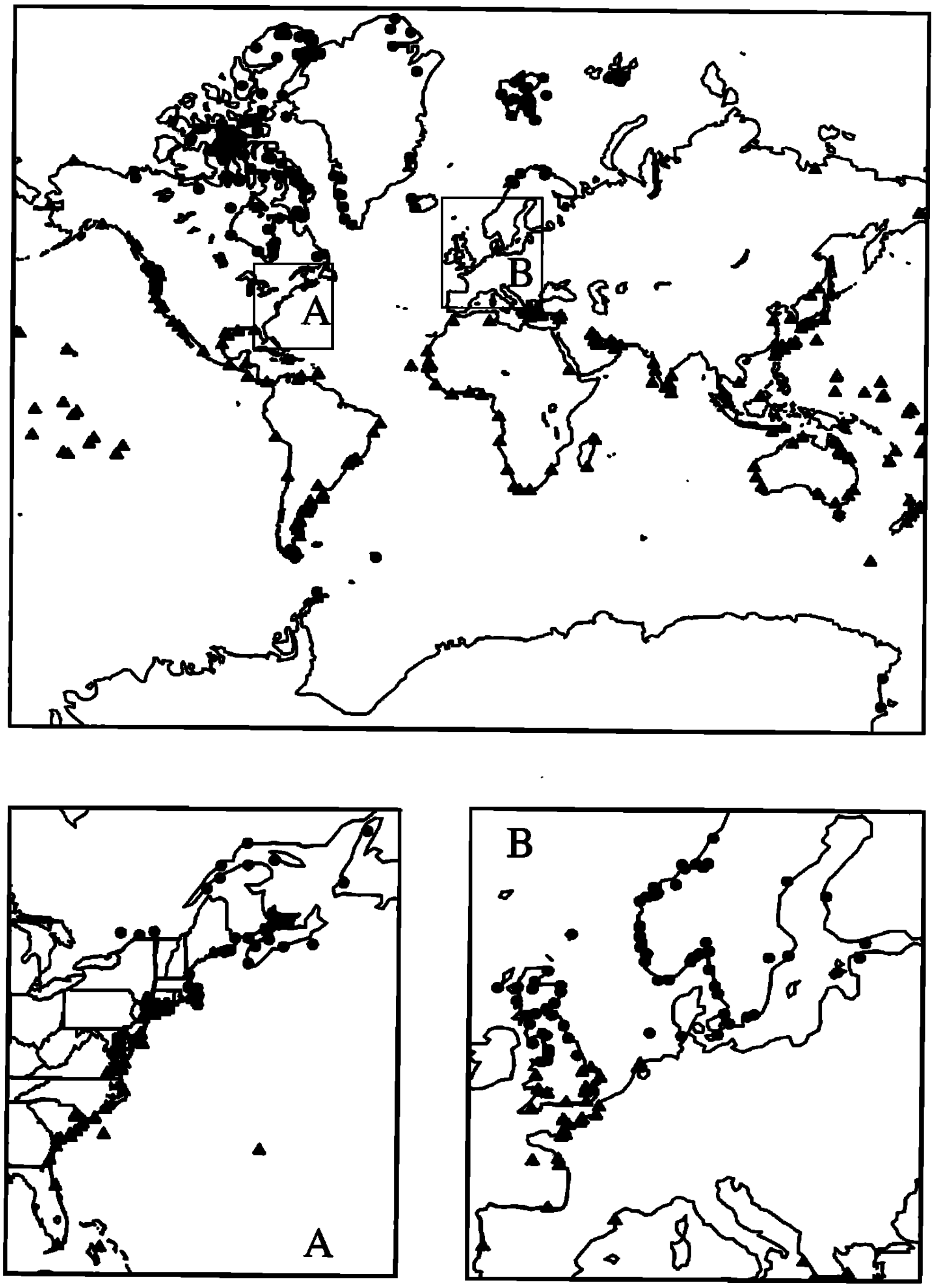

Figure 1. Location maps of sites on the Earth's surface from which ^{14}C dated time series of relative sea level history through the Holocene epoch are available and recorded in the University of Toronto archive. Circles denote sites that were ice covered at Last Glacial Maximum, whereas triangles denote sites that were not.

data sets. In performing such data analyses it is often important to first adjust the raw elevations (listed in Table 1 for southeast Hudson Bay) by adjusting them downward by a distance determined by the storm-beach effect (see *Allard and Tremblay* [1983] for a detailed discussion of this effect for the southeast Hudson Bay region). This is especially important when driftwood samples are employed to help constrain the most recent portion of the rsl curve. In our analysis we conventionally estimate the storm-beach offset directly by performing the Monte Carlo fit of the two-parameter model (A, T) as a function of the assumed storm-beach offset and then define the offset as that which minimizes the chi-square misfit between the exponential model defined above and the observations. Figure 3d shows the results of this analysis of the southeast Hudson Bay data which delivers an estimate of the storm-beach offset of 6 m, essentially identical to the value determined by *Allard and Tremblay* [1983] on other grounds. The data shown for the Angerman River site in Sweden on Figure 3b

Figure 2. Photograph of the flight of raised beaches at Richmond Gulf, Quebec, which is located on the southeast coast of Hudson Bay near the center of the ongoing postglacial rebound of the Laurentian Shield of Canada. Present-day sea level is located in the lower right-hand corner.

were originally dated using the varve-based chronology of *Lidén* [1938], the essential validity of which was subsequently confirmed using ^{14}C measurements. Inspection of the information shown on Figures 3a and 3b demonstrates that the data from the center of Laurentian rebound (southeast Hudson Bay) and those from the center of Fennoscandian rebound (Angerman River) are characterized by relaxation times of ~3.4 and 4.2 kyr, respectively. The latter number may somewhat underestimate the actual relaxation time at the center of Fennoscandian rebound, as analysis of the recompilation of the data provided by *Cato* [1992] delivers a value of ~5 kyr. Also shown are predictions of the rsl histories that should be observed at these sites based upon the ICE-4G model of the last deglaciation event of the current ice age [*Peltier*, 1994] and for both the VM1 (dotted curves) and VM2 (dashed curves) viscosity models which will play an important role in the discussion to follow. Inspection will show that the theoretical model of the GIA process fits the observations well and that the VM2 viscosity model is preferred over VM1 on the basis primarily of the Angerman River data from Fennoscandia.

As we move farther away from the ice-covered regions into the immediately peripheral areas, we observe a radical change in the nature of the rsl history. This is illustrated on Figure 4 on which I have shown a series of four high-quality records from Great Britain. This geographical region is probably the most exotic on Earth from the perspective of GIA as it is not only immediately peripheral to the large ice sheet that covered Scandanavia, and therefore subject to the process of "*proglacial forebulge* collapse," but it was itself also glaciated in the north, with the thickest ice cover found over the Scottish Highlands. In moving from the Tay Valley and Solway Firth sites in Scotland, south to the Fenlands on the east coast, and finally to the Bristol Channel in the southwest of England, one observes radically different styles of postglacial relative sea level change to have been characteristic of the different locations. At Tay Valley and Solway Firth, which are located near what was the center of the Scottish ice sheet, the rsl records are highly

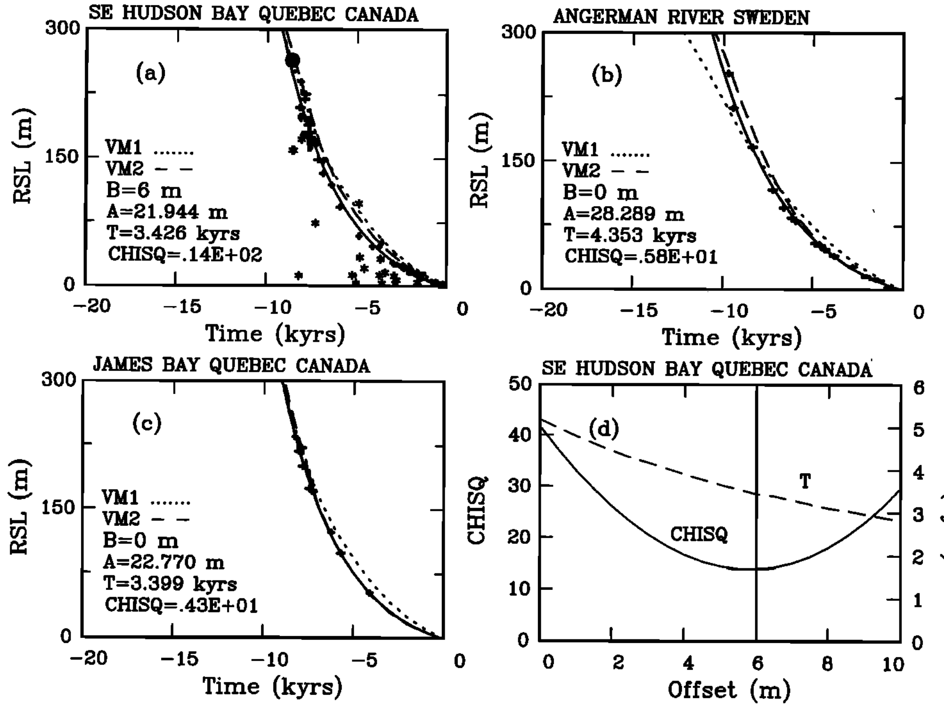

Figure 3. (a) Relative sea level data from the entire southeast Hudson Bay region as listed in Table 1. Radiocarbon ages have been converted to sidereal age using the Calib. 3.0 software of *Stuiver and Reimer* [1993]. The data denoted by the asterisks are believed not to relate directly to sea level for geomorphological reasons. The solid curve denotes the best fit exponential function of the form $\mathrm{rsl}(t) = A\,[\exp(t/T) - 1]$ to the data after correction for the storm-beach effect, which amounts to a positive offset that must be subtracted from the raw heights listed in Table 1. The two parameters of the exponential model, A and T, are determined by application of a Monte Carlo procedure. This procedure is applied for a range of assumed storm-beach offsets, and the model is selected which minimizes the variance between the model and the totality of the data. (d) The results of this detailed analysis for the southeast Hudson Bay data which delivers a best estimate for the relaxation time T of ~3.4 kyr and a value for the storm-beach offset of 6 m, consistent with the inference (by other means) of *Allard and Tremblay* [1983]. Also shown in Figure 3a are the predictions of the ICE-4G (VM1) and ICE-4G (VM2) models of the glacial isostatic adjustment process. (b) Same as Figure 3a but for the rsl data from Angerman River in Sweden. (c) Same as Figure 3a but for a subset of the southeast Hudson Bay data, namely, that from the east coast of James Bay of *Hardy* [1976].

nonmonotonic with early and late sea level fall interrupted by a period of sea level rise centered on ~10 kyr B.P. This nonmonotonicity is caused when the diminishing postglacial rebound of the crust induced by the removal of the Scottish ice sheet becomes so slow that it is insufficient to overcome the influence of rising sea levels caused by the continuing melting of glacial ice elsewhere on Earth's surface (primarily Antarctica). As one moves farther to the south in Britain, the rsl records are transformed into histories of monotonic postglacial submergence. This submergence is strongly influenced by the collapse of the forebulge of the Fennoscandian ice sheet but also by that associated with the deglaciation of Scotland as well as by the deglaciation of North America and Antarctica. The glacial forebulge, a feature that will figure prominently in the analyses to follow, consists of an uplift of the solid-Earth exterior to an ice sheet that is created simultaneously with the depression of the crust that is induced beneath the ice load itself. An early appreciation of this subtle feature of the glacial isostatic adjustment process was presented by *Daley* [1934]. When an ice sheet disintegrates, not only does the crust rebound in the once loaded region, but the forebulge also collapses, thus causing sea level to rise in such regions by an amount which is in excess of that which would otherwise occur. The region of the surface of Earth in which the forebulge effect is strongest is that which lay to the south of the North American ice sheet along the east coast of the continental United States. Each of the records from the British Isles shown in Figure 4 is also compared with predictions based upon variants of the global theory of GIA, shown as the solid and dashed curves, that is discussed section 3.

A further set of ^{14}C dated rsl records is presented for comparison on Figure 5, and each of these records is taken from individual sites in what I have previously referred to as the "far field" of the ice sheets, namely, from positions well removed from any concentration of land ice. One of these four records is taken from the coast of the South American continent in (Santos-Itan-

TABLE 1. Complete Collection of Available ^{14}C Data for the Southeast Hudson Bay Region

Reference	*Latitude °N*	*Longitude °W*	*Altitude, m*	*Sample*	*Laboratory*	*^{14}C Age†*	*±1σ*	*Cal. Age‡*	*Area*	*Altitude Correction§*
1	56.28	76.50	172	*Mytilus edulis*	GSC 1261	6430	150	7300	RG	
1	56.28	76.49	77	*Mytilus edulis*	GSC 1328	6390	180	7260	RG*	
1	56.45	76.50	154	*Mytilus edulis*	GSC 1364	6230	220	7100	RG	
1	56.28	76.50	138	*Mytilus edulis*	GSC 1287	6000	160	6850	RG	
2	55.58	77.32	58	*Mytilus edulis*	GSC 2070	3330	60	3560	CIs	
2	55.58	77.30	44	*Mytilus edulis*	GSC 2348	2760	80	2850	CIs	
2	55.58	77.30	29	*Mytilus edulis*	GSC 2129	2030	60	1980	CIs	
2	55.58	77.30	22	*Mytilus edulis*	GSC 2074	1790	50	1710	CIs	
3	55.58	77.20	0	*Mytilus edulis*	GSC 2470	0	60	0	CIs*	
4	60.05	77.33	35	*Mytilus edulis*	GSC 1588	3380	130	3630	PV*	
5	60.21	77.26	35	*Mytilus edulis*	Gif 1818	3400	80	3630	PV*	
7	55.58	77.30	13.31	*Mytilus edulis*	Qu-1064	890	100	780	CIs	
7	55.36	77.62	8.89	*Mytilus edulis*	Qu-1068	490	80	520	NIs	
7	55.36	77.62	13.21	*Mytilus edulis*	Qu-1081	580	70	550	NIs	
7	55.39	77.50	21.43	*Mytilus edulis*	Qu-1087	1680	390	1550	NIs	
7	55.36	77.62	31.71	*Mytilus edulis*	Qu-1097	2470	100	2700	NIs	
7	55.36	77.62	29.94	*Mytilus edulis*	Qu-1098	2230	100	2300	NIs	
7	55.36	77.62	28.91	*Mytilus edulis*	Qu-1099	2430	100	2430	NIs	
7	55.36	77.62	27.26	*Mytilus edulis*	Qu-1100	2026	100	1955	NIs	
7	55.36	77.62	26.57	*Mytilus edulis*	Qu-1101	2260	100	2320	NIs	
7	55.36	77.62	23.69	*Mytilus edulis*	Qu-1102	2020	100	1950	NIs	
7	55.36	77.62	21.94	*Mytilus edulis*	Qu-1103	2050	100	1990	NIs	
7	55.36	77.62	20.38	*Mytilus edulis*	Qu-1104	1760	90	1690	NIs	
7	55.36	77.62	18.80	*Mytilus edulis*	Qu-1105	1680	90	1550	NIs	
7	55.36	77.62	17.26	*Mytilus edulis*	Qu-1106	1490	90	1350	NIs	
7	55.63	77.13	34.25	*Mytilus edulis*	Qu-1288	2860	100	2950	Man.	
7	55.63	77.13	52.30	*Mytilus edulis*	Qu-1290	3480	100	3710	Man.	
7	55.63	77.13	31.5	*Mytilus edulis*	Qu-1295	2410	90	2360	Man.	
7	55.63	77.13	32	*Mytilus edulis*	Qu-1296	2750	80	2850	Man.	
7	55.63	77.13	4.75	*Mytilus edulis*	Qu-1298	670	80	650	Man.	
8	53.67	78.33	99	*Mytilus edulis*	Qu-120	4320	150	4860	JB*	100
9	53.55	77.67	178	*Mytilus edulis*¶	GSC-1959	6500	90	7380	JB	
1	56.35	76.45	24	*Hiatella arctica*	GSC-1326	4070	140	4530	RG*	
1	56.45	76.42	153	*Hiatella arctica*	GSC-1725	6000	210	6850	RG*	
1	56.27	76.50	172	*Hiatella arctica*	GSC-1238	6720	150	7540	RG	
8	53.67	78.33	99	*Hiatella arctica*	Qu-256	5080	180	5890	JB	
8	53.62	77.72	168	*Hiatella arctica*	GSC-2244	6810	80	7610	JB	
9	51.47	77.42	205	*Hiatella arctica*	GSC-2135	7360	100	8130	JB	
3	53.15	76.90	174	*Hiatella arctica*	GSC-1928	6640	180	7520	JB	
9	51.60	77.40	203	*Clinocardium cilantrum*	GSC-2161	7130	110	7910	JB	
7	55.58	77.30	16.02	mixed shells	Qu-1065	3460	90	3690	CIs*	
7	55.39	77.50	6.41	mixed shells	Qu-1066	3310	100	3550	MIs*	
7	55.39	77.50	6.41	mixed shells	Qu-1007	4420	100	4985	MIs*	
7	55.39	77.50	19.17	mixed shells	Qu-1082	3160	360	3370	MIs*	
7	55.39	77.50	15.21	mixed shells	Qu-1083	2780	110	2860	MIs*	
7	55.39	77.50	15.24	mixed shells	Qu-1084	1360	230	1285	MIs	
7	55.39	77.50	10.41	mixed shells	Qu-1085	2560	350	2730	MIs*	
7	55.39	77.50	6.32	mixed shells	Qu-1086	2720	370	2790	MIs*	
7	55.63	77.13	8	mixed shells	Qu-1292	1680	90	1550	Man.*	
7	55.63	77.13	65	mixed shells	Qu-1294	4270	100	4840	Man.	
8	53.75	78.87	16	mixed shells	Qu-248	4470	170	5200	JB*	
8	53.73	78.75	37	mixed shells	Qu-121	4110	120	4785	JB*	40
8	53.68	78.15	123	mixed shells	Qu-119	5560	130	6380	JB	125
8	53.72	77.97	172	mixed shells	Qu-172	6810	200	7610	JB	180
8	53.73	77.87	183	mixed shells	Qu-247	6910	350	7670	JB	186
8	53.70	77.87	166	mixed shells	Qu-245	7110	180	7910	JB	183
8	53.58	77.50	175	mixed shells	GSC-2239	7290	90	8070	JB*	
9	53.57	77.67	171	mixed shells	GSC-1959	6500	90	7380	JB	174
8	53.47	77.65	164	mixed shells	Qu-249	6660	190	7520	JB	177
8	53.35	77.57	162	mixed shells	Qu-124	7880	160	8580	JB*	
8	53.35	77.57	162	mixed shells	Qu-122	7750	180	8490	JB*	
8	52.78	77.33	235	mixed shells	Qu-369	7370	100	8130	JB	245
8	52.77	77.30	170	mixed shells	Qu-250	6930	190	7690	JB	195

TABLE 1. (continued)

Reference	*Latitude °N*	*Longitude °W*	*Altitude, m*	*Sample*	*Laboratory*	*^{14}C Age†*	*±1σ*	*Cal. Age‡*	*Area*	*Altitude Correction§*
8	52.57	77.33	200	mixed shells	Qu-253	6950	210	7710	JB	201
8	52.42	77.27	200	mixed shells	Qu-258	7440	210	8170	JB	215
8	52.22	77.92	15	mixed shells	Qu-368	7440	180	8170	JB*	
8	52.30	77.08	218	mixed shells	Qu-254	7140	210	7920	JB	225
9	52.22	77.13	222	mixed shells	Qu-252	7030	210	7880	JB	231
9	51.47	77.43	203	mixed shells	GSC-2135	7360	100	8130	JB	
8	51.47	77.43	203	mixed shells	Qu-370	7120	210	7910		
7	55.34	77.65	11.76	driftwood	Qu-1088	410	80	490	BP	
7	55.34	77.65	11.8	driftwood	Qu-1089	0		0	BP*	
7	55.34	77.65	7	driftwood	Qu-1090	130	80	255	BP	
7	55.34	77.65	6.91	driftwood	Qu-1091	0		0	BP*	
7	55.34	77.65	6.2	driftwood	Qu-1092	40	80	40	BP	
7	55.34	77.65	6.2	driftwood	Qu-1093	190	90	275	BP	
7	55.34	77.65	5.62	driftwood	Qu-1094	70	90	70	BP	
7	55.34	77.65	4.5	driftwood	Qu-1095	60	80	60	BP	
7	55.34	77.65	4.5	driftwood	Qu-1096	20	80	20	BP	
7	55.36	77.62	8.53	driftwood	Qu-1107	720	80	660	NIs	
7	55.36	77.62	7.55	driftwood	Qu-1108	120	90	240	NIs	
7	55.36	77.62	9.12	driftwood	Qu-1201	210	80	280	CIs	
7	55.39	77.50	12.86	driftwood	Qu-1202	720	80	660	MIs	
7	55.39	77.50	12.86	driftwood	Qu-1203	680	80	650	MIs	
7	55.39	77.50	12.86	driftwood	Qu-1204	570	90	550	MIs	
7	55.39	77.50	6.32	driftwood	Qu-1205	350	80	330	MIs	
7	55.39	77.50	5.45	driftwood	Qu-1206	150	80	260	MIs	
7	55.39	77.50	8.90	driftwood	Qu-1207	400	90	480	MIs	
7	55.39	77.50	6.76	driftwood	Qu-1208	180	80	270	MIs	
7	55.36	77.62	4.83	driftwood	Qu-1209	160	100	270	NIs	
7	55.36	77.62	9.12	driftwood	Qu-1210	130	100	250	CIs	
7	55.36	77.62	5	driftwood	Qu-1211	0		0	NIs*	
7	55.34	77.65	10.30	driftwood	Qu-1212	150	100	260	BP	
7	55.63	77.13	4.75	driftwood	Qu-1299	480	90	510	Man.*	
10	53.83	79.00	53	driftwood	L-443A	3700	130	4070	JB	
5	60.03	77.20	10	beluga	Gif-1819	500	80	520	PV	
6	55.28	71.77	30?	charcoal	Gif-1567	3300	110	3480	GWR*	

References: Haselton (as cited by *Hillaire-Marcel* [1976]); 2, Craig and R. I. Walcott (as cited by *Walcott* [1980]); 3, *Lowdon and Blake* [1980]; 4, *Portman* [1970]; 5, *Bournerias* [1972a, b, c]; 6, *Plumet* [1974]; 7, *Allard and Tremblay* [1983]; 8, *Hardy* [1976]; 9, Vincent (as cited by *Hardy* [1976]); 10, *Lee* [1962]. Areas are RG, Richmond Gulf; CIs, Castle Island; PV, Povungnituk; NIs, Nielsen Island; MIs, Merry Island; Man., Manitounuk Peninsula; JB, eastern James Bay; BP, Bill of Portugal Island; and GWR, Great Whale River.

*Shells clearly displaced below sea level and excluded from compilation used to construct the Monte Carlo fit shown on Figure 3a.

†Ages (in years) without correction for aging effect of seawater and without normalization (approximately conventional ages as both corrections are 400–450 years but of opposite sign; see *Bard* [1988] and *Hillaire-Marcel* [1981]).

‡Cal. ages (in years) are ages calibrated through use of the Calib 3.0 program [*Bard*, 1988].

§Mean corrected elevation for the presumed corresponding paleo-sea level based upon geomorphological criteria as discussed by *Hardy* [1976].

¶A replicate measurement at the same site but on *H. arctica* shells yielded an age of 5080 ± 180 (QU-256), raising concern about the validity of this datum (which is critical as the mid-SL curve interval is supported by very few data).

haen) Brazil, one is from the Persian Gulf in the Middle East (Kuwait Bay), another is from New Zealand (Christchurch), and the last is from the Island of Oahu in the Hawaiian chain in the central Pacific Ocean. Inspection of these records will demonstrate that they are each dominated through late Holocene time by a period of falling sea levels, following a time of maximum sea level (a so-called "highstand") that occurs at roughly 4–5 kyr B.P. Typically, in these far-field regions the highest stand of sea level forms ~2 m above present sea level. Thereafter, sea level is said to "regress." The processes that contribute to this characteristic nonmonotonicity are intimately connected with the fact that mean sea level, by definition, is a surface of constant gravitational potential. Both during and following the period of land ice melting, water must be continuously redistributed over the surface of the oceans in such a way as to preserve the constancy of the gravitational potential on the ocean surface, the precise value of which is, of course, time-dependent. In the presence of the strong deformations of planetary shape that accompany the GIA process, this is possible only if the depth of the water in the oceans is a continuously changing function of geographical location. In particular, water is continuously drawn into the regions of proglacial forebulge collapse and also into the regions immediately peripheral to the continents in the far field of the ice sheets. Across the coastlines of these continents, and due in part to the increasing weight of

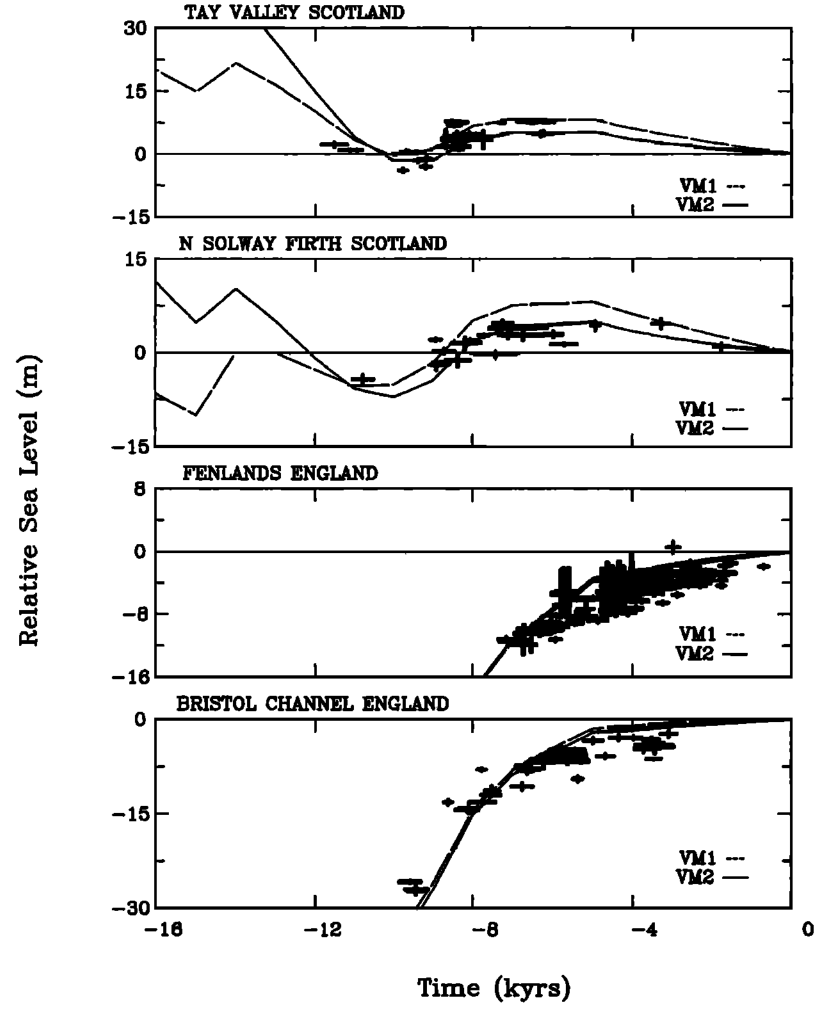

Figure 4. Examples of ^{14}C dated relative sea level curves from four sites in the British Isles: Tay Valley and Solway Firth in the once ice-covered region of Scotland and the Fenlands and Bristol Channel, which were both beyond the southernmost extent of the Scottish ice sheet. As discussed in text, the records from Scotland are highly nonmonotonic due to the superposition at these locations of the influence of rebound of the crust due to ice removal and the influence of the collapse of the Fennoscandian forebulge and continuing addition of mass to the oceans caused by the melting of (primarily) the Antarctic ice sheet. The observed records of postglacial sea level change are compared to the predictions of two variations on the ICE-4G (VM2) model that differ from one another only by slight changes in the history of disintegration of the local Scottish ice sheet.

the offshore water load caused by the melting ice sheets, so-called "*hydroisostatic*" tilting occurs as matter is forced to flow from the mantle under the ocean basins toward the continents, thus causing the continents to be uplifted and sea level to regress. From a global perspective the simple physical constraint that mean sea level be defined by a surface of constant gravitational potential therefore leads to extremely complex spatial structure in rsl history. Each of the far-field rsl histories shown on Figure 5 is also compared to the predictions of the global theory (based upon the ICE-4G (VM2) model) to be described in section 3, and once again it is clear that the observations are extremely well fit by the theory.

All of the rsl histories described to this point have been based upon the ^{14}C dating of appropriate sea level indicators and have consisted of time series which, for the most part, were limited to the Holocene epoch, none being sufficiently long to extend to LGM. This is clearly extremely unfortunate as it means that if such records were the only ones available, then no information would exist that was capable of providing a direct measure of the amount of ice that melted across the last glacial interglacial transition. Fortunately, there does exist at least one such high-quality record of the glacial to *interglacial* change in sea level, and this consists of the previously mentioned U/Th dated coral-based record from the Island of Barbados in the Caribbean Sea [*Fairbanks*, 1989; *Bard et al.*, 1990]. This record is shown on Figure 6 along with the fit to it of the same theoretical ICE-4G (VM2) model used to predict the ^{14}C dated records discussed above. Inspection of these data will demonstrate that the total rise of sea level from LGM to present at this site has been ~120 m. In the analyses of the GIA data that will be provided in section 3 this coral-based record will come to assume considerable importance, as will additional coral-based records from the Pacific Ocean region, including those from the Huon Peninsula of Papua New Guinea, Morley and Sumba Islands in the west equatorial Pacific, and the Island of Tahiti in the central Pacific.

Even with the availability of the record of rsl rise based upon Barbados corals, however, there remains an extremely important characteristic of the record of late Pleistocene sea level change that is not adequately constrained. This concerns the question of the duration of the period during which sea levels remained near the LGM lowstand. This issue is extremely important from the perspective of the global theory of GIA to be dis-

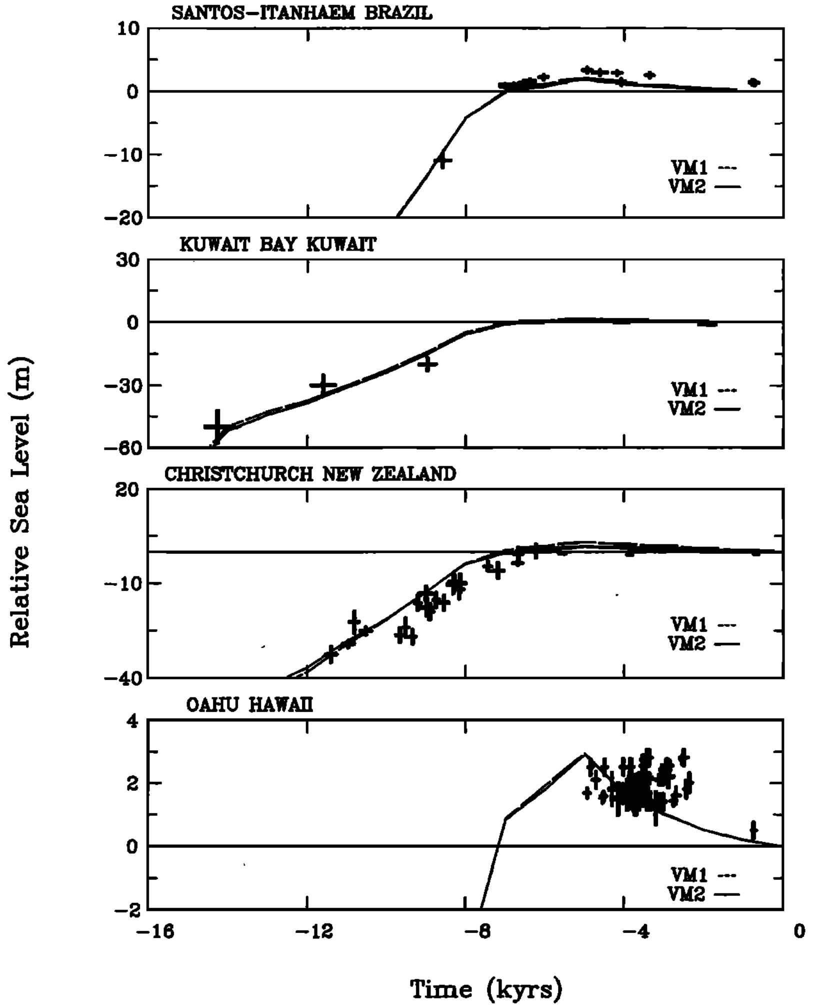

Figure 5. Examples of ^{14}C dated relative sea level curves from four sites in the region to which I refer to as the "far field" of the ice sheets. These include Santos-Itanhaem, Brazil, on the northeast coast of the South American continent; a site in the Persian Gulf in the Middle East; another from Christchurch, New Zealand; and finally, a fourth from the Island of Oahu in the Hawaiian Emperor Chain in the Pacific Ocean. Also shown are predictions of the histories of sea level change that should be observed at these sites based upon the ICE-4G (VM2) model.

cussed in section 3. Depending upon the timescale over which the full glacial state is maintained, the departure of the system consisting of ice, ocean, and solid Earth from a state of isostatic equilibrium at LGM may be either large or small. If the ice sheets that accumulate during the glaciation phase of the ice age cycle accrete monotonically and uniformally over this typically 90-kyr period, then the system will quite likely be close to isostatic equilibrium at LGM, as we will see. If, on the other hand, a very substantial fraction of the total mass were to accumulate over the 10 kyr prior to LGM, for example, implying that the sea level depression during *oxygen isotope stage* 3 was small, then a significant degree of isostatic disequilibrium would have existed at LGM, and this would have interesting consequences. It is therefore extremely important that a very recent advance has occurred [*Chappel et al.*, 1996] that has much more strongly constrained the global variations of sea level through the glaciation phase of the ice age cycle than was previously possible. This advance is connected to the coral-based record from the Huon Peninsula and its relation to the longer sea level record based upon the *oxygen isotope stratigraphy* in Ocean Drilling Program (ODP) core V19-30 of *Shackleton* [1987]. *Shackleton* [1967] established that $\delta^{18}O$ measured on benthic foraminifera in deep-sea sedimentary cores constitutes a reliable proxy for continental ice volume and thus sea level. More accurate dating of the coral samples from the Huon Peninsula has now led [*Chappel et al.*, 1996] to the *Eemian interglacial* to Holocene sea level history at Huon shown on Figure 7b where it is compared to the previously incorrect history (on Figure 7a) as well as to the history inferred on the basis of the oxygen isotope record from the Shackleton core. It will be clear by inspection of this comparison that the redated record of rsl change at Huon now fits the independent inference of the Eemian to Holocene change of sea level based upon oxygen isotopes through the entire cycle of glaciation and deglaciation. Furthermore, it is clear by inspection of both of these records that they imply glaciation to have been a predominantly slow and approximately monotonic process, modulated weakly by orbital forcing, which was not significantly interrupted until the onset of deglaciation that occurred subsequent to LGM at 21 kyr B.P. (not withstanding the millennium scale variability in the mass of Laurentian ice that occurred during OIS 3, which is required to understand the so-called *Heinrich* [1988] events and the Dansgaard-Oeschger oscillation

[*Sakai and Peltier*, 1997] phenomenon). This additional piece of information from the geological record at Huon will also play an extremely important role in the discussion to follow.

2.2. Geophysical Signatures of the Ice Age Cycle

Probably the most important geophysical signature of the ice age cycle, at least from an historical perspective, consists of observations of the so-called free air gravity anomaly over the formerly glaciated regions of the surface of the planet. Since the *free air gravity anomaly* provides a direct measure of the existing degree of isostatic disequilibrium and since this will depend strongly upon the radial profile of mantle viscosity as well as upon deglaciation history, its importance has long been recognized, perhaps most clearly by, for example, *Walcott* [1973]. A negative free air gravity anomaly is expected to be characteristic of a geographical region in which postglacial rebound of the crust is still ongoing. Figure 8 shows geoid anomaly maps for both Canada and Fennoscandia based upon the satellite-derived GEM-T2 field of *Marsh et al.* [1990]. An anomaly in geoid height is simply related to the free air anomaly. Inspection of the anomalies in these regions reveals an extremely large negative geoid anomaly, of magnitude in excess of 70 m, centered over the Hudson Bay region of Canada and therefore well correlated with the central dome of the ancient Laurentide ice sheet, the largest of the continental ice sheets which existed at LGM and which subsequently disappeared. Given the good spatial correlation of the negative geoid anomaly over Hudson Bay with the position of this ice sheet, it is not at all unreasonable that one should entertain the idea that the anomaly could be related to incomplete glacial isostatic adjustment. For example, *Walcott* [1980] was a strong advocate of this view. As I will discuss in section 4.3, however, the anomaly is also perfectly correlated with the continental craton itself, and recent analyses have clearly shown it to be supported for the most part by the mantle convection process [*Peltier et al.*, 1992; *Pari and Peltier*, 1996]. Turning attention to Figure 8b, which shows the GEM-T2 geoid anomaly field over northwestern Europe, it is clear that no distinct negative free air anomaly exists over Fennoscandia at all. This does not, of itself, immediately imply that the anomaly over Canada is unlikely to be associated with glacial isostatic disequilibrium, since the spatial scales of the ice sheets that covered these two regions were so discrepant. If the viscosity of the upper mantle and transition zone were relatively low while the viscosity of the lower mantle were high, it is conceivable that the free air anomaly over the smaller-scale region of Fennoscandia, in which the GIA process is relatively insensitive to lower mantle viscosity (see section 4), could already have relaxed to a very small value, whereas that over the much larger-scale region of Canada (which is highly sensitive to lower mantle viscosity) could have remained high. As I will discuss below, viscosity models of this kind turn out to be untenable as they are firmly rejected by the relative sea level observations discussed in section 2.1. Indeed, we have already seen (Figure 3) that the relaxation time that is characteristic of the GIA process in Laurentia is lower than that in Fennoscandia. Models which fit observed relative sea level histories predict present-day free air gravity (and geoid) anomalies that are rather small, insignificantly small, in fact, when compared to the observed free air anomaly over Hudson Bay. Since models of the mantle convection process, based upon the use of seismic tomographic imaging to constrain the internal mantle density heterogeneity and tuned to fit the global geoid, accurately predict the observed free air anomaly over Hudson Bay, as will be discussed in section 4, it is now clear that the GIA process plays no significant role in determining this signal.

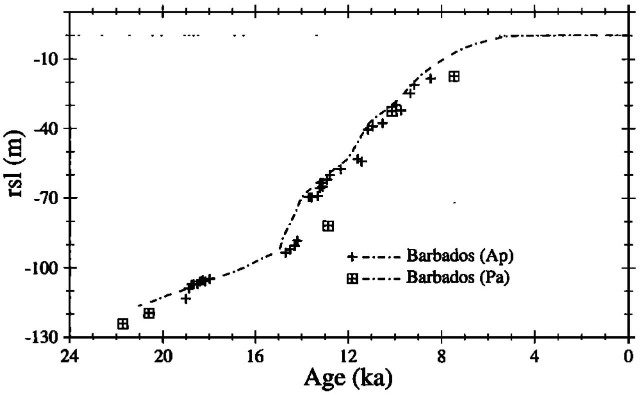

Figure 6. The U/Th dated coral-based record of postglacial relative sea level change at Barbados of *Fairbanks* [1989] and *Bard et al.* [1990], which extends from the Last Glacial Maximum (LGM) and which shows sea level to have been depressed by ~120 m at LGM. The data have been corrected for an assumed rate of tectonic uplift of 0.34 mm yr^{-1}, and they are compared to the prediction of the ICE-4G (VM2) model. These data were, in fact, employed to tune the model in order refine the time control on the bulk rate at which water from all sites of deglaciation enters the oceans. Primary time control on the disintegration of the northern hemisphere ice sheets is, of course, provided by ^{14}C dates on the terminal moraines that developed during the retreat phase. The data denoted by the crosses derive from measurements on the *A. Palmata* (Ap) species of coral, whereas those denoted by the boxed crosses are from the species *Porites* (Pa). The former species invariably lives within about 5 m of sea level and therefore is an accurate sea level indicator, whereas the latter species may live at substantial depth.

An additional solid-Earth geophysical signature of the GIA process, and one that has only recently come to be measurable, involves the instantaneous rates of material displacement of individual points on the surface of the solid Earth. It is a consequence of the extraordinary increase of the precision of space geodetic measurement techniques, primarily the *very long baseline interferometry* (VLBI) and *Global Positioning System* (GPS) methods, that measurements of this kind, which require accuracies higher than millimeters per year from repeated mea-

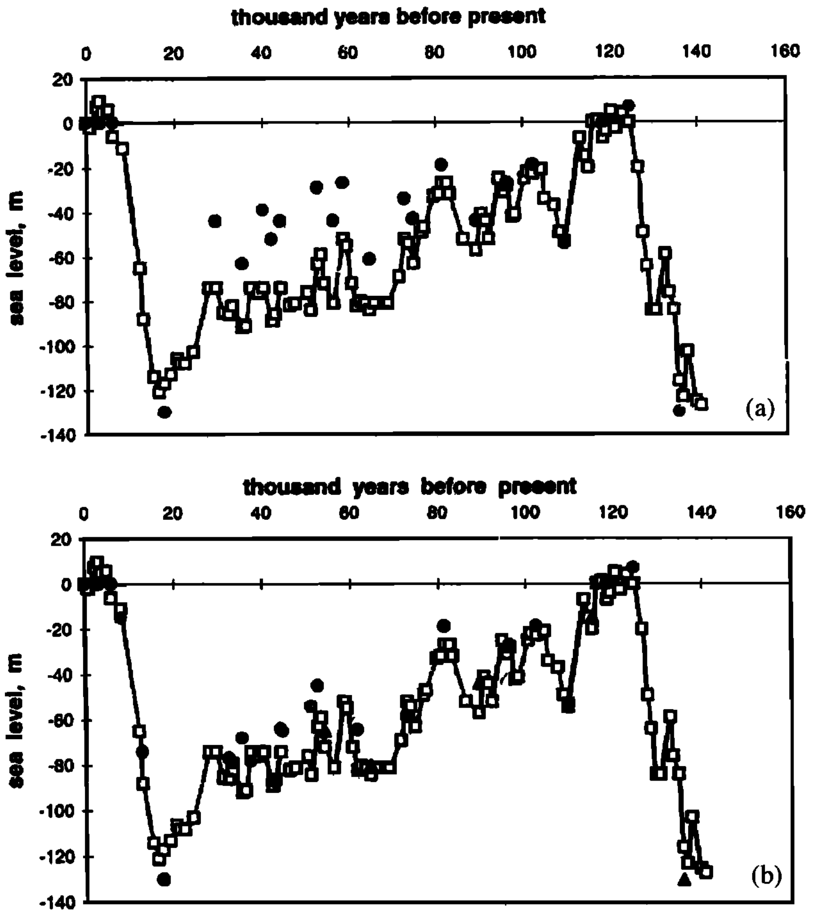

Figure 7. The sea level history at the Huon Peninsula of Papua New Guinea over the last 140 kyr based upon dated corral terraces (dots) compared to estimates based upon combined benthic and planktonic deep-sea core $\delta^{18}O$ data of *Shackleton* [1987] based upon his analysis of cores V19-30 and RC17-177 (squares). (a) The results obtained previously by *Chappell and Shackleton* [1986]. (b) The more recent results of *Chappell et al.* [1996] based upon redetermination of the age of the corals employed as sea level markers. Reprinted from *Chappell et al.* [1996], copyright 1996, with permission from Elsevier Science.

surements, can now be made. In assessing the impressive technical accomplishment that is represented by an ability to make repeated distance measurements of this quality, it is useful to recall the enormous impact that was achieved by the VLBI community when, in the 1980s, it was shown that this method could be employed to directly measure the rates of relative motion of the Earth's tectonic plates [e.g., *Herring*, 1986], whose relative speeds vary approximately from 4 to 10 cm yr^{-1}. The first successful space geodetic measurement of rates of displacement of points on the surface of the solid Earth that are unambiguously related to GIA consisted of the VLBI-based measurements of rates of vertical motion of a large number of radio telescopes reported by *Argus* [1996] based upon reductions of the VLBI data of *Ma and Ryan* [1995] at the Goddard Space Flight Center. Figure 9 shows comparisons of the radial motion observations for 12 radio telescopes with the predictions of the same global model of the GIA process used to make the rsl predictions described in section 2.1. Depending upon the frame of reference in which the comparison is made, the correlation coefficient between the observations and the GIA prediction varies from 0.76 to 0.87. Given that the observed rates of vertical motion are in general less than 3 mm yr^{-1} in magnitude, this result is truly extraordinary. Very recently, in the context of the Fennoscandian BIFROST [*BIFROST Project Members*, 1996] program it has also proven possible, in the region surrounding the Baltic Sea, to observe the horizontal motions of the surface of the solid Earth that occur in response to the postglacial rebound phenomenon. The expected patterns of both radial and tangential motion over each of the main centers of GIA will be discussed at length in section 4.

2.3. Astronomical Signatures of the Ice Age Cycle

Given the extraordinary scale of the redistribution of mass that occurs during the ice age cycle, which significantly perturbs the moment of inertia tensor of the planet, it should come as no surprise that the Earth's rotational state is also significantly affected. The impact of the glacial cycle upon the rotational state of the planet, because this impact is small in a sense that we will define rigorously in what follows, may be thought of as consisting of two distinct components: polar motion and Earth rotation, respectively. It is interesting that both of these GIA-related anomalies in Earth rotation were first and most clearly observed using methods that might best be considered astronomical. More recently, these observations have been confirmed using the space geodetic technique of *satellite laser ranging* (SLR), in the case of the anomaly in Earth rotation, and VLBI, in the case of the anomaly in polar motion.

Focusing first upon the anomaly in Earth rotation,

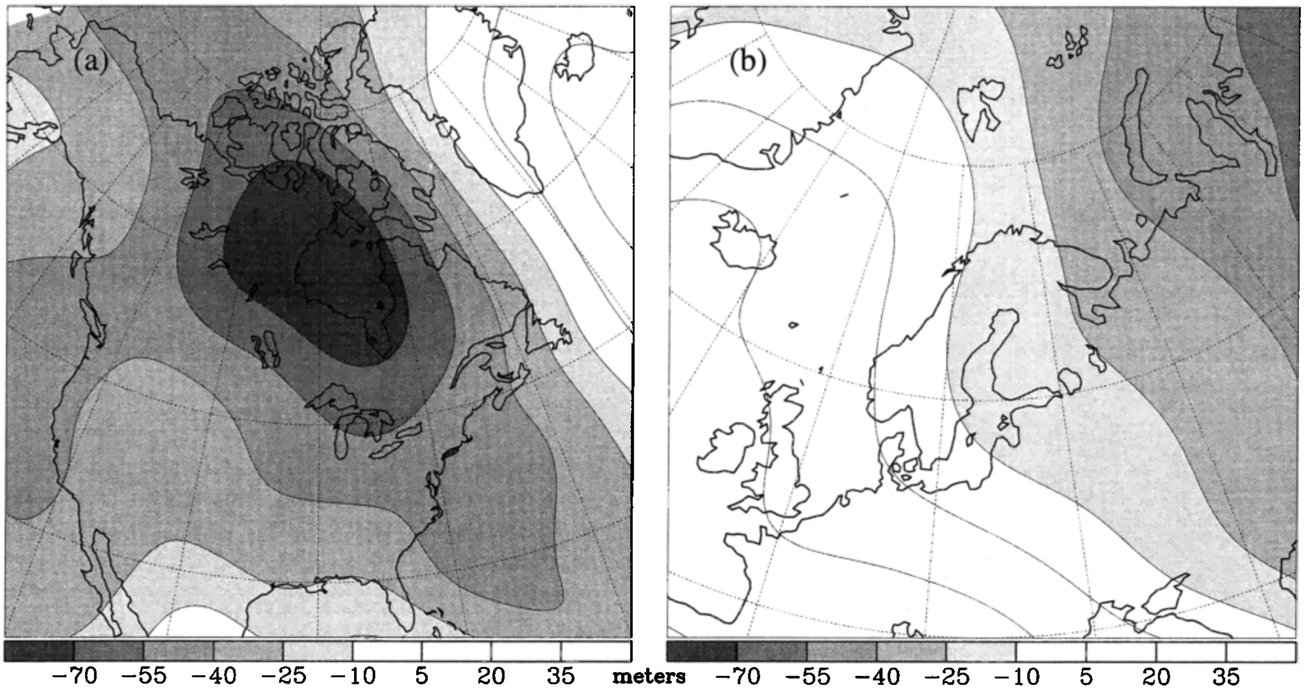

Figure 8. Gravity anomaly maps expressed in terms of geoid height for (a) North America and (b) Fennoscandia based upon the GEM-T2 satellite data derived model of *Marsh et al.* [1990]. Note the large negative geoid height anomnaly that is centered over the Hudson Bay region of Cabada, which was the location of the greatest thickness of glacial ice (~4 km) at Last Glacial Maximum. Inspection of Figure 8b demonstrates that there is no equivalent anomaly centered over Fennoscandia.

which is probably the more subtle of the two, it will be instructive to consider in historical order the two ways in which this anomaly in the rate of change in the Earth's angular velocity about its own axis of figure has been measured. That some such anomaly existed, beyond the slow decrease in the Earth's rate of rotation that is ongoing due to tidal friction, was first suggested [e.g., *Newton*, 1972; *Morrison*, 1973; *Müller and Stephenson*, 1975] based on analyses of ancient eclipse data extending back more than 2.5 kyr. For a considerable part of the earliest period of this interval, in both Babylon and China, naked eye astronomers kept careful records of the times and places of the occurrence of total eclipses of the Sun and the Moon. On the basis of the assumption that tidal friction has remained constant over this interval, a reasonable assumption given that sea level has not changed dramatically in this late postglacial (Holocene) period, one may, of course, accurately predict when and where in the past such total eclipses should have been observed. Analyses of such data, the most recent and complete being that of *Stephenson and Morrison* [1995], have clearly shown that the further back in time a prediction is made, the larger the error incurred in the timing of a particular eclipse, the sign of the error being such as to imply the action of an acceleration of rotation tending to counter the influence of tidal friction. The compilation of data recently presented by *Stephenson and Morrison* [1995] is shown on Figure 10. Using ancient records of solar and lunar eclipses ranging from 700 B.C. to A.D. 1600, they report an increase in the length of the mean solar day (l.o.d.) of 1.7 ± 0.05 ms yr^{-1}, which implies a rate of decrease of the angular speed of rotation of $(-4.5 \pm 0.1) \times 10^{-22}$ rad s^{-2} on the average over the past 2.7 kyr. After subtracting the contribution due to tidal friction they infer an average *nontidal acceleration of* Earth's *rotation* of $(1.6 \pm 0.4) \times 10^{-22}$ rad s^{-2} over this period. This nontidal acceleration corresponds to a value for $\dot{J}_2$ of $(-3.5 \pm 0.8) \times 10^{-11}$ yr^{-1}. Here J_2 is the amplitude of the degree 2 axial harmonic in the spherical harmonic expansion of the gravitational potential of the planet, which is a measure of the oblateness of figure (such that the larger J_2, the greater the oblateness) and the "overdot" denotes time differentiation. A negative value of $\dot{J}_2$ therefore implies decreasing oblateness and therefore decreasing polar moment of inertia. Since angular momentum is conserved in the absence of applied torques, it is then clear that the rate of axial rotation must increase (see Figure 11).

Beginning with the analyses of laser ranging data to the Laser Geodynamics Satellite (LAGEOS) by *Yoder et al.* [1983], presented simultaneously with the appearance of theoretical predictions of the GIA effect by *Peltier* [1982, 1983], the validity of the eclipse-based inference of the magnitude of the nontidal acceleration of rotation was clearly established. Many estimates of the nontidal acceleration based upon analyses of SLR data have now appeared (the effect observed is an acceleration in the

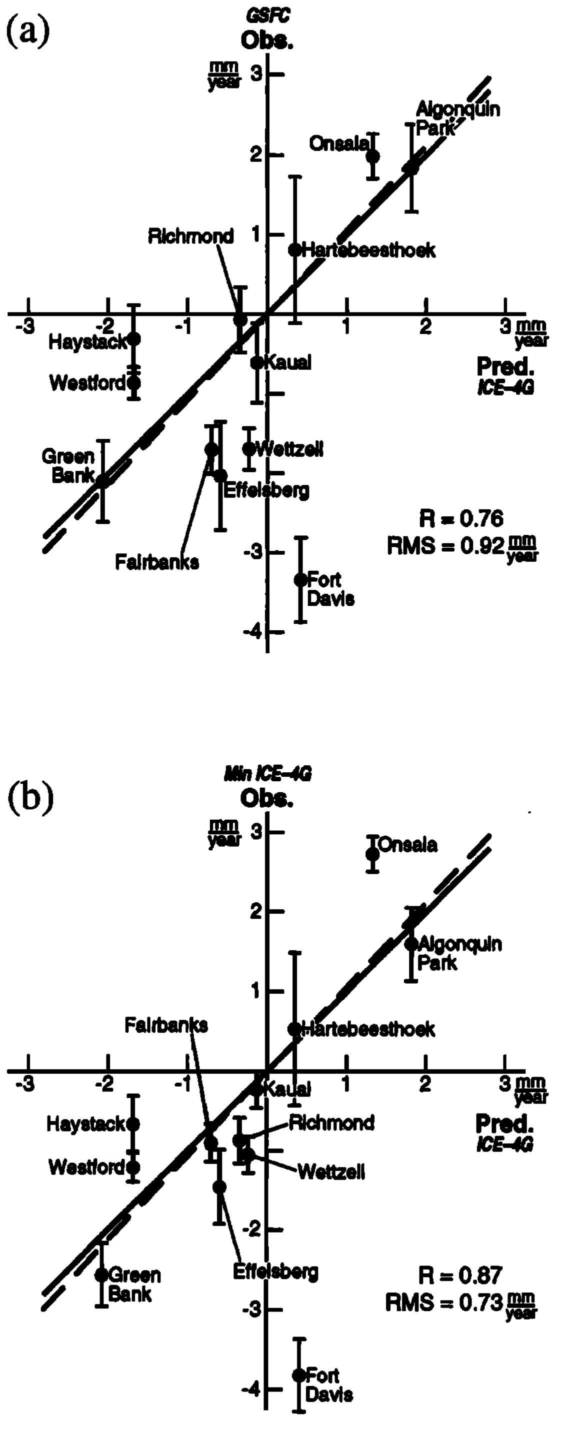

Figure 9. Comparison of the predictions of the ICE-4G (VM1) model of postglacial rebound to VLBI-determined rates of vertical motion in two different reference frames. Observed vertical rates are (a) in the reference frame of *Ma and Ryan* [1995] and (b) in the reference frame in which the differences between the predictions and the observations are minimized. The translation to the latter frame, which is 1.7 mm yr^{-1} toward 36°N, 111°E, significantly improves the agreement. The root-mean-square (RMS) of residuals decreases by 20% to 0.73 mm yr^{-1}, the correlation coefficient (R) increases to 0.87, and the best fitting straight line, which is dashed, becomes nearer to the ideal. The vertical rate at Fort Davis has been excluded from these statistics as it is clearly an outlier. After *Argus* [1996]. The theoretical predictions for VM1 are those tabulated by *Peltier* [1995b].

node of the orbit; see Figure 11), and these are tabulated on Figure 12a where they are all expressed in terms of $\dot{J}_2$.

Concerning the second anomaly in Earth rotation, namely, the polar motion anomaly, the data on the basis of which this anomaly has been most accurately inferred are presented on Figure 13. This shows the data collected by the International Latitude Service [*Vincente and Yumi*, 1969, 1970] in the period 1900–1982 based upon the observation of star transits using a northern hemisphere array of photozenith tubes. The data consist of time series for the x and y coordinates of the position of the north pole of rotation relative to a reference frame fixed to the Earth's crust with origin at the Conventional International Origin (CIO). This reference frame is shown on the inset polar projection in Figure 13 and has its x axis aligned along the Greenwich meridian. Inspection of the data on Figure 13 will show that it is dominated by an oscillatory pattern of beats with a period of ~7 years. It is well known that this pattern is created by the interference between the 12-month annual wobble that is forced by the atmosphere and the 14-month Chandler wobble or free Eulerian nutation. There remains considerable controversy over the mechanisms(s) responsible for exciting the 14-month Chandler wobble, although the dominant excitation appears to be atmospheric. What is of greatest interest from the sea level perspective, however, as we shall see, is the slow secular drift of the pole upon which these oscillatory variations are superimposed. According to *Dickman* [1977] this "*true polar wander*" is occurring at a rate near 0.95° per million years along the 76°W meridian as shown on the inset polar projection. The unambiguous connection between this polar wander and the GIA process was first established by *Peltier* [1982] and *Wu and Peltier* [1984], whose detailed theoretical analysis, since further generalized by *Peltier and Jiang* [1996a], showed that the initial analysis of the GIA effect provided by *Munk and MacDonald* [1960] did not, in fact, rule out a significant ongoing wander due to this cause, as they had imagined, even though the surface mass load during the present interglacial period is very nearly time invariant. The analysis of the data by *Dickman* [1977] has now also been performed by many others, and their results are all compiled on Figure 12b. Also shown on Figure 12b is the result of an additional measurement based upon VLBI data by *Carter et al.* [1986]. Given this discussion of the main types of observational data that we intend to explain and explore, it will be most informative to next consider the theory that has been devised to make this possible.

3. SEA LEVEL EQUATION AND ITS ITERATIVE SOLUTION

On the basis of the qualitative discussion provided in sections 1 and 2 it will be clear that in order to predict the variations in the relative level of the sea that accom-

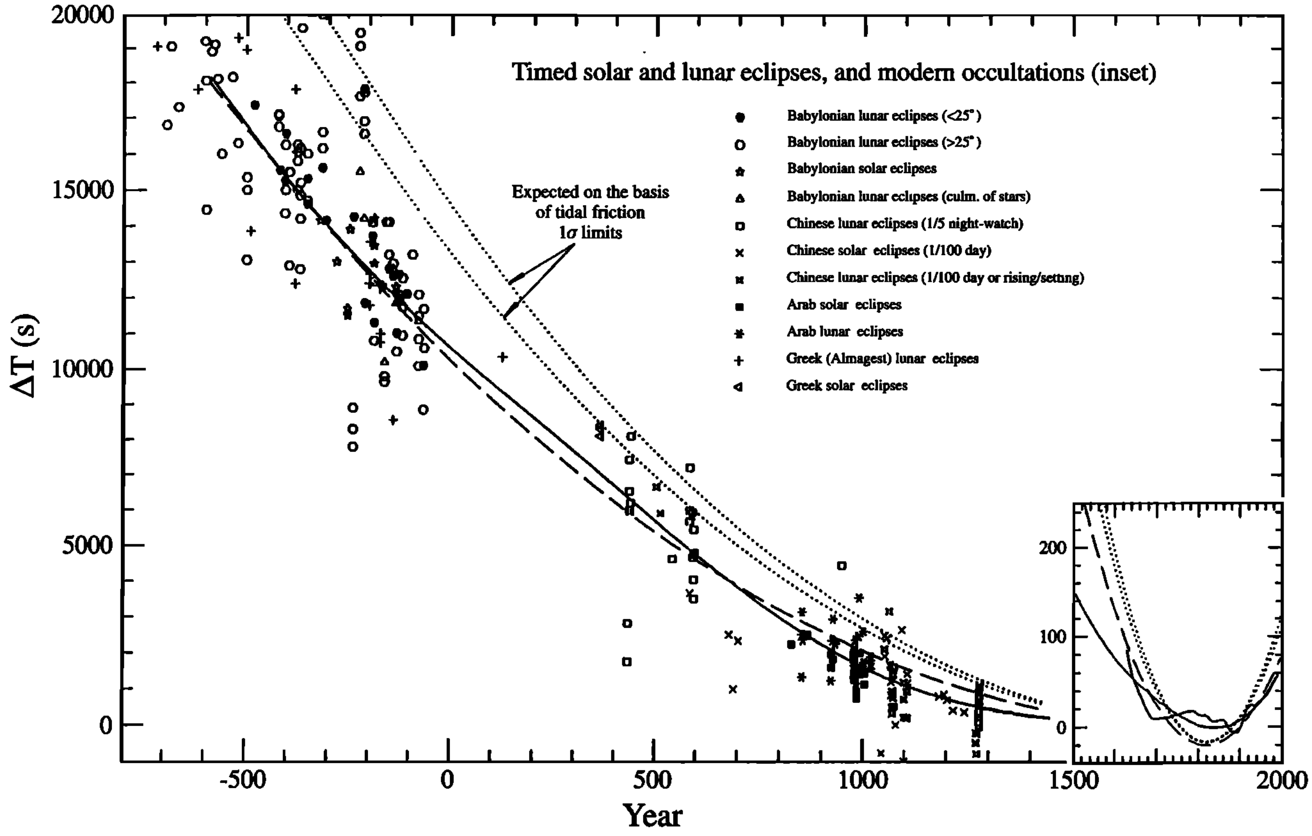

Figure 10. Plots of results obtained for the time difference between the observed time of a total eclipse of the Sun or the Moon and the time at which the event was predicted to occur based upon the assumption of constant tidal torque. The inset (on a scale 25 times greater) includes the continuous curve derived from the lunar occultations in the period 1620–1955.5 A.D., and the difference TAI-UT1 + 32.1845 from 1955.5 to 1990. The dashed curve is the best fitting parabola 31 $t^2 s$. The solid curve is fitted using cubic splines. This curve, the best fitting parabola, and the parabola expected on the basis of tidal friction are continued on the inset. From *Stephenson and Morrison* [1995].

pany the ice age cycle of glaciation and deglaciation we will be obliged to obtain explicit expressions for each of the terms that appear in the following schematic equation. If we define the relative sea level history at latitude θ and longitude λ by $S(\theta, \lambda, t)$, then clearly

$$S(\theta, \lambda, t) = C(\theta, \lambda, t)[G(\theta, \lambda, t) - R(\theta, \lambda, t)]. \qquad (1)$$

In (1), $C(\theta, \lambda, t)$ is the so-called "ocean function" which is by definition equal to unity where there is ocean and zero where there is land. It is time-dependent in general because as ice sheets melt or accrete, land may be both inundated by the sea or come to be elevated above it. The function $G(\theta, \lambda, t)$ in (1) is the geoid of classical geodesy which is defined by the surface of constant gravitational potential that is coincident with mean sea level (msl) over the oceans. The function $R(\theta, \lambda, t)$ is simply the local radius of the solid Earth. In order to determine S at any point on the planetary surface we are obliged to calculate the triplet of functions (C, G, R) given only the history of glaciation and deglaciation to which the surface is subject.

The theory which is now widely in use to perform this

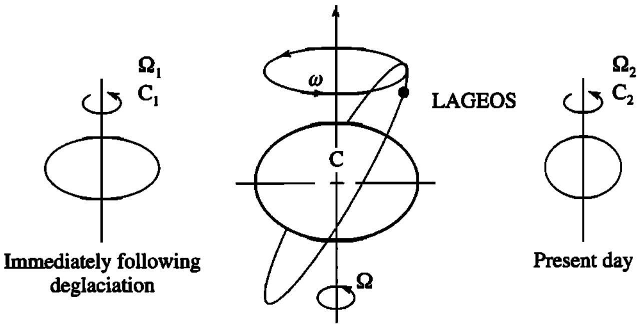

Figure 11. Sketch of the way in which the global process of postglacial rebound leads to a nontidal acceleration of planetary rotation. Immediately following deglaciation, at say 4 kyr B.P., the axial moment of inertia is C_1 and the angular velocity of rotation is Ω_1. As the GIA process proceeds, the shape of the planet becomes less oblate, and thus $C_2 < C_1$. Since angular momentum is conserved in the absence of applied external torques, $C_1\ \Omega_1 = C_2\ \Omega_2$, and therefore $\Omega_2 > \Omega_1$, corresponding to an acceleration in the rate of axial rotation. The time variation of the oblateness is observable in the orbit of an artificial Earth satellite such as LAGEOS as an acceleration in the rate of precession of the node, i.e., $\dot{\omega} \neq 0$.

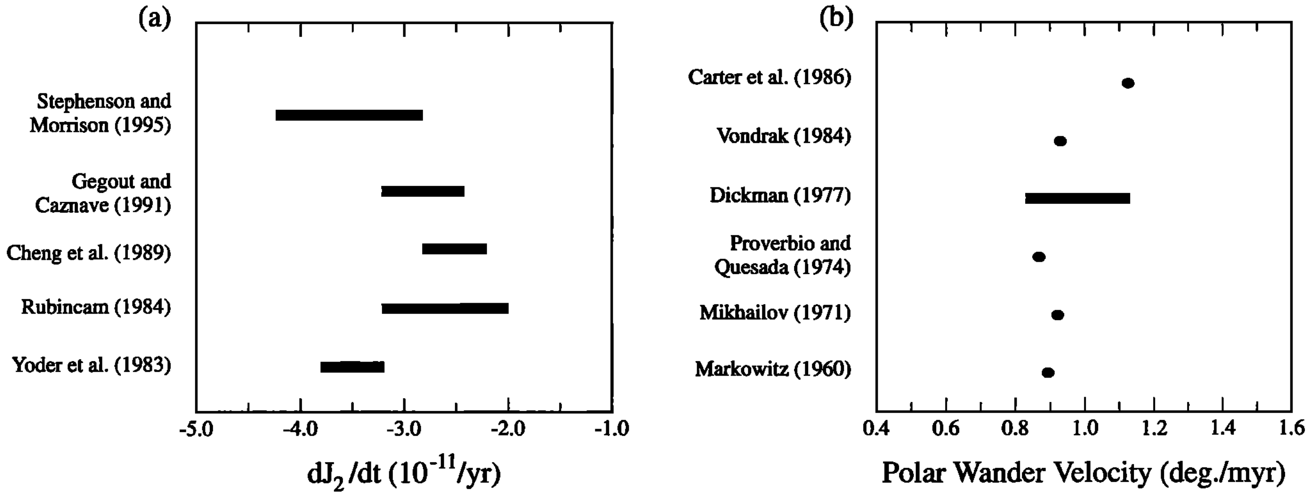

Figure 12. (a) Recent determinations in the value of $\dot{J}_2$; (b) recent determinations of polar wander velocity.

analysis was developed in a series of papers published ~20 years ago by *Peltier* [1974], *Peltier and Andrews* [1976], *Farrell and Clark* [1976], *Peltier* [1976], *Clark et al.* [1978], and *Peltier et al.* [1978]. It is based, at a fundamental mathematical level, on the same methodology that has been developed to do low-frequency seismological analyses of the elastic gravitational free oscillations of the Earth [e.g., see *Gilbert*, 1971] and more specifically on the static limit of this formalism which is employed to calculate the surface load and tidal Love numbers that are required, for example, to describe the elastic solid-Earth tides and the process of ocean tidal loading [*Farrell*, 1972]. In this analysis, one employs first-order perturbation theory to derive explicit formulae for the changes to G and R that are induced by a surface mass load. Assuming these changes to be small, it is demonstrated explicitly by *Peltier* [1974] how one may derive Green functions for linearly viscoelastic models of the planet such that when these are convolved with the space- and time-dependent surface mass load, one may obtain δG and δR, respectively, and thus from (1),

$$\delta S = C[\delta G - \delta R] + \delta C[G - R]. \qquad (2)$$

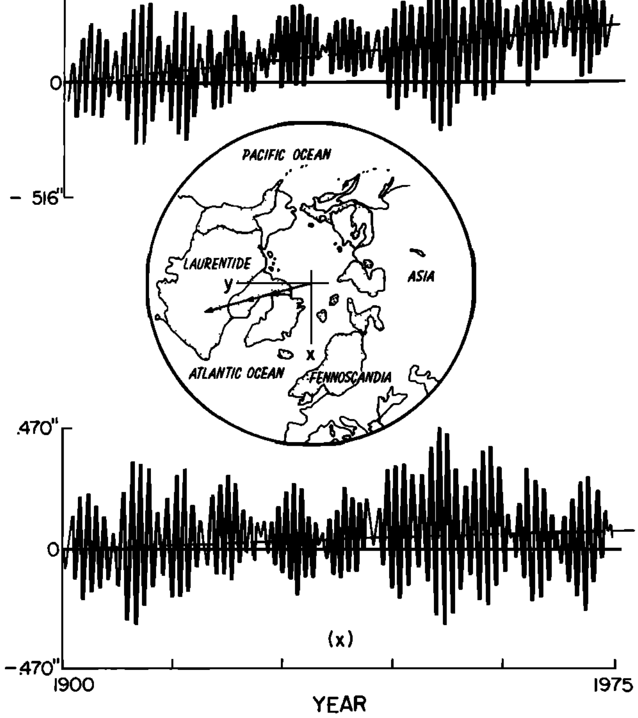

Figure 13. Time series for the location of the north pole of rotation of the planet as x and y coordinates relative to the coordinate system shown on the inset polar projection. These data are those of the International Latitude Service [*Vincente and Yumi*, 1969], and they reveal the secular drift of the pole at a rate near 0.95° Myr^{-1} approximately along the 76°W meridian.

Neglecting for the moment the influence of δC, the most primitive form of the "sea level equation," and the one discussed by *Farrell and Clark* [1976] for simple point load models of deglaciation, is, for general space-time histories of surface loading, explicitly

$$\delta S(\theta, \lambda, t) = C(\theta, \lambda, t)\left[\int_{-\infty}^{t} dt' \iint_{\Omega} d\Omega L(\theta', \lambda', t') \cdot \left(\frac{\phi^L(\gamma, t-t')}{g} - \Gamma^L(\gamma, t-t')\right) + \frac{\Delta\Phi(t)}{g}\right] \qquad (3)$$

in which $L(\theta', \lambda', t')$ is the surface load, expressed in terms of mass per unit area, which may be understood to have the composite property:

$$L(\theta, \lambda, t) = \rho_I \delta I(\theta, \lambda, t) + \rho_w \delta S(\theta, \lambda, t), \qquad (4)$$

in which ρ_I and ρ_w are the densities of ice and water, respectively, and where δI and δS are the changes in ice thickness and water thickness (relative sea level), respectively. The functions $\phi^L(\gamma, t - t')$ and $\Gamma^L(\gamma, t - t')$ are viscoelastic Green functions for the gravitational potential perturbation and for the radial displacement of the solid Earth to be discussed next, and g is the surface gravitational acceleration in the unperturbed and assumed spherical basic state. The remaining term in (3), namely, that involving the factor $\Delta\Phi(t)$, must be incorporated in (3) in order to ensure that the system conserves mass. Specifically, we must ensure that the integral of the product of $\rho_w \delta S$ over the surface area of the global ocean ($A(t)$) equals the mass $M(t)$ that has been lost by the ice sheets in melting by time t. That is, schematically,

$$\int_c \rho_w \delta S \, d\Omega = \int_c \rho_w L(\theta, \lambda, t)[G - R] \, d\Omega = -M_I(t)$$

so that

$$-\frac{M_I(t)}{\rho_w A(t)} = \frac{1}{A(t)} \int_c L[G - R] \, d\Omega.$$

If, at each instant of time in the solution of (3), we then include the term

$$\frac{\Delta\Phi(t)}{g} = \frac{-M_I(t)}{\rho_w A(t)} - \frac{1}{A(t)} \int_c L[G - R] \, d\Omega \qquad (5)$$

on the right-hand side, then mass conservation will automatically be assured.

Now there are two physical effects that are not accounted for in the form equation (3) of the sea level equation, namely, (1) that due to the fact that the ocean function C is time-dependent and (2) that due to the fact that as water and ice distributions vary over the surface of the planet in the course of the glaciation-deglaciation cycle, the Earth's rotational state is modified. Since changes in rotation also lead to changes of the effective gravitational potential and since mean sea level is forced to lie on a surface of constant potential, it will be clear that one must also include this influence in the general form of (3). Since both of these effects are small, it proves possible to incorporate their influence by using an iterative technique for the solution of (3) that was first described by *Peltier* [1994] in an analysis of the impact of ocean function time dependence. It will prove helpful to first complete our discussion of the primitive form (3) before describing these generalizations. *Peltier* [1974, 1976, 1985b] showed that the viscoelastic surface load Green functions $\phi(\gamma, t)$, $\Gamma(\gamma, t)$ may be written in the respective forms

$$\phi^L(\gamma, t) = \frac{ag}{m_e} \sum_{\ell=0}^{\infty} (1 + k_\ell^L(t)) P_\ell(\cos\gamma) \qquad (6a)$$

$$\Gamma^L(\gamma, t) = \frac{a}{m_e} \sum_{\ell=0}^{\infty} h_\ell^L(t) P_\ell(\cos\gamma), \qquad (6b)$$

if the viscoelastic Earth model is assumed to be spherically symmetric and where γ is the angular separation between source point (θ', λ') and field point (θ, λ). The $k_\ell^L(t)$ and $h_\ell^L(t)$ are the so-called surface load Love numbers whose time-independent forms appear in the elastic problem of ocean tidal loading [e.g., see *Farrell*, 1972].

The time-dependent forms which are required to describe the GIA process are dependent upon specification of a particular rheological model of the Earth's interior. In all of the work that I have done on this problem to date it has proven entirely adequate to employ a linear Maxwell rheology for this purpose, and this rheology, in the domain of the Laplace transform variable s, satisfies the stress-strain relation, with τ_{ij} and e_{ij} being the stress and strain tensors, respectively:

$$\tau_{ij}(s) = \lambda(s) e_{ii}(s) \delta_{ij} + 2\mu(s) e_{ij}(s) \qquad (7)$$

in which the viscoelastic compliances $\lambda(s)$ and $\mu(s)$ are simply

$$\lambda(s) = \frac{\lambda s + \mu\kappa/\nu}{s + \mu/\nu}, \qquad (8a)$$

$$\mu(s) = \frac{\mu s}{s + \mu/\nu}. \qquad (8b)$$

Since the bulk modulus $K = \lambda + 2\mu/3 = \lambda(s) + 2\mu(s)/3$ is independent of s, this model has no bulk dissipation. The quantity $\nu/\mu = T_M$ is called the Maxwell time and is the timescale that must be exceeded in order to effect the transition from Hookean elastic to Newtonian viscous behavior in response to an applied shear stress. Since the mantle of the Earth is known on the basis of seismological observations to behave very nearly elastically on short timescales and since it is required to behave viscously on long timescales in order to allow thermal convection to occur, it is clear that the Maxwell model is asymptotically correct in this sense. The assumption of linearity of the stress-strain relation in the viscous regime, however, is an assumption that we will be obliged to justify.

On the basis of this Maxwell model of the viscoelasticity, it has been shown that the Love numbers $k_\ell^L(t)$ and $h_\ell^L(t)$ in (6a) and (6b) may usually be written in the form [*Peltier*, 1976]

$$h_\ell^L(t) = h_\ell^{L,E} \delta(t) + \sum_{j=1}^{M} r_j^\ell e^{-s_j^\ell t} \qquad (9a)$$

$$k_\ell^L(t) = k_\ell^{L,E} \delta(t) + \sum_{j=1}^{M} q_j^\ell e^{-s_j^\ell t} \qquad (9b)$$

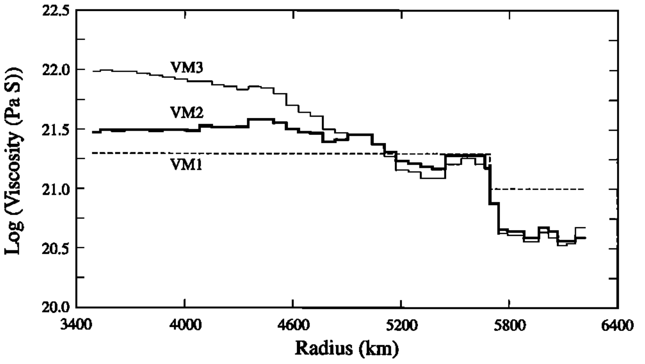

Figure 14. Viscosity models VM1, VM2, and VM3 that are discussed in detail in text.

where the $h_\ell^{L,E}$ and $k_\ell^{L,E}$ are precisely the elastic surface load Love numbers of *Farrell* [1972] and the $(r_j^\ell, q_j^\ell, s_j^\ell)$ are amplitudes and inverse relaxation times of the set of M purely exponential decays that is required to specify the time domain behavior of $h_\ell^L(t)$ and $k_\ell^L(t)$. As discussed in detail by *Peltier* [1974, 1976, 1985b], these parameters of the model are determined once radial profiles of the elastic properties (ρ, g, λ, μ) are specified and once a model of the radial variation of viscosity $\nu(r)$ has been chosen. For the purpose of all of the results that will be discussed in this article, I will assume that the elastic structure of the Earth model is given by the preliminary reference Earth model (PREM) of *Dziewonski and Anderson* [1981]. Since the various procedures required to determine the parameters $(r_j^\ell, q_j^\ell, s_j^\ell)$ and the $h_\ell^{L,E}$ and $k_\ell^{L,E}$ are mathematically involved and have been described in detail elsewhere (see *Peltier* [1982, 1989] for recent reviews), no useful purpose will be served by revisiting these methods here. I will simply comment, however, that recent discussion [*Fang and Hager*, 1995] concerning the possible lack of generality of the normal mode expansions (9), connected with the existence of a continuous part of the relaxation spectrum that for some viscosity models exists in the vicinity of $T_M(r)$, is irrelevant to any of the results to be presented herein (serious fault has also been found with the mathematical analysis performed by *Fang and Hager* [1995]; see *Vermeersen et al.* [1996]). Examples of these structural parameters of the viscoelastic normal mode theory will be useful to have at hand, and on this basis, for the three different viscosity models shown on Figure 14 that will figure prominently in what follows, Figure 15 shows the relaxation spectra s_j^ℓ. These models will be referred to as VM1, VM2, and VM3. Figure 16 shows the amplitude spectra r_j^ℓ, q_j^ℓ, and t_j^ℓ for model VM2 where the t_j^ℓ are the amplitudes in the normal mode expansion of the ℓ Love number that is required for the representation of tangential displacement. It has a similar expansion to (9a) and (9b), namely,

$$\ell_\ell^L(t) = \ell_\ell^{L,E}\delta(t) + \sum_{j=1}^{M} t_j^\ell e^{-s_j^\ell t}. \tag{9c}$$

It will be important to understand that the viscoelastic Love numbers h, ℓ, k are related to the radial displacement U_ℓ, tangential displacement V_ℓ, and the potential perturbation Φ_ℓ, respectively, as (see *Peltier* [1974] for detailed discussion)

$$\begin{bmatrix} U_\ell \\ V_\ell \\ \Phi_{3,\ell} \end{bmatrix} = \Phi_{2,\ell} \begin{bmatrix} h_\ell/g_0 \\ \ell_\ell/g_0 \\ k_\ell \end{bmatrix}. \tag{10}$$

At this point we are in a good position to return to the problem of generalizing (3) so as to enable it to incorporate the influence of both time dependence of the ocean function and the impact of the changing rotation. This may be accomplished iteratively as follows. Suppose we have solved the integral equation (3) to determine $\delta S(\theta, \lambda, t)$ for some deglaciation history $\delta I(\theta, \lambda, t)$, assuming $C(t)$ constant and equal, say, to the present ocean function and under the assumption that the changing rotation has had no impact on sea level. We now know the complete history of surface mass loading $L(\theta, \lambda, t)$, having determined the sea level contribution by solving the integral equation, and we may therefore compute the viscoelastic rotational response to this excitation by employing the theory of *Peltier* [1982] and *Wu*

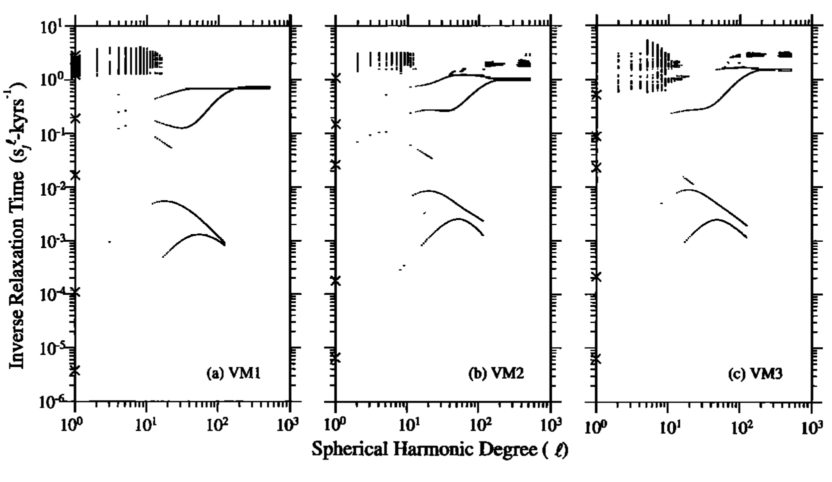

Figure 15. Relaxation spectra for the spherically symmetric viscosity models (a) VM1, (b) VM2, and (c) VM3. The primary modes of viscoelastic decay are those denoted MO, CO, M1, M2, and LO according to the nomenclature of *Peltier* [1976]. The dense set of modes in the vicinity of $s_j^\ell = 1$ kyr are the transition modes also identified by *Peltier* [1976]. As demonstrated by *Peltier* [1995b], these transition modes generally play a minor role in the time domain behavior of the h and k Love numbers, but they make an important contribution to the ℓ Love number.

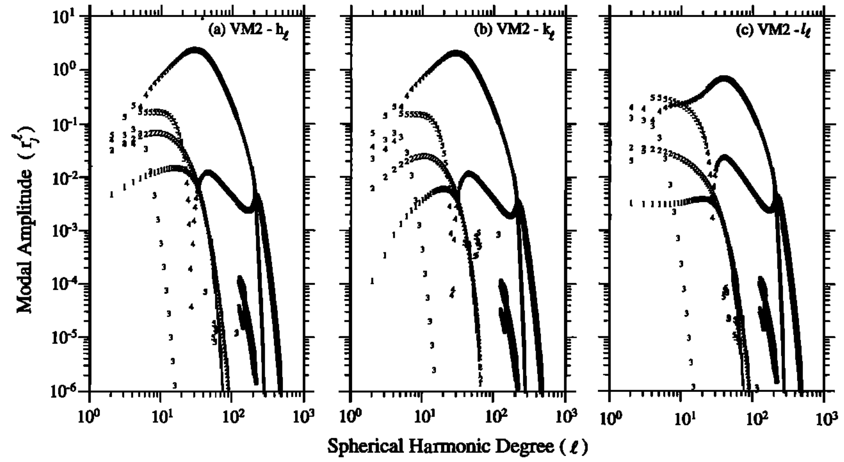

Figure 16. Amplitude spectra of the (a) h, (b) k, and (c) ℓ Love numbers for viscosity model VM2 in Figure 14. The amplitudes of the individual modes have been determined using the theory of residues method developed by *Wu* [1978] for application to simple models and extended for application to the complete compressible Maxwell model by *Peltier* [1985b].

and Peltier [1984] as follows. The rotational response is first determined by solving the Euler equation:

$$\frac{d}{dt}(J_{ij}\omega_j) + \varepsilon_{ijk}\omega_j J_{k\ell}\omega_\ell = 0, \tag{11}$$

in which J_{ij} is the moment of inertia tensor of the planet, ω_j are the components of its angular velocity vector, and ε_{ijk} is the Levi-Cevita alternating tensor. Assuming a biaxial model for the undeformed shape of the system (see *Peltier and Jiang* [1996a] for the complete, but unnecessary, triaxial theory), highly accurate solutions to (11) for present purposes may be constructed by employing the standard perturbation expansion:

$$\begin{aligned} \omega_i &= \Omega(\delta_{ij} + m_i) \\ J_{ij} &= I_{ij}, \quad i \neq j \\ J_{11} &= A + I_{11} \\ J_{22} &= A + I_{22} \\ J_{33} &= C + I_{33} \end{aligned} \tag{12}$$

in which (A, A, C) are the principle moments of inertia, Ω is the basic state angular velocity of the Earth, and I_{ij} and m_i are assumed small fluctuations away from the basic state values. To first order in the fluctuations [see *Munk and MacDonald*, 1960], substitution of (12) into (11) delivers the decoupled system for polar motion and rotation, respectively:

$$\frac{i}{\sigma_r}\dot{\mathbf{m}} + \mathbf{m} = \boldsymbol{\psi}, \tag{13a}$$

$$\dot{m}_3 = \dot{\psi}_3, \tag{13b}$$

in which the overdot over a quantity indicates a time derivative, the excitation functions are $\boldsymbol{\psi}$ and ψ_3, $\sigma_r = \Omega(C - A)/A$ is the Chandler wobble frequency of the rigid Earth, $\mathbf{m} = m_1 + i\, m_2$, $\boldsymbol{\psi} = \psi_1 + i\,\psi_2$, $i = \sqrt{-1}$, and the ψ_i are

$$\psi_1 = \frac{I_{13}}{(C-A)} + \frac{\dot{I}_{23}}{\Omega(C-A)}, \tag{14a}$$

$$\psi_2 = \frac{I_{23}}{(C-A)} + \frac{\dot{I}_{13}}{\Omega(C-A)}, \tag{14b}$$

$$\psi_3 = -\frac{I_{33}}{C}, \tag{14c}$$

respectively. As discussed in detail by *Peltier* [1982] and *Wu and Peltier* [1984], equations (13) may be most efficiently solved using Laplace transform techniques to determine the $\omega_i(t)$ once $L(\theta, \lambda, t)$ has been fully determined by solving the integral sea level equation (3). It will serve no useful purpose in the present context to repeat the details of these procedures here.

Given a solution to (13), however, we are in a position to incorporate the influence of varying rotation into (3) by modifying it into the form

$$\begin{aligned} \delta S(\theta, \lambda, t) = C(\theta, \lambda, t) \\ \cdot \Bigg[\int_{-\infty}^{t} dt' \iint_{\Omega} d\Omega' \{L(\theta', \lambda', t') G_\phi^L(\gamma, t - t') \\ + \Psi^R(\theta', \lambda'\, t') G_\phi^T(\gamma, t - t')\} + \frac{\Delta\Phi(t)}{g} \Bigg] \end{aligned} \tag{15}$$

in which the Green function $G_\phi^L = [\phi\,(\gamma, t - t')/g - \Gamma(\gamma, t - t')]$ is the same kernel as in (3), $\Psi^R(\theta', \phi', t')$ is the variation of the centrifugal potential due to the changing rotational state which, following *Dahlen* [1976], may be written (to first order in perturbation theory in order to be consistent with the approximations employed to solve (11)) as

$$\Psi^R = \Psi_{00}Y_{00}(\theta, \lambda) + \sum_{m=-1}^{+1} \Psi_{2m}Y_{2m}(\theta, \lambda) \tag{16}$$

where

$$\begin{aligned} \Psi_{00} &= \tfrac{2}{3}\omega_3(t)\Omega_0 a^2 \\ \Psi_{20} &= -\tfrac{1}{3}\omega_3(t)\Omega_0 a^2 \sqrt{4/5} \\ \Psi_{2-1} &= (\omega_1 - i\omega_2)(\Omega_0 a^2/2)\sqrt{2/15} \\ \Psi_{2+1} &= (\omega_1 + i\omega_2)(\Omega_0 a^2/2)\sqrt{2/15} \end{aligned} \tag{17}$$

and the tidal loading Green function G_Φ^T has the expansion

$$G_\Phi^T(\gamma, t) = \frac{1}{g}\sum_{\ell=0}^{\infty} (1 + k_\ell^T(t) - h_\ell^T(t))P_\ell(\cos\gamma). \tag{18}$$

In (18), the $k_\ell^T(t)$ and $h_\ell^T(t)$ differ from the $k_\ell^L(t)$ and the $h_\ell^L(t)$ in that they are "tidal" rather than "surface load" Love numbers, determined subject to the boundary conditions discussed by *Farrell* [1972]. The viscoelastic normal mode software developed by *Peltier* [1974, 1976, 1985b] and reviewed by *Peltier* [1982, 1989] has always included the capability to determine these tidal Love numbers. It is therefore clear on the basis of this discussion that the influence of varying rotation may be directly incorporated into the sea level equation and the influence of "rotational feedback" on rsl history investigated. Initial investigations of some aspects of this feedback have recently been presented by *Peltier* [1998a, b].

It remains then to describe the way in which this theory may be further refined so as to incorporate the influence of time variations of the ocean function $C(\theta, \lambda, t)$ and thus to describe the off-lap from, and on-lap onto, the continents, which is a continuing phenomenon throughout the ice age cycle. Because this effect is small, the second term in (2) is always very much smaller than the first term, and we may therefore incorporate the influence of δC in an iterative fashion as follows:

1. We first solve the integral equation (3) keeping C fixed to its present functional form and neglecting the influence of rotation.
2. We next solve equations (13) to determine what the rotational response to this history of surface loading would have been, expressed in terms of the $\omega_i(t)$.
3. We next solve the extended form of the sea level equation (15) using these $\omega_i(t)$ to determine a first approximation to the rotationally influenced relative sea level history $\delta S(\theta, \lambda, t)$.
4. Finally, we infer the time dependence of $C(\theta, \lambda, t)$ by exploiting the fact that equation (15), being a result of first-order perturbation theory, is written relative to an arbitrary datum. This is based on the procedure defined by *Peltier* [1994].

Having completed step 4, we repeat the entire sequence of steps until convergence is achieved. This process is extremely efficient because the influences of both δC and rotation are rather small. Step 4 itself involves the following sequence of analytical procedures first detailed by *Peltier* [1994].

1. Given the output from step 3, namely, $\delta S(\theta, \lambda, t)$, we note that where there is ocean, $\delta S(\theta, \lambda, t)$ is the predicted variation of the level of the sea with respect to the deforming surface of the solid Earth. This gravitationally self-consistent solution may be made topographically self-consistent by exploiting the arbitrariness of the datum relative to which δS is defined to determine a field $T'(\theta, \lambda)$ such that

$$\delta S(\theta, \lambda, t_p) + T'(\theta, \lambda) = T_p(\theta, \lambda) \tag{19a}$$

in which t_p is the present time and $T_p(\theta, \lambda)$ is the present-day topography with respect to sea level defined, say, by the ETOPO5 model.

2. On the basis of the $T'(\theta, \lambda)$ computed using (19a), it is therefore clear that the topography of the "rocky part" of the planet relative to sea level at arbitrary time t will simply be

$$T(\theta, \lambda, t) = \delta S(\theta, \lambda, t) + [T_p(\theta, \lambda) - \delta S(\theta, \lambda, t_p)]. \tag{19b}$$

3. Using (19b), we may therefore compute a first approximation to the time-dependent paleotopography that includes the contribution from ice thickness by simply calculating, with $\delta I(\theta, \lambda, t)$ the time-dependent ice thickness as before:

$$PT(\theta, \lambda, t) = T(\theta, \lambda, t) + \delta I(\theta, \lambda, t). \tag{19c}$$

(Note that there is an additional subtlety here connected with the variations of ice thickness δI and derivative of the perturbation theory based nature of the sea level equation. As I will discuss fully in section 5.2, one must also account for the "implicit ice" that is introduced in the calculation when regions that are initially ice-covered become inundated by the sea.)

4. Equation (19c) provides a basis in terms of which we may compute the time dependence of the ocean function $C(\theta, \lambda, t)$. I simply note that were PT is negative there is ocean, whereas where PT is positive there is (perhaps ice-covered) continent. This then defines a first approximation to the time-dependent function $C(\theta, \lambda, t)$. A next approximation follows once the loop 1–4 is repeated.

Discussion of the procedures that have been developed to solve the sea level equation is therefore complete. The full algorithm involves a double iteration and is implemented by defining all fields on a basis of spherical harmonics that is typically truncated to degree and order 512, which is equivalent to a distance on the surface of the Earth of a fraction of a degree. Such high resolution is required to capture the details of the time-dependent coastline. A description of an initial form of the spherical harmonics based algorithm that has been developed to solve the most primitive form of the sea level equation is given by *Mitrovica and Peltier* [1991]. The final form differs from this only in details related to the way in which ocean function time dependence exerts its influence, details that influence the calculation in an important way only in regions where the continental shelf is especially broad and land bridges become inundated by the sea. I refer to this algorithm as being semispectral as its execution requires continuous transformation of the model fields between the space domain and the wavenumber domain. Methods of precisely this kind are, of course, standard in the literature on modeling the atmospheric general circulation, on the basis of which I first considered that they might be especially well suited to the spectral solution of the sea level equation.

It will be useful prior to discussing the detailed results which are now being obtained through the application of this theory to illustrate the nature of the predictions that are currently being made by a single example. Now the inputs that are required in order to fully specify the theory consist of two functions. First, a model of the radial variation of viscosity from the surface of the Earth to the center of mass is required. For initial illustrative purposes, I will employ model VM2 for reasons that will become clear in what follows. This model was shown previously in Figure 14. The second function required to fully specify the theory is a model of the space and time dependence of ice sheet thickness. For this purpose, I will employ the ICE-4G model derived by *Peltier* [1994] for the history of deglaciation from LGM to present. For the history of ice sheet thickness variations prior to LGM which is important for computation of the rotational response, I will employ the SPECMAP δ^{18}O record of *Imbrie et al.* [1984] to modulate in time the LGM thickness map embodied in the ICE-4G deglaciation model. This record will be discussed explicitly in section 4. Plate 2 presents a series of six time slices through the northern hemisphere component of the ICE-4G deglaciation model for reference. Also included in this model are significant time variations of ice thickness in the southern hemisphere, particularly in Patagona and Antarctica. These components of the model will also be discussed in greater detail in section 4.

Given these two inputs to the model, the doubly iterative procedure discussed above may be completely implemented to determine a global solution for relative sea level history $\delta S(\theta, \lambda, t)$. I will illustrate this global solution at this point with only a single representative result, namely, that for the present-day rate of relative sea level change. This is the signal that would be observed as a secular rate of change on a tide gage installed anywhere on the surface of the Earth if the only process active in the system were that associated with the late Pleistocene ice age cycle. Plates 3a and 3b show two versions of the solution, one that excludes (Plate 3a) and one that includes (Plate 3b) the influence of rotational feedback. Plate 3c shows the difference between the results of Plates 3a and 3b and therefore is the contribution to the present-day rate of relative sea level change due to the variation of Earth rotation alone. The latter clearly constitutes a rather small perturbation to the solution that is obtained by solving equation (3) rather than equation (15). This is important as it demonstrates that the impact of rotational feedback, which is clearly dominated by the degree 2 and order 1 terms in equation (17), is between 1 and 2 orders of magnitude smaller than was recently suggested on erroneous grounds by *Bills and James* [1996].

From careful inspection of Plate 3, all of the major signatures of the global processes of GIA that were discussed in section 2 from a qualitative perspective are clearly evident. In regions that were once ice covered and which are currently experiencing postglacial rebound of the crust, sea level is currently falling. In the peripheral regions that are dominated by the collapse of the proglacial forebulge, such as the east coast of the North American continent, sea levels are currently rising. In the far field of the ice sheets, one will also observe the characteristics of the global GIA process previously mentioned, namely, the ongoing fall of sea level at the rate of a fraction of a millimeter per year in ocean basin interiors remote from the ice sheets, the rise of sea level in "haloes" surrounding the far-field continents, and the falling sea levels on far-field continental coastlines. As previously mentioned, the edge effects that are observed across continental coastlines in the far field are produced by the hydroisostatic tilting that occurs across the coast due to flow of the mantle from beneath the far-field ocean basins inward toward the continents which causes them to be uplifted and sea level thereby to fall. Figure 17 explicitly compares relative sea level histories predicted at six different sites for the versions of the sea level equation that include and exclude the influence of rotational feedback. These intercomparisons, at two of the sites from which the most important coral-based rsl records are available and from the four locations in the Toronto rsl database that are closest to the extrema of the theoretically predicted rotational effect, demonstrate that the feedback effect is so small as to be negligible compared with the errors in the observational data.

In sections 4 and 5, my purpose will be to demonstrate the manner in which the observational data described in section 2 may be combined with the theory discussed in this section in order to address interesting and important questions in both solid-Earth geophysics and climate dynamics. Section 4 will focus upon solid-Earth geophysics, whereas section 5 will consider issues in climate dynamics.

4. IMPLICATIONS FOR SOLID-EARTH GEOPHYSICS

From a solid-Earth geophysical perspective the most important contribution of GIA data to the understanding of the physics of the planetary interior is certainly connected with the fact that these data may be employed to infer the viscosity of the planetary mantle, along with

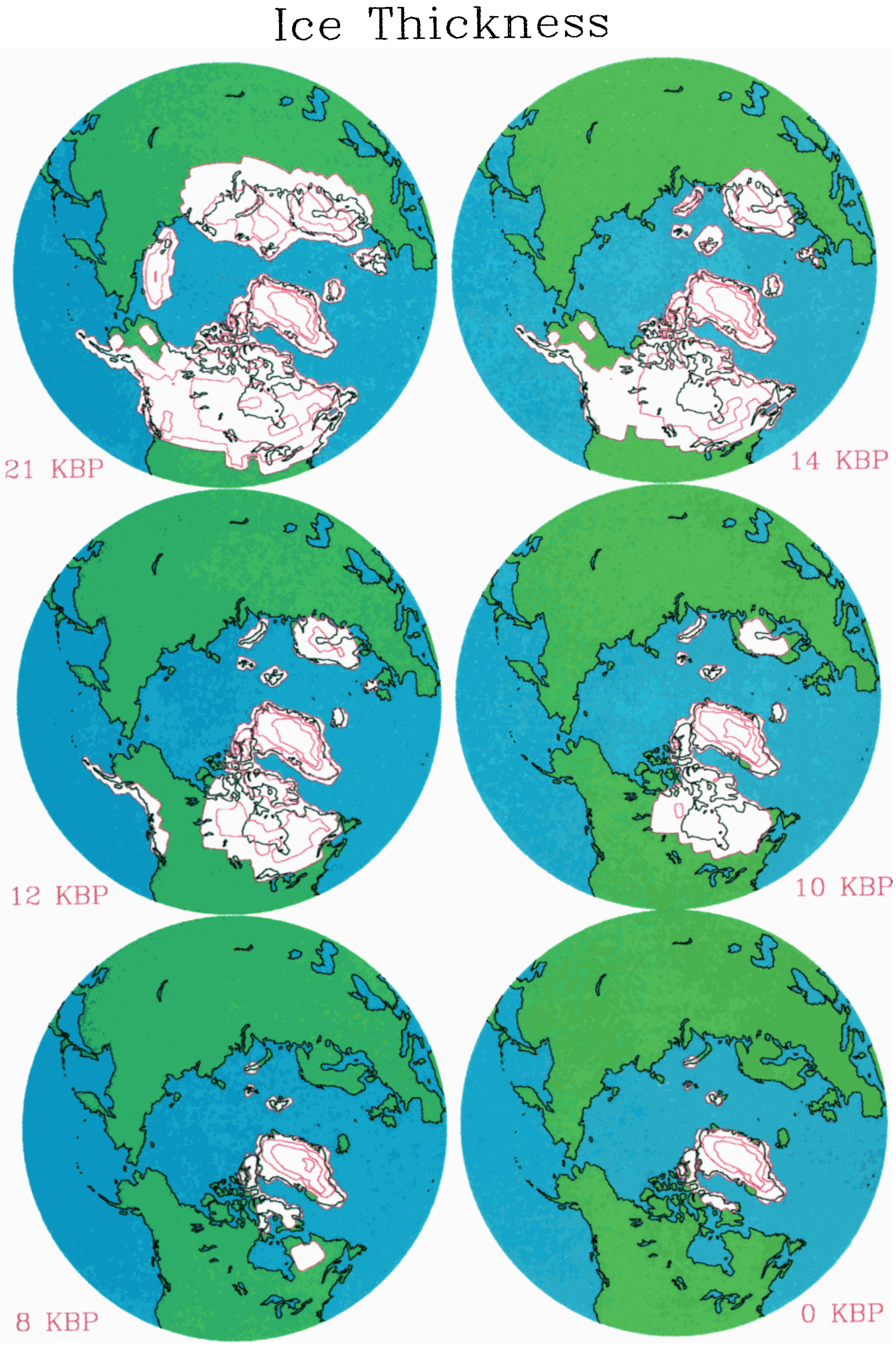

Plate 2. Time slices through the ice thickness maps that constitute the ICE-4G model of deglaciation.

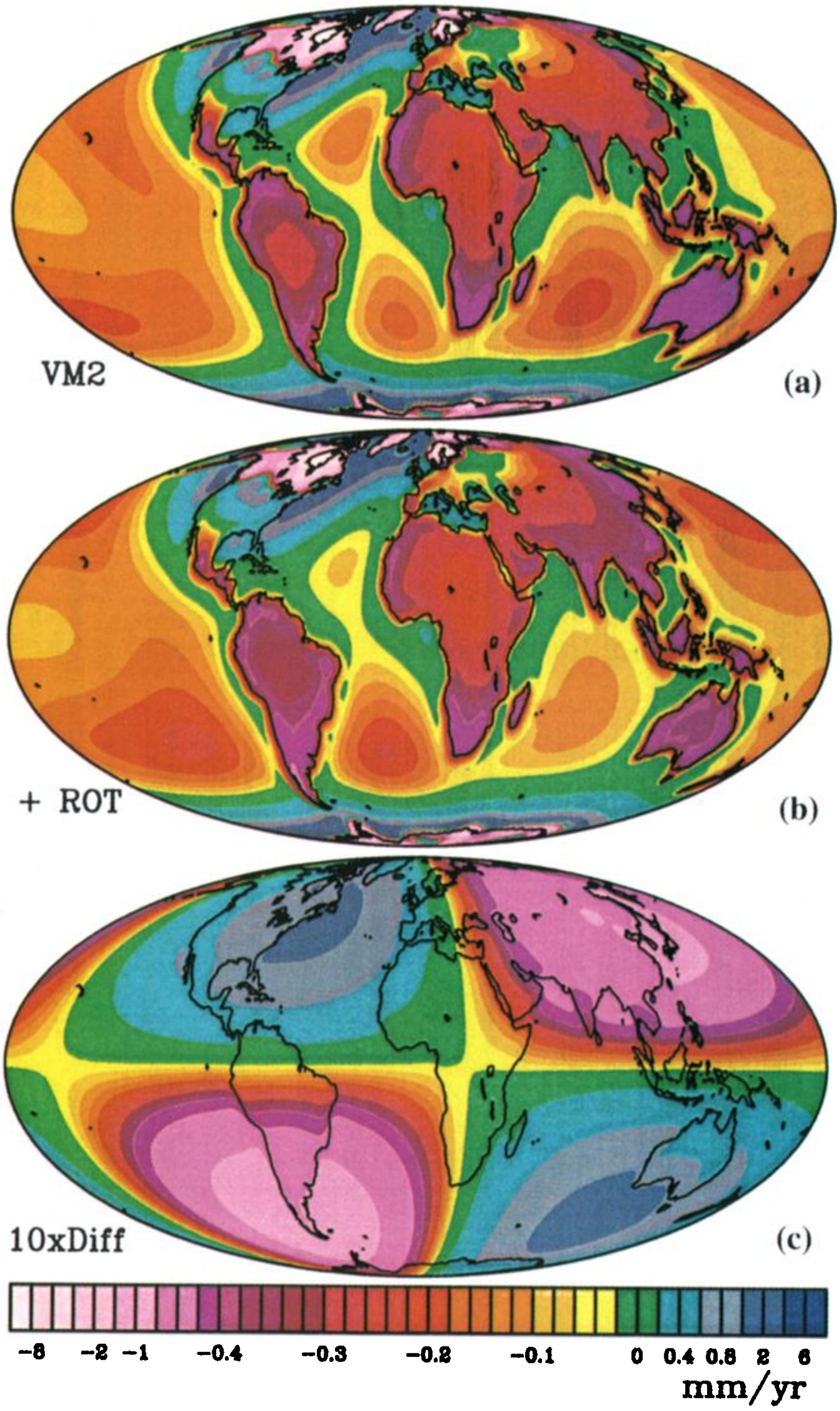

Plate 3. Predictions of the present-day rate of relative sea level rise using the VM2 viscosity model and the ICE-4G deglaciation history. Results are shown for analyses performed that both (a) exclude and (b) include the influence of rotational feedback and (c) the difference between these predictions which isolates the influence of the changing rotation alone.

its depth variation. As previously mentioned, knowledge of this physical property is critical to our ability to construct an acceptable model of the mantle convection process that drives continental drift. Furthermore, since the characteristic timescale of the GIA process (thousands of years) is dramatically less than the characteristic timescale of the convection process (hundreds of millions of years), it is not clear on a priori grounds that the viscosity which governs these processes should be the same. This issue was most clearly raised in the early literature by *Weertman* [1978] and has been more recently discussed at some length by *Peltier* [1985a, 1986], who sought to address the possible implications of the initial inferences of mantle viscosity based directly upon

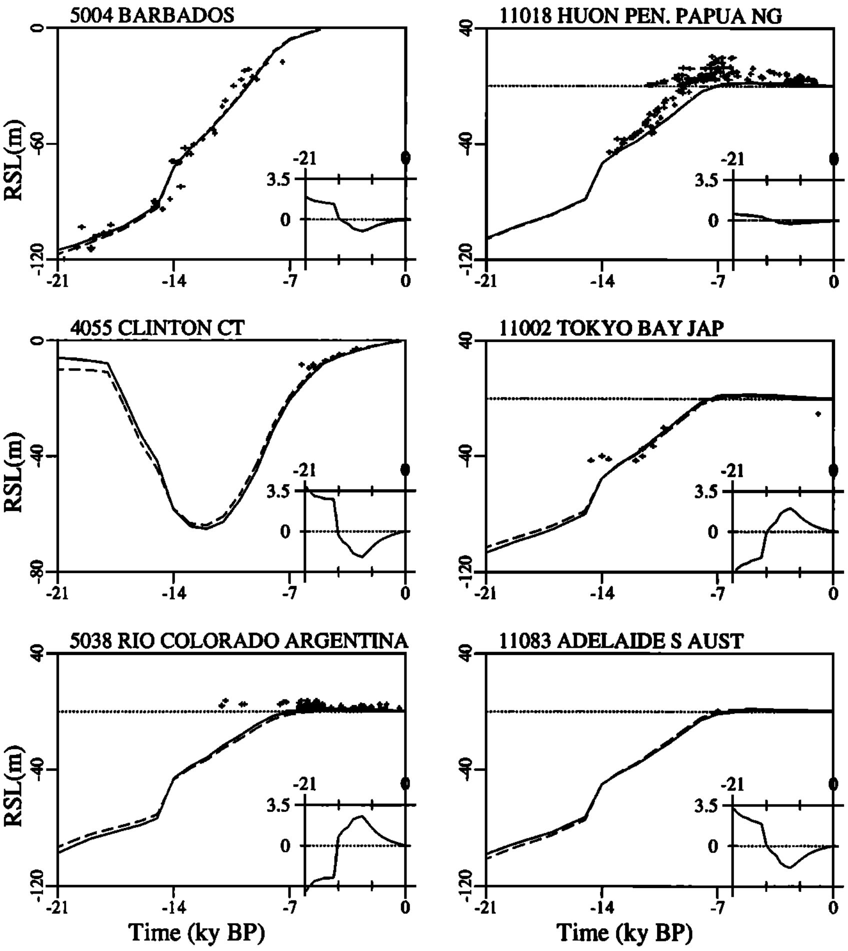

Figure 17. Relative sea level histories predicted by models that both include (dashed curves) and exclude (solid curves) the influence of rotational feedback on postglacial sea level. The numbers adjacent to the names of the individual sites are those used in the Toronto database of relative sea level histories. Crosses denote the sea level observations at each site.

the convection timescale constraints provided by observed nonhydrostatic geoid anomalies [*Hager*, 1984; *Richards and Hager*, 1984]. This question is clearly related to the issue of whether the rheology of the mantle is Newtonian or non-Newtonian. If mantle rheology were non-Newtonian, then "the" viscosity would, of necessity, involve transient behavior, with the effective viscosity which governs a short timescale phenomenon being lower, perhaps considerably lower, than the viscosity that governs a long timescale phenomenon (in a strain-hardening rheology of the kind that has been inferred on the basis of deformation experiments on single crystals of olivine [e.g., *Kohlstedt and Goetze*, 1974]). If, on the other hand, mantle rheology were Newtonian, then it would follow, of equal necessity, that the steady state viscosity that controls processes on all timescales would be the same. As I will show, it has recently been proven to be possible, in fact, to demonstrate that the viscosity profile that is required to reconcile observations of the GIA process may be for the most part compatible with the viscosity profile that is required to reconcile the convection timescale constraints. It follows from this that the rheology of the mantle, sufficiently beneath the surface lithosphere, may not be significantly influenced by non-Newtonian behavior. This is an exceptionally important conclusion since it may effectively resolve an issue that has remained outstanding for many decades. In this section, I will begin by revisiting the inverse problem for mantle viscosity through the solution of which the inference of the depth dependence of mantle viscosity is made. Thereafter the inferred model or class of models will be tested by employing a subset of the rsl observations that was not employed in the inversion. Finally, the model will be employed to make predictions of various signatures of the GIA process that have yet to be directly observed in detail. Section 4.5 discusses the question of the compatibility of the convection timescale inferences of viscosity with the GIA inferences and thus of the issue of Newtonian or non-Newtonian rheology.

4.1. Inverse Problem for Mantle Viscosity

The history of the application of formal inverse theory to the inference of mantle viscosity, based upon the use of signatures of the GIA process, really began with the work of *Parsons* [1972]. Parsons' work was based upon the use of the relaxation spectrum for Fennoscandian rebound that had earlier been deduced by *McConnell* [1968]. Parsons did not employ a viscoelastic field theory as basis of his work but rather used a Newtonian viscous fluid model just as McConnell had done in fitting his relaxation spectrum using forward problem calculations. *Peltier* [1976] developed the main ingredients of a formal inverse theory based upon the same Maxwell viscoelastic field theory that was employed to derive the impulse response Green functions that are central to construction of the sea level equation (3) or (15). This analysis was performed for spherical geometry and involved the derivation of a viscoelastic extension of Rayleigh's variational principle of elasticity to determine the so-called Fréchet derivatives (more on this to follow) that are a central element of modern geophysical inverse theory. Further advances were necessary, however, before the application of this theory would be warranted, the primary requirements being an improved model of the glaciation-deglaciation process and the compilation of a global database of relative sea level histories, both for use in the inversion process itself and for verification of the model thereby inferred. As I will discuss, it was also necessary to develop the mathematical apparatus required to solve the forward problem for the rotational response to a given history of ice sheet loading and unloading. Fully realistic global models of the deglaciation process were not available prior to construction of the ICE-3G model of *Tushingham and Peltier* [1991], and an initial global database of rsl histories was similarly unavailable prior to the work by *Tushingham and Peltier* [1992]. It will be important for present purposes to realize that both of these ingredients required for the solution of the inverse problem have now been superseded: the ICE-3G model by ICE-4G [*Peltier*, 1994] and the compilation of rsl histories by a much expanded database in which only the raw age-height pairs have been recorded rather than a sampled envelope representation of the data that was for the most part employed in the reconnaissance compilation of *Tushingham and Peltier* [1992]. This new database will be published separately and made available to the community.

In bringing these ingredients together to construct solutions to the inverse problem for mantle viscosity we base the inversion procedure on the existence of a functional relationship between the variations in some aspect of the GIA response to a specific deglaciation history and variations to the viscosity model. If $\mathcal{R}$ denotes some aspect of the response, say the relaxation times inferred on the basis of Monte Carlo fits to individual sea level histories at sites that were once ice covered (examples of these fits are shown on Figure 3), or an observed rate of polar wander or nontidal acceleration and if we parameterize the viscosity model in terms of its logarithm to the base 10 as log $\nu(r)$, then this functional relation may be written in the general form

$$\frac{\delta \mathcal{R}}{\mathcal{R}_0} = \int_b^a FK^{\mathcal{R}}(r)\delta \log \nu(r) r^2 \, dr. \qquad (20)$$

In (20), $FK^{\mathcal{R}}(r)$ is therefore a functional derivative that determines the depth dependence of the sensitivity of the response $\mathcal{R}$ to depth-dependent variations in the viscosity model δ log $\nu(r)$. The scales b and a are the radii of the core-mantle boundary and the Earth's surface, respectively, and $\mathcal{R}_0$ is the response calculated for a reference viscosity model log $\nu_0(r)$. The functionals $FK^{\mathcal{R}}(r)$ are the so-called *Fréchet derivatives*. The analysis of *Peltier* [1976] demonstrated that when the viscosity model is parameterized in terms of its logarithm, the associated $FK^{\mathcal{R}}(r)$ allow the perturbation in the response to be calculated to quite high accuracy for variations of viscosity in excess of an order of magnitude. The inverse problem for viscosity is therefore very effectively linearized by use of the logarithmic viscosity parameterization just as the inverse problem for electrical conductivity is similarly linearized [*Parker*, 1977]. *Peltier* [1976] derived exact forms for $FK^{\mathcal{R}}(r)$ when the observed response was assumed to be characterized by the inverse relaxation time s_k^ℓ of a single mode of viscoelastic relaxation in a spectrum such as one of those shown on Figure 15. In fact, the inferred spectrum for the postglacial rebound of Fennoscandia does constitute just such

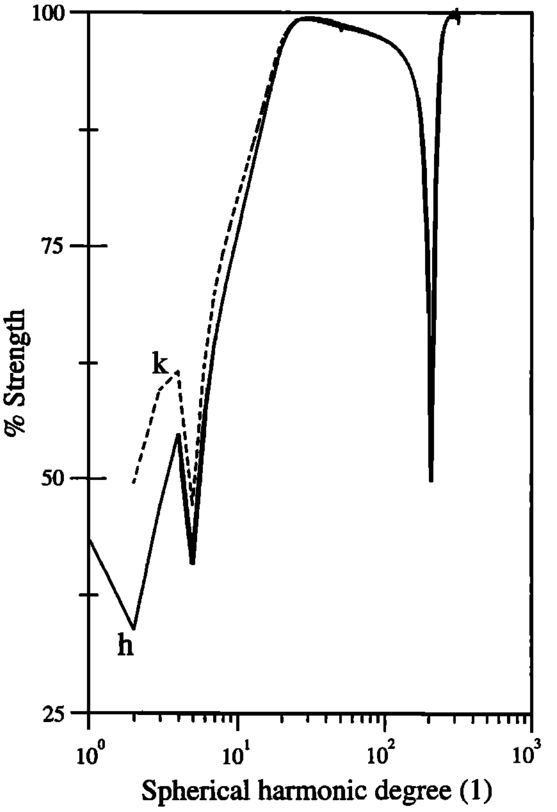

Figure 18. Variation of the fractional strength of the total amplitude of relaxation that is carried by the dominant mode in the expansions for both the h and k Love numbers for viscosity model VM2. Inspection demonstrates that beyond spherical harmonic degree 20 the dominant mode carries almost all of the relaxation strength. Since the relaxation spectrum of *McConnell* [1968] for the postglacial rebound of Fennoscandia has a lower bound at $\ell \simeq 14$, it is clear that a one-mode approximation is adequate to represent the relaxation of shape in this region.

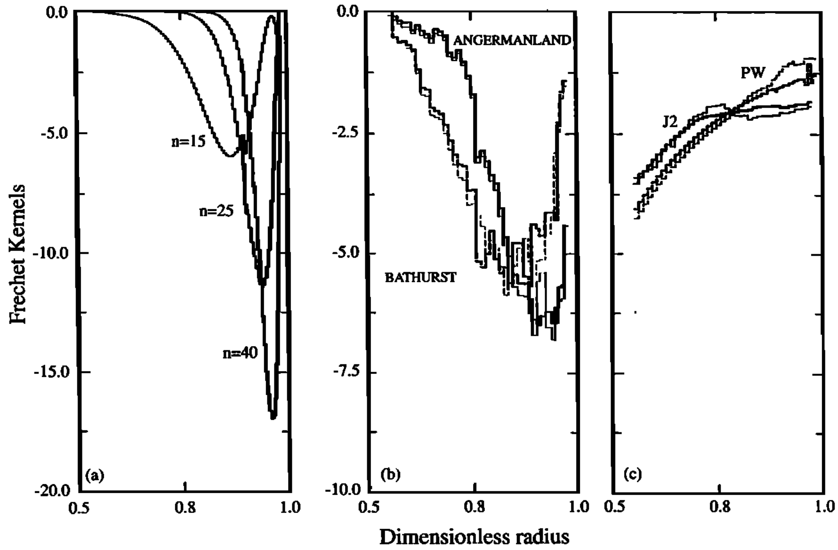

Figure 19. Fréchet derivatives for a representative set of the data related to the GIA process. (a) A sequence of kernels for the inverse relaxation times of a number of spherical harmonic degrees of the *McConnell* [1968] relaxation spectrum based upon the analytic formula of *Peltier* [1976]. (b) Fréchet derivatives for the site specific relaxation times at a site near the center of Laurentide rebound (Bathurst Inlet, this is actually a high Arctic site) and at the center of Fennoscandian rebound (the Angerman River site). (c) Kernels for the nontidal acceleration of rotation ($\dot{J}_2$) and polar wander speed (PW) that were determined numerically using the procedure embodied in equations (21) and (22). Inspection of this suite of kernels demonstrates that the observables, whose sensitivity to viscosity variations they represent, offer the potential of significant resolution from the Earth's surface to the core-mantle boundary (CMB). In Figures 19b and 19c the solid lines denote kernels for VM1, whereas the dashed lines are those for a constant mantle viscosity of 0.9×10^{21} Pa s. Ongoing work has shown that the kernels for the rotational data are somewhat inaccurate owing to the severe modal truncation employed to obtain them. The modest impact of the use of the revised kernels on the VM2 model will be discussed elsewhere.

data since in the degree range to which this relaxation spectrum applies, $\ell \geq 14$, the relaxation process is strongly dominated by a single mode of decay (see Figures 15 and 16). This fact is further clarified by Figure 18 which shows the percent contribution of the dominant mode of viscous relaxation to the total viscous response for both the h^L and k^L Love numbers of the VM2 viscosity model.

For other aspects of the GIA response the associated $FK^{\mathcal{R}}(r)$ must be computed numerically, and this calculation is simply done as follows: Assuming a starting model such as VM1 in Figure 14, we perturb this radial viscosity structure ($\nu_0(r)$, say) with a dense set of delta-function-like perturbations and then, for each such perturbation, say the one localized at radius r', we evaluate

$$\frac{\delta\mathcal{R}}{\mathcal{R}_0} = -\bar{F}\bar{K}^{\mathcal{R}}(r') \int_{r'-\delta}^{r'+\delta} r^2\Delta(r)\, dr \qquad (21)$$

to obtain

$$\bar{F}\bar{K}^{R}(r') = -\frac{\delta\mathcal{R}/\mathcal{R}_0}{\displaystyle\int_{r'-\delta}^{r'+\delta} r^2\Delta(r)\, dr} \qquad (22)$$

in which $\mathcal{R}_0$ is the solution of the forward problem for the model log $\nu_0(r)$, $\Delta(r)$ is the delta-function-like (localized) perturbation added to it which induces the variation in the response $\delta\mathcal{R}$, and $\bar{F}\bar{K}^{\mathcal{R}}(r')$ is the average value of the Fréchet derivative in the interval $r' - \delta$, $r' + \delta$. It is important to note that we compute Fréchet kernels for the entire set of observables using the normalized measure of the response $\delta\mathcal{R}/\mathcal{R}_0$ so that different observational data that have different physical dimensions may be jointly inverted.

Examples of the Fréchet derivatives for each of the three types of data that we will simultaneously invert are shown on Figure 19. All of the kernels denoted by the solid lines are computed for viscosity model VM1 shown on Figure 14. Figure 19a illustrates Fréchet kernels based upon the explicit formula provided by *Peltier* [1976] for individual elements of the *McConnell* [1968] relaxation spectrum which, although this was originally inferred based upon the use of a Cartesian half-space model, has been converted to spherical harmonic degree ℓ using the Earth-flattening transformation between horizontal wavenumber k and spherical harmonic degree ℓ as $k = (\ell + 1/2)/a$. Inspection of the suite of kernels shown in Figure 19a demonstrates that the McConnell spectrum provides information on viscosity that

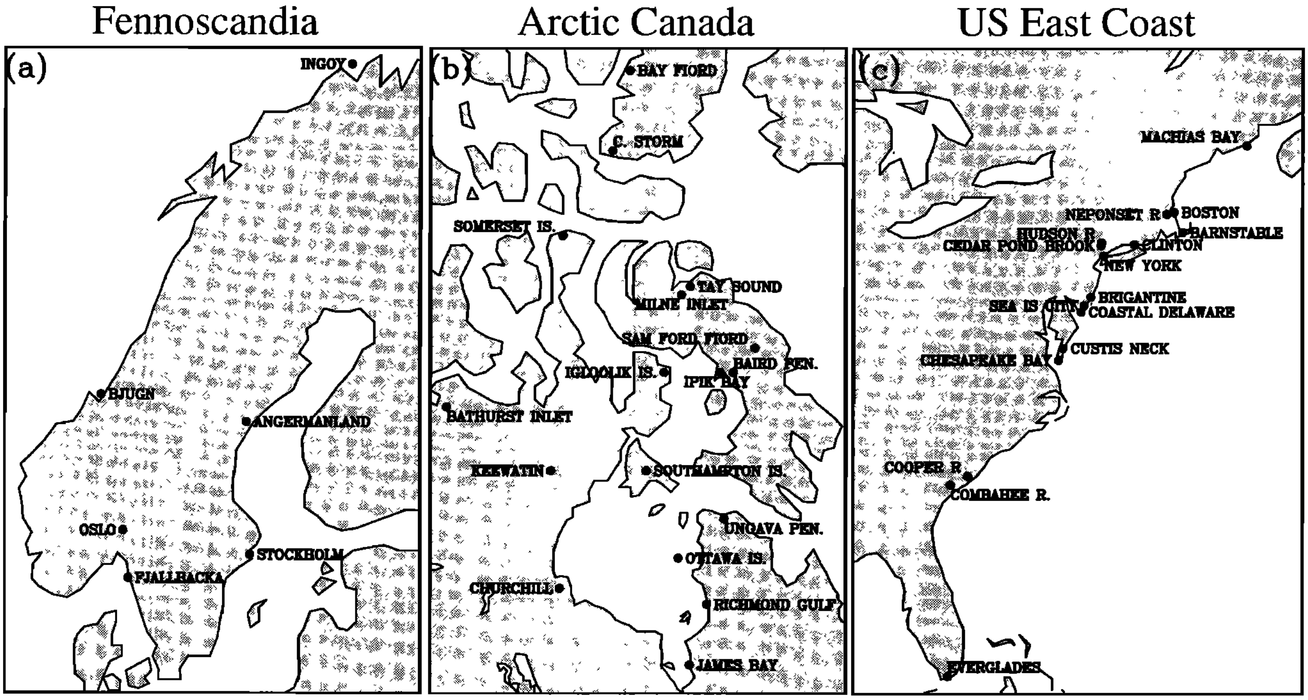

Figure 20. Site location maps for the ice-covered sites in North America and Fennoscandia from which site specific relaxation time data are extracted for use in the inverse problem for mantle viscosity. Also shown are a set of locations along the U.S. east coast from which ^{14}C dated rsl histories are available that may be employed for the purpose of verifying the plausibility of the viscosity model determined through application of the formal inversion procedure.

is almost entirely restricted to the upper mantle and transition zone. Figure 19b compares the numerically inferred Fréchet kernels using the procedure embodied in equations (21) and (22), for the individual relaxation times (lumped relaxation times since several individual modes are usually involved) inferred on the basis of Monte Carlo relaxation time fits to individual relative sea level records from sites in Canada and Fennoscandia that were once ice covered. An example of such data was previously presented in Figure 3 for a location (southeast Hudson Bay) near the center of Laurentian rebound and from an equivalent location (Angerman River) in ice-covered Sweden. The procedure that I employ to extract the observed relaxation time data and the forward predictions of the relaxation time data themselves are fully discussed by *Peltier* [1996a, 1998c], and no purpose will be served by repeating that discussion here. Inspection of the kernels shown in Figure 19b demonstrates that the relaxation time observed at the Angerman River site, which is near the center of Fennoscandian rebound (see Figure 20), provides information which is most sensitive to viscosity in the transition zone of the mantle, whereas that from the Canadian site (Bathurst Inlet in the Canadian Arctic, see Figure 20) is primarily sensitive to the viscosity in the upper part of the lower mantle. Figure 19c shows Fréchet kernels for both polar wander speed (PW) and nontidal acceleration (J2). Since these two GIA effects depend solely upon the degree 2 spherical harmonic constituents of the deformation spectrum, it is clear that they should sample the viscosity of the mantle to the greatest possible depth, and inspection of the sensitivity kernels shows that this is indeed the case. Both data sets essentially provide a constraint on the average value of the viscosity of the mantle from the base of the lithosphere, which we have been assuming to be 120.6 km thick and to have infinite viscosity, to the core-mantle boundary (CMB). On the basis of the totality of such data it should therefore be clear that sensitivity exists in the combined data such that we might reasonably hope to adequately constrain the viscosity profile all the way to the CMB, at least in terms of large-scale depth averages. A preliminary assessment of the implications of a small subset of the Hudson Bay relative sea level data using these methods was presented by *Mitrovica and Peltier* [1995].

Examples of mantle viscosity profiles obtained by the application of the formal process of Bayesian inference based upon the above described Fréchet kernels are shown on Figure 21. In all of these analyses (details of which are given by *Peltier* [1998c]) the simple viscosity model VM1 has been employed as starting model, and the inversion is performed in a single step of an iterative Bayesian procedure (see *Tarantola and Valette* [1982a, b], *Jackson and Matsu'ura* [1985], and *Backus* [1988] for a general discussion of this methodology). Figure 21a compares two final models that have been inferred on

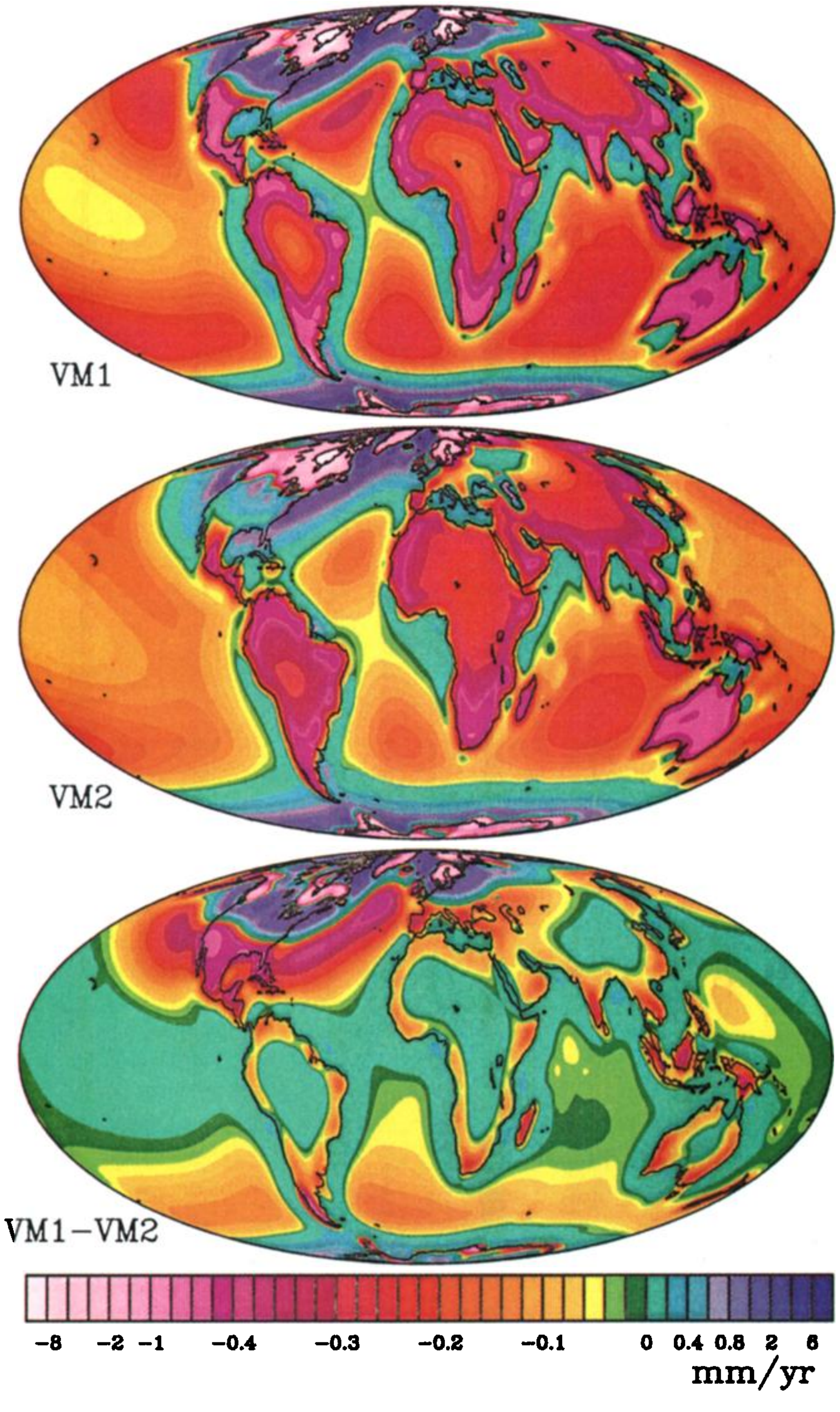

Plate 4. Predictions of the present-day rate of relative sea level rise for the VM1 and VM2 models as well as for the difference between them. This difference is clearly largest along the east coast of the continental United States, making the rsl histories observed along this coast exceptionally well placed to allow an unambiguous test of the improvement to the radial viscosity structure represented by the VM2 structure over that embodied in the simple model VM1.

the basis of inversions that differ from one another only in the way in which the site specific relaxation times for the Fennoscandian and Laurentian sea level curves have been inferred from the ^{14}C data. For the model shown as the heavy solid curve the data analyzed using the Monte Carlo procedure consisted of exactly the envelope-sampled forms recorded in the compilation of *Tushingham and Peltier* [1992]. For the model shown as the thin solid curve, on the other hand, the data to which the Monte Carlo procedure was applied consisted of the raw age-height pairs of the individual sea level sample indicators that were actually measured at each location. Comparing these two final models demonstrates that they do not differ significantly.

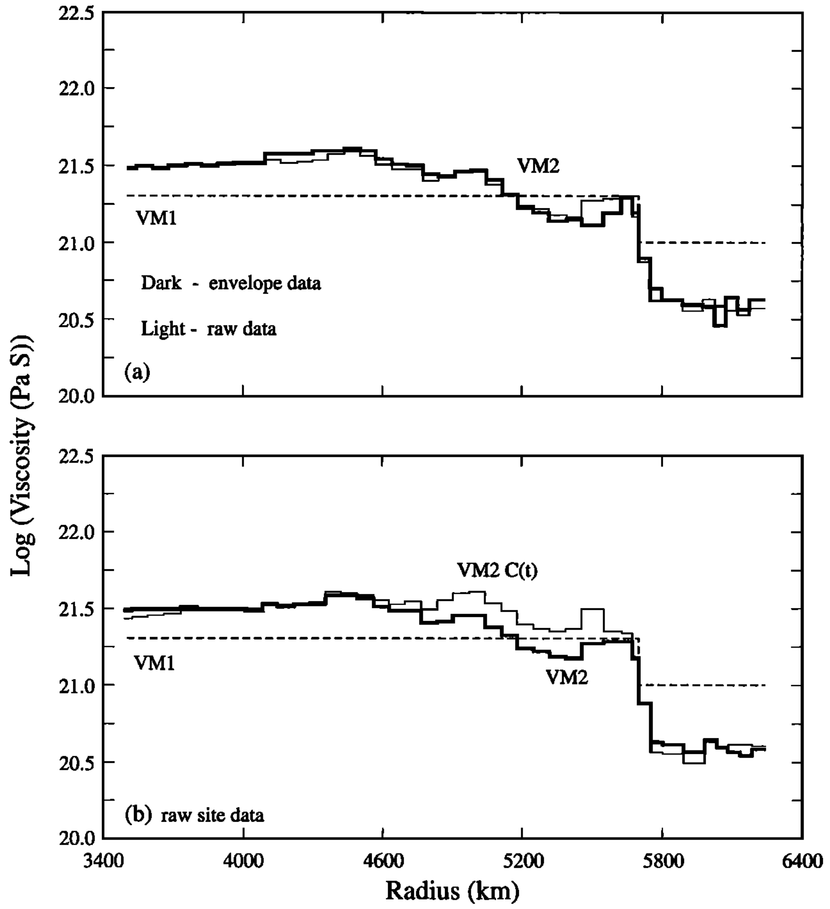

Figure 21. Viscosity profiles determined by simultaneous formal Bayesian inversion of the Fennoscandian relaxation spectrum of *McConnell* [1968], the site specific relaxation times from the 23 ice-covered sites in Canada and Fennoscandia whose locations are shown on Figure 19, and the nontidal acceleration of the rate of axial rotation. In Figure 21a the dashed curve is the VM1 viscosity profile employed as starting model in the inversion process, while two versions of the final model are shown as the dark and light solid curves, respectively, these being distinct versions of VM2. The former of these two inferred models has been obtained using site specific relaxation times obtained from fits to the envelope sampled data compiled by *Tushingham and Peltier* [1992], whereas the latter was obtained on the basis of site specific relaxation times deduced from the raw data themselves. In Figure 21b, the dashed curve also indicates VM1, and the two versions shown of the final model VM2 are based upon use of the raw data to determine the site specific relaxation times and a further version in which the starting model predictions were made with the version of the model that included the full influence of time dependence of the ocean function. Incorporation of the latter effect in the forward model slightly decreases the forward predictions for the site specific relaxation times and therefore slightly increases the inferred viscosity in the upper part of the lower mantle, essentially back to the value of 2×10^{21} Pa s that is characteristic of the starting model VM1 in this region.

Figure 21b shows an additional model inferred through a further variation on the basic analysis procedure [see *Peltier*, 1998c]. Whereas for the models shown on Figure 21a the forward predictions of the individual relaxation times at the Canadian and Fennoscandian sites were based upon solutions to equation (3) in which the ocean function was assumed to be time-independent, the forward predictions used in the inversion that generated the new model incorporated the full influence of ocean function time dependence. Comparing the results on Figure 21a to those on Figure 21b again demonstrates that the inferred final model is modified only slightly. In comparison to the starting model VM1, the VM2 family of models is slightly softer in the upper mantle and transition zone (by a factor of ~2), somewhat softer also in the uppermost 500–700 km of the lower mantle, and slightly stiffer in the lower half of the mantle. Since the VM1 model accurately predicts all of the Earth rotation related observations (polar wander speed and direction as well as the nontidal acceleration as explicitly demonstrated in section 4.3) and since these data essentially constrain the average viscosity of the entire mantle, it will be clear that if for some reason the viscosity must be reduced in one region, the rotational constraints require that this be compensated by an increase elsewhere so as to preserve the average.

Inspection of Figure 22 will demonstrate the reason for the reduction in upper mantle and transition zone viscosity that is delivered by the inversion procedure. This shows the relaxation spectrum for Fennoscandian rebound deduced by *McConnell* [1968] along with the predictions of this spectrum for the VM1, VM2, and VM3 models discussed here. Inspection of Figure 22 will demonstrate that the VM1 model systematically misfits the McConnell spectrum so as to imply that the viscosity of the upper mantle and transition zone in VM1, which is 1×10^{21} Pa s, is somewhat high. On the other hand, the formally derived VM2 model fits the McConnell spectrum quite well. On the long-wavelength asymptote on which the relaxation time is essentially constant and near 4.2×10^3 years (equal to the relaxation time characteristic of the Angerman River curve) the fit is excellent. At the shortest wavelengths the fit is worse, but since these data were not employed in the inversion, this is entirely expected. The wavenumber (spherical harmonic degree) beyond which relaxation time decreases is

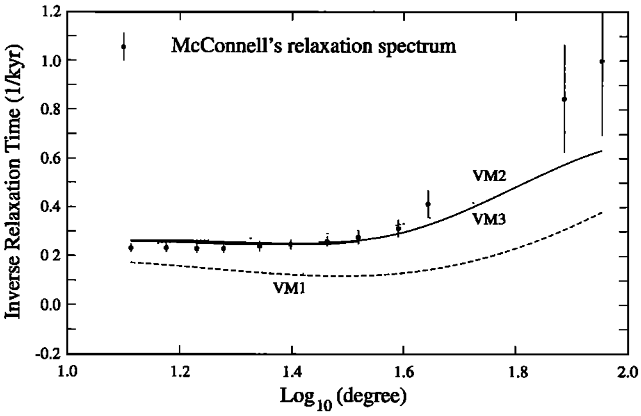

Figure 22. The relaxation spectrum for Fennoscandian rebound of *McConnell* [1968] along with predictions of this spectrum for models VM1, VM2, and VM3. Note that model VM1 predicts relaxation times that are in excess of those inferred by McConnell at every spherical harmonic degree. Models VM2 and VM3, on the other hand, fit the observed spectrum nicely. Note that the error bars assigned to the relaxation time observations of McConnell may be somewhat overly optimistic. However, it is clear that at lowest wavenumber one must have a relaxation time that agrees with the site specific relaxation time at the Angerman River location, which is very close to 4.2 kyr (as demonstrated previously on Figure 3b), and on this basis, since the long-wavelength asymptote of the McConnell spectrum does indeed fit this observation, I have supposed it mandatory that the inferred viscosity models should fit this spectrum to within the 10% error bounds shown. Again, this may be somewhat excessively confining, in which connection it is important to note the concerns expressed by *Wolf* [1996] concerning the accuracy of McConnell's spectrum.

determined by lithospheric thickness, and with the thickness fixed to the 120.6 km value that characterizes both VM1 and VM2 the location of this corner in the spectrum is also well predicted. It must be recognized, however, that the short-wavelength edge of the relaxation spectrum is not accurately determined by McConnell's analysis, so that the constraint on lithospheric thickness cannot be considered robust. A preliminary formal analysis of the implications of the *McConnell* [1968] relaxation spectrum for Fennoscandia was presented by *Mitrovica and Peltier* [1993a].

It is also important at this juncture to note the recently published comments of *Wolf* [1996], who has drawn attention to the revisions of the *Sauramo* [1958] shoreline diagram (on which *McConnell* [1968] based his inference of the relaxation spectrum) that have been suggested by *Donner* [1980] and *Eronen* [1983]. As yet uncompleted ongoing work suggests that this spectrum is actually rather accurate (D. Wolf, personal communication, 1998). If these initial results are confirmed, then the VM2 family of models may not require significant further revision.

As we will discuss more fully in section 5.1, the extent to which the VM2 models may be considered secure also depends upon the validity of the other assumptions concerning the input data that we are obliged to make to perform the formal inversion. Taken at face value, however, it is clear that the VM2 models do not differ significantly from VM1. Whereas the viscosity contrast across the mantle is a factor of 2 in VM1, in VM2 it is a factor of ~8. Furthermore, whereas the entire factor of 2 contrast in VM1 is focused across the 660-km discontinuity, the contrast across this horizon in VM2 is only slightly increased to a factor of ~3. This contrast is clearly very much less than that which has been inferred on the basis of some analyses of nonhydrostatic geoid anomalies (see section 4.5). There are, however, conditions under which the required contrast would be higher, at least in the lowermost mantle and also conditions in which models that exhibit much more radical variations of viscosity with radius than those which characterize the VM2 sequence would be required, and these will be considered in section 4.5.

4.2. Relative Sea Level Tests of the Spherically Symmetric Reference Model(s) VM2

It will be clear on the basis of the preceding discussion of the inverse problem that only a very small and highly selected fraction of the totality of the data related to the glacial isostatic adjustment process has been employed to define the VM2 class of models of the radial viscosity variation. In particular, we have employed (1) the relaxation spectrum for Fennoscandian rebound inferred by *McConnell* [1968]; (2) a set of 23 relaxation times obtained on the basis of Monte Carlo fits to individual relative sea level time series from sites that were ice covered at LGM (17 sites from Canada and 6 sites from Fennoscandia as shown on Figure 20); and (3) the satellite-observed nontidal acceleration of axial rotation and the speed of polar wander that has been inferred on the basis of the previously discussed International Latitude Service (ILS) pole path. Since none of the relative sea level data from sites beyond the ice sheet margins have been employed in the construction of the VM2 sequence of models, all of these data may be employed to test their predictive capacity. Only if the models are able to successfully reconcile data not employed to construct them may we have confidence in their quality. In the remainder of this section I will specifically consider data from only three especially significant geographical regions selected on the basis of the quality and quantity of the information available from them.

4.2.1. East coast of the continental United States. Plate 4 presents predictions of the present-day rate of sea level rise based upon the solution of the form of the sea level equation (3) which neglects the (small) influence of rotational feedback. These results are based upon the use of the ICE-4G deglaciation history and the assumption that isostatic equilibrium was obtained at LGM, an assumption that will be explicitly tested in section 4.2.4 but which has received scant attention in the past. The predicted present-day rate of sea level rise is shown on Plate 4 for both the VM1 and VM2 models

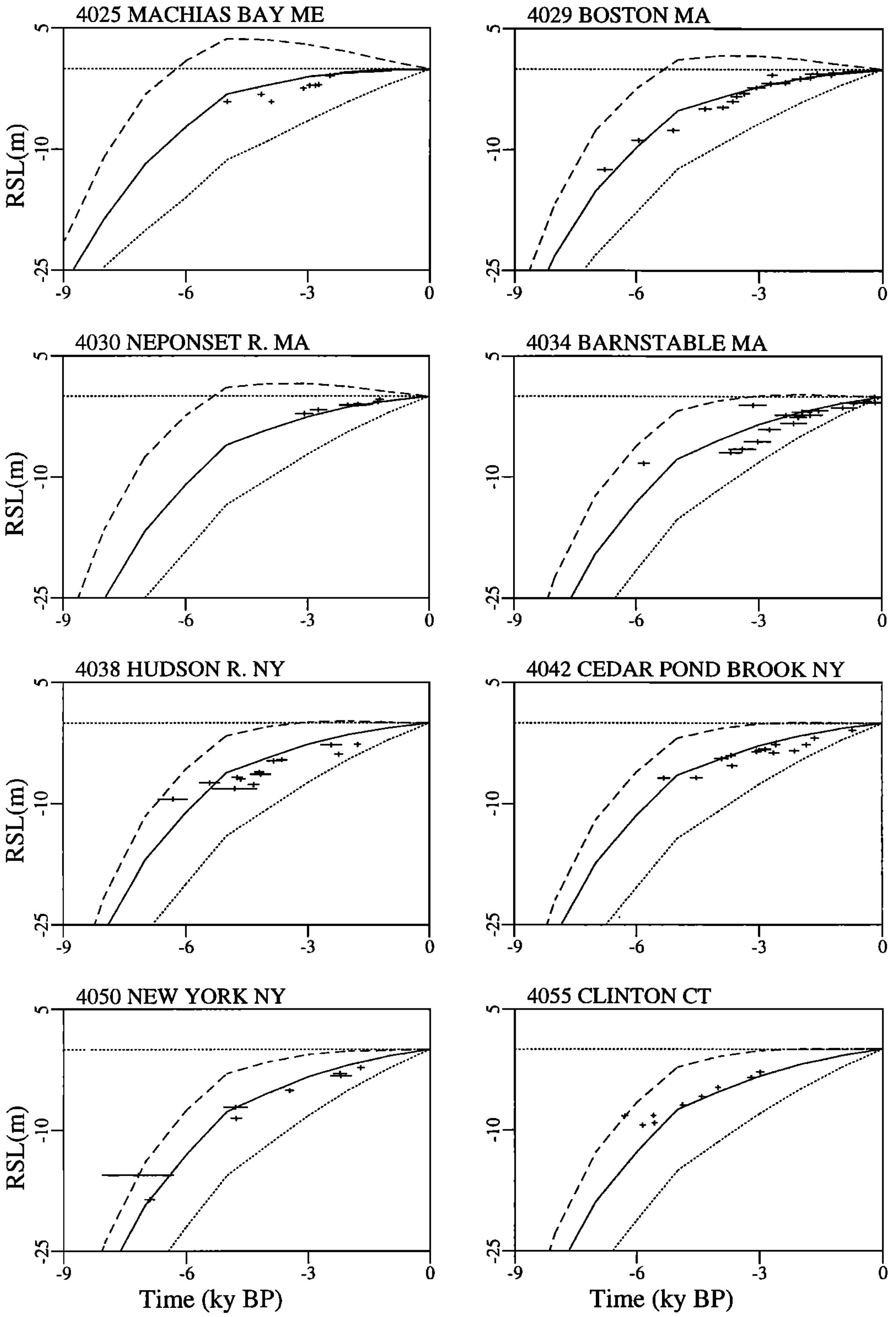

Figure 23. Comparisons between the observed ^{14}C records of relative sea level history from sites along the U.S. east coast (timescale corrected) and those predicted by the VM1, VM2, and MF viscosity models based on theoretical calculations performed using the ICE-4G model of the glaciation history. Results for the VM1 model (shown as dotted curves) substantially overpredict the present-day rate of relative sea level rise at all sites along the northernmost segment of the coast shown on Figure 20. The predictions for the VM2 model, on the other hand (shown as solid curves), clearly fit the data extremely well at every location. The predictions for the MF model of *Mitrovica and Forte* [1997] (shown as dashed curves), which are discussed in detail in section 4.5, drastically misfit almost all of the U.S. east coast observations, especially in the northernmost and southernmost regions. At each site the observations together with their error bars are denoted by pluses.

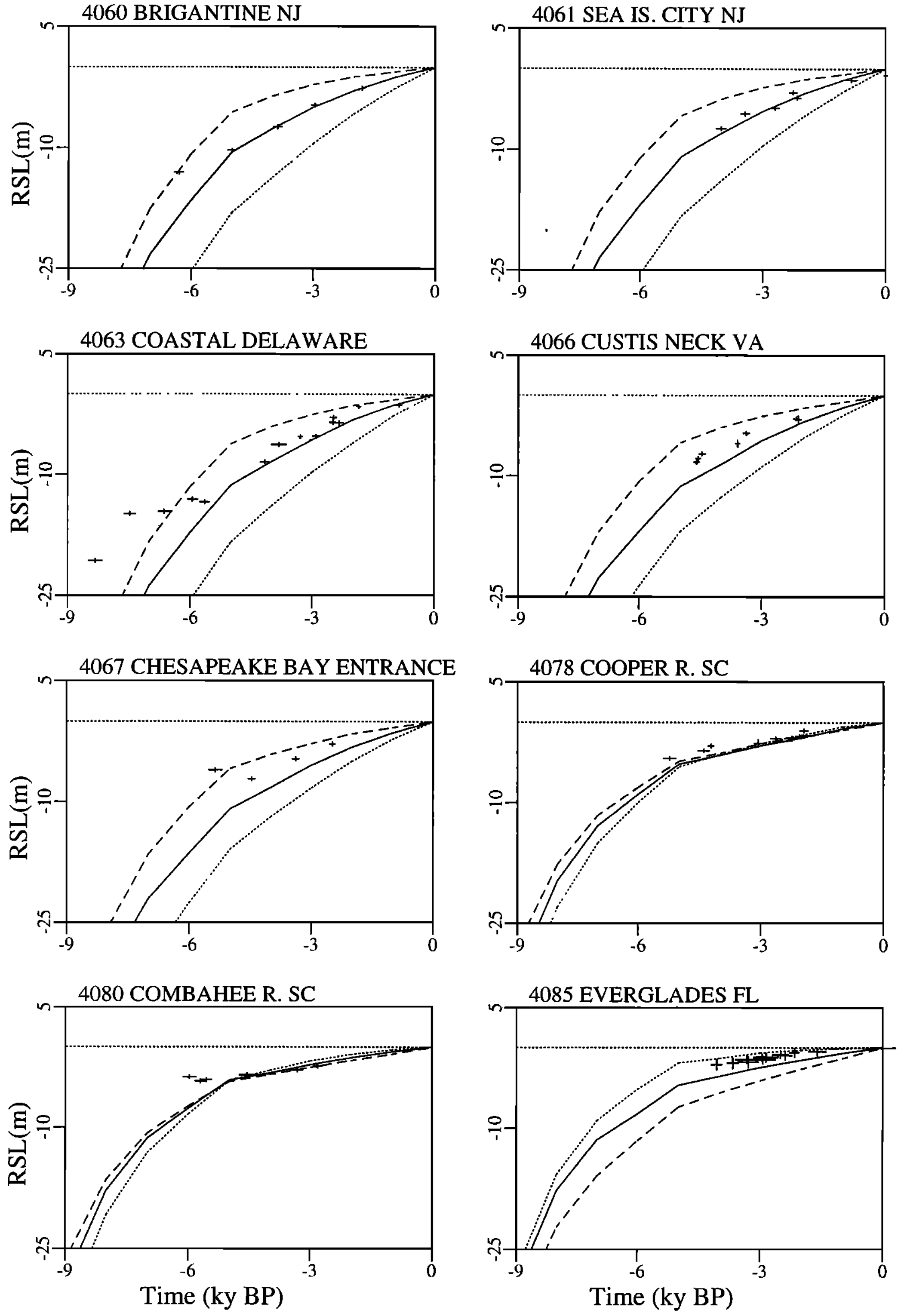

Figure 23. (continued).

(the latter result being based upon the version of VM2 for which relaxation time estimates were inferred from the raw rsl data and for which the forward predictions were made excluding the influence of ocean function time dependence). Also shown on Plate 4 is the difference between these two global predictions, inspection of which clearly demonstrates the large impact that the modification to the viscosity profile embodied in VM2 has on the predicted rate of rsl rise along the U.S. east coast. Since this region was previously identified [*Tushingham and Peltier*, 1992] as one in which the VM1 model failed to adequately reconcile the ^{14}C dated ob-

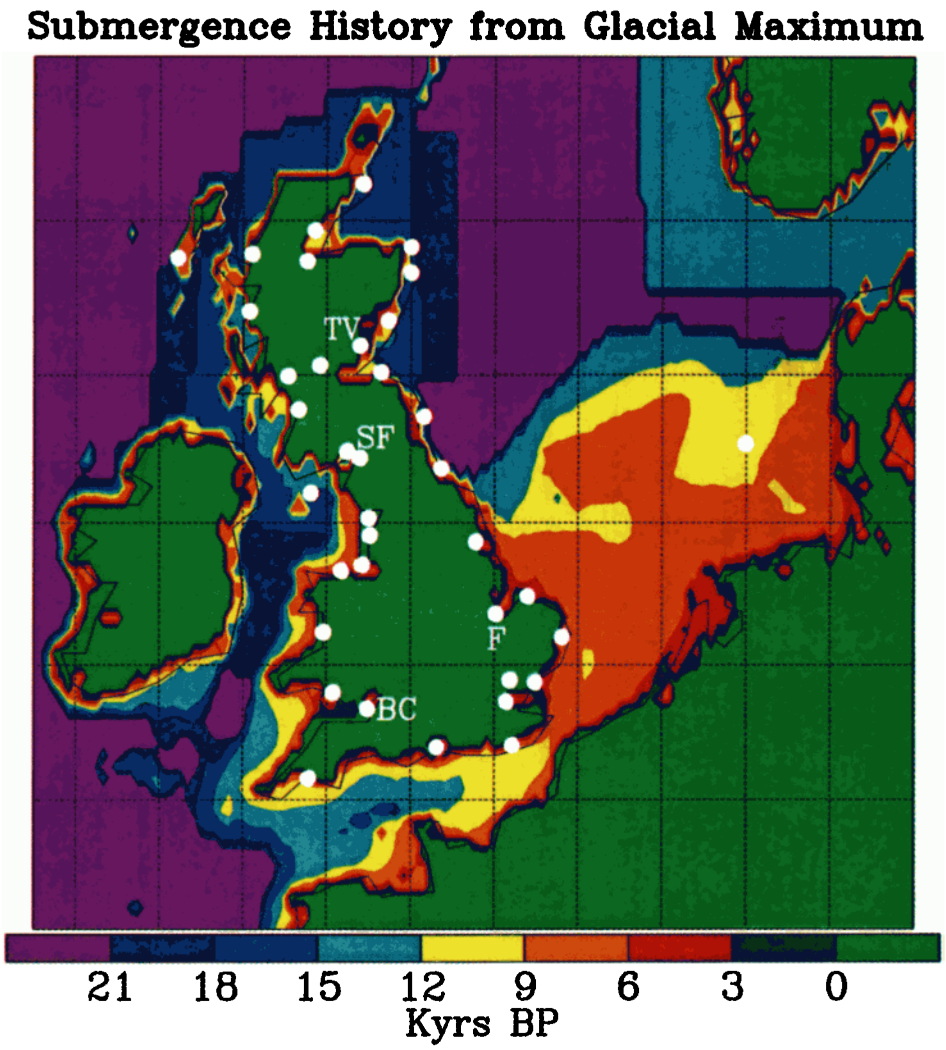

Plate 5. Predicted time-dependent evolution of the coastline in the region of northwestern Europe centered on the British Isles obtained by solution of the sea level equation (3) to obtain the time-dependent ocean function $C(t)$ using the procedure discussed in section 3. The large solid dots superimposed upon the modern coastline represent the location of sites from which ^{14}C dated relative sea level histories are available (see W. R. Peltier and I. Shennan (manuscript in preparation, 1998) for a detailed discussion). The sites explicitly labeled are TV, Tay Valley; SF, Solway Firth; F, Fenlands; and BC, Bristol Channel.

servations of postglacial relative sea level change, it is clearly of interest whether the formally inferred VM2 model removes the previously recognized misfits. That this question may be answered in the affirmative is demonstrated on Figure 23, in which the raw ^{14}C data from the U.S. east coast sites whose locations were shown previously on Figure 20 are compared with the rsl predictions based upon the VM1 and VM2 viscosity models as well as with the predictions of the model of *Mitrovica and Forte* [1997], which will be further discussed in section 4.5. Inspection of these intercomparisons provides a very convincing demonstration that the VM2 model, by substantially reducing the predicted rates of rsl rise along the northeast segment of this coast, essentially eliminates the misfits to the data in this region, as recently discussed at considerable length by *Peltier* [1996a, b] and *Peltier and Jiang* [1997].

4.2.2. British Isles.

Probably the most interesting region from the point of view of testing the ICE-4G (VM2) model of postglacial sea level history consists of the British Isles, as mentioned in section 2.1. There are several reasons for this. First, Great Britain sits astride the peripheral bulge of the Fennoscandian ice sheet and in this sense lies in a similar dynamical regime to the U.S. east coast. Second, however, Great Britain was itself heavily glaciated over both Scotland and somewhat to the south at LGM. Finally, the coastline of the region was strongly time-dependent through the deglaciation period, the LGM epoch being characterized by an extensive land bridge over the present-day English Channel that then connected England to France. Plate 5 shows the evolution of the coastline in this region determined on the basis of the ICE-4G (VM2) model in the form of time-dependent contours. Superimposed on

Plate 5 are a sequence of large solid dots indicating the locations of the sites from which ^{14}C dated rsl data are available. The totality of these data and the implications of the extent to which they are reconciled by the VM1 and VM2 models are discussed by W. R. Peltier and I. Shennan (manuscript in preparation, 1998). Here I will discuss only four examples for illustrative purposes (the data from which along with the theoretical comparisons were previously shown on Figure 4). These correspond to Tay Valley and Solway Firth in the north, sites that were under the Scottish ice sheet, and the Fenlands (east coast) and the Bristol Channel (southwest coast) in England.

Inspection of the two representative data sets from the northern region (Figure 4) that was once ice covered demonstrates that the rsl histories are distinctly nonmonotonic as mentioned in section 2.1. The theoretical predictions, which are shown for both the VM1 and VM2 viscosity models, are such that relative sea level is first predicted to fall subsequent to LGM, a process that continues with a brief hiatus near 15 kyr ago until about 10 kyr ago. The brief hiatus in this period of falling sea level that occurs near 15 kyr ago is undoubtedly associated with what has often been referred to as meltwater pulse 1a, which is evident in the Barbados-derived sea level record of *Fairbanks* [1989] as the first episode of rapid sea level rise (see Figure 6). Clearly, during this episode the rate of postglacial rebound of the crust of Scotland that is caused by the meltback of the Scottish ice sheet is not sufficiently rapid to overcome the rising sea levels caused by the dramatic meltback of (primarily) Laurentide ice that occurred at this time. No sea level record is available from Scotland during this period because the surface had yet to become ice free. By 10 kyr ago the rate of crustal rebound had decreased to such an extent that given the sudden onset of rapid retreat of the Antarctic ice sheet (see Figure 37), relative sea level again began to rise locally. This period of rising level is well recorded in the data at both sites shown and ends between 4 and 5 kyr ago, subsequent to which sea level continues to fall due to continuing crustal rebound once the deglaciation event is complete, which in ICE-4G is about 5 kyr ago. It is clear by inspection of the examples of the rather complex postglacial rsl variations from Scotland that the ICE-4G (VM2) model fits these data quite well as, in fact, does ICE-4G (VM1), demonstrating that these data are not especially useful for mantle viscosity discrimination.

Also shown on Figure 4 are comparisons between theory and observations for the two previously mentioned sites in southern England, a region that was not glaciated at LGM. Both the Fenlands and Bristol Channel data sets, which extend from present to ~9 kyr ago, demonstrate that rising sea levels have been characteristic of this period in this region of England. In both cases the model predictions also fit the observations rather well, providing further confirmation of the quality of the model. The rising sea levels in this region are clearly controlled by the same process of forebulge collapse that is occurring along the U.S. east coast. Here, however, the rsl record is governed not only by the collapse of the forebulge of the Fennoscandian ice sheet to the east but also by that of the Scottish ice sheet which lay to the north at LGM.

In connection with understanding the implications of the excellent fit to the British Isles data provided by the ICE-4G (VM2) model, I note the significant difference between the VM2 viscosity model and that suggested by *Lambeck et al.* [1996] to be required by these observations. The model suggested by Lambeck et al. has the viscosity of the upper part of the lower mantle bounded below by 10^{22} Pa s, more than 5 times higher than in VM2, yet VM2 fits the observations beautifully. Clearly, the high value of lower mantle viscosity preferred by Lambeck et al. is not, in fact, required by the data from the British Isles. It is actually ruled out by the relative sea level data from Canada as demonstrated by the results obtained through formal inversion for viscosity (see the further detailed commentary in section 4.5).

4.2.3. Equatorial Pacific Ocean and its western margin. Although somewhat less exotic in the mix of GIA-related processes that control rsl history in this region, the western equatorial Pacific Ocean and its margin have recently "emerged" as the region of greatest contention insofar as understanding the global record of postglacial rsl variability is concerned. This is clear from the exchange between *Edwards* [1995] and *Peltier* [1995a], which concerned the interpretation of the coral-based record from the Huon Peninsula of Papua New Guinea [e.g., *Chappell et al.*, 1996, and references therein] (see also discussion of Figure 7). *Peltier* [1994] employed the Huon record to provide "far-field" verification of the quality of the ICE-4G model of deglaciation. The timing of the various deglacial components of the ICE-4G model was adjusted from ICE-3G so as to enable a good fit to the coral-based record from Barbados to be obtained. The theory was then employed to predict the history that should be observed on the Huon Peninsula. It was shown that when the latter data were not corrected for the large rate of tectonic uplift that it has become standard to assume for this region, then the theoretical predictions reasonably agreed with the observations. *Edwards* [1995] pointed out that if the standard correction to the data was applied, then a large misfit existed, and he suggested that this could imply a significant error in the model, while *Peltier* [1995b] replied that there seemed to be no clear evidence that the rate of tectonic uplift characteristic of the Holocene could not be substantially smaller than that corresponding to the late Pleistocene average rate that had been derived on the basis of a straight-line fit to the sequence of interglacial terraces that are found at Huon, at heights above present-day sea level that are an increasing function of age.

Very recent further analyses of this issue have enabled an entirely satisfactory resolution of this debate to

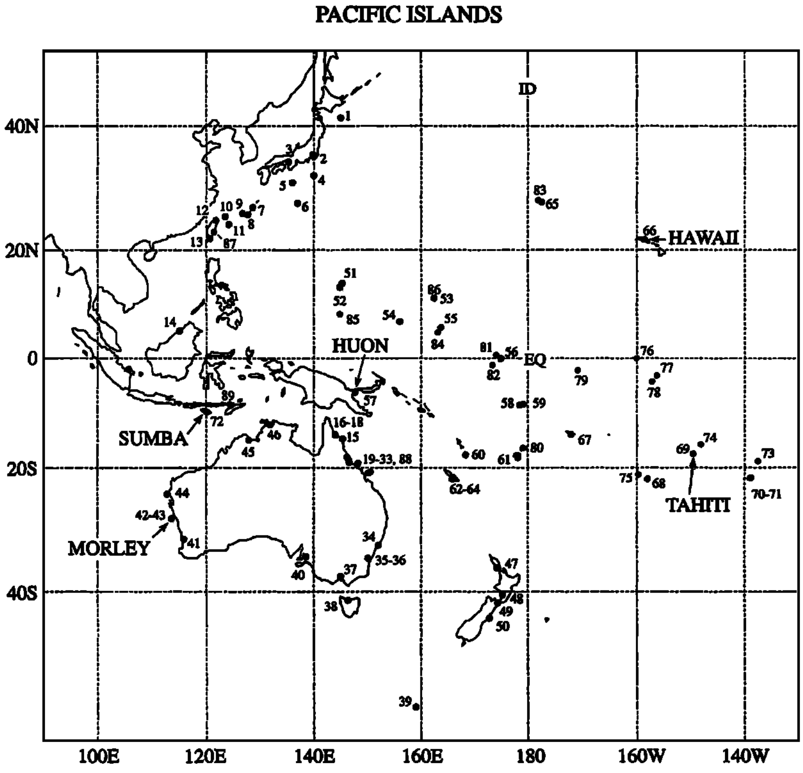

Figure 24. Location map for the equatorial Pacific Ocean region showing the locations of the islands from which information on relative sea level history is available. The data from those islands for which names are explicitly provided are discussed in the text. The numbering scheme for the other locations is that employed in the global recompilation of rsl data that has been ongoing at Toronto for the past several years.

be achieved. These analyses have been based on rsl observations at the Pacific Ocean sites shown on the location map of Figure 24. Figure 25 shows the raw and "tectonics corrected" coral-based records from New Guinea [*Chappell and Polach*, 1991; *Ota et al.*, 1993], Tahiti [*Bard et al.*, 1996a], Morley Island [*Eisenhauer et al.*, 1993], and Sumba Island [*Bard et al.*, 1996b]. Also shown is the predicted sea level history based upon the ICE-4G (VM2) model of the GIA process. The open symbols shown for the New Guinea, Tahiti, and Sumba Island sites indicate the relative level implied when the conventional constant tectonic uplift velocity (v_t) appropriate to each site is employed to correct the data. For Sumba and Morley Islands the data are well fit by the theory. When the conventional correction is applied to the New Guinea data, as pointed out by *Edwards* [1995], the misfit of the theory to the observations is extremely large. For the data from Tahiti, for which the sign of the tectonic correction is opposite to that at Huon but which is not accurately known, the misfit of the theory to the observations is also very large. Careful inspection of the data for Huon, however, will demonstrate that the uncorrected data do lie somewhat above the theoretical prediction and do contain a similar mid-Holocene highstand of sea level to that predicted by the theoretical model at all Pacific Ocean locations (recall the Oahu data shown on Figure 5), subsequent to which rsl is both predicted and observed to fall. This same feature of falling present-day sea levels is, of course, clearly evident in both Plates 3 and 4. On the basis of all previous work on the postglacial sea level history of the Pacific Ocean region it is very well known that sea level did, in fact, achieve a highstand at 4 to 6 kyr ago, by which time deglaciation is essentially complete. ICE-4G (VM2) well predicts the amplitude and timing of this highstand at all of the numbered island locations shown on Figure 24 from which information on actual shorelines is available. Here it is important to recognize that coral-based records of rsl do not generally record shoreline. It was, in fact, the success of the earliest version of the global model of the GIA process in predicting this highstand [*Clark et al.*, 1978; *Peltier et al.*, 1978] that attracted so much attention from the geological community.

Inspection of Figure 25 demonstrates that when the late Pleistocene average rate of tectonic uplift is used to correct the Huon data, the mid-Holocene highstand evident in the raw data is entirely eliminated. Furthermore, if the coral-based record from Tahiti is corrected by assuming the conventional small rate of thermal subsidence to have been characteristic of the Holocene period, then the coral-based record at Tahiti also does not contain the mid-Holocene highstand known to be characteristic of the surrounding islands from which actual shoreline information is available. At the Huon site, there now seems to be agreement that the large rate of tectonic uplift that has been conventionally assumed (1.9 mm yr^{-1}) is, in fact, too high to be characteristic of the Holocene (J. Chappell, personal communication, 1997). A new determination of the Holocene rate is provided on Figure 26 in which all of the available data from Huon [*Chappell and Polach*, 1991; *Edwards et al.*, 1993; *Ota et al.*, 1993] have been employed to define a

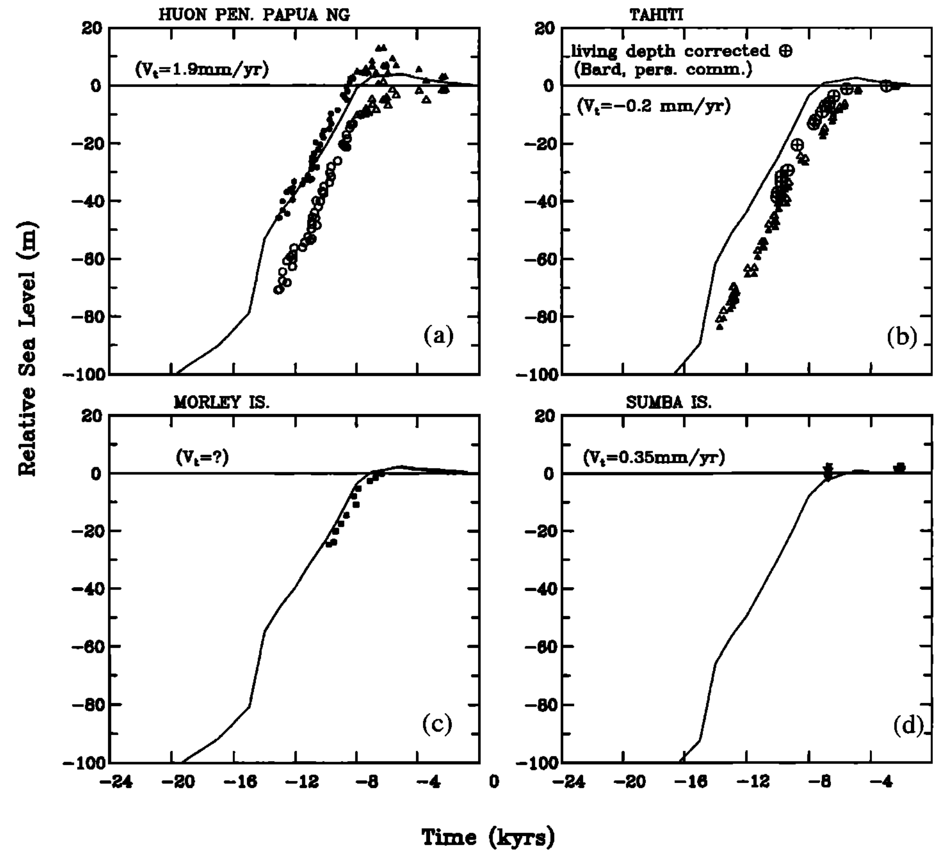

Figure 25. The raw and tectonic uplift corrected coral-based records are shown, along with the predicted sea level histories based upon model ICE-4G (VM2) for (a) the Huon Peninsula, (b) Papeete Harbour, Tahiti, (c) Morley Island, and (d) Sumba Island. The solid symbols denote the raw data, and the open symbols denote the same data corrected by assuming the conventional rate of tectonic uplift v_t. In Figure 25b the additional points denoted by a circled plus denote the data corrected by the assumption of a particular "living depth" to be characteristic of the coral species.

root-mean-square deviation of the observations from the theory as a function of the assumed rate of tectonic uplift employed to correct the data. Depending upon the timescale over which the misfit is computed (all data or only the data from 9 kyr ago to present), one obtains best estimates of the rate of tectonic uplift between 0.30 and 0.65 mm yr^{-1}, respectively, that is, between a sixth and a third of the late Pleistocene average rate. It seems clear therefore that the Huon Peninsula data do not, in fact, conflict with the theoretical model predictions. Unless they are corrected properly so as to fit these predictions, they are, in fact, in conflict with actual shoreline data from all surrounding sites. How the issue of the proper interpretation of the Tahiti data will be resolved is as yet unclear. It will probably involve recognizing that this island has been subjected to a greater rate of tectonic subsidence than is presently thought to be operative and perhaps also the recognition of a substantial living depth correction for the assemblage of species of coral that make up the reef structures in this location (a preliminary estimate of this correction was kindly provided by E. Bard and is shown on Figure 25b).

4.2.4. On the influence and extent of glacial isostatic disequilibrium at Last Glacial Maximum.

All of the rsl analyses discussed in this section as well as the implementation of the inverse theory for mantle viscosity using the rsl data discussed in section 4.1 have been based upon the assumption that insofar as these particular data were concerned, it was acceptable to assume that the ice sheets, oceans, and solid Earth were in a state of isostatic equilibrium at Last Glacial Maximum. If the system were not in a state sufficiently close to equilibrium at this time, it is quite conceivable that large errors might be made, for example, in inferring the viscosity of the mantle in the way we have done. It is therefore possible that the quality of the ICE-4G (VM2) sequence of models could be significantly compromised. Now the issue of the degree of isostatic equilibrium that existed at LGM clearly depends upon the relationship between the characteristic timescale of the GIA process, which is determined by mantle viscosity, and the timescale/nature of the glaciation process. If the mantle relaxes sufficiently quickly (its viscosity is low enough) relative to the timescale on which the continental ice

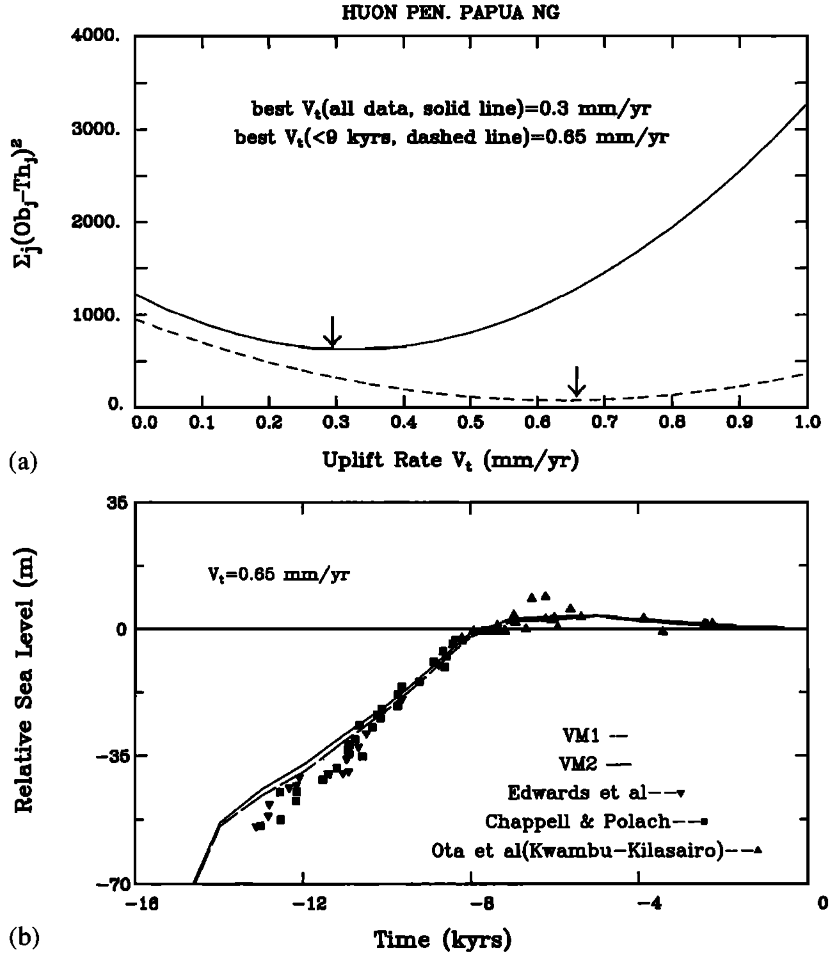

Figure 26. (a) Variance reduction between the prediction of the relative sea level history on the Huon Peninsula for the ICE-4G (VM2) model and the observations as a function of the rate of tectonic uplift assumed for the purpose of connecting the observations. Variance reduction is shown based upon the use of all available data and the use of only data younger than 9 kyr. With the former assumption the "best fitting" rate of tectonic uplift is found to 0.35 mm yr^{-1}, whereas for the latter assumption it is found to be 0.65 mm yr^{-1}. (b) Fit of the tectonically corrected data to the ICE-4G (VM2) prediction.

sheets accumulate, then equilibrium at LGM may be assumed. Otherwise, appreciable disequilibrium may exist.

In order to assess the relative timescales of relaxation and ice sheet accretion we clearly require direct information on the latter as well as the former. Prior to the appearance of the recent paper by *Chappell et al.* [1996], there existed a distinct possibility that the system could have been significantly out of equilibrium at LGM. This is because, based upon the incorrectly dated coral sequence from Eemian to LGM that was previously believed to provide control on the variation of global sea level (shown on Figure 7a), it was apparently the case that sea level during oxygen isotope stage 3 (roughly 70 to 35 kyr B.P.) remained very high relative to the 120-m eustatic depression that was characteristic of the LGM state. If a substantial fraction, say half, of the total glacial sea level fall were to have occurred over a timescale of less than 10 kyr, it would then be rather unlikely that equilibrium could have been substantially achieved by LGM. As mentioned in section 2.1, the recently revised dating of the Huon core discussed by *Chappell et al.* [1996] would appear to have eliminated this possibility by showing that the late glacial rsl history at Huon was in very good accord with the sawtooth inference previously made by *Shackleton* [1987] based upon the $\delta^{18}O$ sea level proxy contained in benthic foraminiferal tests from deep-sea cores. We may therefore test the self-consistency of the ICE-4G (VM2) model of the GIA process by using, say, the previously mentioned SPECMAP $\delta^{18}O$ record [*Imbrie et al.*, 1984] to extend the LGM to present deglaciation history of ICE-4G back to 780 kyr ago so as to provide a complete history of the glaciation-deglaciation process. The SPECMAP record itself is shown in Figure 27a. To obtain the pre-LGM space-time history from SPECMAP, I have assumed that prior to LGM the spatial distribution of glacial ice was fixed to its LGM distribution but that its thickness varied in proportion to the magnitude of the $\delta^{18}O$ anomaly, just as was assumed in section 3 for analysis of the rotational response (see section 4.3). Complete rebound calculations were then performed by keeping the ocean function *C* fixed to its present form and focusing upon the difference between the rsl predictions and the observations at the formerly ice-covered sites that were employed for the purpose of mantle viscosity inference. A representative set of such comparisons is shown in Figure 28, which, for eight locations, shows both predictions based upon the assumption of isostatic equilibrium at LGM and those which incorporate the specific degree of disequilibrium that is obtained using ICE-4G (VM2) in conjunction with the SPECMAP-controlled loading history. Data are

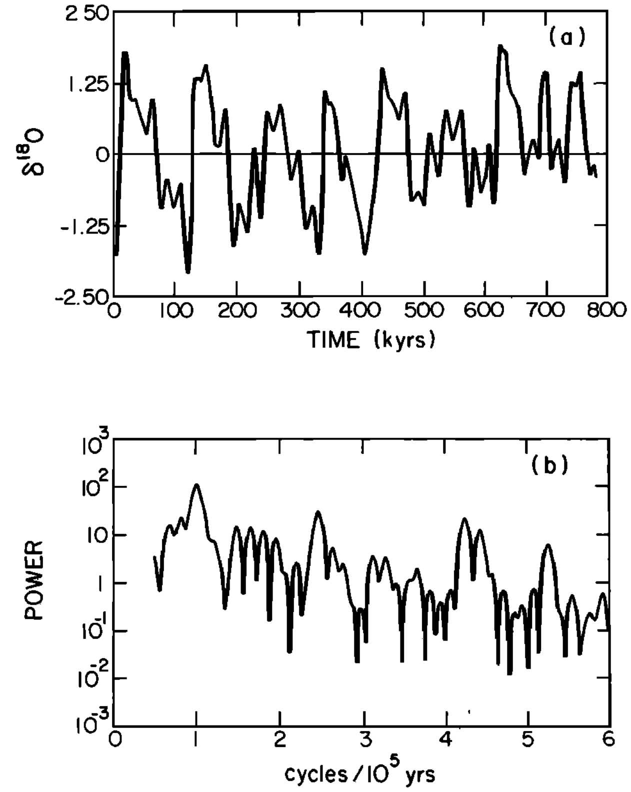

Figure 27. (a) The SPECMAP $\delta^{18}O$ record of *Imbrie et al.* [1984] and (b) its power spectrum.

shown for four sites in both Canada and Fennoscandia. Inspection of these comparisons will demonstrate that the differences in the rsl predictions are confined to the immediate post-LGM period during which no data are recorded on the landscape because it is still ice covered. Over the period in which data are available the rsl predictions obtained using the two different sets of assumptions concerning the LGM state are essentially identical. We may therefore conclude that the ICE-4G model of deglaciation, when coupled with the VM2 viscosity model, constitutes an entirely self-consistent (though not entirely unique) solution to the GIA problem.

4.3. Anomalies in Earth Rotation, Polar Motion, and Gravity Field

Because the present-day anomalies in Earth rotation, polar motion, and the gravitational field are absolute rather than relative measures of the response to the glaciation-deglaciation cycle, it is important for the calculation of each of them to take into account the prehistory of loading and unloading as discussed in section 4.2.4. A detailed review and discussion of the Earth rotation and polar motion observations have recently been provided by *Peltier and Jiang* [1996a]. Here I will begin by first reviewing and then extending these results in an important way. In order to solve equations (13) we require time series for the I_{13}, I_{23}, and I_{33} elements of the inertia tensor perturbation that would be obtained from the surface loading and unloading cycle if the Earth were perfectly rigid. Since these inertia perturbations depend not only upon the ice but also upon the ocean components of the surface mass load variation, the solution of (13) first requires that we solve (3) to obtain the gravitationally self-consistent history of ocean mass loading. Given this, we may then evaluate I^R_{13}, I^R_{23}, and I^R_{33}, and Figure 29 shows results for two different representations of the loading history, one based upon SPECMAP (solid lines) and discussed in section 4.2.4, and another consisting of a simple sawtooth-shaped time series with a period of precisely 100 kyr (dashed lines). Figure 30 shows present-day predictions of both the nontidal acceleration of rotation and the polar wander speed for a sequence of simple two-layer models of the radial variation of viscosity in which the upper mantle and transition zone value ν_{UM} is held fixed to the nominal *Haskell* [1935] value of 10^{21} Pa s and the lower mantle value ν_{LM} is varied (lithospheric thickness is held fixed to 120.6 km). Results are shown for both the I^R_{ij} models of Figure 29 which do not include the influence of gravitationally self-consistent ocean loading and for the SPECMAP-based model in which this influence is fully incorporated, the latter result corresponding to the curve marked by crosses. Inspection of these two predictions demonstrates that they depend upon the upper mantle–lower mantle viscosity contrast in a radically different way. Whereas the nontidal acceleration may be fit by two widely seperated values of lower mantle viscosity, one near 2×10^{21} Pa s and another near 10^{23} Pa s, the polar wander speed observation (both observations are denoted by the shaded regions on Figure 30) may apparently be fit by only one value (or a relatively narrow range of values) of this parameter. The fact that both Earth rotation related observables are fit by precisely the same simple two-layer model is very convincing evidence, in my view, that both of these Earth rotation anomalies are indeed primarily associated with the GIA process. Given that these effects are caused by entirely independent inertia perturbations, it would otherwise be entirely improbable that they could be simultaneously reconciled in this way. This is not to say, however, that other processes might not contribute somewhat to them, as we will now specifically discuss. Before doing so, however, it will be important to note that the two-layer model of the radial viscosity variation which fits both rotational observables is precisely the VM1 model that has been previously employed as starting model in the formal Bayesian inversions for viscosity. Since the Earth rotation observations essentially constrain the average value of mantle viscosity and since VM1 fits these observations, it should be clear that the average viscosity of VM1 is close to that of the real Earth.

As I will discuss in greater detail in section 5.4, it is very clear that global sea level is currently rising at a rate near 2 mm yr^{-1} [see also *Peltier and Jiang*, 1997]. This global rise of sea level could be due to one or the other

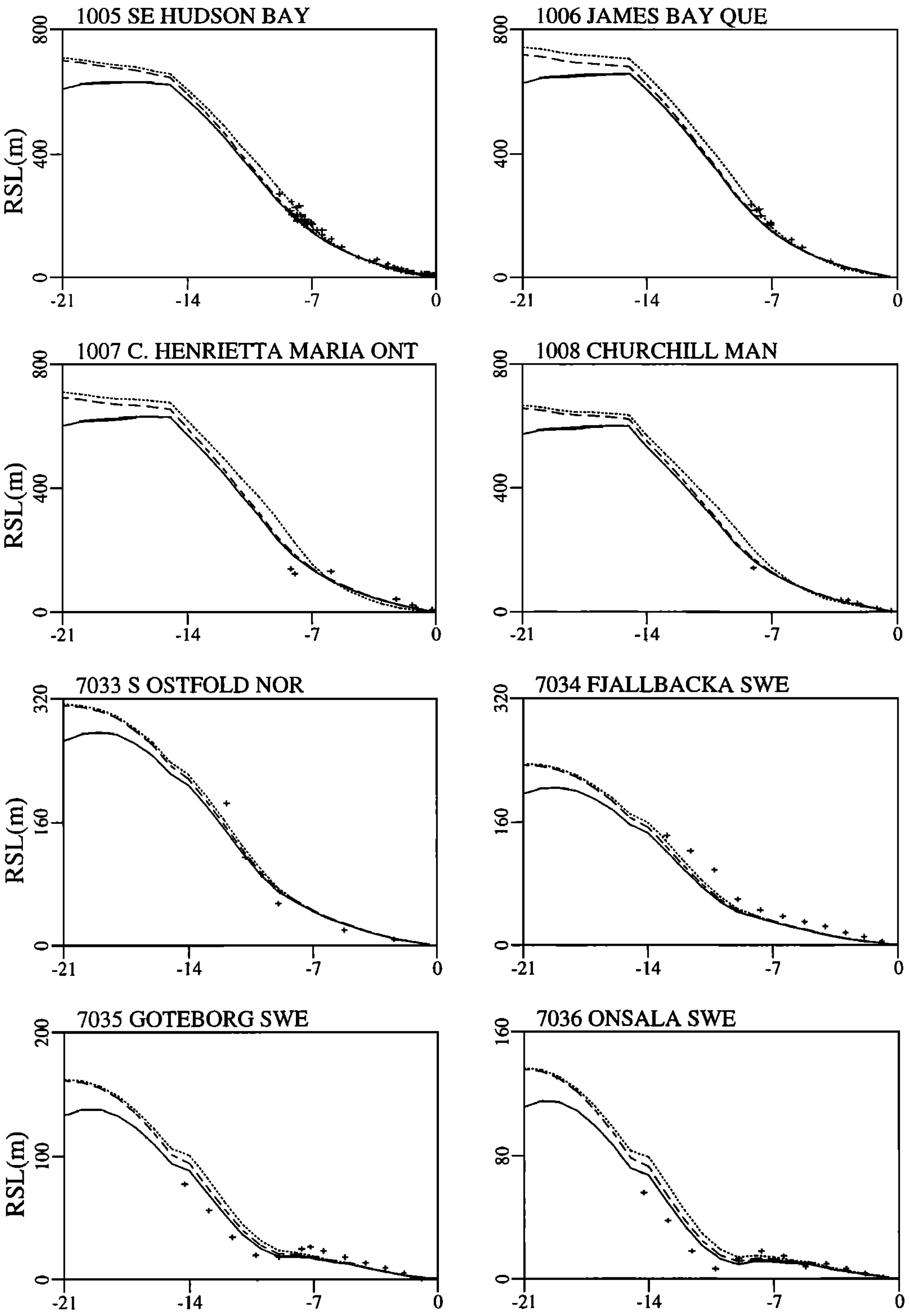

Figure 28. Comparisons between ICE-4G (VM2) predictions of rsl history at four sites in Canada and four sites in Fennoscandia. The dashed and solid curves are predictions based upon the assumption of time-independent ocean function, the former assuming initial isostatic equilibrium and the latter employing SPECMAP-controlled glacial prehistory. The dotted curve incorporates the influence of time-dependent ocean function on the calculation that assumes initial isostatic equilibrium. Data from the individual sites are denoted by crosses.

of two primary causes, either to the steric effect of thermal expansion of the oceans in response to global warming of the overlying atmosphere or to the addition of water to the ocean basins due to the melting of the great continental scale ice sheets that now cover Greenland and Antarctica and/or to the melting of small ice sheets and glaciers documented by *Meier* [1984]. If it is caused by the melting of land ice, then the impact on

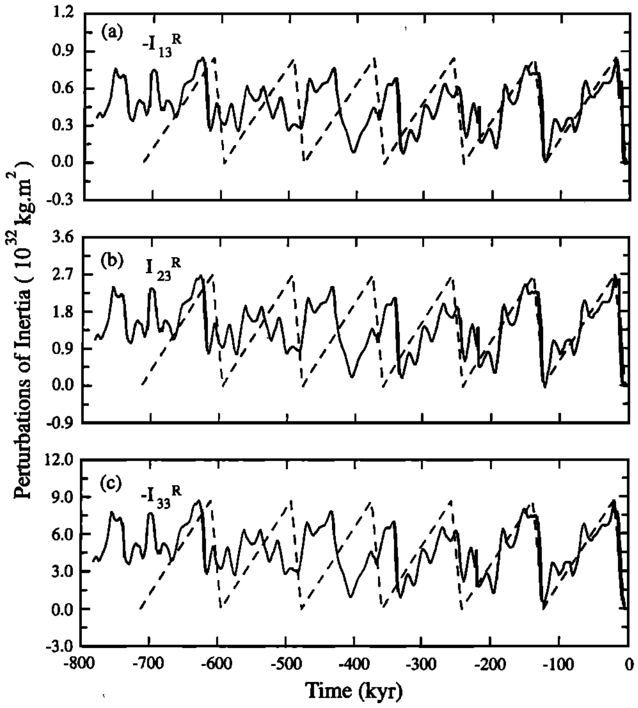

Figure 29. Time series for the perturbations of inertia (a) I^R_{13}, (b) I^R_{23}, and (c) I^R_{33} for two different models of the history of glaciation and deglaciation, one based upon the SPECMAP $\delta^{18}O$ record shown in Figure 27 (solid curve) and the other simply assumed to consist of a 100-kyr periodic sawtooth (dashed curve). For both models the deglaciation history from LGM to present is assumed to be identical to the ICE-4G model.

each rotational observable could be significant, whereas if it is caused by the steric effect of thermal expansion, then the impact on rotation would be insignificant. *Peltier* [1988] provided a first assessment of the impact of land ice melting on both the nontidal acceleration and polar wander which focused upon the small ice sheets and glaciers component of *Meier* [1984], and this analysis was subsequently refined with respect to the nontidal acceleration by *Mitrovica and Peltier* [1993b]. Focusing first upon the nontidal acceleration, the results of these papers may be converted into a good estimate of the magnitude of the impact of a particular rate of polar ice sheet melting into a good estimate of the impact on present-day $\dot{J}_2$. This is such that a 1 mm yr^{-1} rate of melting of either Greenland or Antarctica produces a $\dot{J}_2$ response that is slightly greater than $+0.4 \times 10^{-10}$ yr^{-1}. Since the system is linear,

$$\dot{J}_2(\text{total}) = \dot{J}_2(\text{GIA}) + \dot{J}_2(\text{CLIMATE}) \qquad (23a)$$

and thus

$$\dot{J}_2(\text{GIA}) = \dot{J}_2(\text{total}) - \dot{J}_2(\text{CLIMATE}). \qquad (23b)$$

Since $\dot{J}_2$ (CLIMATE) is positive, as must be the case on physical grounds, and since $\dot{J}_2$ (total) is negative, it therefore follows that the $\dot{J}_2$ signal that must be explained as a consequence of GIA could be more negative than the total observed signal. Inspection of Figure 30 will therefore demonstrate that the viscosity contrast in the two-layer model would then have to be increased to accommodate the "contamination" of the observed GIA signal by the climate effect.

Since it is clearly far more interesting to investigate the impact on viscosity structure in the context of formal inversion than in the context of the fitting of overly simple two-layer models to the observations, Figure 31 shows a series of viscosity models derived from variants on the VM2 inversion that successively incorporate the impact of ever larger excitation associated with the present-day melting of land ice, corresponding to global rates of sea level rise from 0.5 to 1.5 mm yr^{-1}, the upper bound being determined by invoking the usual assumption (which may be erroneous) that thermal expansion accounts for ~0.5 mm yr^{-1} of the observed (~2 mm yr^{-1}) rate of global sea level rise [*Intergovernmental Panel on Climate Change* (*IPCC*), 1996]. Inspection shows that the larger the contamination assumed to be due to land ice melting, the larger the viscosity is inferred to be in the lower half of the lower mantle. The reason why the viscosity adjustment occurs in the deepest mantle alone will be clear on the basis of the Fréchet kernels for the various data types employed in the Bayesian inversion (see Figure 19). The viscosity of the mantle is strongly constrained to remain near the VM2 value in both the upper part of the lower mantle (by the rsl-based relaxation times from Canada) and in the upper mantle and transition zone (by the *McConnell* [1968] relaxation spectrum as well as the Fennoscandian rsl time series). All of the adjustment to the viscosity model must therefore occur in the lowermost mantle. The final model that incorporates the influence of the largest contamination of the $\dot{J}_2$ observation is the model labeled VM3 for which a relaxation diagram was previously presented on Figure 15. Whether or not a model of this kind will also allow the accommodation of the polar wander speed and direction observations will be discussed in section 5.4, where this observation will be employed to address the question as to where the melting of land ice is most likely to be occurring, if it is occurring at all.

A final piece of information concerning the nature of the GIA predictions that follow on the basis of the ICE-4G (VM2) class of models concerns the free air gravity anomaly that one would expect to observe over the main centers of postglacial rebound due to the degree of isostatic disequilibrium that must currently exist in these regions. For the purpose of these analyses we once more employ the SPECMAP extension of the ICE-4G deglaciation model, and Plates 6a and 6b show the observed anomaly and that which is predicted to exist over Hudson Bay for the VM2 model of the viscosity structure. These results are shown for reconstructions in which the spherical harmonic expansion of the free air gravity anomaly is truncated to degree and order

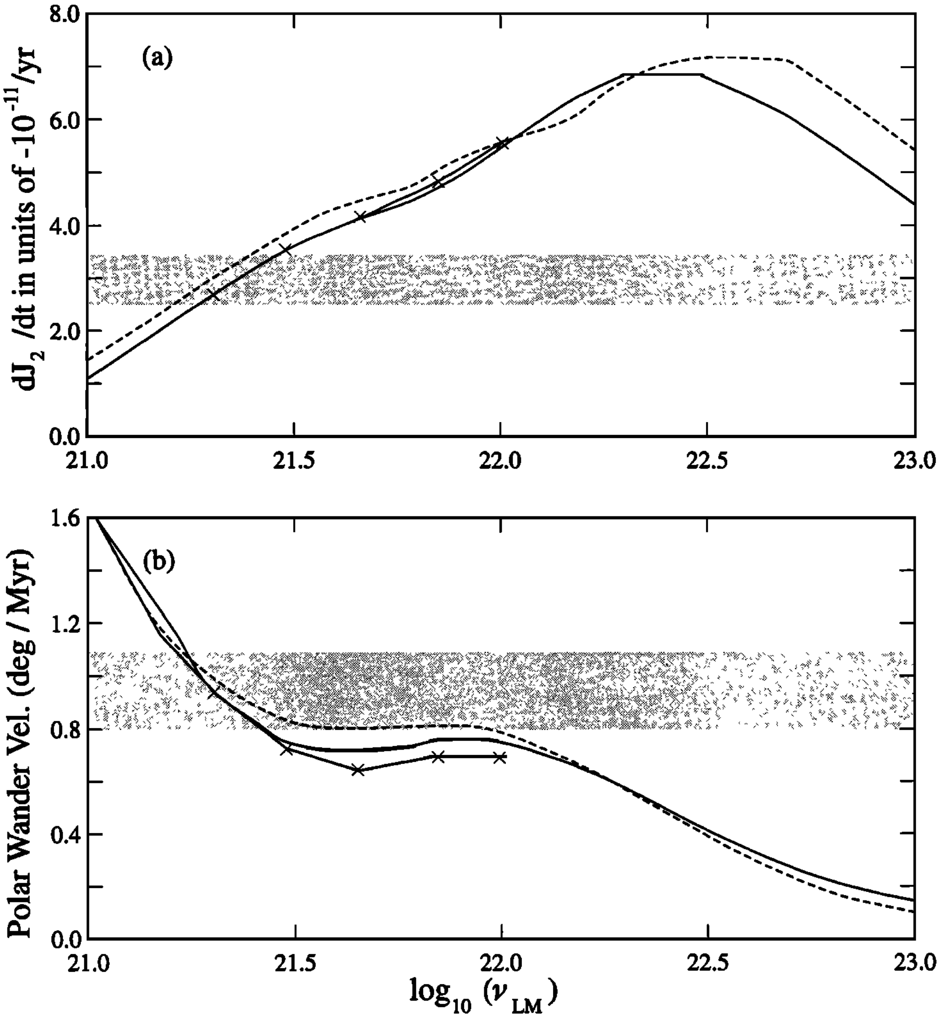

Figure 30 (a) $\dot{J}_2$ as a function of lower mantle viscosity ν_{LM} when the upper mantle and transition zone viscosity is fixed to the value $\nu_{UM} = 1.0 \times 10^{21}$ Pa s and the lithospheric thickness is $L = 120.6$ km. Results are shown for both of the models of glaciation history for which inertia perturbations are shown in Figure 28. (b) Polar wander speed as a function of lower mantle viscosity ν_{LM} with other parameters as in Figure 30a. The third curve represents the result obtained when the full influence of space- and time-dependent ocean loading is incorporated as by *Peltier and Jiang* [1996a].

8, and these results, computed on the basis of the spectral evaluation of the convolution integral derived by *Peltier* [1976], replace the results shown by *Peltier* [1996a] and *Pari and Peltier* [1996], who showed the field at a truncation level corresponding to spherical harmonic degree and order 16. The peak anomaly predicted to exist over Hudson Bay in this degree range is in any event extremely small for the VM2 viscosity model, being only of order 4 mGal.

Also shown on Plate 6c is the free air gravity anomaly predicted by a model of mantle convection in which the internal density heterogeneity that drives the circulation is assumed to be determined on the basis of seismic tomographic imaging (see *Pari and Peltier* [1996] for detailed discussion). In the calculation of the convection contribution to the free air anomaly, the tomographic model SFIK of *Forte et al.* [1993b] has been employed along with a conversion factor from seismic shear wave velocity anomaly to density which is close to the requirements of laboratory data [*Duffy and Ahrens*, 1992]. The anomaly shown in Plate 6c clearly provides a good fit to the peak free air anomaly over Hudson Bay determined on the basis of satellite observations (in this respect, we are again employing the GEM-T2 model of *Marsh et al.* [1990]). Clearly, the GIA-related anomaly shown on Plate 6b, for which the peak value is near 4 mGal, is extremely small compared to the 28-mGal peak anomaly that is observed. This is in accord with the conclusion of *Cathles* [1975] but discordant with the conclusion of *Walcott* [1980], who believed that the large free air gravity anomaly observed over Hudson Bay was due to incomplete glacial isostatic adjustment. Plate 6d shows the superposition of the rebound and convection model predictions, inspection of which demonstrates that the model in which the anomaly is dominated by the convection contribution explains not only the peak negative

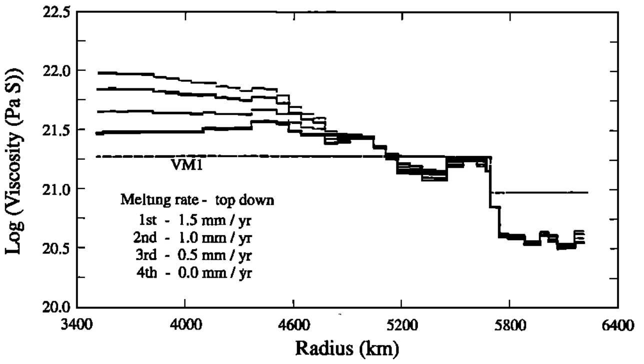

Figure 31. Radial viscosity profiles determined by formal Bayesian inversion of the same data set employed to derive the profiles shown previously on Figure 21. In these analyses, however, the observed value of J_2 has been adjusted by removal of an assumed contamination associated with the melting of land ice from either Greenland or Antarctica. The impact on the inferred viscosity profile is shown for several assumed values of the global rate of eustatic sea level rise due to such polar ice sheet melting.

anomaly over Hudson Bay but also the flanking anomalies observed over the entire surrounding region.

4.4. Three-Dimensional Crustal Motion and Space Geodesy

As mentioned in section 1, the "final frontier" in the observational study of the GIA process would appear to lie in the use of space geodetic techniques such as VLBI, GPS, and satellite laser ranging (SLR) to directly monitor the phenomenon, just as VLBI is now employed to directly monitor the horizontal motions of Earth's tectonic plates. In section 2.2 I discussed the recently reported results of *Argus* [1996] (Figure 9), who compared the northern hemisphere vertical motion predictions made with the ICE-4G (VM1) model [*Peltier*, 1995b] with the VLBI observations of *Ma and Ryan* [1995] of the Goddard Space Flight Center. On the basis of these radio telescope based observations it is very clear that the VLBI system is actually observing the extremely small signal associated with the GIA phenomenon.

Equally exciting is the fact that both the VLBI and GPS systems are now beginning to directly observe the horizontal motions associated with GIA, since these are generally weaker than the vertical signal by approximately one order of magnitude. The mathematical forms for the prediction of radial (U) and tangential ($\mathbf{V}$) displacement are simply as follows [e.g., *Peltier*, 1995b]:

$$U(\theta, \lambda, t) = \sum_{\ell=0}^{\infty} \sum_{m=-\ell}^{+\ell} \left[\frac{4\pi a^3}{(2\ell + 1)m_e} \left(L_{\ell m} h_\ell^E + \sum_{k=1}^{k(\ell)} q_k^\ell \beta_{\ell m}^k \right) \right] Y_{\ell m} \tag{24a}$$

$$\mathbf{V}(\theta, \lambda, t) = \sum_{\ell=0}^{\infty} \sum_{m=-\ell}^{+\ell} \left[\frac{4\pi a^3}{(2\ell + 1)m_e} \left(L_{\ell m} h_\ell^E + \sum_{k=1}^{k(\ell)} t_k^\ell \beta_{\ell m}^k \right) \right] \underline{\nabla} Y_{\ell m} \tag{24b}$$

in which m_e is the mass of the Earth, a is the Earth's radius, $L_{\ell m}(t)$ are the time-dependent spherical harmonic components of the surface mass load, and $\beta_{\ell m}^k$ are functions introduced by *Wu and Peltier* [1982] to allow one to accurately account for an arbitrary history of surface mass loading. They are explicitly

$$\beta_{\ell m}^k(t) = \int_{-\infty}^{t} L_{\ell m}(t') e^{-s_k^\ell (t-t')} \, dt'. \tag{25}$$

Equations (24) derive from the evaluation of the convolution integrals of the surface mass load with appropriate Green functions for the signal of interest using the spectral method discussed by *Peltier* [1976]. The form $\underline{\nabla} Y_{\ell m}$ involving the tangential gradient of the spherical harmonics $Y_{\ell m}$ is nontrivial, but an analytic form for it is provided by *Forte and Peltier* [1994] and will be used here as it was by *Peltier* [1995b].

Figure 32 shows superimposed fields of present-day radial displacement rate $\dot{U}$ and present-day tangential displacement rate $\dot{\mathbf{V}}$, with the former shown as a contour-mapped scalar field and the latter represented by a field of arrows whose length represents the magnitude of the tangential displacement rate and whose direction is indicated by the direction of the arrows. Scales for both fields are shown on Figure 32, and results are provided for both Laurentia and Fennoscandia and for both the VM1 and VM2 viscosity models. The first feature to note with respect to the horizontal motion is that it is directed outward away from the centers of deglaciation [see also *James and Morgan*, 1990; *James and Lambert*, 1993; *Mitrovica et al.*, 1994]. The second feature to note is that it is clear by inspection of these theoretical predictions that although the horizontal motion is not strongly affected in Fennoscandia by the use of the VM2 viscosity model in place of VM1 (when the Fennoscandian ice sheet load is modified to preserve the fit to the observed magnitude of the relative sea level signal as discussed by *Peltier* [1996a]), the same is clearly not the case in North America. In the latter region the magnitude of the horizontal motion is increased dramatically when VM1 is replaced by VM2, sufficiently so that one might reasonably hope to further distinguish between the quality of these models by this means [*Peltier*, 1998a].

As discussed in section 4.2, the VM2 model dramatically improves the fit of the global theory of the GIA process to U.S. east coast rsl observations. As we have seen here, however, it also results in a dramatic increase of the predicted rates of horizontal motion, so much so, that this difference in signal strength should be easily observable using space geodetic means. An initial anal-

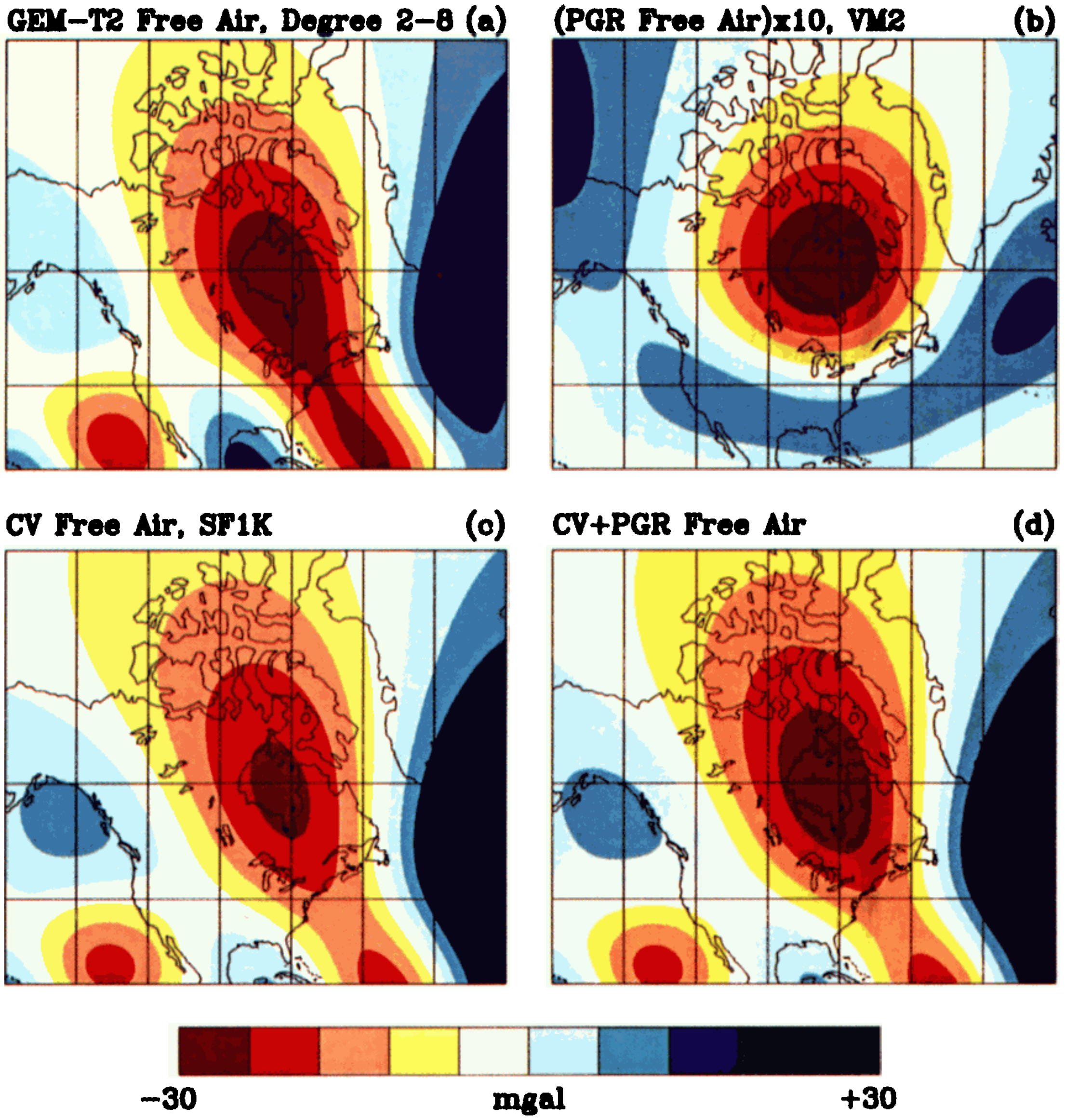

Plate 6. (a) Observed free air gravity anomaly over North America in the degree range $2 \leq \ell \leq 8$ according to the GEM-T2 model of *Marsh et al.* [1990]. (b) Predicted free air gravity anomaly over the Hudson Bay region in the degree range $2 \leq \ell \leq 8$ according to the ICE-4G (VM2) model. (c) Predicted free air gravity anomaly over North America, in the degree range $2 \leq \ell \leq 8$, based on the seismic tomography constrained model of mantle convection of *Pari and Peltier* [1996]. (d) Free air gravity anomaly produced by the superposition of the GIA anomaly in Plate 6b and the convection anomaly in Plate 6c. Clearly, the observed anomaly is strongly dominated by that due to the mantle convection process.

ysis of this issue by D. Argus et al. (Observations of glacial isostatic adjustment with space geodesy: New constraints on mantle viscosity and glaciation history, submitted to *Journal of Geophysical Research*, 1998) suggests that although the VM2 model is indeed the preferred model from the perspective of the vertical motion data, the horizontal motion observations similarly prefer VM1. If this preliminary conclusion should prove to be further reinforced by ongoing work, then the resolution of this somewhat contradictory result should, in fact, prove to be relatively straightforward. It has been clearly demonstrated elsewhere [*Peltier* 1984, 1986] that the vertical motion signal along the U.S. east coast is also strongly sensitive to lithospheric thickness. By somewhat thickening the lithosphere from the 120.6 km value employed in both VM1 and VM2 or by a suitable further alteration of the sublithospheric viscosity profile, it should prove possible to sufficiently diminish the horizontal motions predicted by VM2 while preserving the quality of the fit to the vertical motion observations. Further analyses of this kind will be reported elsewhere.

4.5. Glacial Isostasy and Mantle Convection: Is Mantle Rheology Newtonian?

Given the apparent success of the VM2 model in reconciling an extremely wide range of different obser-

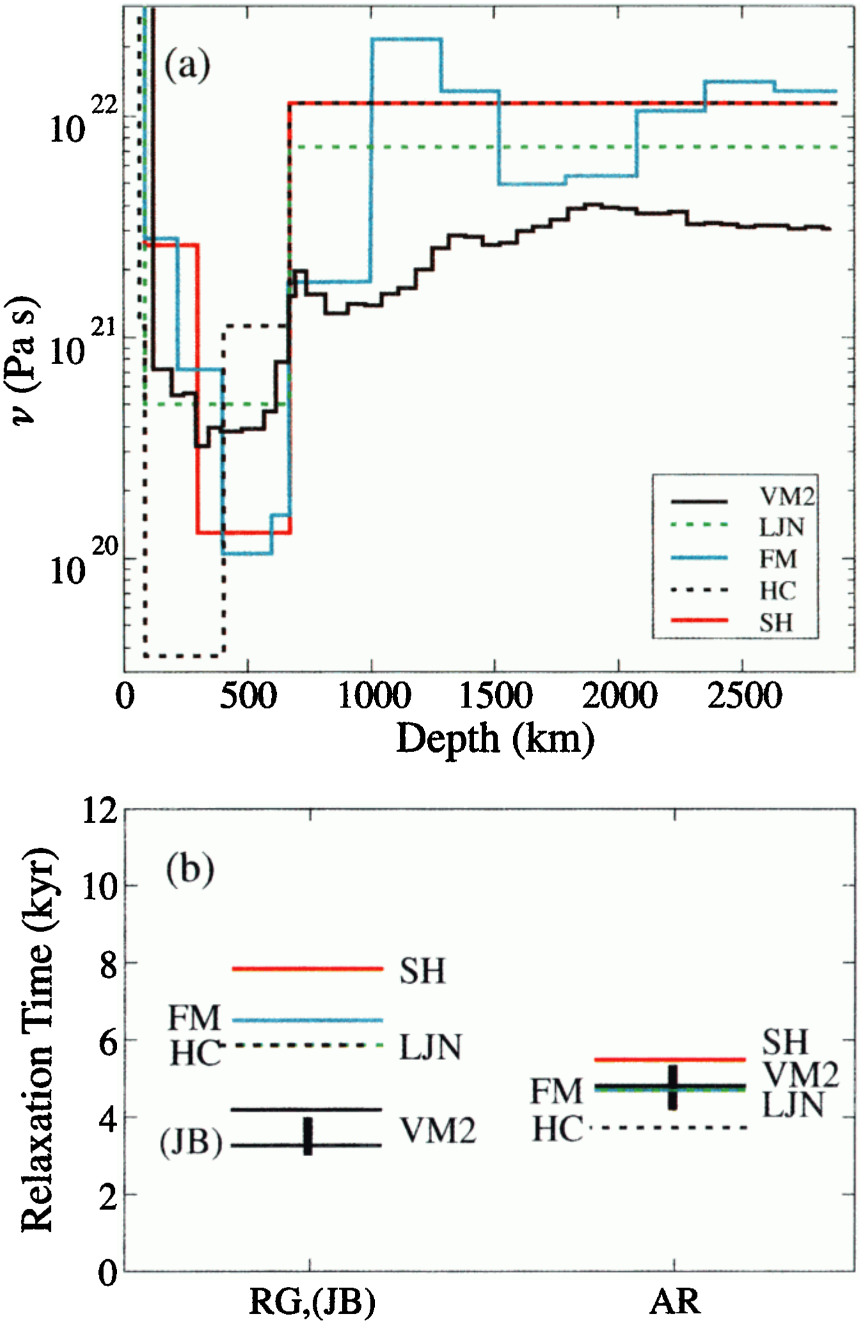

Plate 7. (a) Five profiles of mantle viscosity including the VM2 model and those of *Lambeck et al.* [1990] labeled LJN, *Forte and Mitrovica* [1996] labeled FM, *Hager and Clayton* [1989] labeled HC, and *Simons and Hager* [1997] labeled SH. (b) Predictions of relaxation time for postglacial rebound of the crust based upon each of these models for both the southeast Hudson Bay (Richmond Gulf labeled RG and James Bay labeled JB) and Angerman River (AR) locations. Note that only the VM2 viscosity model fits the timescale that characterizes the postglacial rebound process in Hudson Bay. The other models are therefore entirely ruled out on this basis.

vations related to the GIA process, it would appear warranted to consider the question of the relationship of this radial viscosity structure (or suite of structures) to inferences concerning this parameter that have been derived through other means. Of utmost importance in this connection are inferences that have been based upon the use of convection models constrained by seismic tomography to predict the global pattern of nonhydrostatic geoid anomalies that is now so accurately observed on the basis of satellite tracking data. Over the course of the past decade, beginning with the work by *Hager* [1984], there have been a large number of such analyses performed, analyses which have differed from one another in both major and minor ways. Figure 33 presents a series of five models of the radial viscosity variation that have been inferred in this way, the models

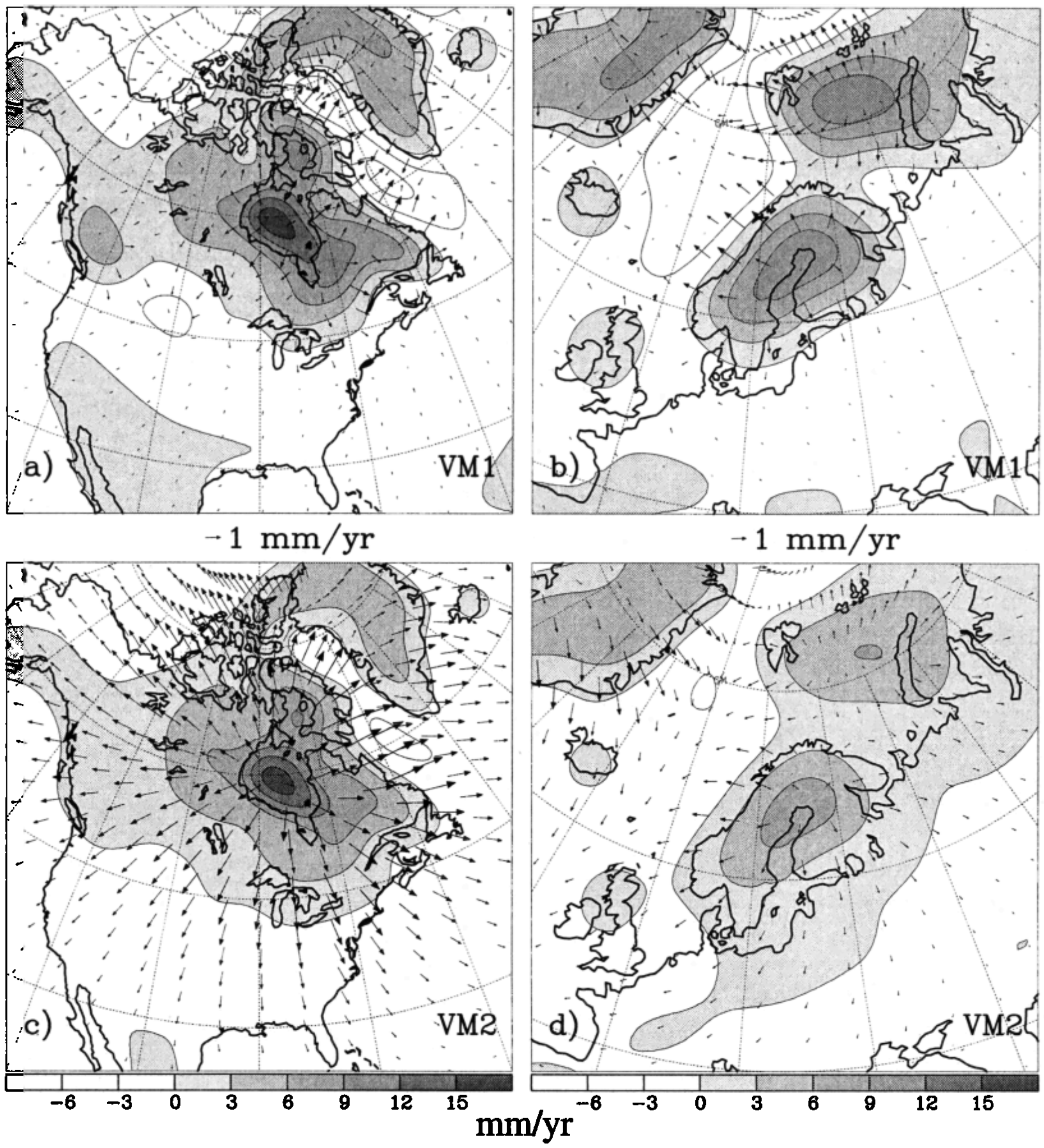

Figure 32. Superimposed fields of the present-day rate of radial displacement rate $\dot{U}$ (shown as a contour mapped scalar field) and horizontal displacement rate $\dot{\mathbf{V}}$ (shown as a field of arrows whose length represents the magnitude of the tangential displacement rate and whose direction is indicated by the direction of the arrows) over both Laurentia and Fennoscandia for the ICE-4G (VM1) and ICE-4G (VM2) models. Note the large increase in the predicted rates of horizontal motion associated with the VM2 viscosity structure.

being presented in normalized form as the ratio $\nu(r)/\nu_0$, where the reference viscosity ν_0 has been selected so as to make the models identical over some range of upper mantle depths. Since the nonhydrostatic geoid data are incapable, in themselves, of determining an absolute value for the viscosity [e.g., see *Forte and Peltier*, 1987; *Forte et al.*, 1991], the theoretical prediction being sensitive only to its relative variation, this normalized representation of the individual models would appear to be required to avoid ambiguity. Of course, in each of the original papers in which these various models were developed, the authors usually invoked some method of converting the geoid-derived relative profile into an absolute profile (e.g., see *Forte et al.* [1991] for a discussion of the way in which observed plate velocities can be used to accomplish this, and see *Pari and Peltier* [1995] for a discussion of the use of surface heat flow observations for the same purpose). Since all of these methods of "dimensionalization" are fraught with considerable error, however, it would appear most sensible to simply allow that the geoid data themselves only determine the relative variations of viscosity.

Inspection of the family of geoid-derived viscosity profiles shown on Figure 33 will demonstrate that they span an extremely wide range of profile types. The most dramatic differences, in fact, exist between the models inferred by *Hager and Richards* [1989] and *Ricard and Vigny* [1989] on the one hand and those inferred by *Forte*

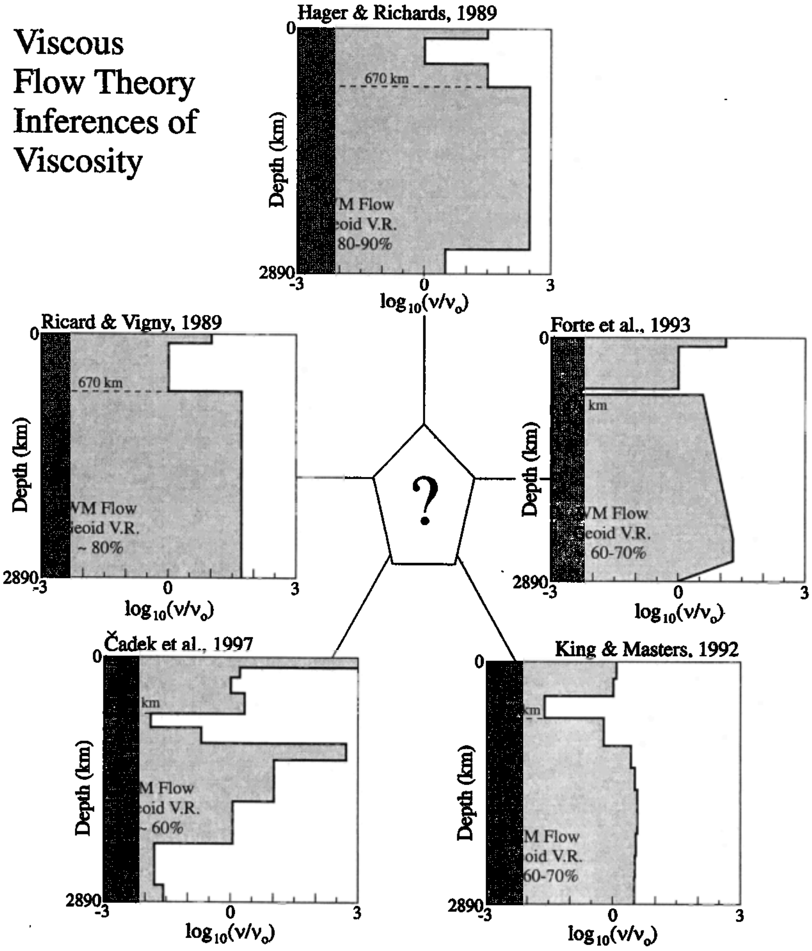

Figure 33. Five models of the relative variation of viscosity as a function of radius in the mantle based upon inversions of nonhydrostatic geoid data. WM, whole mantle; LM, layered mantle.

et al. [1993a, b] and *King and Masters* [1992] on the other. The most wildly variable as a function of depth is the very recent model of *Cadek et al.* [1997]. Insofar as the first two profiles are concerned, they have been based upon the use of seismic tomographic models to define the internal density field, to which additional density heterogeneity has been added to explicitly represent the regions of anomalously high density associated with downgoing slabs, the authors of these papers being of the opinion that this heterogeneity is not adequately represented in the available low-resolution (but one might say high accuracy) global tomography models. The second two models, on the other hand, were inferred by their authors on the basis of Harvard University and Scripps Institution of Oceanography, respectively, global tomography models. The main difference between these two sets of two models concerns the magnitude of the viscosity variation that is inferred to exist across the seismic discontinuity at 660 km depth. In the first two models this variation is extremely large, being typically a factor of order 50. In the latter two models, however, this variation is much less extreme, although both of these models have localized soft layers that lie immediately above the 660-km discontinuity. In the model of *Forte et al.* [1993a, b], the quality of which was confirmed by the further analysis by *Pari and Peltier* [1995], this soft layer is extremely thin, being only 70 km in radial extent and therefore plausibly associated with the dynamical influence of the spinel to postspinel phase transition. *Pari and Peltier* [1995] have demonstrated that in the context of the Harvard model SH8WM13, the greatest variance reduction on the nonhydrostatic geoid data is achieved when this layer is indeed thin and the viscosity contrast through it is large. That such a soft layer might exist was explicitly suggested by *Peltier* [1985b]. The soft layer has the effect of causing the geoid kernel to peak sharply in the transition region wherein the lateral density heterogeneity correlates most strongly with the satellite-observed geoid. A most interesting question concerns the relationship of models of this kind to those in the VM2 class that have been derived on the basis of the analysis of glacial isostatic adjustment observations.

Also of interest, is the connection between VM2 and the sequence of models recently discussed by *Simons and Hager* [1997] in the context of their attempt to infer constraints on viscosity based upon the analysis of local properties of the gravity field in relation to the LGM distribution of the surface ice load, which they took to be represented by the ICE-3G model of *Tushingham and Peltier* [1991]. This sequence of viscosity models is shown in Plate 7 with VM2 superimposed. The models include that favored by *Simons and Hager* [1997] on the basis of

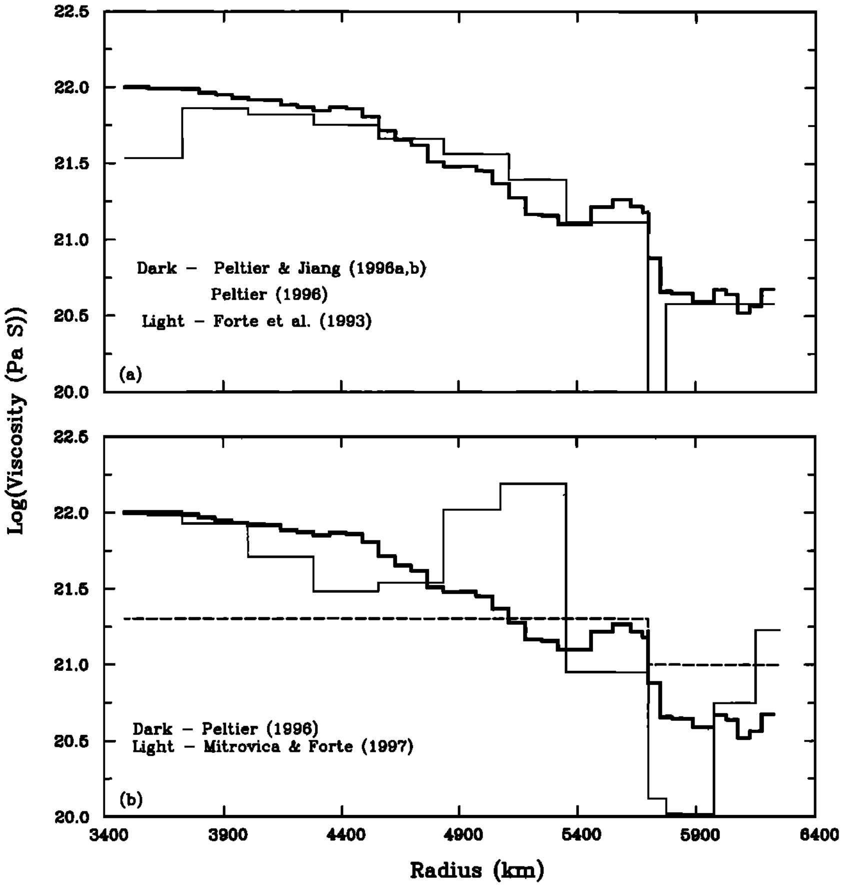

Figure 34. (a) Overlay of the mantle viscosity profile VM3 deduced on the basis of inversions of the GIA data by *Peltier and Jiang* [1996a, b] and *Peltier* [1996a] and the profile inferred by *Forte et al.* [1993a, b] based upon the inversion of nonhydrostatic geoid data. (b) Overlay of the viscosity profile VM3 and the profile inferred by *Mitrovica and Forte* [1997] on the basis of simultaneous inversion of nonhydrostatic geoid and postglacial rebound data. Also, the VM1 viscosity model (dashed curve) is shown for reference.

the analyses that they report, that of *Lambeck et al.* [1990], and one inferred by *Forte and Mitrovica* [1996] on the basis of a joint inversion of GIA and nonhydrostatic geoid data as well as a model due to *Hager and Clayton* [1989] based upon nonhydrostatic geoid analyses alone. Plate 7b shows the predictions that these models make (according to Simons and Hager) of the exponential relaxation times that should characterize the postglacial rebound (PGR) process in southeast Hudson Bay in Canada and at Angerman River in Sweden, the two sites for which detailed analyses of the data were shown in Figure 3. Clearly evident on the basis of these comparisons is that all of these models, excepting VM2, are entirely ruled out by the observed relaxation time that characterizes the postglacial rebound process in southeast Hudson Bay. Mistakenly accepting an estimate of the southeast Hudson Bay relaxation time based upon information compiled originally by *Hillaire-Marcel* [1980] that included very few (uncalibrated) carbon dates and which was analyzed by *Mitrovica and Peltier* [1995], Simons and Hager believed the southeast Hudson Bay relaxation time to be near 7.6 kyr. This is, in fact, more than a factor of 2 larger than the estimate of this timescale of 3.4 kyr based upon the extensive set of data listed in Table 1. *Mitrovica* [1996] initially championed the view that the 7.6 kyr estimate of the SE Hudson Bay relaxation time was accurate, and it was upon the validity of his (mistaken) interpretation that *Simons and Hager* [1997] depended.

Figure 34a shows an overlay of model VM3 on the model of *Forte et al.* [1993a, b] and *Pari and Peltier* [1995] as the latter was recently presented by *Mitrovica and Forte* [1997]. Inspection will show that model VM3, obtained when the $\dot{J}_2$ observation is adjusted to account for a rate of melting of polar ice of 1.5 mm yr^{-1}, overlaps the geoid-derived model everywhere except in the thin soft layer that sits atop the 660-km discontinuity in the geoid-derived model. When no correction is made for such contamination of the $\dot{J}_2$ observation, then the viscosity in the lowermost mantle in VM2 is a factor of ~2 lower than that in the geoid-derived model. Since it is not at all clear that polar ice is indeed melting at a sufficient rate to cause global sea level to rise at a rate near 1.5 mm yr^{-1}, it is useful to ask whether the impact of the thin low-viscosity channel that lies above the 660-km discontinuity in the geoid-derived model may be accommodated by the data related to the glacial isostatic adjustment process.

That the impact of a feature of this kind on the radial profile of viscosity is not at all inconsequential insofar as the GIA-related data are concerned will be clear on the basis of Figure 35a. On Figure 35 I have superimposed upon the observed relaxation spectrum for Fennoscandian rebound, not only the prediction for a model in the

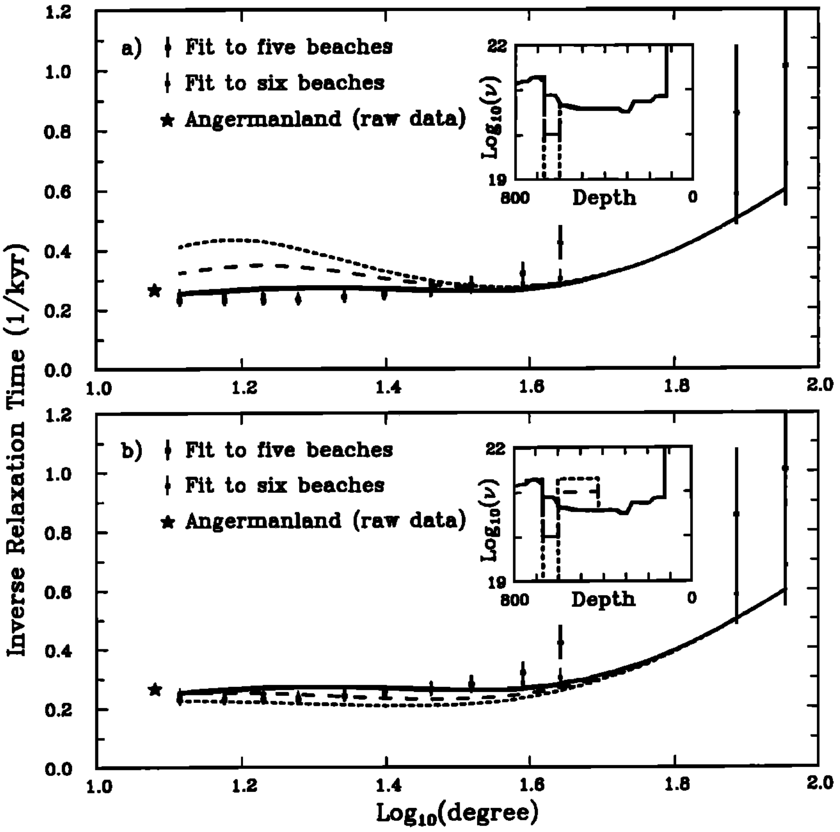

Figure 35. (a) The inverse relaxation time spectrum for Fennoscandian rebound of *McConnell* [1968] compared to the prediction of a model in the VM2 class and compared to the predictions for two additional models that differ from VM2 by the presence of a 70-km-thick layer immediately overlaying the 660-km discontinuity in which the viscosity is reduced either by 1 or 2 orders of magnitude from the value near 0.45×10^{21} Pa s that otherwise obtains in this region of VM2. (b) Demonstration that the misfit to the McConnell spectrum induced by the presence of the soft layer may be removed by increasing the viscosity in the transition zone.

VM2 class, which is shown as the solid line, but also predictions based upon a model that is identical to VM2 everywhere except in a layer that is 70 km thick and which lies immediately above the 660-km discontinuity. In this layer the viscosity is assumed to be reduced by either a factor of 5 or a factor of 50, the resulting model predictions of the Fennoscandian rebound spectrum being depicted by the dashed and dotted curves on Figure 35a, respectively. Inspection of the spectra shown on Figure 35a for the two models that incorporate thin low-viscosity layers above 660 km depth will demonstrate that the incorporation of such a feature in the viscosity model destroys the fit to the *McConnell* [1968] spectrum. One way out of this conundrum, of course, is to assume that the McConnell spectrum is wrong, as recently suggested by *Wolf* [1996], although this is unlikely to be the case. A model like VM3 with a soft layer would then be entirely expected and would not require justification by appeal to a bias on the $\dot{J}_2$ observation due to the present-day melting of land ice.

Sensitivity tests on the solution of the forward problem, of the kind just described, are extremely useful as they raise the critical question of the uniqueness of the viscosity profiles in the VM2-VM3 classes that we have inferred through formal inversion of a wide range of glacial isostatic adjustment related observations. These models are, in a sense, the smoothest models that are both compatible with the data and linearly close to the starting model VM1. There is no guarantee that the actual viscosity profile is, in fact, smooth, and there is, in fact, reason to believe, especially if the convective circulation is significantly layered by the influence of the endothermic phase transformation at 660 km depth, that localized structure of the kind that seems to be required by the nonhydrostatic geoid data is, in fact, expected [*Peltier*, 1985b, 1996c]. If a sharp low-viscosity channel does exist on or above the 660-km discontinuity, then it is clear that one must compensate for its presence by further adjusting the VM2 model or ignoring the fact that the fit to the McConnell spectrum (and related data) is compromised. One way in which one might hope to effect such compensation would be to include a complimentary high-viscosity feature in a layer of the same 70-km thickness immediately below the 660-km discontinuity. That such a feature might also be expected on a priori grounds was in fact suggested by *Peltier* [1985b] and has been very fully discussed recently by *Pari and Peltier* [1995] in connection to its impact on nonhydrostatic geoid data and further by *Peltier* [1996c]. As shown by Pari and Peltier, the geoid data are, in fact, easily able to accommodate a complementary feature of this kind, thus leading to a dipolar variation of viscosity across the endothermic horizon. As it happens, however, the addition of a feature of this kind to the radial viscosity profile is rather ineffective in compensating for the influence of the thin low-viscosity zone on the McConnell spectrum. It appears simplest to effect this compensation, in fact, by increasing the viscosity in the transition zone itself, back toward the value that characterized this region in the VM1 model. That such compensation can be achieved by further such minor modifications to the model is demonstrated explicitly in Figure 35b.

Figure 34b illustrates another viscosity model derived on the basis of the assumption that the McConnell spectrum should be neglected, a model which is a variation on that of *Forte and Mitrovica* [1996] but softer in the upper part of the lower mantle so that the relaxation time that characterizes the PGR process in southeast Hudson Bay is not so seriously in error. This model, derived by *Mitrovica and Forte* [1997], is also capable of reconciling some fraction of both the PGR and convection-related constraints, although it might be seen as implausible on other grounds [see *Pari and Peltier*, 1998; *Peltier*, 1998a], most clearly on the basis of the extremely poor fits that it provides to relative sea level data from the U.S. east coast and to the Fennoscandian relaxation spectrum (if this is accepted as a valid constraint). The fact that the viscosity model of Mitrovica and Forte (MF) very poorly fits the observed relative sea level histories along the U.S. east coast, where such records are strongly dominated by the process of proglacial forebulge collapse, is very clearly evident on the basis of the results for this model shown on Figure 23 (dashed curves). At all sites along the northern part of the coast shown on Figure 20 this model, in fact, predicts the existence of raised beaches, which are not observed (at the northernmost sites), and significantly underpredicts the current rate of sea level rise at sites somewhat farther south. At the southernmost site along the coast for which a comparison is shown (Everglades, Florida), the error is again large but of opposite sign. Although the MF model does not significantly misfit the data in the ice-covered region of North America (not shown), where rsl observations are not especially sensitive to shallow viscosity structure, extremely large misfits are clearly evident in the peripheral region where such sensitivity is pronounced. The MF model is therefore ruled out both by the Fennoscandian relaxation spectrum [see *Peltier*, 1998a] and by these U.S. east coast records. The VM2 model, on the other hand, fits both data sets, having been designed to fit one (the Fennoscandian relaxation spectrum of *McConnell* [1968]) and thereafter shown to automatically fit the other. It is therefore clear that the degree of control exercised over the inversions that led to the MF model by the aspherical geoid data has led to a model that does not, in fact, reconcile the GIA data that were not employed to define it. That the geoid data might be expected to lead to instability of precisely this kind has been discussed recently by *Pari and Peltier* [1998].

The implications of the basic compatibility of the VM2 viscosity profile inferred on the basis of GIA observations and that inferred from the nonhydrostatic geoid anomalies supported by the mantle convection process, not withstanding these remaining issues of uniqueness, appear to be extremely important. When the first results were obtained on the basis of the inversion of nonhydrostatic geoid anomalies, it appeared that the profiles required by these two entirely distinct data sets were so completely discrepant as to require that mantle rheology be strongly transient and therefore nonlinear [*Peltier*, 1986]. On the contrary, it is now clear that the mantle viscosity profiles required to explain the two sets of data are very plausibly identical. To the degree that this is the case, it must follow that mantle rheology is entirely Newtonian, for if it were not, then the GIA and convection processes, whose characteristic timescales differ by 5 orders of magnitude, would have to be governed by distinctly different diffusion coefficients for momentum. It is, of course, important to note that other geophysical observations have recently been suggested to imply the same conclusion, especially the apparent absence of seismic velocity anisotropy at depths greater than ~200 km in the mantle [*Karato*, 1998]. A primary conclusion of this review is that this scenario must now be considered to be entirely plausible [see also *Pari and Peltier*, 1995; *Peltier*, 1996a, b, c]. It may be, however, that the best explanation for the existence of the low-viscosity "notch" above the 660 km discontinuity that convection timescale data appear to require is in terms of "strain softening" associated with the endothermic phase transition itself. This could involve locally non-Newtonian behavior such that the notch would be invisible to the glacial isostatic adjustment process. It remains to be seen whether ongoing analyses will require an interpretation of this kind. We cannot yet rule out the existence of an entirely Newtonian spherically symmetric model that satisfies both data sets.

5. IMPLICATIONS FOR CLIMATE SYSTEM DYNAMICS

Although observations of postglacial variations in the level of the sea do contain an obvious wealth of important solid-Earth geophysical information, especially concerning the creep resistance of the mantle as discussed in section 4, such data also contain important information concerning climate system history and dynamics. This is because the climate regime that obtains in any given epoch of Earth history is a strong function of both surface type and form. For example, the climate at the Last Glacial Maximum was controlled to a significant degree by ice-albedo feedback, the process whereby, because of the increased albedo of ice as compared to "normal" continental or oceanic surface, ice-covered regions reflect more of the incoming solar radiation to space, thereby reducing the energy absorbed by the surface and thus leading to cooling. During the ice age this process is known to have exerted considerable control on mean surface temperature [e.g., *Manabe and Broccoli*, 1985]. The magnitude of this impact will clearly depend not only upon the fractional surface area covered by ice but also upon the geographical region(s) within which the ice is located. As shown in section 4, regions of the surface of the continents that were ice

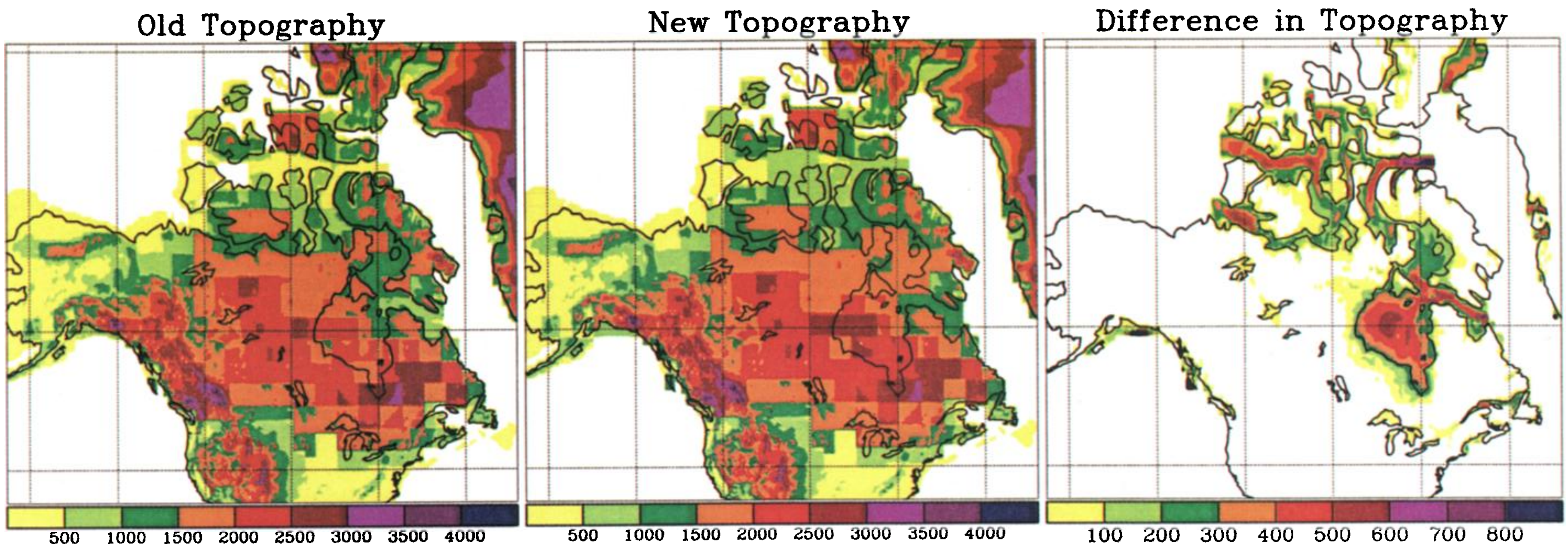

Plate 8a. ICE-4G-derived topography for the North American continent based upon the exclusion of "implicit ice" (old topography) and its inclusion (new topography) along with difference showing the contribution from implicit ice alone.

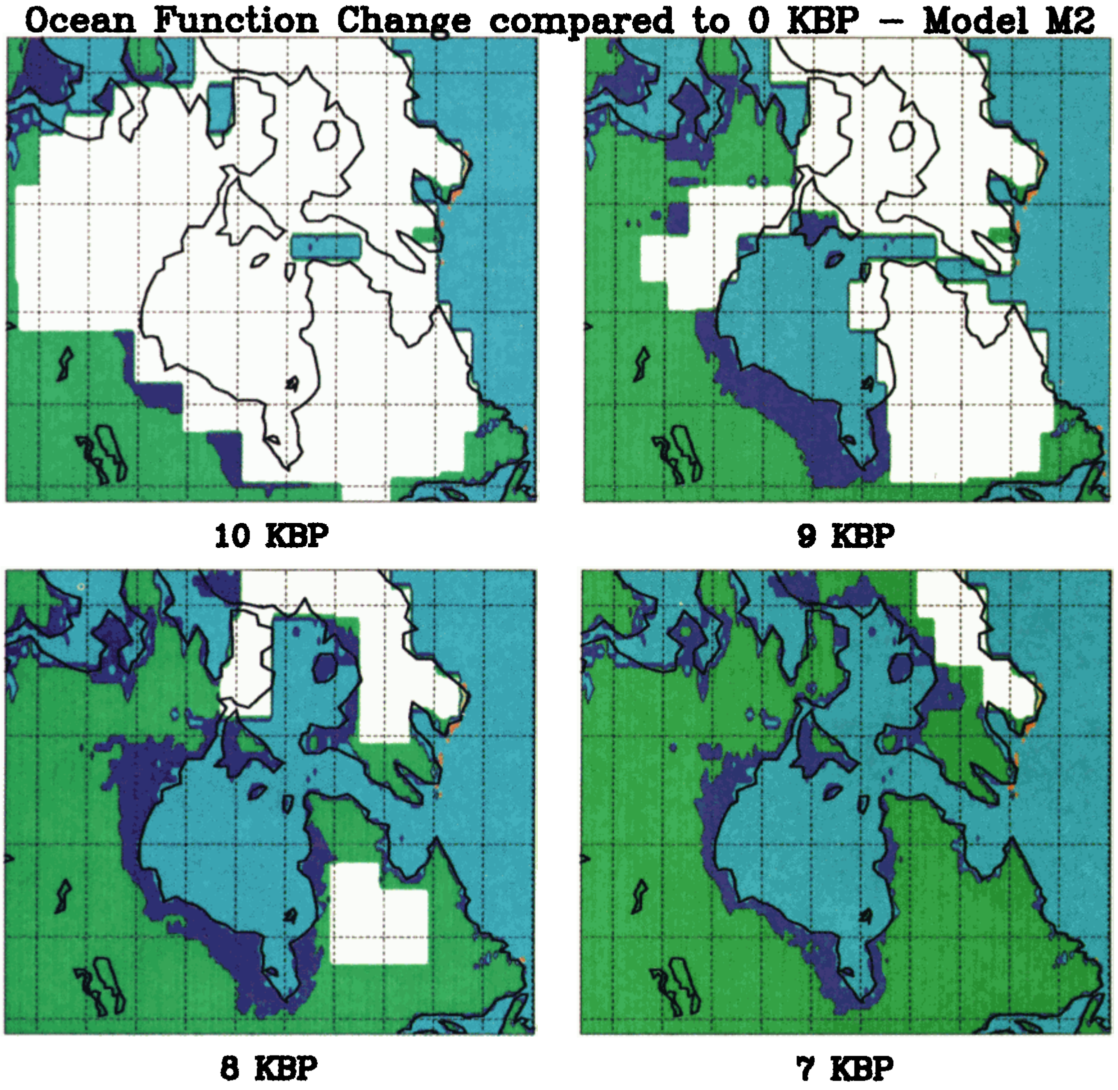

10 KBP 9 KBP

8 KBP 7 KBP

Plate 8b. Variation with time of the ocean function over the critical period of time during which Hudson Bay makes the transition from being ice covered to being ocean connected.

covered are distinguished as being regions of the surface currently experiencing postglacial rebound of the crust. When these ice sheets melt, the meltwater produced is expected to significantly impact the deep thermohaline circulation of the oceans [*Broecker and Denton*, 1989], and the geographical region within which melting occurs will significantly determine how large this impact will be [*Manabe and Stouffer*, 1997; *Fanning and Weaver*, 1997].

Of equal importance insofar as the climate system is concerned, however, is the issue of surface topography itself. When large accumulations of ice appear on the continents, such as existed at LGM, the surface topography is radically modified in these regions, and this modification is expected to have a marked influence on the atmospheric general circulation and thus climate. The early simulations of LGM climate by *Kutzbach and Guetter* [1986], for example, strongly suggested that the midlatitude jet stream would be split by the presence of the Laurentide ice sheet, thus significantly modifying the mean spatial positions of the storm tracks along which midlatitude synoptic scale precipitation systems are steered. This was shown to explain paleoclimatological inferences to the effect that the southwestern portion of the United States was significantly wetter at LGM than is the case under the present climate regime.

Also related to the questions of surface topography and surface type is, of course, the issue as to how the land-sea interface is modified by the glaciation-deglaciation process. Because proximity to the sea has a profound influence upon climate state (e.g., see *Lamb* [1972] for a general discussion), wherever significant migration of the coastline occurs in response to the eustatic fall of sea level that accompanies ice sheet growth, a climate impact may be expected. Of equal importance in this regard, however, is the fact that extremely large expanses of the surface that are presently covered by the sea were exposed land at Last Glacial Maximum, and these continental shelf regions are expected to have been significant sources of the terrigenous dust that was such an evident component of

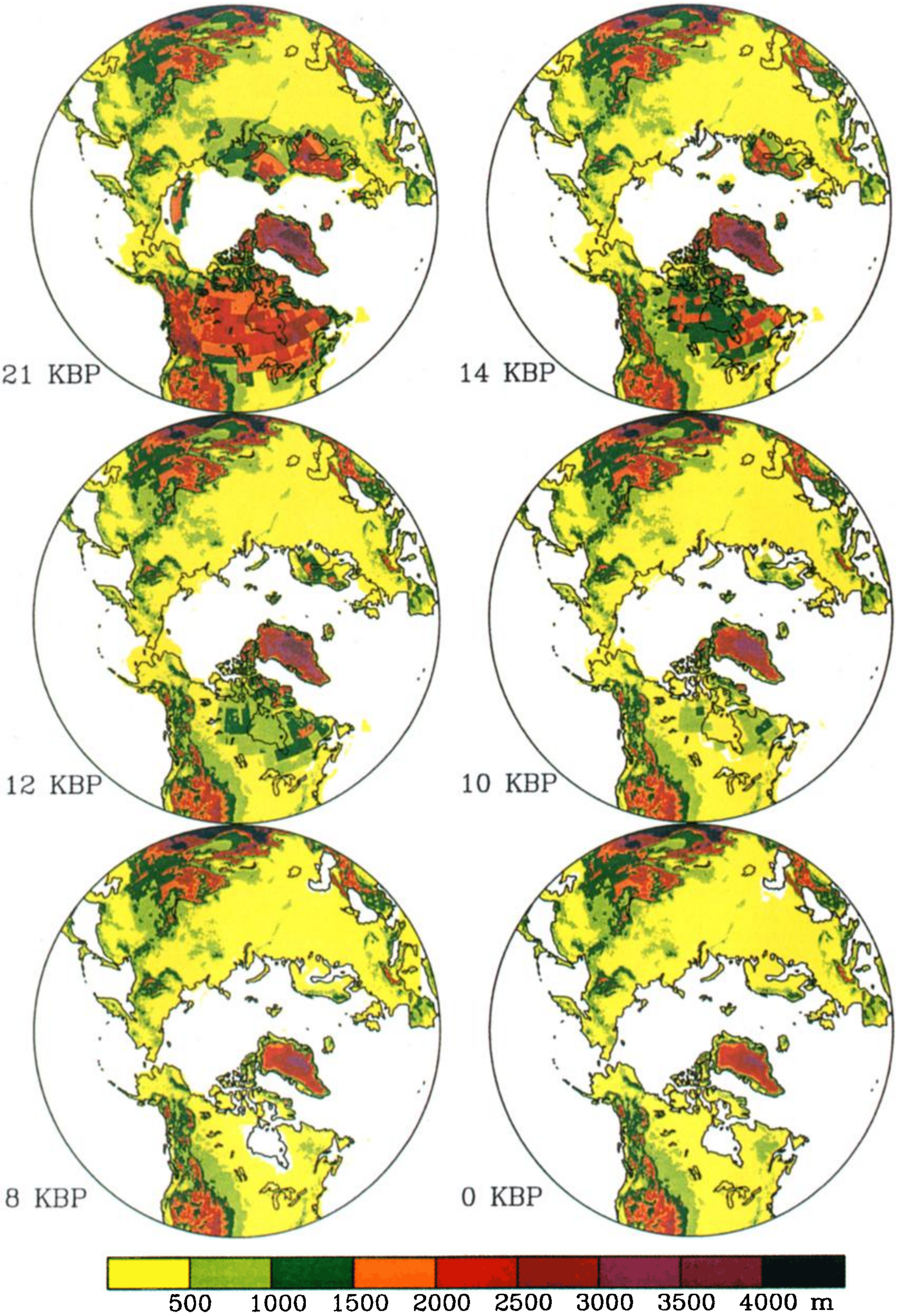

Plate 9. Topography with respect to mean sea level isopachs for the northern hemisphere component of ICE-4G for six times from Last Glacial Maximum to the present day. The times are the same as those for which "explicit" ice thickness was shown previously on Plate 2. Regions that were dry land at each of these times but are water-covered today are evident.

the atmosphere during full glacial conditions [*De Angelis et al.*, 1987]. Through its impact on the radiation regime, this may also have an important influence on climate.

In addition to these direct links between ice age cycle related changes in sea level and climate, there are at least two indirect links that have recently come to be seen as perhaps especially important. The first of these concerns the extent to which ongoing variations of relative sea level connected with the last deglaciation event of the current ice age may be contributing to the secular rate of change of sea level that is observed on modern tide gage recordings. As discussed in an especially careful initial analysis by *Barnett* [1983, 1984], it is quite clear that tide gages located sufficiently far from the main centers of LGM continental glaciation reveal that sea level has been rising over the last 50–100 years. *Peltier and Tushingham* [1989] first showed that the global influence of ongoing GIA contributed significantly to such records. Since the secular signal is strongly expected to be a consequence of ongoing global warming [e.g., see *IPCC*, 1996] it is clear that the GIA "contamination" must be eliminated in order to reveal the climate change signal more clearly.

A second indirect effect of the global GIA process on climate concerns an issue first raised, to my knowledge, by *Thompson* [1990]. Rather than being connected to modern climate change, however, Thomson's idea involves the question as to whether the variations in the Earth's shape through the ice age cycle might themselves have led to significant changes in effective solar insolation and thus indirectly in climate. This is potentially an extremely important issue because it is the orbitally induced variations of insolation that arise due to gravitational many-body effects in the solar system, which cause all of the geometric properties of the Earth's orbit around the Sun to vary with time, that we believe to be responsible for the ice ages themselves (see section 6 for a brief review of the current status of this Milankovitch theory). If the ice age cycle induced feedback onto the Earth's shape and thus rotational state were sufficiently strong, then the current basis upon which the Milankovitch theory is being tested would clearly require significant modification.

In the following subsections these implications for the understanding of climate system dynamics, of ice age cycle related changes in the level of the sea, will be investigated.

5.1. Inverse Problem for Deglaciation History

Central to the climate-related issues of interest to us here are the questions of how much ice existed on the landscape at Last Glacial Maximum and where this ice was located. Although the main centers of continental glaciation are well delineated by the glacial moraines that this process has created (Canada, Fennoscandia, islands both surrounding and in the Barents and Kara Seas, Scotland, Antarctica, western Patagonia), the geomorphological data do not, in general, allow ice thickness to be directly inferred, and therefore ice amount is not directly constrained. Although exceptions to this general rule do exist, for example, the so-called "trim lines" etched into the sides of the mountains of Norway and Antarctica that presumably denote maximum ice height, such indicators are generally difficult to date, and thus other methods must be employed. Two such methods are now available, each having both drawbacks and advantages. The first method employed to infer deglaciation history was that developed by *Denton and Hughes* [1981] and applied in the context of the Climate: Long-Range Investigation, Mapping, and Prediction (CLIMAP) project [*CLIMAP Project Members*, 1976] to produce maps of ice sheet thickness over each of the glaciated regions. This method was based upon the use of a steady state model of ice dynamics to infer ice sheet elevation given the location of the terminal moraines within which the ice sheets were known to exist at each of a number of times from LGM to the end of the deglaciation period. This method has the advantage that the inferred ice sheet topographies thereby determined are glaciologically reasonable. The disadvantage is that ice sheet thickness will generally be overestimated, because of the steady state assumption on the basis of which the thickness reconstruction is performed and because the impact of subglacial processes (sliding, till deformation, etc. [see *Clark et al.*, 1996; *Marshall et al.*, 1996; *Tarasov and Peltier*, 1997a, b, 1998] cannot be adequately described.

The second method that has been developed to infer deglaciation history is that based upon the postglacial rebound process itself as first described by *Peltier* [1994]. This method makes use of the observed postglacial rebound of the crust in the ice-covered regions to infer how thick the ice must have been in these locations; essentially, the observed isostatic response is employed as a "spring balance" to directly "weigh" the mass of ice that must have been removed to produce the observed response. This method relies on the validity of the assumption depicted in Figure 36, which illustrates the exponential fit to a typical rsl curve on the basis of which, using the Monte Carlo algorithm described in detail by *Peltier* [1998c], one may extract both the relaxation time T and the amplitude A that best characterize the postglacial rsl history at each such site, along with estimates of the standard error of fit. Because such postglacial rebound data correspond to memories of the surface response during the period after deglaciation is complete, that is, to an epoch in which the surface deflection is undergoing essentially free viscous decay, the relaxation time T that one observes at such locations is relatively independent of the amount of ice that induced the initial depression of the surface. These data do strongly depend upon mantle viscosity, however, and as discussed in section 4.5, may therefore be employed in the context of a formal inverse theory to strongly constrain the radial variation of this important parameter. Given a mantle viscosity structure inferred in this way,

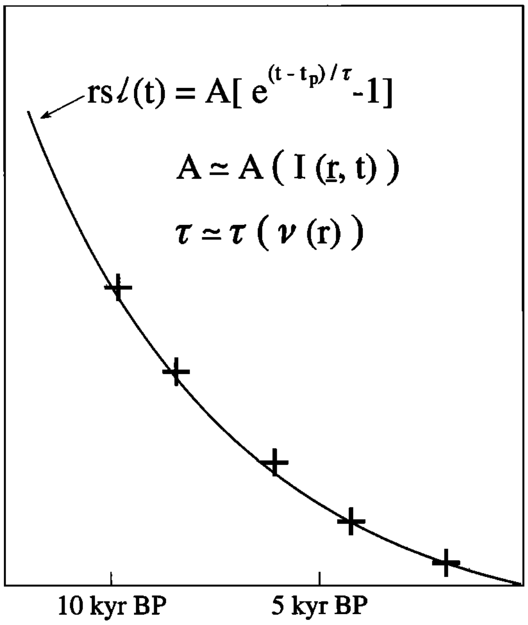

Figure 36. A typical rsl curve from an ice-covered site illustrating the exponential form of the uplift during the epoch of free postglacial rebound in which the relaxation time τ is determined almost entirely by mantle viscosity and the amplitude A is determined almost entirely by ice sheet thickness.

the essentially independent amplitude information (A) may be employed to infer how thick the ice must have been in order to cause the "amount" of uplift that is observed. This method has an advantage over the ice sheet modeling based methodology discussed above in that it does not depend upon the degree to which thermomechanical equilibrium exists for the ice sheets themselves; it is ice mechanics independent. It does suffer the disadvantage, however, that one is obliged either to assume that a state of glacial isostatic equilibrium exists at LGM or to compute the degree of disequilibrium by assuming a particular model of glaciation history. A further drawback of this method lies in the fact that adequate postglacial rebound data are not, in fact, available from at least one region where significant deglaciation is believed to have occurred, namely, Antarctica and more specifically West Antarctica.

The sea level based inversion for deglaciation history also has the additional advantage, however, that there does exist a very strong global constraint on the total amount of continental ice that melted across the last glacial-interglacial transition. This derives from the Barbados sea level record of *Fairbanks* [1989] shown in Figure 6 on the U/Th timescale of *Bard et al.* [1990]. At this site, sea level rose by ∼120 m between LGM and present, and this strongly constrains the total meltwater that entered the ocean due to deglaciation. In solving the inverse problem for deglaciation history as by *Peltier* [1994], one therefore begins by adjusting a first guess to the deglaciation history (e.g., the ICE-1 model in the work by *Peltier and Andrews* [1976] or the ICE-3G model of *Tushingham and Peltier* [1991, 1992]) so as to best fit the amplitude of rebound in the ice-covered regions from which one has data, as well as the integrated global signal that is recorded in the Barbados record. There being no adequate data available from Antarctica, one then adjusts the melting history away from the first guess CLIMAP model of *Denton and Hughes* [1981] in this region so as to remove the remaining misfits to the Barbados record and to other records of rsl history from the Southern Ocean (I have generally employed the data from the Wairu Valley of New Zealand for this purpose). It is this procedure that was followed in the construction of the ICE-4G model of *Peltier* [1994]. A summary of the ICE-4G melting history is presented on Figure 37 in which I show not only the total history that was previously compared, in terms of its local impact, with the Barbados record in Figure 6 but also a disaggregated form in which the contribution to the total meltwater history from each of the main centers of deglaciation is represented.

Also shown on Figure 37, for both the aggregated and disaggregated sea level data, are the contributions from both the "explicit ice" $\delta I(\theta, \lambda, t)$ that is directly employed in solving the integral equation for relative sea level history (either (3) or (15)) and for the "implicit ice" that must also have been removed from those regions that were at first covered by ice but later came to be inundated by the sea [*Peltier*, 1998d]. The existence of the implicit component of the ice load is required to account for the existence of the water in the once ice-covered regions that is later removed as postglacial rebound continues and also for the fictitious fall of sea level that the integral equation predicts should occur in the once ice-covered regions because of the difference in the gravitational potential that instantaneously exists between the regions that are newly declared ocean and the previous ocean on which the gravitational potential has been constrained to remain constant. Both of these contributions to the implicit ice are exactly calculable, and as will be observed from Figure 37, it is only when this implicit contribution is included that the net variation of sea level determined by summing over the volume of ice that is melted actually provides a good approximation to the net rise of sea level of 120 m that is observed at the Barbados location. Both the explicit and implicit components of the ice load are shown on Plate 8a for North America. The primary contribution to the implicit ice is associated with the water required to fill the depression of the surface that exists when the ice load disappears. It may be computed on the basis of the present-day water depth and the known height of the marine limit in the region undergoing postglacial rebound of the crust. Plate 8b illustrates the change of the ocean function with time through the critical period in the transition of Hudson Bay from being ice covered to being ocean connected.

Further inspection of Figure 37 will show that more than 60% of the total meltwater input to the oceans

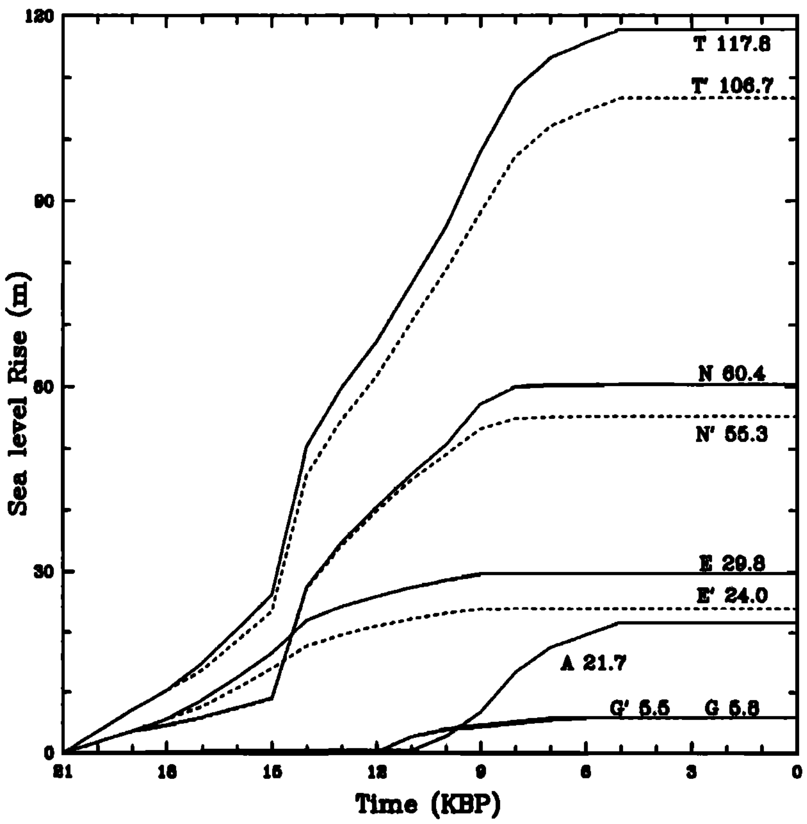

Figure 37. The ICE-4G model history of the last deglaciation event of the current ice age represented in terms of eustatic sea level rise equivalent in meters from Last Glacial Maximum (LGM) at 21 sidereal kyr B.P. until the present day. The curve labeled "T" includes the contributions from all geographic sources of meltwater taken together. Also shown are the contributions from each of the distinct geographic regions separately. The curve labeled N is that for North America, that labeled E includes all Eurasian sources, while that labeled A includes both Antarctic and Patagonian sources. The curve labeled G is that for Greenland. The corresponding dashed curves are those that do not include the contributions due to "implicit ice."

since LGM was derivative of the melting of the North American ice sheet complex composed of its distinct Laurentide, Cordilleran, and Innuitian (Canadian high Arctic) constituents. The amount of ice that melted from the sheets that covered Fennoscandia and the Barents and Kara Seas (see Plate 2) was considerably less than that from North America, amounting to a eustatic equivalent sea level rise near 30 m, whereas the North American complex contributes, according to ICE-4G, ~60 m to the total. Greenland contributed ~6 m according to ICE-4G and this may be somewhat large. The remaining component of ICE-4G is the Antarctic plus Patagonia component which, on Figure 37, is shown to contribute ~22 m to the total eustatic rise of sea level and to significantly lag the melting of the northern hemisphere ice sheets, as one might expect it to do if Antarctic deglaciation is caused by the sea level rise due to the melting of northern hemisphere ice, as has often been (reasonably) speculated to have been the case.

It is important to recognize that the ICE-4G model, a set of northern hemisphere deglaciation maps for which are shown on Plate 2, raises a number of interesting and important issues in both glaciology and climatology (see also section 6). The maximum thickness of Laurentide ice, which is ~3750 m, is rather thin for an ice sheet of such large spatial scale; in fact, its thickness was only slightly larger than that of the modern Greenland ice sheet. That an ice sheet of this kind be rational glaciologically has been assumed to require that its flow be significantly influenced by sliding associated with the deformation of soft underlying sediment [e.g., *Clark et al.*, 1996], and this may, in fact, be expected [see also *Marshall et al.*, 1996]. It could also be the case, however, that the standard Glen flow law, on which basis it has been concluded that this aspect ratio problem exists, could be an insufficiently accurate approximation to the rheology of large ice masses that flow under the action of the stress field that is induced gravitationally (see section 6). A further important issue concerns the magnitude of the deglaciation event that occurred on Antarctica. Although the initial CLIMAP estimate of the scale of this event was such that it delivered an eustatic sea level rise greater than 25 m (in the current version of ICE-4G this event produces an eustatic sea level rise of about 20 m), more recent glaciological estimates [*Huybrechts*, 1992] are such that Antarctic deglaciation could have contributed no more than 17 m of the net glacial-to-interglacial rise of sea level. Although this difference is not extreme, it has been argued [*Huybrechts*, 1992] that the extent of Antarctic melting could have been as little of 10 m in eustatic equivalent. If this extreme case were closer to the truth, then ICE-4G would have to be further modified, perhaps by shifting ice from Antarctica onto North America. Models of this kind are being considered in the context of the construction of the ICE-5G model and will be described elsewhere. Preliminary analyses demonstrate that such reduction in the scale of the Antarctic melting event is easily accommodated.

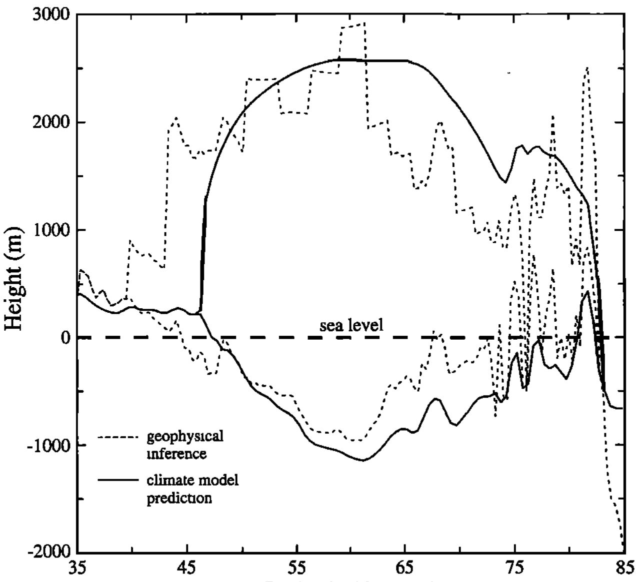

Figure 38. Geophysical inferences of the topography of the Laurentide ice sheet at LGM and of the isostatic depression of the crust that would have existed at that time along a north-south transect at 81.25°W longitude. Also shown are the predictions of these properties of the LGM state delivered by the a priori climate model discussed in section 6.

5.2. Ice Age Paleotopography

As mentioned in the introduction to this section, the time-dependent topography of the planet with respect to sea level that is induced by the ice age cycle is critical to the use of atmospheric general circulation models in the reconstruction of ice age climate regimes. Topography is a vitally important boundary condition in such models. The method whereby its time dependence since LGM may be inferred was previously described in equations (19a)–(19c) and must, in fact, be determined in the process of the iterative solution of the sea level equation (either version (3) or version (15)). Plate 9 shows a sequence of six time slices through northern hemisphere topography with respect to sea level for the same times as those for which the (explicit) ice thickness data were shown on Plate 2. On Plate 9, regions that are water covered at present but were dry land at each of the times shown are clearly visible. Obviously, the regions in which topography was most radically modified are those in which the main ice sheets were located. Over the Hudson Bay region of Canada, maximum topographic height above sea level at LGM was somewhat greater than 2.5 km according to the ICE-4G reconstruction. This is lower by ~1.5 km than the *CLIMAP Project Members* [1976] estimate. As pointed out by *Peltier* [1994], this might reasonably be expected to have a significant impact on the climate state inferred for LGM on the basis of atmospheric general circulation model reconstructions. Figure 38 shows this topography on a north-south cross section through the LGM form of the Laurentide ice sheet at 81.25°W longitude along with the theoretical prediction of the isostatic depression of the crust that would have existed at LGM. Also shown is the a priori prediction of these properties of the system using the climate model to be discussed in section 6. Clearly, the climate model prediction and the geophysical inference are in very close accord, with the maximum ice thickness being only slightly lower than 4 km.

Of additional interest insofar as paleotopography is concerned is the question of the timing of the inundation of the several land bridges that existed at LGM since this not only provides additional information that may be further employed to constrain the parameters of the model but is also, of itself, information that is of enormous interest from the point of view of both archaeology and anthropology. Since the time at which a land bridge comes to be inundated by the sea is often marked by a peat horizon that is datable using the ^{14}C method (e.g., see *Elias et al.* [1992] for an example from the Beringian land bridge to be mentioned further below), the age of inundation can be measured and compared with that predicted by the model. Plate 10 shows examples of what I have previously called inundation maps [*Peltier*, 1994] for three different geographical regions the Bering Strait, Australia and New Guinea, and finally the adjacent Indonesian Archipelago, respectively. Also shown is a map of the increase in land area in the Greek archipelago at LGM. A further example of such inundation maps was presented on Plate 5 to illustrate the way in which the land bridge that connected England to France was submerged as deglaciation proceeded.

Inspection of these maps provides a wealth of information which is of geological/archaeological/anthropological interest. The issue of the timing of the closure of the Beringian land bridge might be seen as especially interesting for reasons to be further discussed below. According to the global GIA theory this is predicted to have occurred just subsequent to 9 kyr ago. The land bridge that joined England to France is predicted to have closed at approximately the same time, while remnants of the bridge between New Guinea and Australia are predicted to have existed until 6 kyr ago. At Last Glacial Maximum the entire Indonesian Archipelago was essentially dry land, but open water continued to separate this large land mass from New Guinea. In the Greek archipelago, there were also considerable changes in the distribution of land and sea from that which exists at present, with several island regions that would have existed at Last Glacial Maximum becoming entirely overcome by the sea. Could one of these islands correspond to Atlantis? There are clearly many candidates! Much higher resolution analyses than those reported here will be required if they are to be truly useful from an archaeological perspective. These are also being pursued by others (e.g., *Lambeck* [1997] described a number of excellent examples of what might be done in this regard when "military accuracy" present-day topography is employed for the purpose of local analysis).

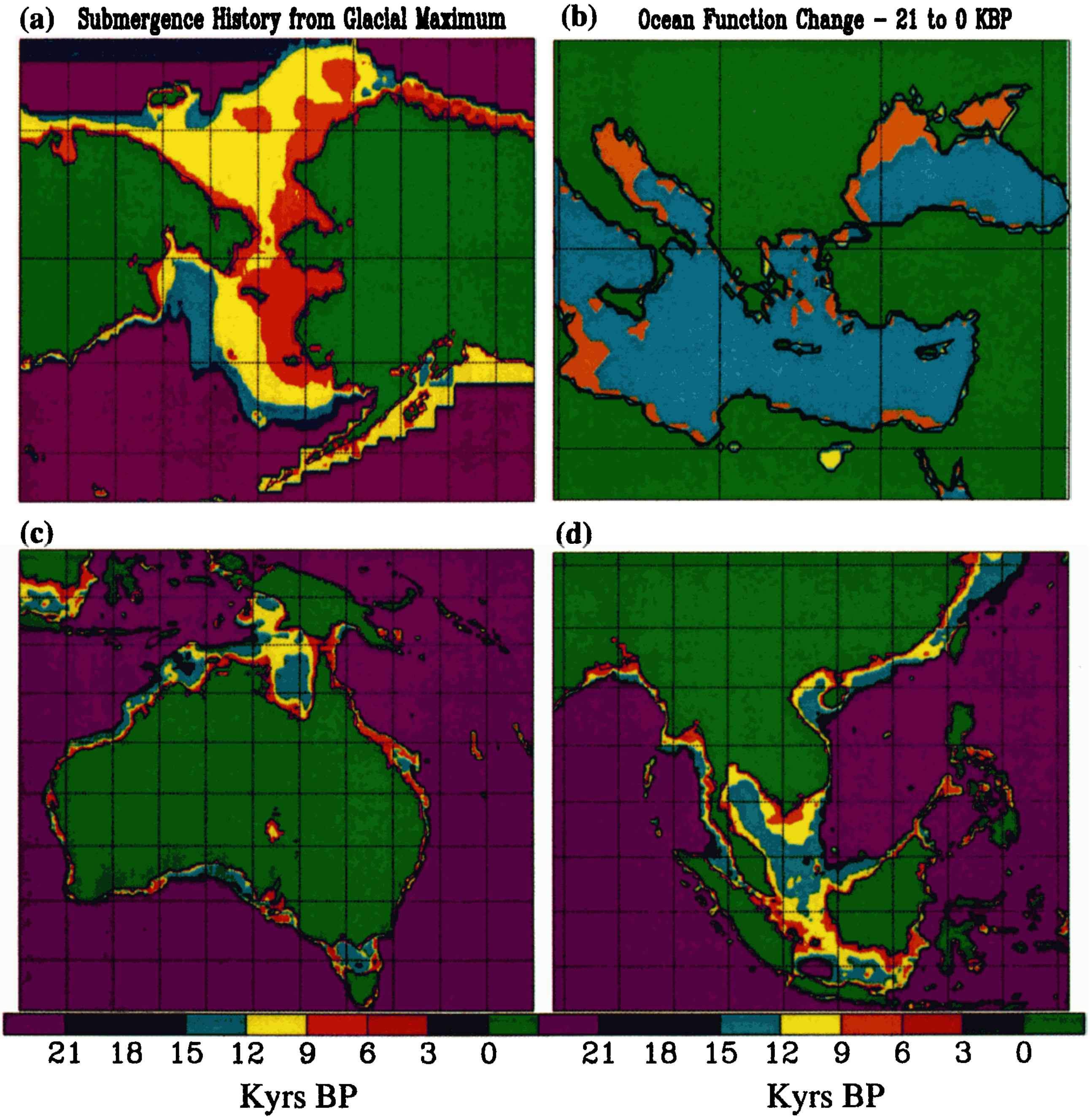

Plate 10. Inundation maps for the (a) Bering Strait, (c) Australia-New Guinea, and (d) the Indonesian Archipelago. (b) A map centered on the Greek archipelago showing the regions that would have been dry land at LGM but which are now water covered.

One final application of the global geophysical theory of GIA that I have developed that is especially interesting is one with a distinctly anthropological connection involving the issue of the time interval within which the human species first occupied the North and South American continents. The recently discovered, or at least recently accepted, Monte Verde site in southern Chile is now recognized as representing the earliest time at which there exists clear and unambiguous evidence of human occupation of the Americas. This time, determined by ^{14}C dating, corresponds to $\sim$12.8 sidereal kyr before present. Given that this time is relatively early in the history of North American deglaciation, there is clearly a question as to the route which ancestral Americans might have travelled from Eurasia to North America, since there was still significant ice cover over all of Canada in this period. Plate 11 shows a map based upon analysis recently performed with the ICE-4G (VM2) model that appeared in a recent article concerning the Monte Verde site [*Gore*, 1997]. This shows possible patterns of human dispersal over the North American landscape at that time. As discussed above, the Bering-

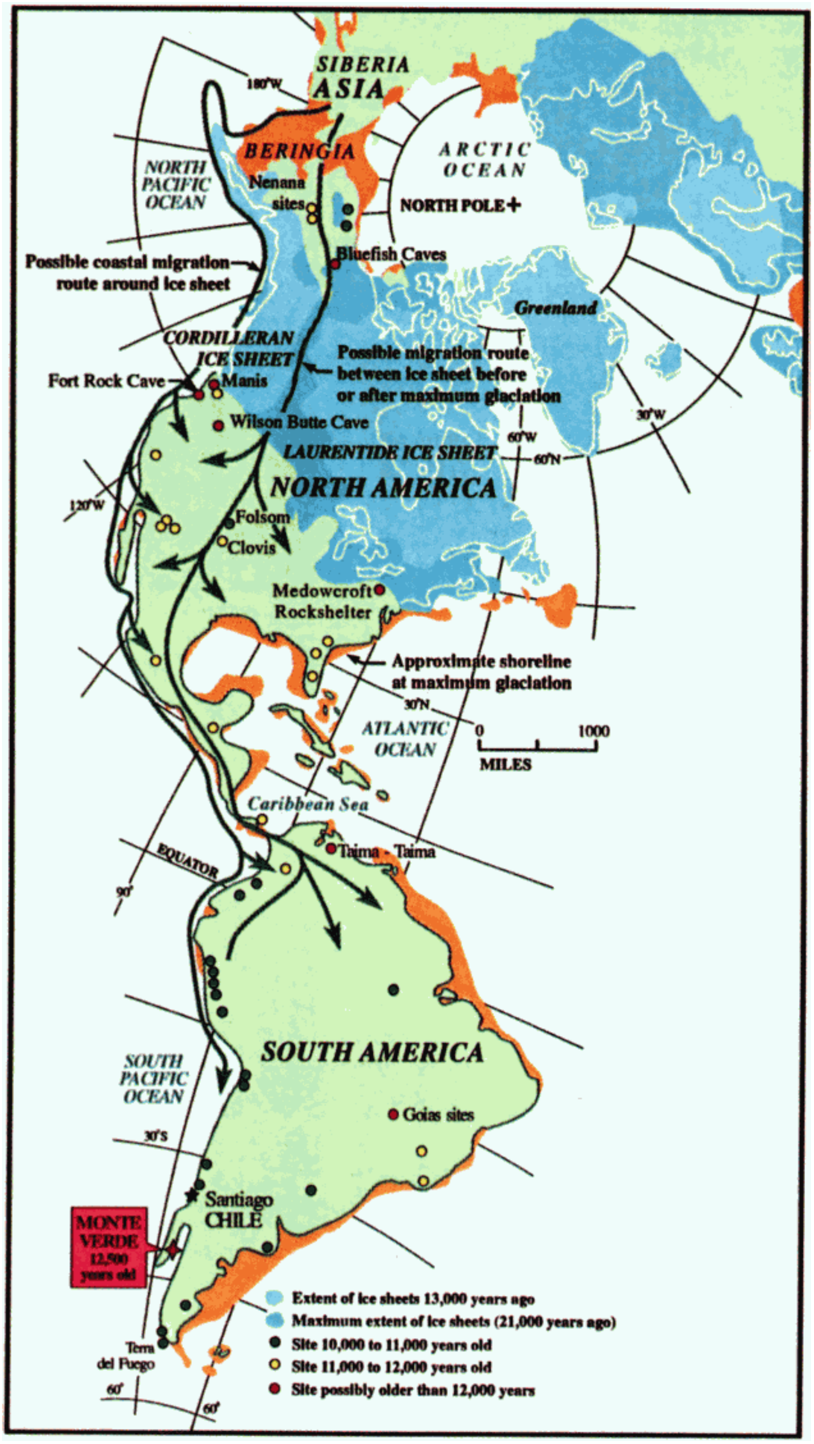

Plate 11. Possible human dispersal patterns over the North American landscape in the period between 11 and 13 kyr ago. The oldest existing site where human settlement is known to have existed is the Monte Verde site. The ice cover and time-dependent continental outlines are based upon the ICE-4G reconstruction of *Peltier* [1994]. Modified after a figure from *Gore* [1997].

ian land bridge was still open then so that ancestral North Americans could have reached Alaska, which remained essentially ice free throughout the glacial period. As clearly shown on Plate 11, on which the outlines of the Laurentide and Cordilleran ice sheets are also superimposed, one possible route by which humans may have reached central North America and South America at this time was along a corridor between the two ice sheets that existed prior to 13 kyr ago, essentially through what is today the Canadian province of Alberta. This is an interesting illustration of the way in which output from the global geophysical model of the GIA process can be employed to provide guidance on the plausibility of anthropologically interesting hypotheses.

5.3. Meltwater Sources and the Thermohaline Circulation

One of the issues of greatest current interest insofar as paleoclimatology is concerned involves the question as to the impact upon the climate system of the deglaciation process itself. This impact is believed to have been rather profound in consequence of the modification to the deep thermohaline circulation of the oceans caused by the addition of large quantities of freshwater to the surface of the high latitude oceans during episodes of anomalously high meltwater production. Figure 39 shows $\delta^{18}O$ from both the Greenland Ice Core Project (GRIP) and Greenland Ice Sheet Project 2 (GISP2) deep ice cores from Summit, Greenland, the atmospheric temperature record from Vostok, Antarctica [*Jouzel et al.*, 1987], and the Barbados sea level curve of *Fairbanks* [1989] on the timescale of *Bard et al.* [1990]. Since the $\delta^{18}O$ record from an ice core is proxy for the temperature of the atmosphere from which precipitation is derived, it is very clear that just prior to the onset of the Younger Dryas cold period (corresponding to low $\delta^{18}O$), which was centered upon 12 sidereal kys B.P., a period of extremely rapid sea level rise occurred that was well captured in the Barbados coral-based record of sea level change. This is the event to which *Fairbanks* [1989] has referred as meltwater pulse 1a, and it apparently occurred during the Bölling-Allerød warm period which preceded Younger Dryas cooling. Figure 40 shows the time derivative of the fit to the Fairbanks sea level record embodied in the ICE-4G deglaciation history, disaggregated into the contributions to the total time-dependent flux originating from each of the major concentrations of land ice. This lumped time series clearly shows the extraordinary concentration of freshwater that was involved in meltwater pulse 1a, and the disaggregated data demonstrate that in ICE-4G the overwhelming fraction of this flux was derivative of the meltdown of the North American ice complex, much of which ran off of the continent through the Gulf of St. Lawrence. This routing of the meltwater (as discussed by *Broecker and Denton* [1989]) would have had a very large impact on the process of North Atlantic Deep Water (NADW) formation and thus on the global thermohaline circulation itself.

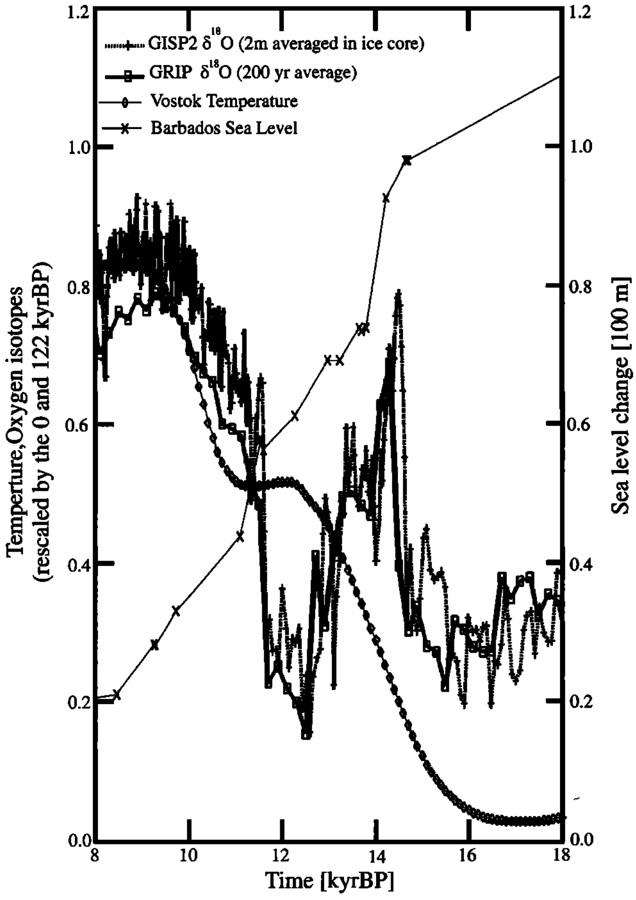

Figure 39. Proxy records of climate variability between 8 and 18 kyr B.P. The Greenland temperature proxies, i.e., oxygen isotope records from the GRIP and GISP2 deep ice cores, are normalized by their maximum deviations in the interval between 0 and 122 kyr B.P. The temperature record from Vostock, Antarctica, is also normalized by its range over the same period.

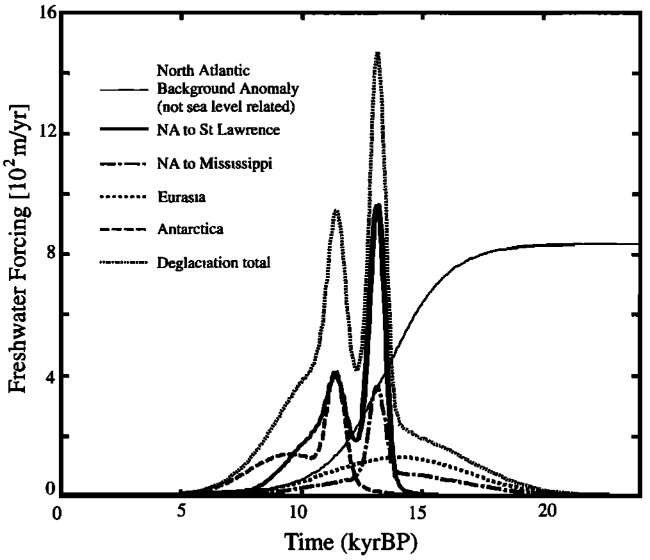

Figure 40. Flux of freshwater released to the oceans as a function of time according to the ICE-4G reconstruction of *Peltier* [1994]. This quite accurately fits the time-dependent flux inferred on the basis of the Barbados sea level record of *Fairbanks* [1989]. Also shown is the result of disaggregating this flux into the contributions from each of the deglaciating regions.

A large number of analyses have recently been performed that investigate whether the Younger Dryas cool period that interrupted the general warming of climate which occurred synchronously with deglaciation could have been caused by a shutdown of the overturning circulation in the Atlantic due to the addition of meltwater to the high-latitude surface of the ocean where deep water forms today. Probably the most complete of these analyses is by *Manabe and Stouffer* [1997] based on integrations performed with the Geophysical Fluid Dynamics Laboratory (GFDL) coupled atmosphere-ocean model. Their analyses rather convincingly show that a meltwater pulse of 1a scale is indeed sufficient to cause a very significant reduction in the strength of the overturning circulation but that this does require that for the most part the runoff be routed through the St. Lawrence estuary. Their results have also been verified using a somewhat simpler coupled atmosphere-ocean model by *Fanning and Weaver* [1997] and in analyses based upon a dimensionally reduced model of the thermohaline circulation (THC) by *Sakai and Peltier* [1995, 1996, 1997]. Of greatest interest, however, is the second of the two meltwater pulses that is evident in *Fairbanks*' [1989] sea level record, which he has called meltwater pulse 1b.

Although the existence of a sharp pulse of meltwater influx following the return to warm conditions after the Younger Dryas is still a subject of active debate [e.g., see *Bard et al.*, 1996a], it is important to note that in the ICE-4G model of the deglaciation process it is the deglaciation of Antarctica which contributes fully 50% of the meltwater influx associated with this event, the rest deriving primarily from the Laurentide and Greenland ice sheets. If most of the meltwater produced during meltwater pulse 1b were derived from the Laurentide ice sheet rather than the Antarctic ice sheet, which would be the case if significant ice mass were moved from Antarctica onto the Laurentide ice sheet so as to increase the aspect ratio (height/width) of the latter and decrease the mass of the former (see section 6 for further discussion of the aspect ratio issue), then an interesting question clearly arises. The total pulse of freshwater exiting onto the high-latitude North Atlantic would then be approximately the same as that which apparently caused the Younger Dryas cooling to occur. Yet no such second Younger Dryas event is visible in the ice core record of North Atlantic climate change. The ICE-4G model of the deglaciation process resolves this issue by postulating a delayed deglaciation of Antarctica that is of significant scale. This is not, of course, to say that no shift of the ICE-4G Antarctic ice load onto Laurentia can be accommodated, only that the shift of the entirety of this load to the northern hemisphere is quite liable to lead to a paleoceanographically untenable situation.

5.4. Global Sea Level Rise and Glacial Isostatic Adjustment

In the context of the ongoing debate concerning the issue of global environmental change a wide range of physical, chemical, and biological arguments have been raised on all sides of the question as to what the future may have in store. Of these arguments, none has received more attention than the question as to whether, and if so by how much, the mean temperature at the surface of the planet can be expected to increase as a consequence of the increasing load of radiatively active trace gases which human activity is continuing to add to the atmosphere. The most recent and detailed appraisal of this question [*IPCC*, 1996] has led to the conclusion that the observed spatial and temporal variation of surface temperature over the past century is such as to strongly suggest that it has been significantly influenced by anthropogenic processes. Although much discussion continues concerning the validity of this conclusion, there is little dispute that mean surface temperature has, in fact, increased over this period by ~0.5°C [e.g., see *IPCC*, 1996]. It is furthermore clear on the simplest physical grounds that this increase of temperature must have an impact on sea level, if only because the temperature of the atmospheric boundary layer is efficiently transferred to the surface mixed layer of the oceans. As the temperature of the surface ocean rises and as such increasingly warm water is subducted to depth in the deep-water formation process, the influence of thermal expansion inflates the volume occupied by a given mass of ocean water, thus causing sea level to rise due to this *steric effect*. One might also expect, perhaps naively, that as surface temperature increases, sea level may be induced to rise by the melting of the large polar ice sheets that presently cover both Greenland and Antarctica (a eustatic effect). It is therefore, and rather clearly, an interesting question as to what can be said concerning the way in which the average level of the sea over the surface of the global ocean has varied over the same period during which mean surface temperature has been increasing.

Given the importance of this question in the general area of global change research, it should not be surprising that a great deal of effort has been expended in attempting to address it, beginning, most interestingly, I believe, with the careful analyses of *Barnett* [1983, 1984]. All of the assessments of this issue since that time have been based upon the data recorded on tide gages, hundreds of which are presently installed along all continental coastlines, if rather nonuniformly. Figure 41 provides a global view of the tide gage installations that currently contribute to the archive of the Permanent Service for Mean Sea Level (PSMSL) that is located in the United Kingdom. Figure 41 shows only 500 or so sites since the complete array of gages reporting to the PSMSL has been culled for the purpose of producing Figure 41 by rejecting all those from which the duration of the record is less than 10 years. As has been known for some time [e.g., *Douglas*, 1991], even records that extend over a full decade are unable to provide any accurate measure of the true secular rate of sea level change that is occurring at a given location. This problem is connected to the intensity of the interdecadal variability that exists in most coastal locations.

As a sample of the sort of histories that are observed on typical long tide gage records, Figure 42 shows a sample of annually averaged records from 12 different locations that are widely distributed over the surface of

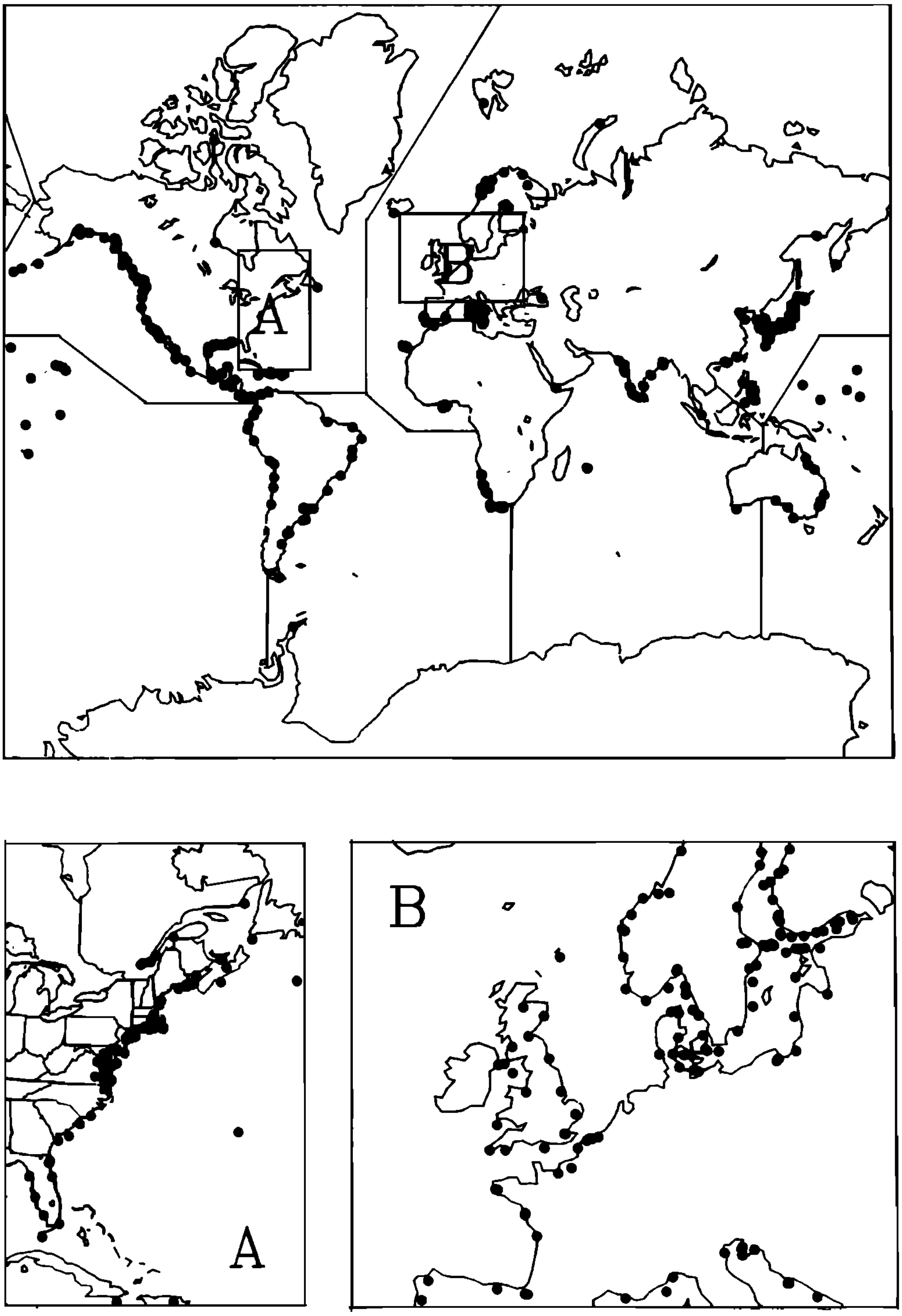

Figure 41. Locations of tide gage installations from which records are available that exceed 10 years duration. All of the data from these locations are available from the Permanent Service for Mean Sea Level (PSMSL).

the Earth. Careful inspection of these records will reveal that with the exception of those records that are recorded on tide gages located in the Baltic Sea, which is the center of ongoing postglacial rebound that was forced by Fennoscandian deglaciation, the data generally do show that sea level is everywhere rising. In order to determine an average rate on the basis of data such as these we are obliged to address the question as to how such an average might best be computed. This requires that we address the issue of data heterogeneity in both space and time. That the question of the temporal heterogeneity of the data is important may be established most directly by fitting individual annually averaged tide gage time series by linear regression and by displaying

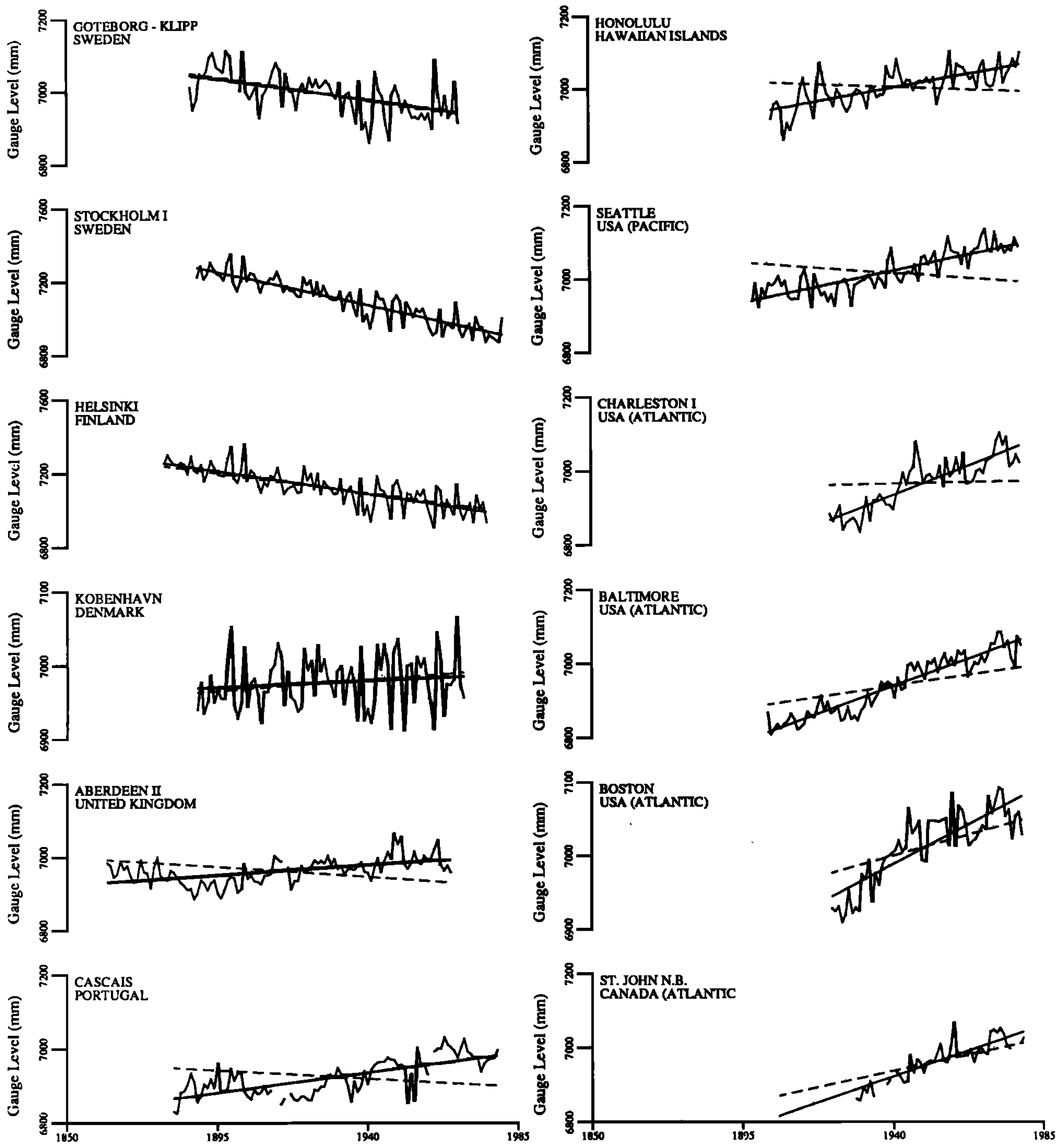

Figure 42. Examples of time series of annually averaged mean sea level from 12 locations on the surface of the Earth from which especially long records are available. Note that only the three records from sites on the coast of the Baltic Sea in Fennoscandia exhibit falling sea levels. This is due to the ongoing postglacial rebound of the crust that is occurring in this region.

the grand average of the averaged rates so determined as a function of the minimum length of the records that are allowed to contribute to the grand average. Such an analysis of the data in the PSMSL archive was performed by *Peltier and Tushingham* [1989] and is reproduced here as Figure 43, on which is shown the result obtained by applying the analysis to the raw tide gage data and also to a "corrected" set of tide gage data created by subtracting the rates predicted by a global model of glacial isostatic adjustment for the individual tide gage sites. Inspection of the results shown on Figure 43 demonstrates two important points. First, these analyses make clear the fact that as the minimum record length is increased, the globally averaged rate of sea

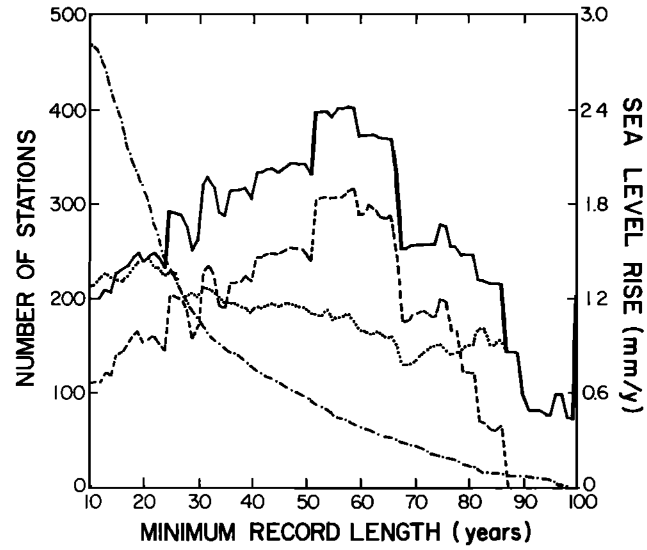

Figure 43. Results for the global rate of relative sea level (rsl) rise obtained on the basis of linear regression analysis. The dash-dotted curve depicts the decrease in the number of tide gages as the minimum record length employed in the analysis increases. The three individual estimates of the globally averaged rate of rsl rise versus minimum record length are based upon equal-area averages of the raw (dashed curve) and GIA-reduced (solid curve) tide gage data and a site by site average of the reduced data (dotted curve). The solid curve should provide the most accurate linear regression estimate of the present-day global rate of rsl rise, and this most accurate estimate should obtain for minimum record length data sets of 50–60 years. Such records are probably sufficiently long to average out the interdecadal variability.

level rise implied by the analysis at first increases and then reaches a plateau near a cutoff length near 60 years. It is therefore clear that the use of overly short tide gage recordings does not lead to a stable estimate of the global rate of sea level rise. When the cutoff length is taken to be too large, however, there are so few gages contributing to the average that the estimate becomes sensitive to fluctuations due to small sample size. Second, it clearly follows for the results shown on Figure 43 that when the tide gage records are corrected for the influence of glacial isostatic adjustment, the influence on the globally averaged rate of sea level rise is such as to increase it by a significant fraction of 1 mm yr^{-1}. On the quasi-plateau that develops for cutoff length of order 60 years the globally averaged rate delivered by these analyses is near 2 mm yr^{-1}. This estimate was further refined by *Peltier and Tushingham* [1989] by applying the technique of empirical orthogonal function analysis which leads to a complementary global estimate of the present-day rate of global sea level rise of 2.4 ± 0.9 mm yr^{-1}, with the error estimate representing the standard deviation rather than the error in the mean.

The original analysis of *Peltier and Tushingham* [1989] based upon the use of tide gage estimates adjusted to account for the influence of the glacial isostatic adjustment process has recently been extended in several ways, which I will briefly review in order to provide a best possible view of the present state of the art. A first issue that this more recent work has addressed concerns the question of the extent to which the GIA-reduced rates

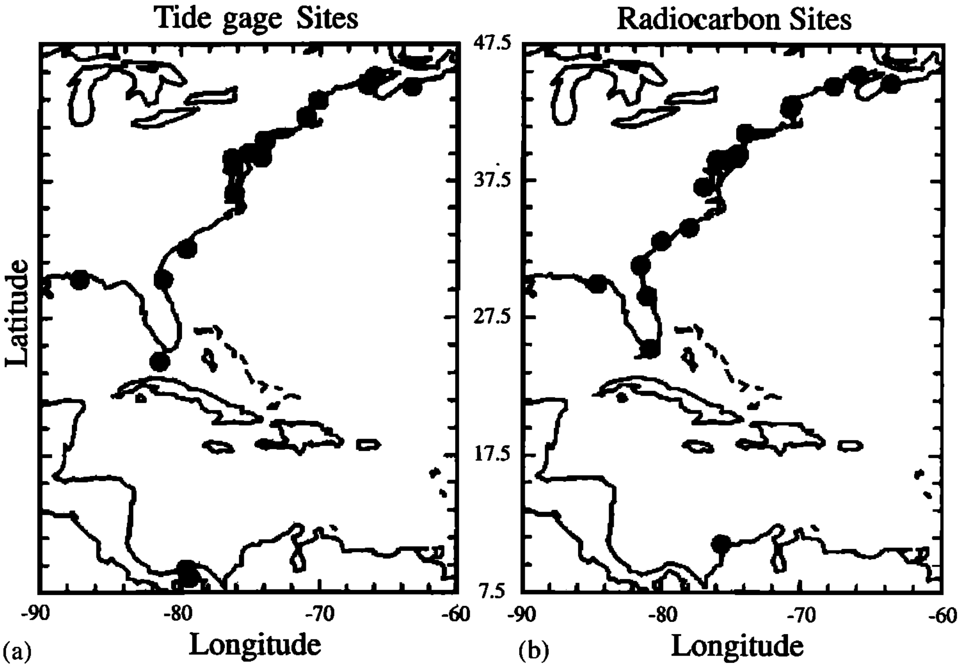

Figure 44. (a) Locations of sites along the east coast of the United States from which tide gage recordings are available that are in excess of 60 years duration. (b) Locations of U.S. east coast sites from which ^{14}C records of late Holocene sea level history are available. Note that for each tide gage site there is a nearby ^{14}C site from which an estimate of the present-day rate of sea level rise may be extracted for use in correcting the tide gage derived rates for the influence of the glacial isostatic adjustment process.

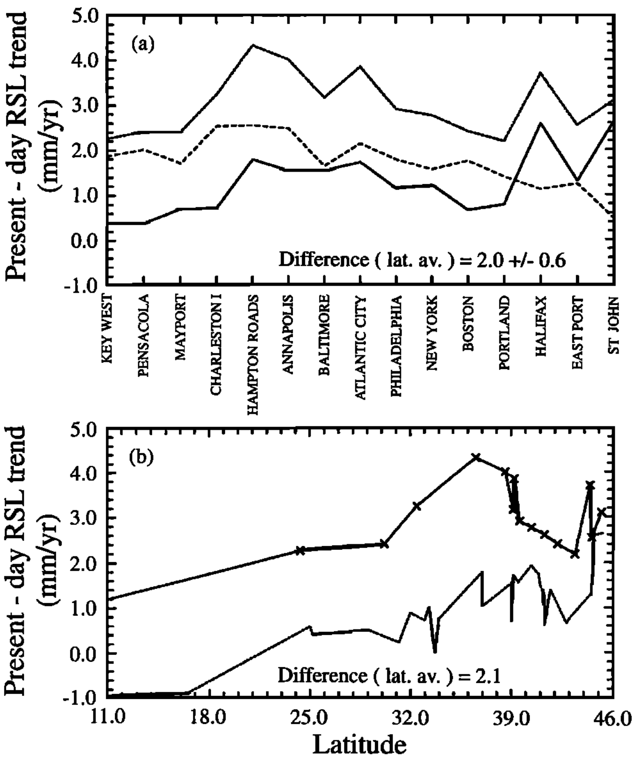

Figure 45. (a) Tide gage derived rates of secular sea level rise for sites along the U.S. east coast and ^{14}C derived rates obtained from late Holocene records at nearby locations. Also shown is the difference between these two short-timescale and long-timescale time series derived rates, which is clearly a much more slowly varying function of position along the coast than either of the individual records that contribute to the difference. (b) Same data as in Figure 45a but shown as a function of latitude rather than in equispaced latitudinal rank.

may be shown to be uniform over a restricted geographical area. It seems clear that only if such can indeed be shown to be the case will there be convincing evidence that it is indeed the GIA process that is responsible for producing the most significant modification to the global signal inferred on the basis of sufficiently long tide gage recordings. As argued by *Peltier* [1996b] and *Peltier and Jiang* [1997], the geographic region in which this test may be most effectively performed consists of the eastern seaboard of the continental United States. The reason for this will be clear by inspection of Figure 44, which shows the locations of sites from which ^{14}C dated records of rsl history exist covering the last several millennia and from which tide gage recordings are available with records of duration in excess of 59 years. All along this coast it is clearly possible to employ the ^{14}C data directly to decontaminate the tide gage data of the influence of the GIA process. That the only process contributing significantly to the ^{14}C records along this coast is, in fact, the GIA process was clearly established in section 4.2, where we actually made use of the ability of the global model of the GIA process to fit U.S. east coast rsl records as a test of its quality.

The results obtained in one sample from the large number of variants upon the basic analysis procedure that I have now performed are shown on Figure 45, which is taken from *Peltier and Jiang* [1997]. Inspection of the results presented on Figure 45 demonstrates two important facts. First, there is the fact that at every site along this coast the tide gage measured rates of secular sea level rise are higher than the rates of sea level rise that are occurring because of the ongoing process of glacial isostatic adjustment. Second, there is the fact that the variations of the rates of rsl rise with position along the coast actually track one another. It will not be surprising therefore that when the ^{14}C rates are subtracted from the tide gage inferred rates, the difference between them is a much more slowly varying function of position along the coast than either of the individual time series themselves. This would appear to constitute a very convincing proof that there is indeed a single large-scale, plausibly climate-related, process that is contributing to the rise of sea level in this relatively localized sector of the Atlantic basin. When we average the difference of the two sets of observations of sea level rise, we obtain a value of 2.0 ± 0.6 mm yr^{-1}, a local value that is very close to the value shown for the GIA-corrected global data on the plateau region of Figure 43 and that deduced by *Peltier and Tushingham* [1989] through the application of empirical orthogonal function analysis.

Although all of these analyses clearly establish the importance of the GIA-related contamination to which tide gage recordings are subject, and which must be removed if we are to have any hope of observing the modern global change related signal, it should be clear that our ability to accurately estimate this signal is significantly compromised at present. The reason for this has to do with the extremely poor coverage of the ocean basins that is presently available from gages for which records are available that are at least 50 years long (this issue has been recently addressed by *Peltier and Jiang* [1997]). If we are ever to have a truly accurate measurement of the present-day average rate of global sea level rise, we will clearly have to acquire it by means other than the use of tide gages. Fortunately, there currently exists at least one space geodetic methodology that will eventually provide the measurement that is of interest to us, namely, satellite altimetry. The presently operating TOPEX/Poseidon system has an accuracy such that we might reasonably expect it to deliver a useful estimate of the globally averaged climate-related signal after approximately one decade or so of operation, sufficient to allow the variability associated with the interannual El Niño process to be effectively averaged out. The current status of the TOPEX/Poseidon inference of the global rate of sea level rise has been recently reviewed by *Nerem et al.* [1997a, b], and the interested reader is referred to them for a detailed discussion of the instrument(s) and the information that they are currently providing. Even more important for the future measurement of the global sea level rise signal, however, may be

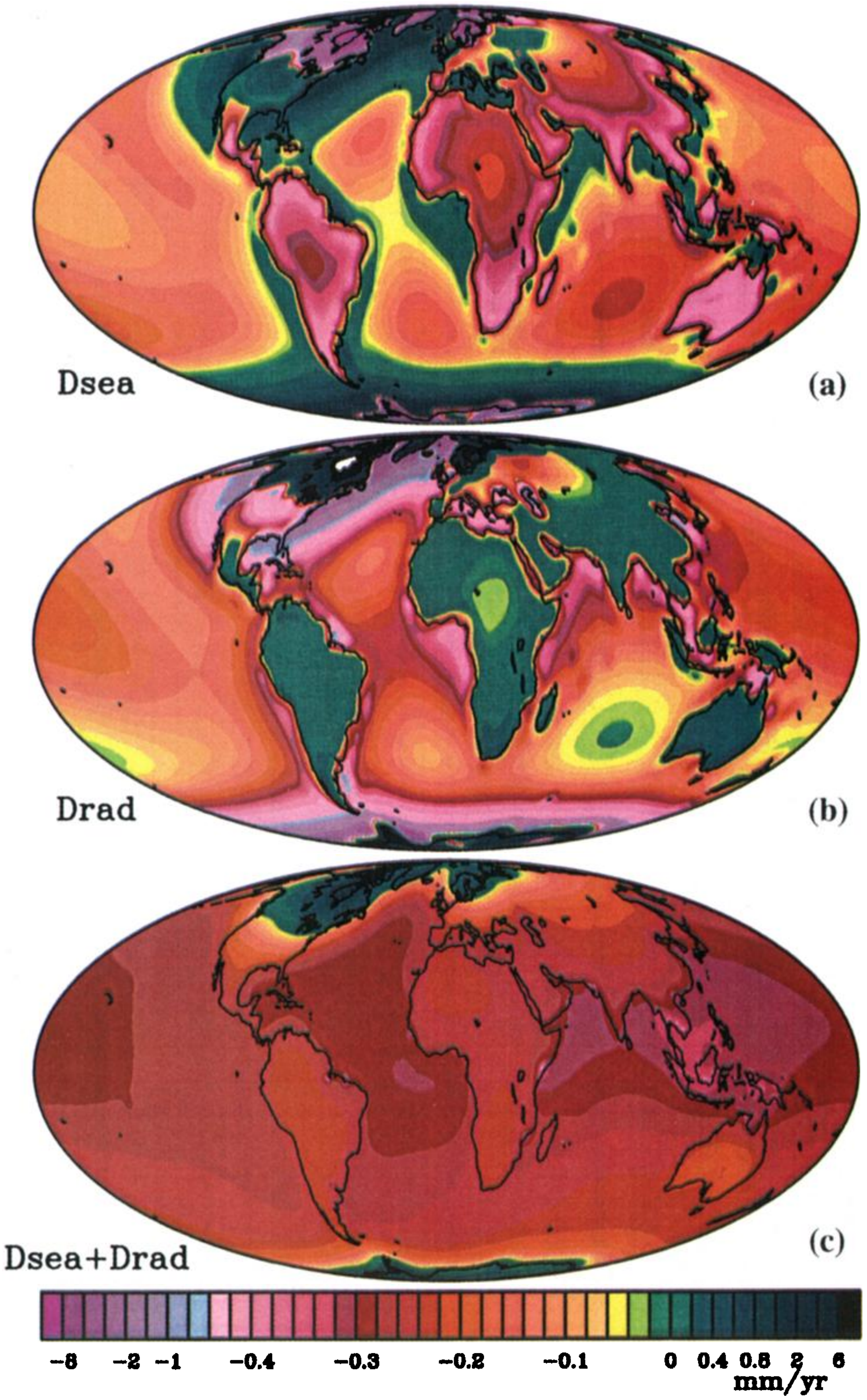

Plate 12. (c) Present-day predicted rate of relative sea level rise relative to the center of mass of the planet (the geocenter) along with its two constituent fields, respectively. (a) The present-day rate of relative sea level rise with respect to the surface of the solid Earth and (b) the present-day rate of radial displacement of the surface of the solid Earth relative to the center of mass.

NASA's geopotential mission Gravity Recovery and Climate Experiment (GRACE) through which it is expected that a complete time-dependent geoid may be obtained.

Of particular interest to us here from the present perspective, however, is the question as to the extent to which TOPEX/Poseidon-type altimetric measurements and the time-dependent GRACE geoid can be expected to be contaminated by the GIA process. This question requires specific analysis that is distinct from those previously presented because a satellite altimeter does not observe relative sea level with respect to the deforming surface of the solid Earth (as does a tide gage), but rather it measures sea level with respect to the center of mass of the planet (the geocenter) since this is the point in space to which the orbit of an altimeter-equipped artificial Earth satellite is referred.

In order to predict the variation of sea level with respect to the center of mass we must add to the present-day rate of relative sea level change at every point on the Earth's surface the present-day rate of change of radial displacement $\dot{U}$. This combined field is, of course, nothing more, or less, that the time rate of change of geoid height. Plate 12c shows the prediction of the present-day rate of change of geoid height based upon the model ICE-4G (VM2) in which the influence of rotational feedback has been suppressed. Plates 12a and 12b show the present-day rates of relative sea level rise and radial displacement, respectively. Inspection of these two constituents of the time rate of change of the geoid height field will demonstrate that they are essentially anticorrelated, as must be the case on physical grounds. Where relative sea level is rising, the crust will be more strongly depressed and vice versa. On the basis of Plate 12c, it is clear that "absolute" sea level is predicted to be falling globally over the entire surface of the planet from both southern and northern midlatitudes to the equator. This clearly implies that the TOPEX/Poseidon inference of global sea level rise will also be contaminated by the ongoing GIA process and that the removal of this contamination will increase the TOPEX/Poseidon inference of the climate-related signal. As has been demonstrated (R. Rapp, personal communication, 1997), however, when the field shown on Plate 12c is averaged over the actual surface tracks of the TOPEX/Poseidon satellite, one finds the average value of the GIA effect to be only 0.08 mm yr^{-1}, which is, in effect, negligibly small.

One further issue which warrants comment concerns the way in which a modern climate change related contribution to global sea level rise may influence our inference of mantle viscosity based upon data related to the GIA process. This question was addressed in a preliminary way in section 4.3, wherein it was shown that if the ongoing rise of global sea level were caused in significant part by the melting of ice from either Greenland or Antarctica, so that the observed $\dot{J}_2$ (or, equivalently, the nontidal acceleration of rotation) was significantly contaminated by this influence, then our inference of the depth dependence of mantle viscosity based upon the GIA data would be modified. Formal analyses reviewed therein showed that when reasonable estimates of this contamination were removed from the observed signal and the totality of the data was once again inverted, the effect on viscosity was such as to generate a new family of viscosity models, labeled VM3, in which the viscosity of the deepest mantle was further increased, the structure in the upper part of the lower mantle and in the upper mantle and transition zone remaining pinned by relative sea level related observations. In this discussion, as in previous publications that have described the results of such analysis [*Peltier and Jiang*, 1996b, 1997; *Peltier*, 1996a, 1998b], no attempt was made to determine whether or not the VM3 class of models was simultaneously able to reconcile the observed speed and direction of polar wander. Unlike the $\dot{J}_2$ observation, which is similarly influenced by equivalently intense rates of melting from Greenland and Antarctica, the polar wander speed and direction observations are highly sensitive to the geographical location of the meltwater source. This implies, in accord with the initial suggestion of *Peltier* [1988], that the rotational data might actually be of considerable use in identifying the most plausible locations from which meltwater could be entering the oceans.

In order to attempt to close this circle, a series of calculations has been performed using the highest-viscosity contrast model VM3, which was inferred on the basis of an inversion in which only the $\dot{J}_2$ rotational datum was employed, along with the sea level related information, and it was assumed that this datum was contaminated by the influence of a rate of polar ice sheet melting corresponding to a rate of global sea level rise of 1.5 mm yr^{-1}. This was based upon the notion that of the total observed rate of global sea level rise near 2.0 mm yr^{-1}, it is conventionally assumed that 0.5 mm yr^{-1} is due to the influence of thermal expansion [*IPCC*, 1996]. Of the remaining 1.5 mm yr^{-1} we will herein assume that a fraction varying between 0.5 and 0.8 mm yr^{-1} is due to the ongoing melting of small ice sheets and glaciers in the geographic locations identified by *Meier* [1984] as perhaps contributing in an important way to the observed signal in global sea level. Given an assumed fixed contribution from Meier's sources, determined simply by scaling his tabulated rates as by *Peltier* [1988] and assuming the ICE-4G (VM3) model of the GIA contribution, I have then investigated a series of scenarios in which the residual rate of sea level rise is partitioned among Greenland, East Antarctica, and West Antarctica.

Figure 46 shows a sequence of depictions of matrices of values of polar wander speed (diagonally cross-hatched between the limits $0.81°/10^6$ years $\leq \dot{PW} \leq 1.11°/10^6$ years), $\dot{J}_2$ (shaded within the observational limits $-3.5 \times 10^{-11}\ \text{yr}^{-1} \leq \dot{J}_2 \leq -2 \times 10^{-11}\ \text{yr}^{-1}$) and polar wander direction (horizontally cross-hatched between the limits $-81/\text{deg} \leq$ PW direction $\leq -71°$) as a function of the assumed rate of melting of Greenland ice and West Antarctic ice, the contribution from East Antarctica then being determined by the requirement that the total sum to one of a number of plausible values when the fixed contribution from *Meier*'s [1984] sources is also included. Two sets of four such matrices are shown, the second set being shown in Figure 47, for two different assumptions as to the contribution from Meier's sources. Within each matrix a set of intersection

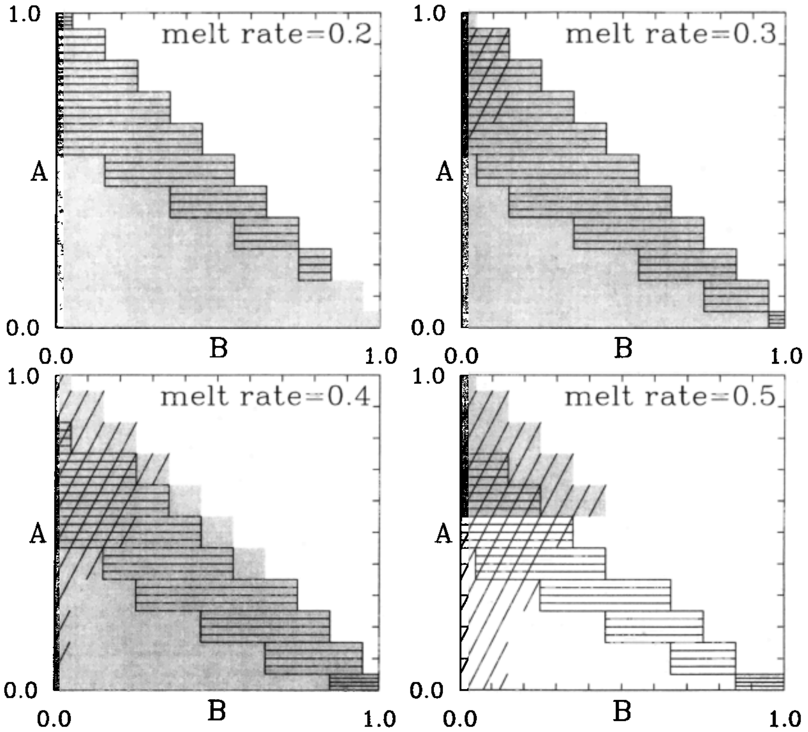

Figure 46. Polar ice sheet meltwater plane with axes A and B in which is shown the region of the plane within which it is possible to fit (1) the observed speed of polar wander, the stippled region, (2) the observed direction of polar wander, the cross-hatched region, and (3) the observed value of J_2, the horizontally hatched region. Also denoted by the solid contour is the region within which all three data are fit to within a generous 20% error with the ICE-4G (VM3) model plus the indicated additional forcing due to the melting of land ice. For each rotational observable the total response R is computed on the basis of the sum: R = ICE-4G (VM3) + Meier (0.5, 0.8) + melt rate [A · GR + B · WA + C · EAA]. In this expression the term Meier consists of the net forcing from the melting of small ice sheets and glaciers documented by *Meier* [1984] and compiled by *Peltier* [1988]. The factor melt rate is the total rate of eustatic sea level rise produced by the melting of Greenland (G), West Antarctica (WA), and East Antarctica (EAA) ice. Clearly, C = 1-*A*-*B*. In constructing these meltwater plane diagrams I have made the choice Meier = 0.5 mm yr^{-1}. The meltwater planes for the case Meier = 0.8 mm yr^{-1} (corresponding to his upper bound) are shown in Figure 47.

will be apparent, constructed on the basis of the above mentioned and extremely liberal assumptions as to the errors to which the rotation observations may be subject, in which we suppose that an acceptable combined solution must be found. Inspection of Figure 46 will show that fully acceptable solutions in terms of the VM3 viscosity model do exist but only for highly restricted combinations of geographical source regions. This is further reinforced by Figure 47, which shows the results of a similar analysis in which Meier's sources are assumed to contribute 0.8 mm yr^{-1} to global sea level rise. If a significant contribution to global sea level rise is provided by the melting of polar ice sheets, these analyses taken together suggest that the geographical region in which this is most easily accommodated is Greenland. All acceptable solutions that I have been able to discover are characterized by the occurrence of little or no net melting deriving at present from either West Antarctica or East Antarctica. Taken in their totality, these results suggest that a much larger fraction of the present-day observed rate of sea level rise may be due to the influence of thermal expansion of the oceans than is currently assumed (the conventional number of 0.5 mm yr^{-1} having been discussed most recently by *IPCC* [1996]).

5.5. Orbital Insolation Change and the Ice Age Cycle

I have previously made reference in section 1 in this article to the fact that the ice age cycle of the late Pleistocene epoch is now generally believed to have developed as a response to variations in effective solar insolation caused by slow variations in the geometry of the Earth's orbit around the Sun. This is, of course, the orbital theory of the ice ages that is usually attributed to the Serbian scientist M. Milankovitch. Although this theory was rather widely considered to be disreputable until the mid-1970s, this view was radically altered with publication of the paper by *Hays et al.* [1976]. Their spectral analyses of oxygen isotopic data ($\delta^{18}O$) from deep-sea sedimentary cores, which *Shackleton* [1967] had shown to be a primary proxy for continental ice volume, demonstrated that ice volume varied signifi-

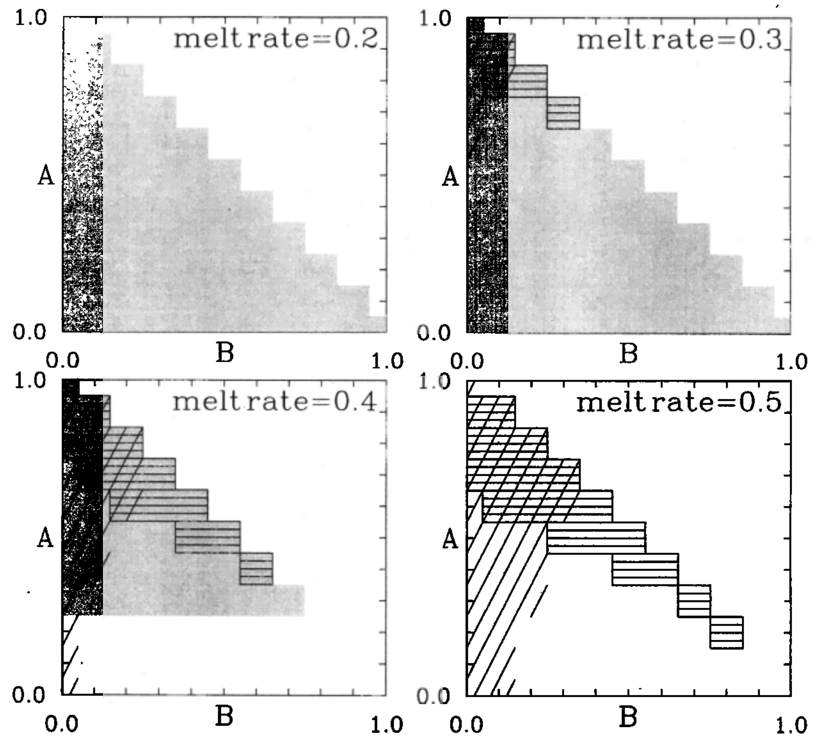

Figure 47. Same as Figure 46 except for the case Meier = 0.8 mm yr^{-1}.

cantly on all of the timescales of orbital eccentricity (100 kyr), *orbital obliquity* (41 kyr), and *planetary precession* (21 kyr) which were precisely those produced by the action of many-body effects in the solar system. As I discuss in section 6, this idea now forms the basis for most of the models that have been constructed to understand the origin of the 100-kyr ice age cycle itself. Of interest to us here, however, is the question as to how strong the feedback could be of the ice age cycle upon Earth's orbit around the Sun and thus on received insolation. Clearly, if this feedback were strong, the problem of constructing a model of the 100-kyr oscillation would be daunting indeed.

Prior to the appearance of the paper by *Thompson* [1990], there had been no suggestion in the literature that any such effect would be sufficient to warrant any attention at all. Thompson's idea was that variations in the precession parameter H, which is clearly connected to J_2 and which is also referred to as the dynamic ellipticity, caused by the ice age cycle of polar glaciation and deglaciation, could have caused significant changes in the precession rate thus causing important variations in the insolation changes that are supposed to be ultimately responsible for the ice ages themselves. Current models of the long-term variations in the orbital and precessional parameters have all been based upon the assumption that the Earth could be treated as a rigid body for the purpose of orbital reconstruction. *Laskar et al.* [1993], however, demonstrated that owing to gravitational perturbations caused by Jupiter and Saturn, both the obliquity and precession rate of the Earth are very sensitive to changes in the dynamic ellipticity, such that a diminution of slightly more than 0.2% in the precession constant could drive the precession at resonance and thereby lead to incommensurately large changes in the obliquity and precession rate. Their analysis clearly indicates that the accurate calculation of orbital and precessional parameters for the Earth depends upon the availability of sufficiently accurate models of changes in the dynamic ellipticity. If the impact of the glaciation cycle upon dynamic ellipticity were sufficiently large, then the currently employed time series for the orbital parameters [*Laskar*, 1988; *Quinn et al.*, 1991] could be significantly in error, thus compromising both the calculations of orbital insolation change and the timescales deduced by orbital tuning of the $\delta^{18}O$ records in deep-sea sedimentary cores. Although this might be considered unlikely based upon the success recently achieved by *Shackleton et al.* [1990] in orbitally tuning the timescale for ODP Core 677 from the Panama Basin, rigorous analysis is clearly required. In suggesting that this effect is unlikely to be important on these a priori grounds, we are then relying upon the fact that an accurate prediction of a revised age for the Brunhes-Matuyama magnetic reversal was made by *Shackleton et al.* [1990] based upon their use of the conventionally accepted orbital insolation time series of *Berger* [1978] to determine the depth-to-time conversion appropriate for this very high resolution record of late *Pleistocene* climate system variability. If the insolation time series were significantly in error, it is highly unlikely that the 7% error predicted in the conventionally accepted age of the

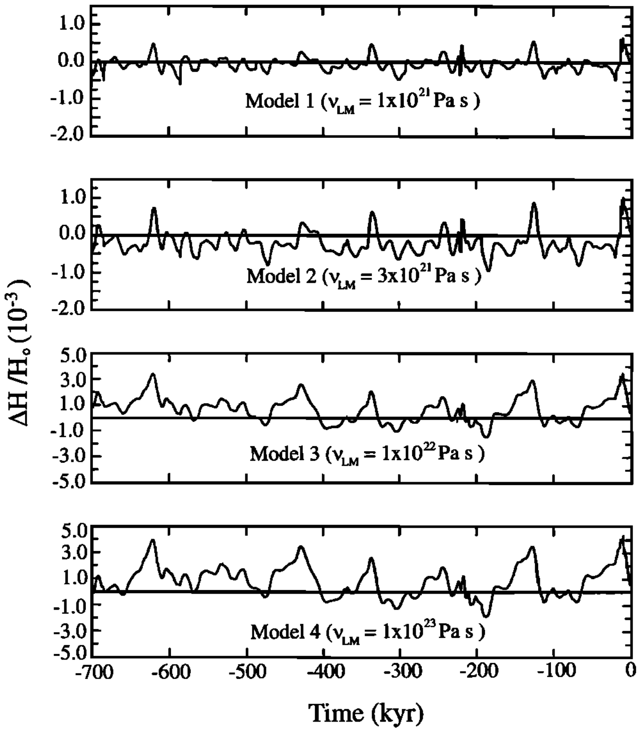

Figure 48. The relative variations in the dynamic ellipticity of the Earth $\Delta H(t)/H_0$ for four different viscoelastic Earth models; ν_{LM} is the viscosity of the lower mantle in these models, in which the viscosity of the upper mantle has been held fixed to $\nu_{\mathrm{UM}} = 1.0 \times 10^{21}$ Pa s.

Brunhes-Matuyama reversal, subsequently verified using precision $\mathrm{Ar}^{39}/\mathrm{Ar}^{40}$ dating [*Baksi*, 1992], would have been possible.

In order to accurately predict the impact on precession and obliquity due to the ice age cycle and thus to assess the modifications to the usually assumed orbital insolation time series that represents the external forcing applied to the climate system, we require a model of the impact of the ice age cycle upon the dynamic ellipticity of the planet. For a triaxial model of the planet this parameter, usually designated H, is defined as

$$H = \frac{2J_{33} - (J_{11} + J_{22})}{2J_{33}}, \tag{26}$$

in which J_{33} is the principal moment of inertia with respect to the axis of rotation and J_{11} and J_{22} are the two equatorial moments. H is clearly time-dependent since all three of these moments of inertia (see equation (12)) are changed by mass redistribution both on and within the Earth associated with the glaciation-deglaciation process. The present-day value of H may be determined from astronomical observations of the precession effect, and the recommended value in the International Astronomical Union (IAU) nutation model [*Seidelman*, 1982] is 1/305.43738. If the departure of the three principal moments from their equilibrium values is small, then changes in the off-diagonal elements of the inertial tensor make no significant contribution to changes in the diagonal moments in a theory accurate to the first order in inertia perturbations. To calculate the variations in H, we therefore require only the changes of the three principal moments, J_{jj} (as in equation (12)). Substitution of (12) into (26) and retaining only first-order terms then leads to the following expression for the perturbation to H:

$$\Delta H(t) = \frac{2I_{33} - I_{11} - I_{22}}{2C} - \frac{H_0 I_{33}}{C} \tag{27}$$

in which H_0 and C are the present-day observed values of H and J_{33}, respectively. The first term on the right-hand side of (27) dominates since H_0 is small.

For a viscoelastic Earth the total perturbations of the moments of inertia consist of the direct effects of mass redistribution associated with the surface load and the indirect effects due to the deformation of the underlying planet. *Peltier* [1982] and *Wu and Peltier* [1984] have shown that the combination of these two effects may be expressed as

$$I_{jj}(t) = [1 + k_2^L(t)] * I_{jj}^R(t) \tag{28}$$

in which the $I_{jj}^R(t)$ are the perturbations of the three principle moments of inertia due to the direct effect of

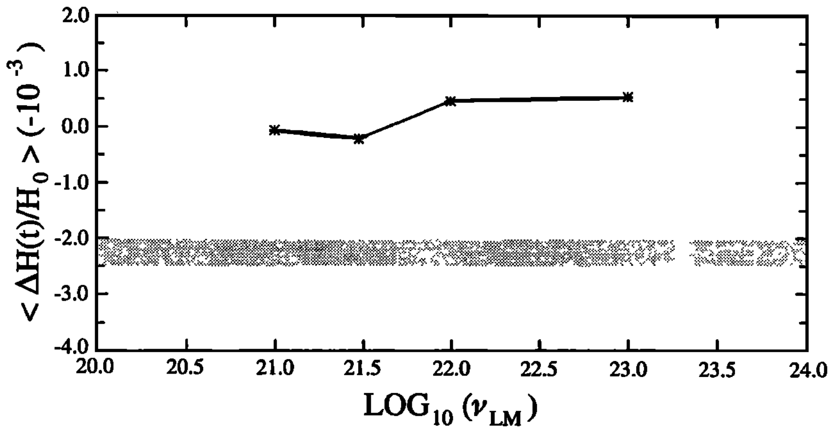

Figure 49. The average relative changes in $\Delta H(t)/H_0$ over the period from 780 kyr ago to the present day for the series of models of $\Delta H(t)/H_0$ shown on Figure 48. The shaded area illustrates the range of $\langle \Delta H(t)/H_0 \rangle$ in which the resonance occurs due to the gravitational perturbations of Jupiter and Saturn.

the change in surface load, assuming that the Earth was perfectly rigid. Time series for I_{33}^R and for the off-diagonal components I_{13}^R and I_{23}^R were shown on Figure 29. In (28) the asterisk denotes the operation of time domain convolution, whereas $k_2^L(t)$ is the time domain surface load Love number defined in (9b). Using the ICE-4G model of the deglaciation history from LGM to present and the SPECMAP δ^{18}O record to extend this record back into the past, as previously, we then obtain the required $I_{jj}^R(t)$ time series. Following the detailed procedures recently described by *Jiang and Peltier* [1996] to evaluate (28), we then obtain the time series for $\Delta H(t)/H_0$ shown on Figure 48 for four different models of the radial variation of mantle viscosity. The viscosity models 1–4 in this sequence are simple two-layer models with upper mantle and transition zone viscosity fixed to the value 1×10^{21} Pa s and with lower mantle viscosities increasing through the sequence 1×10^{21} Pa s, 3×10^{21} Pa s, 1×10^{22} Pa s, and 1×10^{23} Pa s. The elastic structure of these models is fixed to PREM and the lithospheric thickness is held fixed to 120.6 km.

Inspection of the results obtained in this sequence of analyses demonstrates that the maximum negative excursion from H_0 is ~0.1% if ν_{LM} has a value near 3×10^{21} Pa s, as is in rough accord with the results discussed in section 4.1 obtained on the basis of formal inversion of the GIA data set. Even in the limit in which the viscosity of the lower mantle is fixed to the highest value, which is entirely discordant with the requirements of the GIA data, the maximum reduction in the dynamic ellipticity that is ever realized during the SPECMAP period is 0.2%. Equally important to the magnitude of the fluctuations $\Delta H(t)/H_0$ is the magnitude of the temporally averaged value of $H(t)$ over the SPECMAP period since this represents the secular change of the Earth's shape induced by the glaciation-deglaciation process. Figure 49 shows the average relative change $\langle \Delta H(t)/H_0 \rangle$ over the SPECMAP period as a function of the viscosity of the lower mantle. The shaded region of Figure 49 denotes the relative change in dynamic ellipticity for which *Laskar*'s [1988] prediction of the resonant excitation of the precession rate should take place. Examination of these results clearly establishes the fact that the ice age cycle is far too weak in forcing strength to induce this resonance. Complete analyses of the impact of these variations on the gravitational n-body problem of *Jiang and Peltier* [1996] demonstrate rather conclusively that the orbital time series based upon the assumption of a rigid Earth of *Laskar* [1988] and *Quinn et al.* [1991] are entirely adequate for use in the evaluation of the climatological forcing function to which the planet has been subject through Pleistocene time. There do exist rather appreciable errors in the results of *Berger* [1978], however, as one moves back in time beyond about 10^6 years ago. These become important in analyses such as that by *Lourens et al.* [1996], in which astronomical tuning is extended back through Pliocene time, in which case the more accurate analyses of Laskar must be employed in place of the Berger results. It is important to recognize that the analyses of Lourens et al. agree fully with the results of *Peltier and Jiang* [1994] and *Jiang and Peltier* [1996] in strongly suggesting that no significant deviation from the H = const solution of Laskar has occurred for at least the last 5 Myr.

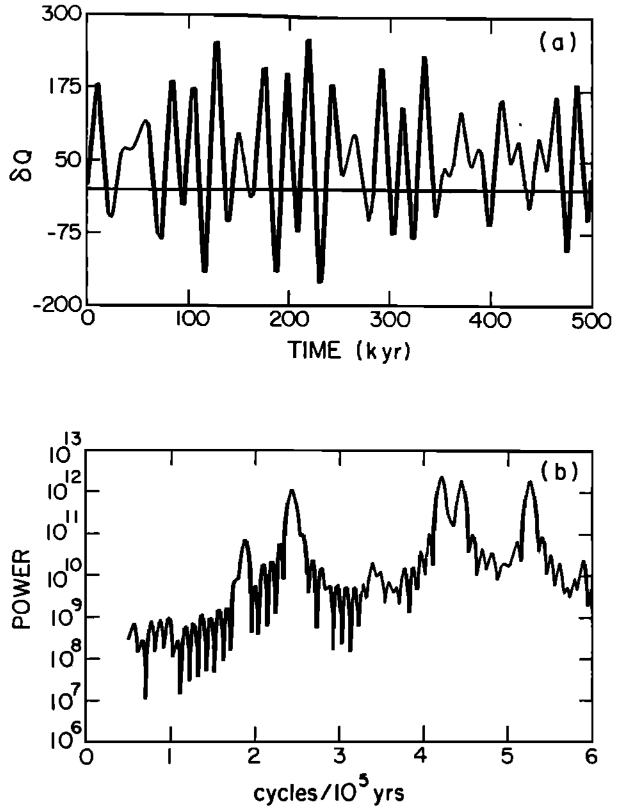

Figure 50. (a) Summertime seasonal insolation anomaly at 65°N latitude over the last 500 kyr and (b) the power spectrum of this synthetic insolation anomaly time series.

6. THEORIES OF ICE AGE OCCURRENCE: A STATUS REPORT

In sections 4 and 5 I focused successively on two sets of interlinked issues concerned with what can be learned about the Earth's deep interior based upon analyses of the response to the late Pleistocene ice age cycle and with what can be learned regarding climate system dynamics on the basis of the same observations. An important and, I will argue, closely connected issue, concerns the question as to what role the response of the solid Earth may play in the 100-kyr climate cycle of the ice age itself.

Although it has been quite clear since the previously referenced analysis of *Hays et al.* [1976] that orbitally induced variations in the effective solar insolation reaching the Earth are deeply implicated in the variations of continental ice volume that are inferred to have occurred during the Pleistocene epoch, it is equally clear

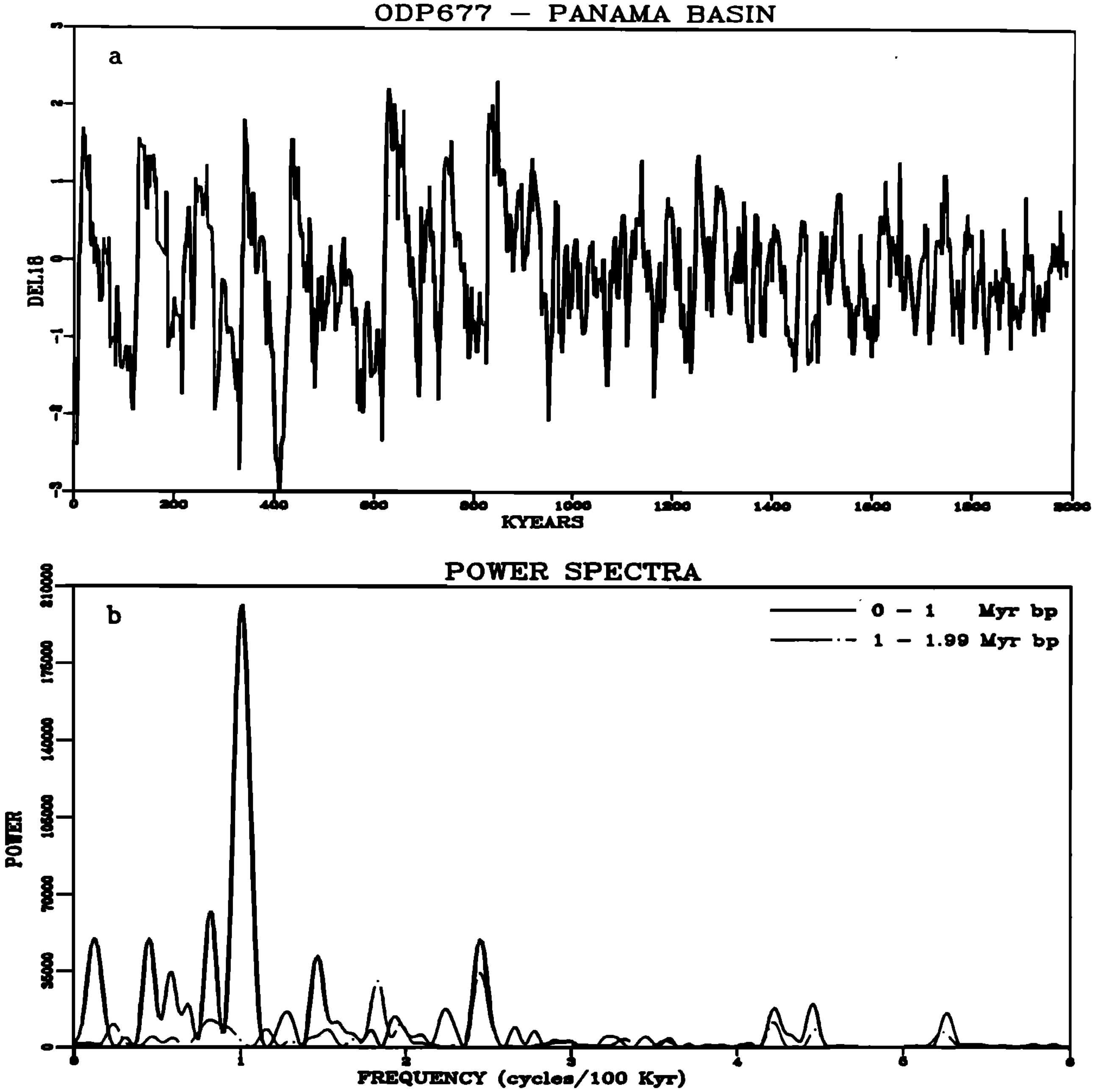

Figure 51. (a) The record of $\delta^{18}O$ as a function of time from ODP Site 677 in the Panama Basin with timescale developed on the basis of orbital tuning [*Shackleton et al.*, 1990]. Clearly evident is the mid-Pleistocene climate transition that occurred near 10^6 years B.P. Prior to the transition the series shows no evidence of any 10^5 year cycle, while after the transition has occurred, the record is dominated by the 10^5 year cycle. (b) Power spectra for the two 10^6 year segments of the record. The four prominent spectral peaks at frequencies higher than one cycle per 10^5 years are those due to the variation of orbital obliquity (41 kyr period), and the triplet of lines in the eccentricity-precession band with period of 19 kyr, 21 kyr, and 23 kyr.

that the response of the climate system to this forcing is intensely nonlinear. This will be apparent on the basis of the data shown in Figures 50 and 51. Figure 50a shows a time series of the summertime seasonal insolation anomaly at 65°N latitude over the most recent 500 kyr of Earth's history. Figure 50b shows the power spectrum of this time series, inspection of which will demonstrate that there is essentially no power in this forcing function at the period of 100 kyr. Rather, the time series is dominated by sharp spectral lines at the 41 kyr period of the variation in orbital obliquity (ε) and at 19, 21, and 23 kyr that are produced by the eccentricity "splitting" of the precessional "singlet." The latter triplet of spectral lines may best be understood on the basis of the expression for the summertime seasonal insolation anomaly of Milankovitch, which has the explicit form

$$\delta Q = A\varepsilon(t) + Be(t)(\cos \omega_p t) \tag{29}$$

in which $\varepsilon(t)$ is the orbital obliquity, $e(t)$ is the orbital eccentricity and ω_p is the precession frequency. Because $e(t)$ is dominated by a temporal oscillation at a period of 100 kyr, it constitutes a low-frequency modulation of the influence on insolation of the higher-frequency precessional oscillation which has a dominant period of 21 kyr. Clearly, the Fourier expansion of the second term in (29) will include spectral lines at the usual sum and difference frequencies as well as at the precession frequency itself, thus explaining the reason for the split singlet.

Figure 51a shows the δ^{18}O time series from ODP Core 677 that was employed by *Shackleton et al.* [1990] to redefine the timescale of the Pleistocene period. Figure 51b shows power spectra for both the first and second million years of this record of climate variability through the entire Pleistocene period of 2 Myr. Inspection of the power spectra demonstrates that although the earliest segment of this orbitally tuned record contains only those spectral lines expected to exist if the ice volume response to the forcing function (29) were linear, the most recent segment of the record is dominated by the variations associated with the 100 kyr ice age cycle. Given the power spectrum of the forcing shown in Figure 50b, it will be clear why the theory developed by Milankovitch to explain the ice ages has come to be seen as being unsatisfactory in detail. Recognition of the challenge posed by this circumstance has led to the suggestion of a large number of, sometimes rather exotic, theories that do not invoke the "Milankovitch effect" at all in attempting to explain the 100-kyr cycle. A good example of suggestions of this kind from the recent literature is that by *Müller and MacDonald* [1995], who argue that the 100-kyr cycle is most probably a direct response to the forcing at this period which they believe should arise due to 100-kyr periodic crossings by the Earth of the invariable plane of the solar system. Their idea is that the "dust" in this plane [*Sykes et al.*, 1989] will cause a sharp reduction of the radiative forcing to which the planet is subject during the epochs of crossing. A possible flaw in this suggestion is that there is no guarantee that the dust vail in the invariable plane is sufficiently dense to cause any appreciable radiative effect at all.

A more reasonable explanation for the existence of the 100-kyr ice age cycle, in my view, given that orbital insolation change is so strongly implicated in variations of the δ^{18}O proxy for continental ice volume, is that the response of the climate system to orbital forcing is not linear. In a nonlinear system it is quite conceivable, even very likely, that the eccentricity modulation of the precessional effect (the second term in equation (29)) at the period of 100 kyr would be made prominent in the response. In order to investigate this possibility, there have been a number of attempts to design explicit models of the climate system capable of being integrated for the very long timescales required. In what follows, I will review analyses that have been performed over the past several years using a model whose initial form was developed by *Deblonde and Peltier* [1991a, b], *Deblonde et al.* [1992], and *Deblonde and Peltier* [1993] based upon earlier ideas presented by *Peltier* [1982]. The model of Deblonde and Peltier has recently been further developed by *Peltier and Marshall* [1995] and *Tarasov and Peltier* [1997a, b, 1998]. The latter analyses are, in fact, the first to have produced an acceptably accurate simulation of the 100-kyr cycle that has not required the introduction of any ad hoc nonlinear feedback mechanisms that are not widely understood and well constrained by observations.

This model consists of two primary ingredients: a model of the atmosphere and the forcing to which it is subject because of the variations of effective solar insolation due to the changing geometry of Earth's orbit around the Sun, and a model of the accumulation and flow of ice on the solid surface of the planet that incorporates the influence of the isostatic adjustment of the Earth under the weight of the ice. As we will see, the feedback of glacial isostatic adjustment onto the ice age cycle may be extremely important. The atmospheric climate model component of the coupled structure is taken to be adequately represented by a modified version of the energy balance model of *North et al.* [1983] as

$$C(\mathbf{r})\,\frac{\partial T}{\partial t} = \left\{\frac{Q}{4}\,a(\mathbf{r}, t)S(\theta, t) + \mathrm{NAHF}(\mathbf{r}, t)\right\} - \{A + BT(\mathbf{r}, t) - \boldsymbol{\nabla}_h[D(\theta)\boldsymbol{\nabla}_h T(\mathbf{r}, t)]\} \tag{30}$$

in which the North Atlantic heat flux due to the deep-water formation process is NAHF, the sea level temperature is $T(\mathbf{r}, t)$, the surface heat capacity employed to distinguish land from sea and ice is $C(\mathbf{r})$, and the two terms on the right-hand side are the energy input to and output from a particular atmospheric column, respectively. The former of these terms is composed of the solar short wave illumination with solar constant Q (1360 W m^{-2}), coalbedo $a(\mathbf{r}, t)$, and solar distribution function $S/4$, with time-dependent orbital parameters to be computed following *Berger* [1978] over the most recent 100-kyr cycle, on the simulation of which I will focus entirely below. The remaining terms on the right-hand side of (30) consist of (a linear approximation to) the infrared emission to space ($A + BT$) and a diffusive parameterization to the heat flux divergence associated with baroclinic eddies in the atmosphere.

The second component of the coupled structure is that for ice accumulation and flow, and this also takes the form of a nonlinear diffusion equation for ice thickness H, namely,

$$\frac{\partial H}{\partial t} = \boldsymbol{\nabla}_h[2A(T)(\rho_I g)^m H^{m+2}(\boldsymbol{\nabla}_h h \cdot \boldsymbol{\nabla}_h h)^{(m-1)/2}\boldsymbol{\nabla}_h h] + G(\mathbf{r}, t) \tag{31}$$

in which $A(T)$ is a temperature-dependent flow parameter which is determined by the rheological law that ice deformation is assumed to obey, ρ_I is the density of ice as before, h is the local height of the ice sheet above sea level, and $G(\mathbf{r}, t)$ is the mass balance. The latter function is positive over the portion of the ice sheet that realizes net accumulation and negative in the ablation zones. I will first illustrate results obtained by the direct integration of the model consisting of (30) and (31) in which the vertically integrated horizontal component of ice velocity $\mathbf{V}$ has the following relation [*Nye*, 1959] to the basal shear stress σ_b:

$$\mathbf{V} = B|\sigma_b|^{m-1}\sigma_b \tag{32}$$

rather than that appropriate for the more traditional Glen flow law [e.g., *Paterson*, 1994], that is the basis of (31) and for which

$$\mathbf{V} = B'H|\sigma_b|^{m-1}\sigma_b. \tag{33}$$

The two nonlinear diffusion equations (30) and (31) are strongly coupled by the influence of surface elevation on temperature, an important contribution to which occurs as a consequence of the isostatic adjustment process. For present purposes, I will focus on models in which the latter process is described by the assumption of a simple local damped return to isostatic equilibrium of the form

$$\frac{dh'}{dt} = -\frac{h' - h_0'}{\tau} + \frac{\rho_I}{\rho_M}\frac{H}{\tau} \tag{34}$$

in which $h'(\mathbf{r}, t)$ is the bedrock response to the surface load of thickness H, h_0' is the present day bedrock elevation above sea level, $\tau = 4$ kyr is the single relaxation time that is assumed to control the isostatic adjustment process, and ρ_M is the mean density of the solid Earth whose surface is deflected by the weight of the ice. The $\tau = 4$ kyr choice for the bedrock relaxation time is consistent with the Monte Carlo fits to rsl curves from ice-covered sites previously discussed; it is, in fact, near the average of the value of the relaxation time in southeast Hudson Bay of 3.4 kyr and that at Angerman River of 4.2 kyr.

As recently discussed by *Tarasov and Peltier* [1997a, b], the system consisting of (30), (31), and (34) may be simultaneously integrated to determine the response of the cryosphere to orbital insolation variations. Subtleties in the implementation of this model, including the use of (30) in perturbative mode to determine only the perturbation away from an observational climatology, the way in which the mass balance $G(\mathbf{r}, t)$ is evaluated using the positive degree day (PDD) formalism, the manner in which the term NAHF in (30) is modulated in order to introduce the influence of atmospheric heating due to the North Atlantic Deep Water formation process, and the way in which the infrared emission term $A + BT$ is modified to account for the changing atmospheric concentration of carbon dioxide that accompanies the ice age cycle, are all discussed in detail by *Tarasov and Peltier* [1997a, b]. My purpose here will first be to illustrate the extent to which models of this kind have recently been shown to provide an acceptable explanation of the 100-kyr cycle.

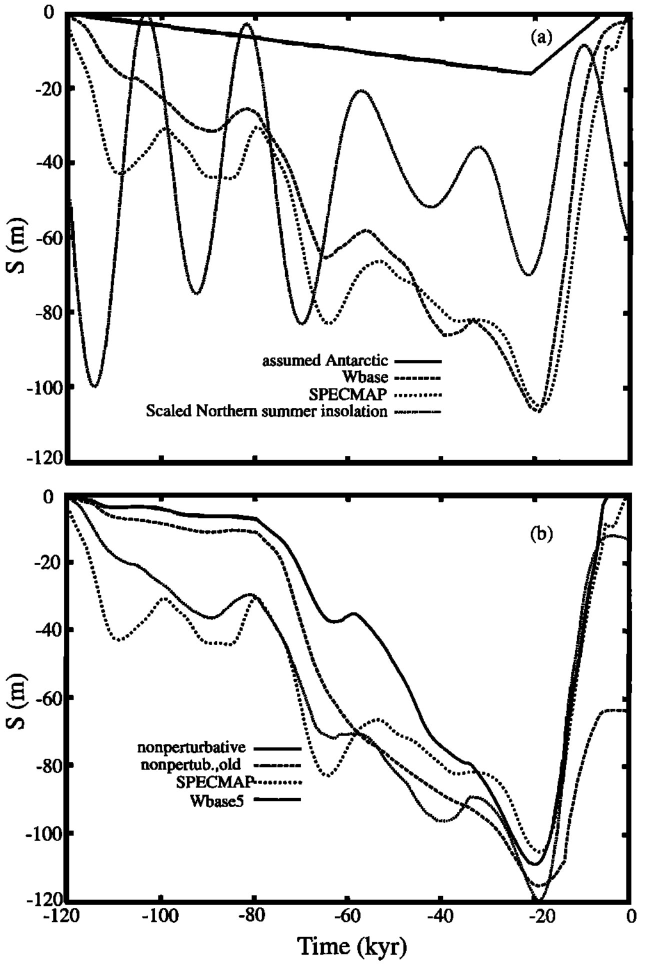

Figure 52. Model-predicted histories of eustatic sea level change over the last ice cycle. (a) An assumed Antarctic contribution of 16 m at −21 kyr. The curve labeled SPECMAP is the SPECMAP δ^{18}O time series [*Imbrie et al.*, 1984] scaled to a particular LGM ice volume. Wbase is the time series predicted by the control model with 0.5° spatial resolution and an assumed temperature lapse rate of 7.5°K km^{-1}. Also shown for reference is a summertime seasonal insolation time series (July at 65°N latitude) rescaled to sea level. (b) Wbase 5, which is as Wbase except for a modification of the PDD scheme used to compute ablation (see *Tarasov and Peltier* [1997a] for details). The curve denoted "nonperturbative" uses updated mass balance parameterizations, input topography, and input precipitation fields, but it does not correct the energy balance model (EBM) output with reanalysis climatology. The curve labeled "nonperturb., old", is the result obtained by *Peltier and Marshall* [1995] with 1° resolution, reduced precipitation, and reduced flow parameter and which fails to deliver the observed termination. See *Tarasov and Peltier* [1997a] for details.

Figure 52a shows a comparison of the global response of the isothermal version of this model to the applied insolation forcing in the form of a synthetic global history of sea level change, called Wbase. The model prediction is compared with the SPECMAP $\delta^{18}O$ sea level proxy, with the northern hemisphere summer insolation, and with the assumed contribution to the global sea level signal derived from the melting of Antarctic ice (not explicitly modeled). It will be clear that the model very nicely predicts the sawtooth-shaped form of the 100-kyr sea level cycle with a glaciation phase lasting ~90 kyr years and a deglaciation phase lasting ~10 kyr. Further variations on this calculation are presented on Figure 52b and are described in the figure caption.

When the model embodied in (30), (31), and (34) is augmented by simultaneously solving the following evolution equation for the temperature field within the ice sheet itself,

$$\rho_i C(T)\frac{\partial T}{\partial t} = \frac{\partial}{\partial z}\left(k(T)\frac{\partial T}{\partial z}\right) - \rho_i C(T)\mathbf{V}\cdot\nabla T + Q_a + Q_s \qquad (35)$$

then we are able to directly address the extent to which the geophysical inference of LGM ice sheet form shown previously for the Laurentide on Figure 38 is rational from a glaciological perspective. This requires the specification of appropriate temperature boundary conditions which we may take specifically to be

$$T_{\text{ice}}(z = h) = T_{\text{climate}}(z = h) \qquad (36a)$$

$$k(T)\partial_z T(o) = G_f(\theta, \phi) \qquad (36b)$$

in which G_f is a longitude- (ϕ) and latitude- (θ) dependent map of geothermal heat flux (I employ that of *Pollack et al.* [1993]) and T_{climate} is the surface temperature obtained from the solution of (30). In (35), Q_a and Q_b are the heating due to internal friction within the ice itself and that due to sliding at the base, respectively. Also required is an explicit choice for the rheology of ice, all of the possibilities for which are encompassed by the general form

$$\dot{\varepsilon} = fA\frac{\sigma^n}{d^p}\exp\left[-\frac{Q}{RT^\#}\right] \qquad (37)$$

in which $\dot{\varepsilon}$ is the strain rate, A is a material parameter, σ is differential stress, d is grain size, Q is activation energy for creep, R is the gas constant, and $T^\#$ is absolute temperature corrected for the pressure melting point. The conventional Glen flow law corresponds to the case $p = 0$ and $n \simeq 3$; f is a factor that is unity for clean ice in the laboratory. Modern ice mechanical analyses [*Paterson*, 1994] based upon the Glen flow law usually assume $(A, Q) = (1.14 \times 10^{-5}\ \text{Pa}^{-3}\ \text{yr}^{-1}$, 60 kJ $\text{mol}^{-1})$ for $T^\# < 263.15°\text{K}$ and $(A, Q) = (5.47 \times 10^{10}\ \text{Pa}^{-3}\ \text{yr}^{-1}$, 139 kJ $\text{mol}^{-1})$ for $T^\# > 263.15°\text{K}$. Very recently, however, *Goldsby and Kohlstedt* [1997a, b] and *Goldsby* [1997] have suggested that this conventional flow law may not be the most appropriate rheology with which to describe the flow of large ice sheets under the action of the gravitational force. They demonstrate that the mechanism of dislocation creep that underlies the Glen law is replaced by the grain boundary sliding (GBS) mechanism at low stress levels. This mechanism is characterized by $n = 1.7$ and $p = 1.4$ and has $(A, Q) = (3.9 \times 10^{-3}\ \text{MPa}^{-1.7}\ \text{s}^{-1}\ \text{m}^{1.4}$, 49 kJ $\text{mol}^{-1})$ for $T^\# < 257°\text{K}$ and $(A, Q) = (5.19 \times 10^{27}\ \text{MPa}^{-1.7}\ \text{s}^{-1}\ \text{m}^{1.4}$, 197 kJ $\text{mol}^{-1})$ for $T^\# = 257°\text{K}$. The form of the geophysically reconstructed Laurentide ice sheet is most easily explicable in terms of this new rheology.

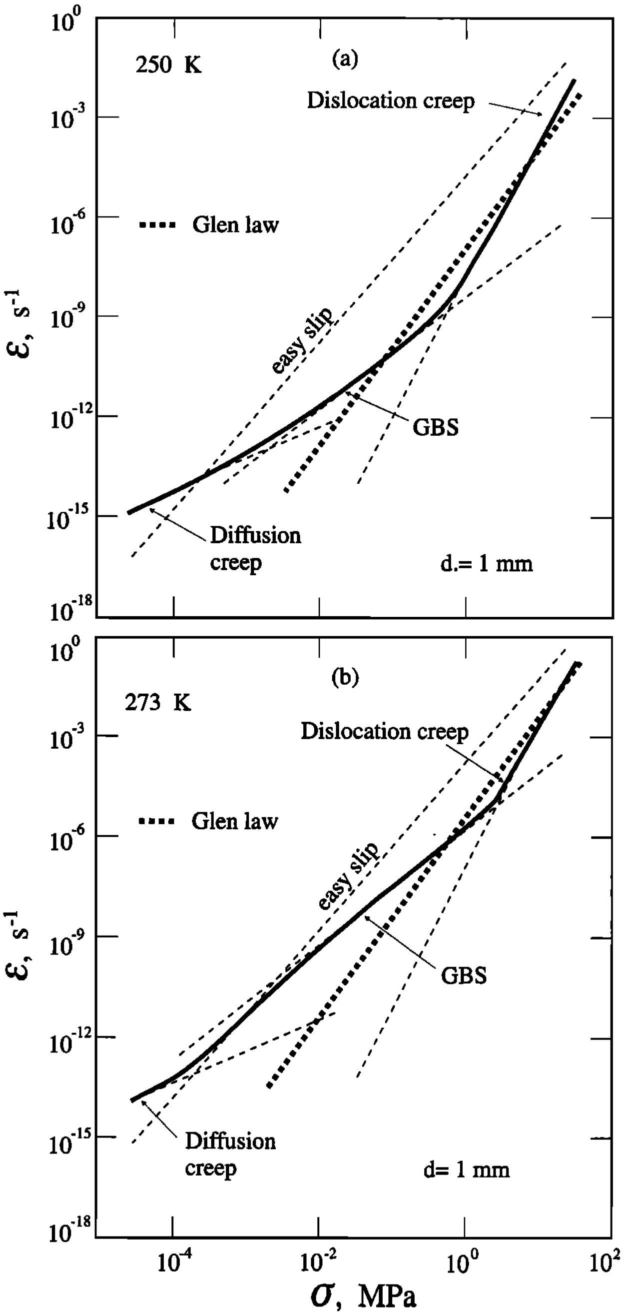

Figure 53. The rheology of coarse-grained (d = 1 mm) ice, calculated using the constitutive relation in equation (38) and the creep data from *Goldsby and Kohlstedt* [1997a] and *Wakahama* [1967] along with the diffusion creep rate, for temperatures of (a) 250°K and (b) 273°K. The dotted curve shows the predicted creep rate for the Glen flow law for comparison.

Figure 53 shows the rheology of ice at 250°K and 273°K for a grain size of 1 mm as strain rate $\dot{\varepsilon}$ versus differential stress σ. The solid curve on each frame is the variation of $\dot{\varepsilon}$ with σ calculated using a modified (composite) version of the constitutive equation of Goldsby and Kohlstedt, namely,

$$\dot{\varepsilon} = \dot{\varepsilon}_{\mathrm{diff}} + \left(\frac{1}{\dot{\varepsilon}_{\mathrm{es}}} + \frac{1}{\dot{\varepsilon}_{\mathrm{GBS}}}\right)^{-1} + \dot{\varepsilon}_{\mathrm{disl}} \qquad (38)$$

where diff denotes diffusion creep, es denotes slip on the easy (basal) slip system for single-line crystals, GBS denotes grain boundary sliding, and disl denotes true dislocation creep with stress exponent $n = 4$. The Glen flow law is indicated on Figure 53 by the heavy dotted curve. In constructing Figure 53, which D. Goldsby provided, the diffusion creep rate was estimated using the diffusion creep equation discussed by *Nabarro* [1948], *Herring* [1955], and *Coble* [1963] together with the material parameters for ice provided by *Frost and Ashby* [1982] and using an activation energy equal to that for grain boundary diffusion of 49 kJ mol^{-1} as given by *Ramseier* [1967]. The strain rate due to easy slip, which limits the creep rate of polycrystalline ice at lower stresses [*Goldsby and Kohlstedt*, 1997a] is calculated from the single-crystal data of *Wakahama* [1967].

Inspection of Figure 53 demonstrates that at the levels of differential stress typically found to characterize large ice sheets, namely, 10^{-1}–10^{-2} MPa, the creep rates delivered by GBS are typically 1–2 orders of magnitude higher than those delivered by the traditional (Glen) model. This has profound consequences. These are most easily appreciated by first employing the model embodied in (30), (31), (34), and (35) to reconstruct the modern day Greenland ice sheet. For this purpose, we may replace (35) by the synthetic climate forcing that has been inferred on the basis of oxygen isotopic measurements from Summit, Greenland, ice cores and which is now being employed as a standard in the context of the European Ice Sheet Modelling Initiative (EISMINT) collaboration [*Huybrechts et al.*, 1996]. The present-day topography of the Greenland ice sheet that we predict using the standard Glen flow law with $f = 4$ is then shown on Plate 13b, and this obviously compares exceedingly well with the observed topography shown on Plate 13a. Plate 13c shows synthetic ice volume time series predicted by the model over the last two ice age cycles. On Plate 13, the result for the conventional Glen model with $f = 4$ is compared to the result predicted for various versions of the new Goldsby and Kohlstedt rheology with $d = 1$ mm and $f = 1$ and for $f = 0.5$ and $f = 2.0$. Clearly, the result for the new rheology with $d = 1$ mm and $f = 1$ delivers an essentially identical match to the Greenland ice sheet as that provided by the conventional Glen model with $f = 4$. If we employ the recently published grain size measurements for Wisconsin ice in the Greenland core of 2.7 mm [*Thorsteinsson et al.*, 1997], then the new rheology again fits Greenland but now also requires $f = 4$ as in the fit of the conventional Glen model.

The point of these results in the present context of discussions related to the implications of observations of postglacial variations in the level of the sea is made clear in Plate 14. Plate 14a shows the predicted LGM form of the Laurentide ice sheet based upon use of the conventional Glen model but with an enhancement of the rheology by a factor of $f = 80$ which is required in order to fit the geophysically inferred aspect ratio of this ice sheet based upon the sea level data (see *Tarasov and Peltier* [1998] for a detailed discussion of this requirement). Although it has been suggested that this extreme enhancement of the rheology might be understood on the basis of the influence of basal sliding [*Clark et al.*, 1996], the enhancement is so extreme as to verge on the implausible. As it happens, and as shown explicitly in Plate 14b, when the new *Goldsby and Kohlstedt* [1997a, b] rheology is introduced into the model, the aspect ratio problem is immediately resolved. Plate 14b compares synthetic ice volume predictions made using the complete orbitally forced climate model and the new rheology with the prediction labeled T_{base} that was made using the conventional Glen model with an enhancement factor $f = 80$. The prediction made with the new rheology fits the T_{base} prediction extremely well, although some enhancement may be required to recover a sufficiently pronounced termination. Topographies of these various model predictions are shown in Plate 14c on the basis of which the previously shown Plate 9 was constructed. The use of the Goldsby and Kohlstedt rheology clearly provides a most economical explanation of the geophysically inferred aspect ratio of the Laurentide ice sheet.

An issue that is especially relevant in the context of this presentation of ideas connected to the understanding and use of postglacial variations in the level of the sea concerns the question of the role that the glacial isostatic adjustment process plays in the ice age cycle itself. This is addressed on Figure 54, which illustrates the way, in the context of the isothermal version of model, that the elimination of the isostatic adjustment process modifies the predicted glaciation-deglaciation process. Clearly, when the relaxation time that is assumed to govern this process in the "local-damped-return-to-equilibrium" representation is set to infinity, so that no isostatic adjustment occurs at all, then the model no longer predicts the dramatic termination that is probably the most pronounced feature of the cycle. This may be very easily understood by considering the processes that come into play when the ice sheets are beginning to disintegrate. Because the Earth sinks appreciably under the weight of the ice, when a large continental ice sheet retreats, it does so into the deep depression caused by the adjustment process. Because atmospheric temperature is a strongly decreasing function of height (typical lapse rates are near 7°C km^{-1}), as the ice sheet melts back into the depression, the tem-

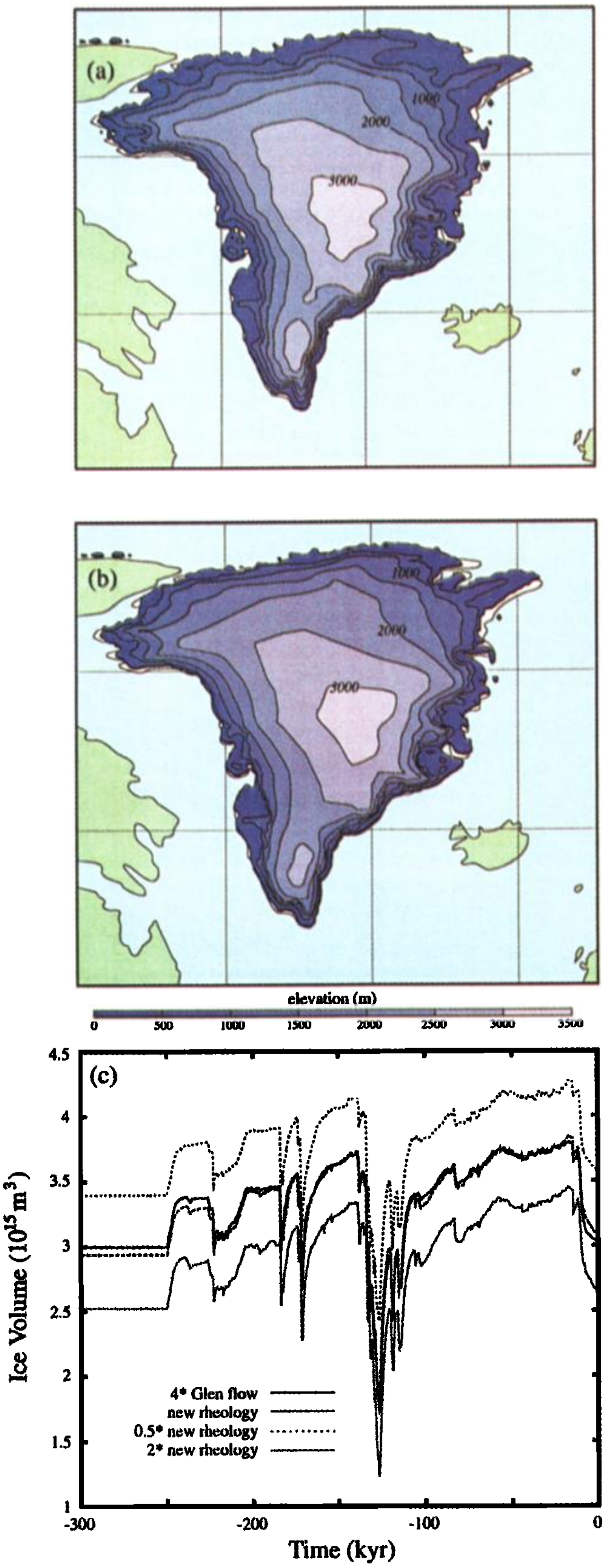

Plate 13. (a) The observed modern topography of the Greenland ice sheet. (b) The present-day topography of the Greenland ice sheet predicted on the basis of a full transient analysis in which the ice sheet is subjected to climate forcing inferred on the basis of the Summit, Greenland, ice core record. (c) Ice volume time series from a series of Greenland simulations that differ only in the rheological model assumed to represent the constitutive relation between stress and strain.

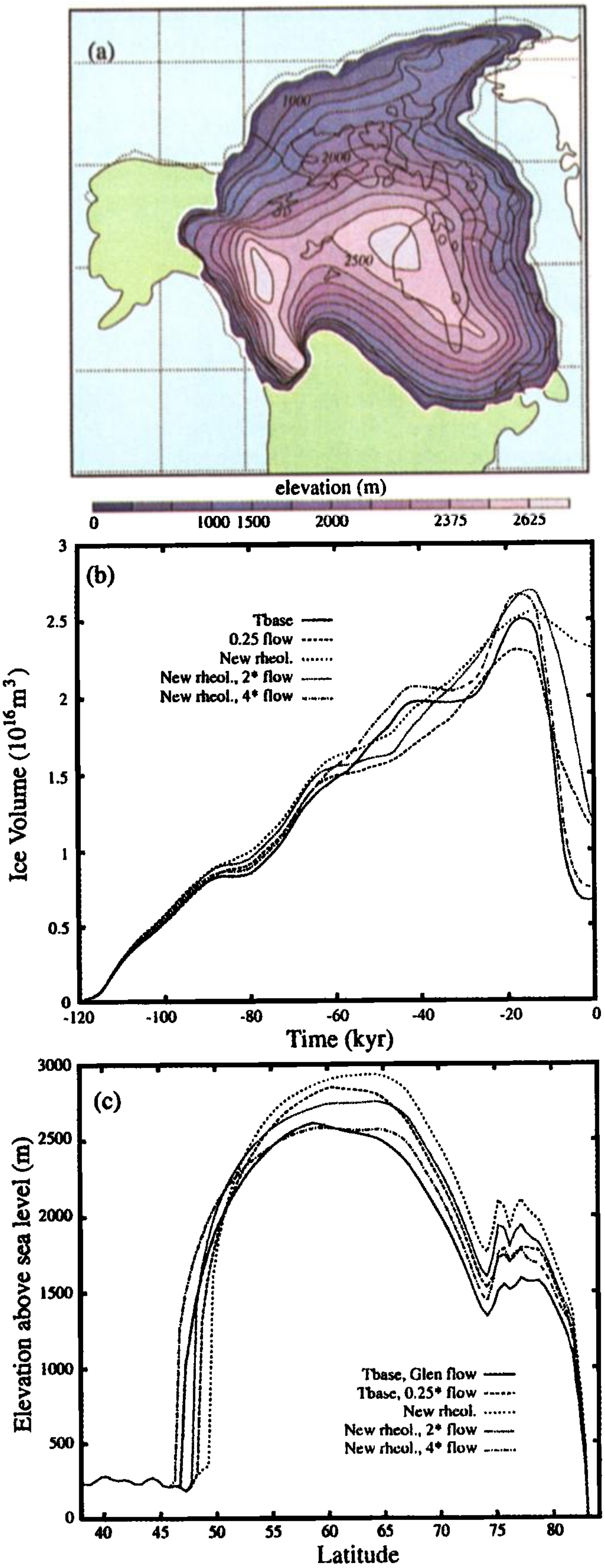

perature in the ablation zone rises rapidly, and this leads to a considerable increase in the ablation rate. The glacial isostatic adjustment process thereby leads to a positive feedback during retreat, a feedback that dramatically accelerates ice sheet disintegration. This is clearly a rather important result as the termination process has not previously been explained except by recourse to the introduction of rather ad hoc additional feedbacks (see *Tarasov and Peltier* [1997a, b] for a detailed review of this earlier work, and L. Tarasov and W. R. Peltier (manuscript in preparation, 1998) for a detailed analysis of the influence of the glacial isostatic adjustment process).

7. CONCLUSIONS

In the preceding review and discussion of recent analyses of the implications of observed postglacial variations in the level of the sea the intention has been to demonstrate the wide range of geophysical science related issues on which this subject impinges. These recent analyses have settled a large number of previously outstanding issues and thereby considerably refined our understanding of related Earth system processes. It will be useful to summarize succinctly, in point form, the primary conclusions of this continuing body of work that follow from the analyses already performed. These comprise the following:

1. The extended form of the integral sea level equation, the primitive original form of which was originally developed in the work of *Peltier* [1974], *Peltier and Andrews* [1976], and *Farrell and Clark* [1976], in which the iterative extension to include the time dependence of the ocean function [*Peltier*, 1994] and rotational feedback [*Peltier*, 1998b, c] is incorporated, may now be considered to be as fully articulated as possible within the context of models based upon the assumption of spherically symmetric Earth properties.

2. Analyses of the impact of rotational feedback upon the predicted history of postglacial sea level change demonstrate that this feedback is extremely weak, being between 1 and 2 orders of magnitude smaller than the recently published suggestion by *Bills and James* [1996].

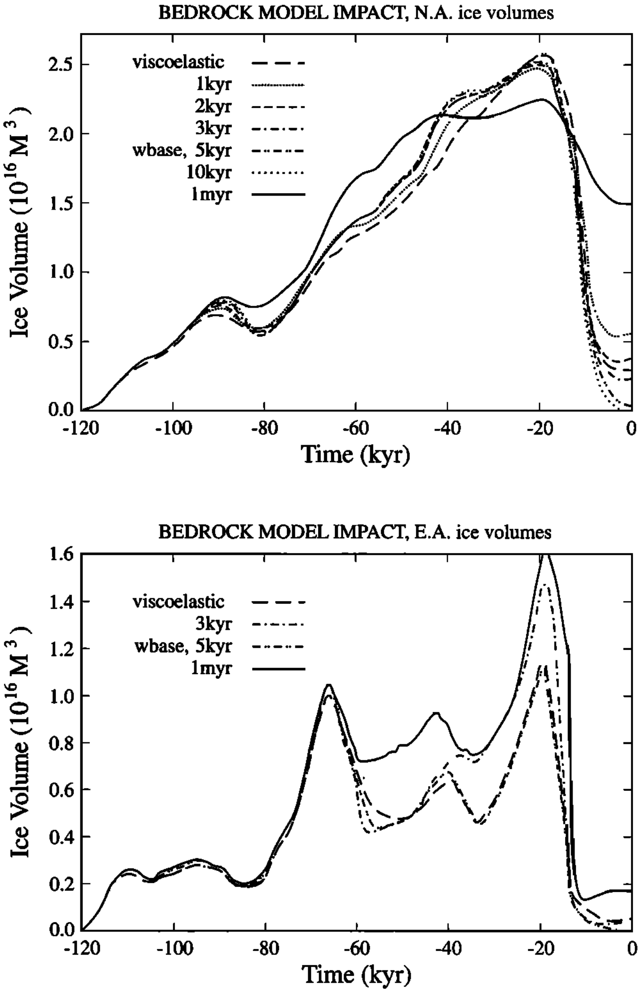

Figure 54. Model-predicted ice volume time series from Eemian to present as a function of the way in which the GIA process is treated in the climate model. When the relaxation time employed in the context of the locally damped return to equilibrium model is made, so large that no subsidence under the ice sheets occurs, then the model fails to predict the termination.

3. Formal solutions of the inverse problem for mantle viscosity in which an appropriately selected subset of the total database of GIA-related observations are employed as basis for inversion deliver "smoothest models" of the radial structure that are "linearly close" to the VM1 model. This VM1 model was previously inferred, on the basis of multiple solutions of the forward problem, to be the model with least radial variation that was most compatible with a wide range of observations. The VM2 class of models, which are obtained on the basis of single-step Bayesian inversions in which VM1 is employed as starting model, are modestly softer than VM1 in the upper mantle and transition zone and modestly stiffer than VM1 in the lowest part of the lower mantle. If the rotational constraints are assumed not to be significantly influenced by processes other than glacial isostatic adjustment, then one obtains models VM2 that are characterized by a sharp though modest increase of

---

Plate 14. (opposite) (a) The topography of the Laurentide ice sheet predicted by the complete thermomechanical model developed in equation (14) when the rheology is taken to be represented by the Glen flow law with $n = 3$ and the factor f in equation (1) is taken to be equal to 80 in order to obtain a best fit to the geophysically inferred topography shown on Figure 9. (b) Time series of the orbitally forced evolution of Laurentide ice sheet volume predicted by the thermomechanical ice sheet coupled climate model as a function of the assumed ice sheet rheology. (c) North-south cross sections through the predicted LGM Laurentide ice sheet along 81.25°W longitude as a function of the assumed rheology.

viscosity across the 660-km seismic discontinuity by a factor of ~3 from an average value through the upper mantle and transition zone near 0.4×10^{21} Pa s to an average value over the upper 500–700 km of the lower mantle near 1.2×10^{21} Pa s. In the lowermost mantle the viscosity continues to increase by an additional factor of 2–4, leading to a net contrast in the smooth models of a factor of ~8. These models differ dramatically from those that have been suggested by Lambeck and coworkers [e.g., *Lambeck et al.*, 1990], whose preferred models are characterized by a very sharp increase in viscosity, by a factor of 10–20, across the 660-km discontinuity. Such models have never been shown to be able to fit the observations over the Laurentide platform of Canada and must be ruled out on this basis (see Plate 7). Although various attempts have been made to discover some missing ingredient in the viscoelastic normal mode theory of *Peltier* [1974, 1976, 1982], that would enable the rebound model to deliver acceptably low relaxation times in this region in the presence of large viscosity contrast (see, for example, the recent analyses by *Johnston et al.* [1997], who provide a further assessment of the possible importance of the way in which the phase transition at 660 km depth is treated). In my work this boundary has always been treated as a material boundary based upon the assumption that GIA timescales were too short for the phase boundary to achieve thermodynamic equilibrium [*Peltier*, 1982]); no such missing ingredient has yet been identified.

4. If it is assumed that the rotational observables are in fact "contaminated" by the influence of a process other than GIA (for example, by the influence of present-day global sea level rise that is significantly caused by the melting of the polar ice sheets of Greenland and/or Antarctica) then, depending upon the extent of this forcing, removal of the contamination and reanalysis of the inverse problem for viscosity leads to new models of the type referred to herein as VM3 in which the viscosity of the lowermost mantle is further increased by an additional factor of 2–3 leading to a lowermost mantle viscosity close to 10^{22} Pa s. In the VM3 profile, however, the viscosity throughout the remainder of the mantle remains "pinned" to that of the VM2 model by the relative sea level observations.

5. Comparison of the VM2–VM3 type models deduced on the basis of the inversion of data related to the GIA process with models previously inferred on the basis of analyses of data, primarily nonhydrostatic geoid anomalies, related to the mantle convection process, demonstrates that the GIA-derived models are very close to the geoid-derived models in terms of the depth variation of relative viscosity (recall that the geoid data are insensitive to the absolute value of viscosity; see *Forte and Peltier* [1987] for a discussion of this point). If one scales the geoid-derived model using the GIA information (as did *Pari and Peltier* [1995] and *Peltier* [1996a]) then the only disagreement between the two profiles concerns the existence of the thin layer of very low viscosity that is required by the geoid data to exist in the region immediately above the 660-km discontinuity [*Forte et al.*, 1993a, b; *Pari and Peltier*, 1995]. Although the existence of this feature has a significant impact upon the GIA data, particularly the *McConnell* [1968] relaxation spectrum, it may be compensated for by a modest increase in the viscosity of the rest of the transition zone, back to values characteristic of VM1. Other means of compensation are also possible, making abundantly clear the inherent nonuniqueness of solutions to the inverse problem for viscosity, a well-known and extremely important issue that is inherent to the solution of all problems of this kind (see *Peltier* [1998b] for a more detailed discussion). It may also be the case [e.g., see *Wolf*, 1996] that the Fennoscandian relaxation spectrum of McConnell is not sufficiently accurate to be employed as a constraint upon viscosity in the upper mantle and transition zone. In this case, there may be no conflict at all between the GIA and convection timescale requirements. An alternative explanation of the preference of the geoid data for models with a low-viscosity zone above the 670 km discontinuity is due to "strain softening" by the phase transition itself which would cause the mantle convection process to "see" a low-viscosity zone that does not exist for the PGR process.

6. Because we have fully established the essential compatibility of the mantle viscosity profiles required by the data related to the GIA process and those related to the mantle convection process, it is now clear that the rheology of the mantle is very plausibly Newtonian [*Pari and Peltier*, 1995; *Peltier*, 1996a]. If the creep resistance of the mantle were not Newtonian, then we would expect that these two processes, which differ in their characteristic timescales by 4–5 orders of magnitude, would be governed by significantly different effective viscosities. They appear not (necessarily) to be. This possibility has also been conjectured by *Karato* [1998] based upon the apparent absence of significant seismic anisotropy beneath a depth of about 200 km in the Earth. In order to effect the alignment of crystal grains required to produce seismic anisotropy, a nonlinear rheology is clearly required. However, we have established compatibility only to within a constant scale factor (aside from the issue of the low-viscosity "notch"), and it remains to be seen whether it will be possible to devise some means by which this scale factor might be directly determined.

7. Application of the topographically self-consistent form of the theory of postglacial sea level change has provided a rigorous means with which to infer the time variation of surface topography with respect to sea level that has occurred through the ice age cycle of glaciation and deglaciation, and these inferences now form the basis of the boundary conditions on this field that are being employed in the context of the international Paleoclimate Model Intercomparison Project (PMIP) in which a large suite of existing atmospheric general circulation models is being compared in terms of the model's ability to simulate planetary climate at a number of

selected epochs from LGM to present. The topographies inferred in this way are considerably different from those previously derived by the *CLIMAP Project Members* [1980], primarily in that ice sheet topographic heights are inferred to have been substantially lower than previously thought.

8. The ICE-4G model of the deglaciation process, on the basis of which these paleotopographies are derived, delivers ~120 m of eustatic sea level rise to the global oceans. This is, in fact, slightly larger than the previously cited value by *Peltier* [1994] and in close accord with estimates derived by other means [e.g., *Chappell and Shackleton*, 1986; *Chappell et al.*, 1996]. The extent to which this eustatic rise of sea level is actually realized at individual far-field locations in the global ocean is closer than previously conjectured by *Peltier* [1995a]. This reconciliation is made possible by recognition of the role of "implicit ice" in the integral sea level equation based theory of glacial isostatic adjustment process [*Peltier*, 1998d].

9. The predicted variations of surface geography through the ice age cycle, especially the appearance and disappearance of land bridges and the exposure of continental shelf areas, are in many regions extreme and could be important for the understanding of local climate variability. Detailed analyses of these effects using very high resolution topographic data could be extremely important to the understanding of a number of issues in archaeology and anthropology, one example from the latter area being the issue of the pathways whereby the Americas were originally populated.

10. A primary characteristic of the ICE-4G deglaciation model concerns its Antarctic component which is assumed to deliver ~20 m to the net increase of eustatic sea level only after the northern hemisphere ice sheets had already experienced significant meltdown. This has important implications for the understanding of the way in which the deep thermohaline circulation of the oceans responded to the deglaciation process.

11. The feedback of the ice age cycle related changes in the Earth's shape onto the evolution of the geometric properties of its orbit around the Sun is sufficiently weak as to not require any significant modification of the methods of solution of the gravitational n-body problem that are employed as basis for computation of the insolation forcing that is apparently responsible for the ice ages themselves.

12. It appears that climate models designed to incorporate only those feedback mechanisms that are known to be operative and whose strengths are well constrained by observations are capable of entirely explaining the observed 100-kyr cycle of the late Pleistocene ice age. Models that reconcile the observations are very substantially influenced by the feedback onto climate associated with the glacial isostatic adjustment process itself. If the GIA effect is removed from such models, then the "terminations" that mark the end of each cycle of glaciation and deglaciation seem not to be explicable.

13. The geophysically inferred low aspect ratio of the LGM Laurentide ice sheet appears to be most easily explained in terms of the new GBS-based rheology of *Goldsby and Kohlstedt* [1997a].

Further progress is, of course, to be expected in the course of continuing exploration of the set of interlinked and fascinating interactions that have occurred in conjunction with postglacial variations in the level of the sea. This will undoubtedly lead to the exploration of further questions that will inevitably arise as one looks ever deeper into the heart of a physical phenomenon as complex as the Pleistocene ice age.

GLOSSARY

^{14}C dating: employment of the radioactive isotope of carbon, with half-life 5730 years, to determine the age of the specimen. The method may be implemented either by counting β decays as in the method of *Libby* [1952] or by direct atom counting using accelerator mass spectrometry (AMS) as discussed, for example, by *Litherland* [1980]. Calibration is required to convert ^{14}C age to calendar age, the current standard procedure being that described by *Stuiver and Reimer* [1993].

Eemian interglacial: the interglacial period previous to the present Holocene period which corresponds to oxygen isotope stage 5e and which has an age in calendar years of ~125,000 years B.P. (before present).

Eustatic sea level variations: variations of the total mass of water in the global oceans.

Fréchet derivative: functional derivative of the response of a model with respect to the variation of one of the model parameters. This is, in general, a function of the space coordinates of the model if the parameter is also space-dependent, also called a "sensitivity kernel."

Free air gravity anomaly: the difference between the local surface gravitational acceleration and the value that would be measured at the same place on a best fitting reference ellipsoid.

Geoid: the surface of constant gravitational potential that is instantaneously coincident with mean sea level over the oceans.

Global Positioning System (GPS): the method whereby ground-based radio receivers are employed to observe the radio signals emitted by members of a constellation of Earth-orbiting satellites and which thereby allows one to determine with high accuracy the positions of the receivers.

Holocene period: the period that began with the end of the most recent glacial cycle of the present ice age ~10 kyr ago and which has continued since.

Hydroisostasy: isostatic adjustment of the Earth's shape induced by the addition of water to the global oceans, as opposed to glacial isostasy in which the adjustment of shape is due to the addition or removal of ice from the surface of the continents.

Interglacial: the relatively ice free period that separates successive epochs of pronounced surface glaciation.

Isostatic sea level variations: variations in the local radius of the solid Earth due to deformations of planetary shape.

Marine limit: the maximum height, above present sea level, at which evidence is found of occupation by the sea in regions that are undergoing postglacial rebound of the crust.

Non-Newtonian rheology: a relationship between strain rate and stress for a fluid which is nonlinear. Nonlinear rheologies are necessarily "transient" rheologies since the effective viscosity is a function of stress and therefore is time-dependent in a typical stress relaxation experiment such as that involved in the glacial isostatic adjustment process.

Nontidal acceleration of rotation: the acceleration of rotation that is currently responsible for the fact that the rate of increase of the length of day (l.o.d.) is less than it would be due to the influence of tidal friction alone.

Orbital obliquity: the angle that the axis of spin of the Earth makes with the normal to the plane of the ecliptic, currently near 23.5°.

Orbital insolation anomaly: the change in the solar insolation received by the Earth at a particular latitude due to variations in the geometry of its orbit caused by the influence of gravitational n-body effects in the solar system.

Oxygen isotope stratigraphy: the ratio of the concentration of the heavy isotope of oxygen [^{18}O] to that of the light isotope [^{16}O], relative to that of a suitable standard, measured as a function of depth in, say, a deep-sea sedimentary core or a coral sequence; usually denoted δ^{18}O.

Oxygen isotope stage (OIS): the stages in the oxygen isotope stratigraphies recorded in deep-sea sedimentary cores. OIS stage 1 is the Holocene, OIS stage 2 is full glacial from roughly 35 kyr B.P. to 21 kyr B.P., and OIS stage 5 is the penultimate interglacial which is divided in substages 5a to 5e in which 5e is the equivalent of the present Holocene period. The age of OIS 5e is ~125 kyr, and it is also referred to as the Eemian interglacial.

Planetary precession: the 21-kyr periodic conical motion of the direction of pointing of the spin axis of the planet around the normal to the ecliptic plane.

Pleistocene period: the period which began ~2.4 Myr ago in which significant accumulations of glacial ice developed on the northern and southern hemisphere continents that are now ice free.

Proglacial forebulge: the regions immediately surrounding an area that was once glaciated. In this region the local radius of the solid Earth is increased during glaciation by the material that is squeezed outward to accommodate the depression of the surface beneath the ice-covered region itself. When the ice load disintegrates, the rebound of the crust in the once loaded region is accompanied by a collapse of the forebulge.

Satellite laser ranging (SLR): the method whereby ground-based lasers are employed to track the orbit of an artificial Earth satellite or the Moon (lunar laser ranging) and to thereby infer properties of Earth's gravitational field.

Steric effect: the sea level variations caused by local or global changes in the temperature or salinity of a fixed mass of water in the global oceans.

Thermohaline circulation of the oceans: the convectively driven deep circulation of the oceans that is forced by variations in surface temperature and salinity, as compared to the wind-driven circulation.

True polar wander: the motion of the Earth's pole of rotation relative to the surface geography.

Very long baseline interferometry (VLBI): the method whereby ground-based arrays of radio telescopes are employed to observe the radio emissions from distant sources (quasars) and to thereby accurately infer the (changing) distance between the telescopes.

ACKNOWLEDGMENTS. This work has been supported both by NSERC grant A9627 and through the Climate System History and Dynamics Programme that is jointly funded by NSERC and by the Atmospheric Environment Service of Canada. I have much benefitted in my understanding of the issues discussed herein from discussions with my Research Associate, Rosemarie Drummond, and with the several previous graduate students and postdoctoral fellows who have worked together with me on these problems, including David Yuen, Patrick Wu, Bill Hyde, Mark Tushingham, Alex Forte, Godelieve De Blonde, Detlef Wolf, Jerry Mitrovica, Roberto Sabadini, Giovanni Pari, Xianhua Jiang, Zhengrong Peng, Lev Tarasov, and, most recently, Dongmei Zhang. I am grateful to all of them for the stimulation provided by their intellectual company. The analyses of the implications of the new GBS-based rheology for ice would not have been possible without the input that I received from David Goldsby of Brown University and David Kohlstedt of the University of Minnesota. Similarly, the complete ^{14}C data set for southeast Hudson Bay was assembled for me by my colleague Claude Hillaire-Marcel of the Université du Québec à Montréal. The photographs of Lövgrunde displayed in Plate 1 were taken by Sue Crane during an expedition financed by the BBC Series "Earth Story," for filming a segment directed by Simon Singh. I immensely enjoyed the company of the BBC crew members and of my colleague, Martin Eckman, from Sweden, who guided our visit. The results of calculations based upon the ICE-4G (VM2) models will be made available to interested users through the IERS (International Earth Rotation Service).

Kevin Furlong and Jim Smith were the Editors responsible for this paper. They would like to thank Peter deMenocal and two anonymous reviewers for their assistance in evaluating this paper.

REFERENCES

Agassiz, L., Etudes sur les glaciers, Neuchâtel, Switzerland, 1840.

Airy, G. B., On the computation of the effect of the attraction of the mountain masses as disturbing the apparent astronomical latitude of stations in geodetic surveys, *Philos. Trans. R. Soc. London*, *145*, 101–115, 1855.

Allard, M., and G. Tremblay, La dynamique littorale des îles Manitounuk durant l'Holocene, *Z. Geomorphol.*, *47*, 61–95, 1983.

Argus, D. F., Postglacial rebound from VLBI geodesy: On establishing vertical reference, *Geophys. Res. Lett.*, *23*, 973–976, 1996.

Backus, G. E., Bayesian inference in geomagnetism, *Geophys. J. R. Astron. Soc.*, *92*, 125–142, 1988.

Baksi, A. K., ^{40}Ar/^{39}Ar dating of the Brunhes-Matuyama geomagnetic field reversal, *Science*, *256*, 356–359, 1992.

Bard, E., Correction of accelerator mass spectrometer ^{14}C ages measured in planktonic foraminifera: Paleoceanographic implications, *Paleoceanography*, *3*, 635–645, 1988.

Bard, E., B. Hamelin, R. G. Fairbanks, and A. Zindler, Calibration of the ^{14}C timescale over the past 30,000 years using mass spectrometric U-Th ages from Barbados corals, *Nature*, *345*, 405–409, 1990.

Bard, E., B. Hamelin, M. Arnold, L. Montaggioni, G. Cabioch, G. Faure and F. Rougerie, Deglacial sea level record from Tahiti corals and the timing of global meltwater discharge, *Nature*, *382*, 241–244, 1996a.

Bard, E., et al., Pleistocene sea levels and tectonic uplift based on dating of corals from Sumba Island Indonesia, *Geophys. Res. Lett.*, *23*, 1473–1476, 1996b.

Barnett, T. P., Recent changes in sea level and their possible causes, *Clim. Change*, *5*, 15–38, 1983.

Barnett, T. P., The estimation of "global" sea level change: A problem of uniqueness, *J. Geophys. Res.*, *89*, 7980–7988, 1984.

Berger, A., Long-term variations of daily insolation and Quaternary climatic changes, *J. Atmos. Sci.*, *35*(12), 2362–2367, 1978.

BIFROST Project Members, GPS measurements to constrain geodynamic processes in Fennoscandia, *Eos Trans. AGU*, *77*, 337, 341, 1996.

Bills, B. G., and T. S. James, Late Quaternary variations in relative sea level due to glacial cycle polar wander, *Geophys. Res. Lett.*, *23*, 3023–3026, 1996.

Bournais, G., Voyage naturaliste au Nouveau Quebec, part 1, *Sci. Nat.*, *109*, 17–27, 1972a.

Bournais, G., Voyage naturaliste au Nouveau Quebec, part 2, *Sci. Nat.*, *110*, 17–28, 1972b.

Bournais, G., Voyage naturaliste au Nouveau Quebec, part 3, *Sci. Nat.*, *112*, 2–62, 1972c.

Braithwaite, R. J., Positive degree-day factors for ablation on the Greenland ice sheet studied by energy-balance modelling, *J. Glaciol.*, *41*(137), 153–160, 1995.

Broecker, W. S., and G. Denton, The role of ocean-atmosphere reorganizations in glacial cycles, *Geochim. Cosmochim. Acta*, *53*, 2465–2501, 1989.

Cadek, O., H. Cizkova, and D. A. Yuen, Can long-wavelength dynamical signatures be compatible with layered mantle convection?, *Geophys. Res. Lett.*, *24*, 2091–2094, 1997.

Carter, W. E., D. S. Robertson, T. E. Pyle, and J. Diamante, The application of geodetic radio interferometric surveying to the monitoring of sea level, *Geophys. J. R. Astron. Soc.*, *87*, 3–13, 1986.

Cathles, L. M., *The Viscosity of the Earth's Mantle*, Princeton Univ. Press, Princeton, N. J., 1975.

Cato, I., Shore displacement data based upon lake isolations confirm the postglacial part of the Swedish Geochronological Time Scale, *Sver. Geol. Unders., Ser. Ca*, *81*, 75–80, 1992.

Chappell, J., and H. A. Polach, Post-glacial sea level rise from a coral record at Huon Peninsula, Papua, New Guinea, *Nature*, *276*, 602–604, 1991.

Chappell, J., and N. J. Shackleton, Oxygen isotopes and sea level, *Nature*, *324*, 137–140, 1986.

Chappell, J., A. Omura, T. Esat, M. McCulloch, J. Pandelfi, Y. Ota, and B. Pillans, Reconciliation of Late Quaternary sea levels derived from coral terraces at Huon Peninsula with deep sea oxygen isotope records, *Earth Planet. Sci. Lett.*, *141*, 227–236, 1996.

Cheng, M. K., R. J. Eanes, C. K. Shum, B. E. Schutz, and B. D. Tapley, Temporal variations in low degree zonal harmonics from Starlette orbit analysis, *Geophys. Res. Lett.*, *16*, 393–396, 1989.

Clark, J. A., W. E. Farrell, and W. R. Peltier, Global changes in postglacial sea level: A numerical calculation, *Quat. Res.*, *9*, 265–287, 1978.

Clark, P. U., J. M. Licciardi, D. R. MacAyeal, and J. W. Jenson, Numerical reconstruction of a soft-bedded Laurentide Ice Sheet during the last glacial maximum, *Geology*, *24*(8), 679–682, 1996.

CLIMAP Project Members, The surface of the ice-age Earth, *Science*, *191*, 1131–1144, 1976.

Coble, R. L., A model for boundary diffusion controlled creep in polycrystalline materials, *J. Appl. Phys.*, *34*, 1679–1682, 1963.

Dahlen, F. A., The passive influence of the oceans upon the rotation of the Earth, *Geophys. J. R. Astron. Soc.*, *46*, 363–406, 1976.

Daley, R. A., *The Changing World of the Ice Age*, Yale Univ., Press, New Haven, Conn., 1934.

De Angelis, M., N. I. Barkov, and V. N. Petrov, Aerosol concentrations over the last climatic cycle (160 kyr) from an Antarctic ice-core, *Nature*, *325*, 318–321, 1987.

Deblonde, G., and W. R. Peltier, Simulations of continental ice sheet growth over the last glacial-interglacial cycle: Experiments with a one-level seasonal energy balance model including realistic geography, *J. Geophys. Res.*, *96*, 9189–9215, 1991a.

Deblonde, G., and W. R. Peltier, A one-dimensional model of continental ice volume fluctuations through the Pleistocene: Implications for the origin of the mid-Pleistocene climate transition, *J. Clim.*, *4*(3), 318–344, 1991b.

Deblonde, G., and W. R. Peltier, Late Pleistocene ice age scenarios based on observational evidence, *J. Clim.*, *6*(4), 709–727, 1993.

Deblonde, G., W. R. Peltier, and W. T. Hyde, Simulations of continental ice sheet growth over the last glacial-interglacial cycle: Experiments with a one level seasonal energy balance model including seasonal ice albedo feedback, *Global Planet. Change*, *98*, 37–55, 1992.

Denton, G. H., and T. Hughes, *The Last Great Ice Sheets*, Wiley-Interscience, New York, 1981.

Devoy, R. J., Introduction: First principles and the scope of sea-surface studies, in *Sea Surface Studies*, edited by R. J. N. Devoy, pp. 1–32, Croom Helm, Beckenham, England, 1987.

Dickman, S. R., Secular trend of the Earth's rotation pole: Consideration of motion of the latitude observatories, *Geophys. J. R. Astron. Soc.*, *57*, 41–50, 1977.

Donner, J., The determination and dating of synchronous Late Quaternary shorelines in Fennoscandia, in *Earth Rheology, Isostasy and Eustasy*, edited by N. A. Morner, pp. 285–293, John Wiley, New York, 1980.

Douglas, B. D., Global sea level rise, *J. Geophys. Res.*, *96*, 6981–6992, 1991.

Duffy, T. S., and T. J. Ahrens, Sound velocities at high pressure and temperature and their geophysical implications, *J. Geophys. Res.*, *97*, 4503–4520, 1992.

Dutton, G. E., On some of the greater problems of physical geology, *Bull. Philos. Soc. Wash.*, *11*, 51–59, 1889.

Dziewonski, A. M., and D. L. Anderson, Preliminary reference Earth model, *Phys. Earth Planet. Inter.*, *25*, 297–356, 1981.

Edwards, R. L., High precision Th-230 ages of corals and the timing of sea level fluctuations in the late Quaternary, thesis, Calif. Inst. of Technol., Pasadena, 1988.

Edwards, R. L., Paleotopography of glacial-age ice sheets, *Science*, *267*, 536, 1995.

Edwards, R. L., J. W. Beck, G. S. Burr, D. J. Donahue, J. M. A. Chappell, A. L. Bloom, E. R. M. Druffel, and F. W. Taylor, A large drop in atmospheric $^{14}C/^{12}C$ and reduced melting in the Younger Dryas, documented with ^{230}Th ages of corals, *Science*, *260*, 962–968, 1993.

Eisenhauer, A., G. J. Wasserburg, J. H. Chen, G. Bonani, L. B. Collins, Z. R. Zhu, and K. H. Wyrwoll, Holocene sea level determination relative to the Australian continent: U-Th (TIMS) and ^{14}C (AMS) dating of coral cores from the Abrolhos Islands, *Earth Planet. Sci. Lett.*, *114*, 529–547, 1993.

Elias, S. A., S. K. Short, and R. L. Phillips, The palaeo sea level history of Beringia, *Quat. Res.*, *38*, 371–383, 1992.

Eronen, M., Late Weichselian and Holocene shore displacement in Finland, in *Shorelines and Isostasy*, edited by D. E. Smith and A. G. Dawson, pp. 183–207, Academic, San Diego, Calif., 1983.

Fairbanks, R. G., A 17,000-year glacio-eustatic sea level record: Influence of glacial melting rates on the Younger Dryas event and deep-ocean circulation, *Nature*, *342*, 637–641, 1989.

Fang, M., and B. H. Hager, The singularity mystery associated with radially continuous Maxwell viscoelastic structure, *Geophys. J. Int.*, *123*, 849–865, 1995.

Fanning, A. F., and A. J. Weaver, Temporal-geographical meltwater influences on the North Atlantic conveyor: Implications for the Younger Dryas, *Paleoceanography*, *12*, 307–320, 1997.

Farrell, W. E., Deformation of the Earth by surface loads, *Rev. Geophys.*, *10*, 761–797, 1972.

Farrell, W. E., and J. A. Clark, On postglacial sea level, *Geophys. J. R. Astron. Soc.*, *46*, 647–667, 1976.

Forte, A. M., and J. X. Mitrovica, New inferences of mantle viscosity from joint inversion of long-wavelength mantle convection and post-glacial rebound data, *Geophys. Res. Lett.*, *23*, 1147–1150, 1996.

Forte, A. M., and W. R. Peltier, Plate tectonics and aspherical Earth structure: The importance of poloidal-toroidal coupling, *J. Geophys. Res.*, *92*, 3645–3679, 1987.

Forte, A. M., and R. Peltier, Viscous flow models of global geophysical observables, 1, Forward problems, *J. Geophys. Res.*, *96*, 20,131–20,159, 1991.

Forte, A. M., and W. R. Peltier, The kinematics and dynamics of poloidal-toroidal coupling in mantle flow: The importance of surface plates and lateral viscosity variations, *Adv. Geophys.*, *36*, 1–119, 1994.

Forte, A. M., W. R. Peltier, and A. M. Dziewonski, Inferences of mantle viscosity from tectonic plate velocities, *Geophys. Res. Lett.*, *18*, 1747–1750, 1991.

Forte, A. M., W. R. Peltier, A. M. Dziewonski, and R. L. Woodward, Dynamic surface topography: A new interpretation based upon mantle flow models derived from seismic tomography, *Geophys. Res. Lett.*, *20*, 225–228, 1993a.

Forte, A. M., A. M. Dziewonski, and R. L. Woodward, Aspherical structure of the mantle, tectonic plate motions, nonhydrostatic geoid, and topography of the core-mantle boundary, in *Dynamics of the Earth's Deep Interior and Earth Rotation, Geophys. Monogr. Ser.*, vol. 72, edited by J.-L. Le Mouel, D. E. Smylie, and T. Herring, pp. 135–166, AGU, Washington, D. C., 1993b.

Frost, H. J., and M. F. Ashby, *Deformation Mechanism Maps*, Pergamon, New York, 1982.

Gegout, P., and A. Cazenave, Geodynamic parameters derived from 7 years of laser data on LAGEOS, *Geophys. Res. Lett.*, *18*, 1739–1742, 1991.

Gilbert, F., Inverse problems for the Earth's normal modes, in *Mathematical Problems in the Geophysical Sciences*, edited by W. H. Reid, pp. 107–128, Am. Math. Soc., Providence, R. I., 1971.

Glen, J. W., The creep of polycrystalline ice, *Proc. R. Soc. London, Ser. A*, *228*, 519–538, 1955.

Goldsby, D. L., Superplasticity in ice, Ph.D. thesis, Univ. of Minn.-Twin Cities, Minneapolis, 1997.

Goldsby, D. L., and D. L. Kohlstedt, Grain boundary sliding in fine grained Ice I, *Scr. Mater.*, *37*, 1399–1406, 1997a.

Goldsby, D. L., and D. L. Kohlstedt, Flow of Ice I by dislocation, grain boundary sliding, and diffusion processes, *Proc. Lunar Planet. Sci. Conf.*, *28th*, 1–3, 1997b.

Gore, R., The most ancient Americans, *Natl. Geogr.*, *192*(4), 92–99, 1997.

Hager, B. H., Subducted slabs and the geoid: Constraints on mantle rheology and flow, *J. Geophys. Res.*, *89*, 6003–6015, 1984.

Hager, B. H., and R. W. Clayton, Constraints on the structure of mantle convection using seismic observations, flow models, and the geoid, in *Mantle Convection, Plate Tectonics and Global Dynamics*, edited by W. R. Peltier, pp. 657–763, Gordon and Breach, Newark, N. J., 1989.

Hager, B. H., and M. A. Richards, Long-wave length variations in the Earth's geoid: Physical models and dynamical implications, *Philos. Trans. R. Soc. London, Ser. A*, *328*, 309–327, 1989.

Hardy, L., Contribution à l'étude géomorphologique de la portion Québecoise de la Baie de James, Ph.D. memoire, 264 pp., McGill Univ., Montreal, Que., 1976.

Haskell, N. A., The motion of a fluid under a surface load, 1, *Physics*, *6*, 265–269, 1935.

Hays, J. D., J. Imbrie, and N. J. Shackleton, Variations in the Earth's orbit: Pacemaker of the ice ages, *Science*, *194*, 1121–1132, 1976.

Heinrich, H., Origin and consequences of cyclic ice rafting in the northeast Atlantic Ocean during the past 130,000 years, *Quat. Res.*, *29*, 142–152, 1988.

Herring, C., Diffusional viscosity of a polycrystalline solid, *J. Appl. Phys.*, *21*, 437–445, 1955.

Herring, T. A., Very long baseline interferometry and its contributions to geodynamics, in *Space Geodesy and Geodynamics*, edited by A. J. Andersen and A. Cazanave, pp. 169–196, Academic, San Diego, Calif., 1986.

Hillaire-Marcel, C., La deglaciation et le relevement isostatique a l'est de la baie Hudson, *Cah. Geogr. Que.*, *20*, 185–220, 1976.

Hillaire-Marcel, C., Multiple component postglacial emergence, eastern Hudson Bay, Canada, in *Earth Rheology, Isostasy and Eustasy*, edited by N.-A. Mörner, pp. 215–230, John Wiley, New York, 1980.

Hillaire-Marcel, C., Paleoceanographie isotopique des mers post-glaciares du Quebec, *Palaeogeogr. Palaeoclimatol. Palaeoecol.*, *35*, 63–119, 1981.

Holmes, A., *Principles of Physical Geology*, Nelson, London, 1965.

Huybrechts, P., The Antarctic Ice Sheet during the last glacial-interglacial cycle: A three-dimensional experiment, *Ber. Polarforschung*, *99*, 1–241, 1992.

Huybrechts, P., et al., The EISMINT benchmarks for testing ice-sheet models, *Ann. Glaciol.*, *23*, 1–12, 1996.

Imbrie, J., J. D. Hays, D. G. Martinsen, A. McIntyre, A. C.

Mix, J. J. Morley, N. G. Pisias, W. L. Prell, and N. J. Shackleton, The orbital theory of Pleistocene climate: Support from a revised chronology of the marine $\delta^{18}O$ record, in *Milankovitch and Climate*, edited by A. Berger et al., pp. 269-306, D. Reidel, Norwell, Mass., 1984.

Intergovernmental Panel on Climate Change (IPCC), *Climate Change, 1995: The Science of Climate Change, Contribution of working Group 1 to the Second Assessment Report of the Intergovernmental Panel on Climate Change*, Cambridge Univ. Press, New York, 1996.

Jackson, D. D., and J. Matsu'ura, A Bayesian approach to nonlinear inversion, *J. Geophys. Res.*, *90*, 581-591, 1985.

James, T. S., and A. Lambert, A comparison of VLBI data with the ICE-3G glacial rebound model, *Geophys. Res. Lett.*, *20*, 871-874, 1993.

James, T. S., and W. J. Morgan, Horizontal motions due to post-glacial rebound, *Geophys. Res. Lett.*, *17*, 957-960, 1990.

Jamieson, T. F., On the history of the last geological changes in Scotland, *Q. J. Geol. Soc. London*, *21*, 161-203, 1865.

Jamieson, T. F., On the course of the depression and re-elevation of the land during the glacial period, *Geol. Mag.*, *9*, 400-407, 457-466, 1882.

Jiang, X., and W. R. Peltier, Ten million year histories of obliquity and precession: The influence of the ice-age cycle, *Earth Planet. Sci. Lett.*, *139*, 17-32, 1996.

Johnston, P., K. Lambeck, and D. Wolf, Material versus isobaric internal boundaries in the Earth and their influence on postglacial rebound, *Geophys. J. Int.*, *129*, 252-268, 1997.

Jouzel, J., C. Lorius, J. R. Petit, C. Genthon, N. I. Barkov, V. M. Kotlyakov, and V. M. Petrov, Vostok ice core: A continuous isotope temperature record over the last climatic cycle (160,000 years), *Nature*, *329*, 403-408, 1987.

Karato, S., Seismic anisotropy in the deep mantle, boundary layers and the geometry of mantle convection, *Pure Appl. Geophys.*, in press, 1998.

King, S. D., and G. Masters, An inversion for radial viscosity structure using seismic tomography. *Geophys. Res. Lett.*, *19*, 1551-1554, 1992.

Kohlstedt, D. L., and C. Goetze, Low-stress and high-temperature creep in olivine single crystals, *J. Geophys. Res.*, *79*, 2045-2051, 1974.

Kutzbach, J. E., and P. J. Guetter, The influence of changing orbital parameters and surface boundary conditions on climate simulations for the past 18000 years, *J. Atmos. Sci.*, *43*(16), 1726-1759, 1986.

Lamb, H. H., *Climate: Present, Past and Future*, vol. 1, 613 pp., Methuen, New York, 1972.

Lambeck, K., Postglacial sea level variations in the Aegean Sea, paper presented at General Assembly, Int. Assoc. of Seismol. and Phys. of the Earth's Inter., Thessaloniki, Greece, Aug. 1997.

Lambeck, K., P. Johnston, and M. Nakada, Holocene glacial rebound and sea-level change in NW Europe, *Geophys. J. Int.*, *103*, 451-468, 1990.

Lambeck, K., P. Johnston, C. Smither, and M. Nakada, Glacial rebound of the British Isles, III, Constraints on mantle viscosity, *Geophys. J. Int.*, *125*, 340-354, 1996.

Laskar, J., Secular evolution of the solar system over 10 million years, *Astron. Astrophys.*, *198*, 341-362, 1988.

Laskar, J., F. Joutel, and F. Boudin, Orbital, precessional, and insolation quantities for the Earth from −20 Myr to +10 Myr, *Astron. Astrophys.*, *270*, 522-533, 1993.

Lee, H. A., Method of deglaciation of submergence and rate of uplift west and east of Hudson Bay, *Biol. Perygl. Lodz*, *11*, 239-245, 1962.

Libby, W. F., *Radiocarbon Dating*, Univ. of Chicago Press, Chicago, Ill., 1952.

Lidén, R., Den senkvartara strandforskjutningens forloop och kronologi i Angermanland, *Geol. Foeren. Stokholm Foerh.*, *60*, 397-404, 1938.

Litherland, A. E., Ultrasensitive mass spectrometry with accelerators, *Annu. Rev. Nucl. Part. Sci.*, *30*, 437-473, 1980.

Lourens, L. J., A. Antonarakou, F. J. Hilgen, A. A. M. Van Hoof, C. Vergnaud-Grazzini, and W. J. Zachariasse, Evaluation of the Plio-Pleistocene astronomical timescale, *Paleoceanography*, *11*, 391-413, 1996.

Lowden, J. A., and W. Blake Jr., Radiocarbon dates XX, *Pap. Geol. Surv. Can.*, *80-7*, 22 pp., 1980.

Ma, C., and J. W. Ryan, NASA space geodesy program—GSFC data analysis—1995: VLBI geodetic results 1979-July 1995, *NASA Tech. Memo.*, *TM-12345*, 1995.

MacLaren, C., The glacial theory of Professor Aggasiz, *Am. J. Sci.*, *42*, 346-365, 1842.

Manabe, S., and A. J. Broccoli, The influence of continental ice sheets on the climate of an ice age, *J. Geophys. Res.*, *90*, 2167-2190, 1985.

Manabe, S., and R. J. Stouffer, Coupled ocean-atmosphere model response to freshwater input: Comparison to Younger Dryas event, *Paleoceanography*, *12*, 321-336, 1997.

Markowitz, W., Latitude and longitude and the secular motion of the pole, *Methods Tech. Geophys.*, *1*, 325-361, 1960.

Marsh, J. G., et al., The GEM-T2 gravitational model, *J. Geophys. Res.*, *95*, 22,043-22,071, 1990.

Marshall, S. J., G. K. C. Clarke, A. S. Dyke, and D. A. Fisher, Geologic and topographic controls on fast flow in the Laurentide and Cordilleran Ice Sheets, *J. Geophys. Res.*, *101*, 17,827-17,839, 1996.

McConnell, R. K., Viscosity of the mantle from relaxation time spectra of isostatic adjustment, *J. Geophys. Res.*, *73*, 7089-7105, 1968.

Meier, M., Contribution of small glaciers to global sea level, *Science*, *226*, 1418-1421, 1984.

Mikhailov, A. A., On the motion of the Earth's poles, *Astron. Zh.*, *48*, 1301-1304, 1971.

Mitrovica, J. X., Haskell [1935] revisited, *J. Geophys. Res.*, *101*, 555-569, 1996.

Mitrovica, J. X., and A. M. Forte, Radial profile of mantle viscosity: Results from the joint inversion of convection and postglacial rebound observables, *Geophys. J. Int.*, *102*, 2751-2769, 1997.

Mitrovica, J. X., and W. R. Peltier, On postglacial geoid subsidence over the equatorial oceans, *J. Geophys. Res.*, *96*, 20,053-20,071, 1991.

Mitrovica, J. X., and W. R. Peltier, The inference of mantle viscosity from an inversion of the Fennoscandian relaxation spectrum, *Geophys. J. Int.*, *114*, 45-62, 1993a.

Mitrovica, J. X., and W. R. Peltier, Present-day secular variations in the zonal harmonics of the Earth's geopotential, *J. Geophys. Res.*, *98*, 4509-4526, 1993b.

Mitrovica, J. X., and W. R. Peltier, Constraints on mantle viscosity based upon the inversion of past-glacial uplift data from the Hudson Bay region, *Geophys. J. Int.*, *122*, 353-377, 1995.

Mitrovica, J. X., J. L. Davis, and I. I. Shapiro, A spectral formalism for computing three dimensional deformations due to surface loads, 2, Present-day glacial isostatic adjustment, *J. Geophys. Res.*, *99*, 7075-7101, 1994.

Morrison, L. V., Rotation of the Earth and the constancy of G, *Nature*, *241*, 519-520, 1973.

Muller, P. M., and F. R. Stephson, The acceleration of the Earth and Moon from early observations, in *Growth Rythms and History of the Earth's Rotation*, edited by G. D. Rosenburg and S. K. Runcorn, pp. 459-534, John Wiley, New York, 1975.

Müller, R. A., and G. J. MacDonald, Glacial cycles and orbital inclination, *Nature*, *377*, 107-108, 1995.

Munk, W. H., and G. F. MacDonald, *The Rotation of the Earth*, Cambridge Univ. Press, New York, 1960.

Nabarro, F. R. N., Report of a conference on strength of solids, report, 75 pp., Dep. of Phys., Univ. of Bristol, Bristol, England, 1948.

Nerem, R. S., B. J. Haines, J. Hendricks, J. F. Minster, G. T. Mitchum, and W. B. White, Improved determination of global mean sea level variations using TOPEX/Poseidon altimeter data, *Geophys. Res. Lett.*, *24*, 1331-1334, 1997a.

Nerem, R. S., K. E. Rachlin, and B. D. Beckley, Characteristics of global mean sea level variations observed by TOPEX/Poseidon using empirical orthogonal functions, *Surv. Geophys.*, *18*, 293-302, 1997b.

Newton, R. R., *Medieval Chronicles and the Rotation of the Earth*, Johns Hopkins Univ. Press, Baltimore, Md., 1972.

North, G. R., J. G. Mengel, and D. A. Short, Simple energy balance resolving the seasons and the continents: Application to the astronomical theory of the ice ages, *J. Geophys. Res.*, *88*, 6576-6586, 1983.

Nye, J. F., The motion of ice sheets and glaciers, *J. Glaciol.*, *3*, 493-507, 1959.

Ota, Y., J. Chappell, R. Kelley, N. Yonekura, E. Matsumoto, T. Nishimura, and J. Head, Holocene coral reef terraces and coseismic uplift at Huon Peninsula, Papua, New Guinea, *Quat. Res.*, *40*, 177-188, 1993.

Pari, G., and W. R. Peltier, The heat flow constraint on mantle tomography-based convection models: Toward a geodynamically self-consistent inference of mantle viscosity, *J. Geophys. Res.*, *100*, 12,731-12,751, 1995.

Pari, G., and W. R. Peltier, The free air gravity constraint on subcontinental mantle dynamics, *J. Geophys. Res.*, *101*, 28,105-28,132, 1996.

Pari, G., and W. R. Peltier, Global surface heat flux anomalies from seismic tomography-based models of mantle flow: Implications for mantle convection, *J. Geophys. Res.*, *103*, 23,743-23,780, 1998.

Parker, R. L., The inverse problem of electrical conductivity in the mantle, *Geophys. J. R. Astron. Soc.*, *22*, 121-138, 1970.

Paterson, W. S. B., *The Physics of Glaciers*, Pergamon, Tarrytown, N. Y., 1994.

Peltier, W. R., The impulse response of a Maxwell Earth, *Rev. Geophys.*, *12*, 649-669, 1974.

Peltier, W. R., Glacial isostatic adjustment, II, The inverse problem, *Geophys. J. R. Astron. Soc.*, *46*, 669-706, 1976.

Peltier, W. R., Dynamics of the ice-age Earth, *Adv. Geophys.*, *24*, 1-146, 1982.

Peltier, W. R., Constraint on deep mantle viscosity from LAGEOS acceleration data, *Nature*, *304*, 434-436, 1983.

Peltier, W. R., The thickness of the continental lithosphere, *J. Geophys. Res.*, *89*, 11,303-11,316, 1984.

Peltier, W. R., New constraints on transient lower mantle rheology and internal mantle buoyancy from glacial rebound data, *Nature*, *318*, 614-617, 1985a.

Peltier, W. R., The LAGEOS constraint on deep mantle viscosity: Results from a new normal mode method for the inversion of viscoelastic relaxation spectra, *J. Geophys. Res.*, *90*, 9411-9421, 1985b.

Peltier, W. R., Deglaciation-induced vertical motion of the North American continent and transient lower mantle rheology, *J. Geophys. Res.*, *91*, 9099-9123, 1986.

Peltier, W. R., Global sea level and Earth rotation, *Science*, *240*, 895-901, 1988.

Peltier, W. R., Mantle viscosity, in *Mantle Convection*, edited by W. R. Peltier, pp. 479-593, Gordon and Breach, New York, 1989.

Peltier, W. R., Ice age paleotopography, *Science*, *265*, 195-201, 1994.

Peltier, W. R., Paleotopography of glacial-age ice sheets, *Science*, *267*, 536-538, 1995a.

Peltier, W. R., VLBI baselines from the ICE-4G model of postglacial rebound, *Geophys. Res. Lett.*, *22*, 465-468, 1995b.

Peltier, W. R., Mantle viscosity and ice-age ice sheet topography, *Science*, *273*, 1359-1364, 1996a.

Peltier, W. R., Global sea level rise and glacial isostatic adjustment: An analysis of data from the east coast of North America, *Geophys. Res. Lett.*, *23*, 717-720, 1996b.

Peltier, W. R., Phase transition modulated mixing in the mantle of the Earth, *Philos. Trans. R. Soc.*, *Ser. A*, *354*, 1425-1447, 1996c.

Peltier, W. R., A space geodetic target for mantle viscosity discrimination: Horizontal motions induced by glacial isostatic adjustment, *Geophys. Res. Lett.*, *25*, 543-546, 1998a.

Peltier, W. R., Global sea level rise and glacial isostatic adjustment, *Global Planet. Change*, in press, 1998b.

Peltier, W. R., The inverse problem for mantle viscosity, *Inverse Problems*, *14*, 441-478, 1998c.

Peltier, W. R., "Implicit ice" in the global theory of glacial isostatic adjustment, *Geophys. Res. Lett.*, in press, 1998d.

Peltier, W. R., and J. T. Andrews, Glacial isostatic adjustment, I, The forward problem, *Geophys. J. R. Astron. Soc.*, *46*, 605-646, 1976.

Peltier, W. R., and X. Jiang, The precession constant of the Earth: Variations through the ice-age, *Geophys. Res. Lett.*, *21*, 2299-2302, 1994.

Peltier, W. R., and X. Jiang, Glacial isostatic adjustment and Earth rotation: Refined constrains on the viscosity of the deepest mantle, *J. Geophys. Res.*, *101*, 3269-3290, 1996a. (Correction, *J. Geophys. Res.*, *102*, 10,101-10,103, 1997.)

Peltier, W. R., and X. Jiang, Mantle viscosity from the simultaneous inversion of multiple data sets pertaining to postglacial rebound, *Geophys. Res. Lett.*, *23*, 503-506, 1996b.

Peltier, W. R., and X. Jiang, Mantle viscosity, glacial isostatic adjustment and the eustatic level of the sea, *Surv. Geophys.*, *18*, 239-277, 1997.

Peltier, W. R., and S. Marshall, Coupled energy-balance/ice-sheet simulations of the glacial cycle: A possible connection between terminations and terrigenous dust, *J. Geophys. Res.*, *100*, 14,269-14,289, 1995.

Peltier, W. R., and A. M. Tushingham, Global sea level rise and the greenhouse effect: Might they be connected?, *Science*, *244*, 806-810, 1989.

Peltier, W. R., W. E. Farrell, and J. A. Clark, Glacial isostasy and relative sea level: A global finite element model, *Tectonophysics*, *50*, 81-110, 1978.

Peltier, W. R., A. M. Forte, J. X. Mitrovica, and A. M. Dziewonski, Earth's gravitational field: Seismic tomography resolves the enigma of the Laurentian anomaly, *Geophys. Res. Lett.*, *19*, 1555-1558, 1992.

Plumet, P., L'archeologie et le relevement isostatique a Poste-de-la-Baleine, Nouveau Quebec, *Rev. Geogr. Montreal*, *28*, 443-446, 1974.

Pollack, H. N., S. J. Hurter, and J. R. Johnson, Heat flow from the Earth's interior: Analysis of the global data set, *Rev. Geophys.*, *31*, 267-280, 1993.

Portman, J. P., Geomorphologie de l'aire myriametrique de Poste-de-la-Baleine, Nouveau Quebec, *Cah. Geogr. Quebec 34*, 53-76, 1970.

Pratt, J. H., On the attraction of the Himalayan mountains and of the elevated regions beyond upon the plumb line in India, *Philos. Trans. R. Soc. London*, *145*, 53-67, 1855.

Proverbio, E., and V. Quesada, Secular variation in latitudes and longitudes and continental drift, *J. Geophys. Res.*, *79*, 4941-4943, 1974.

Quinn, T. R., S. Tremaine, and M. Duncan, A three-million year integration of the Earth's orbit, *Astron. J.*, *101*, 2287-2305, 1991.

Ramseier, R. O., Self-diffusion in ice monocrystals, *Res. Rep.*

232, 40 pp, U.S. Cold Reg. Res. and Eng. Lab., Hanover, N. H., 1967.

Ricard, Y., and C. Vigny, Mantle dynamics with induced plate tectonics, *J. Geophys. Res.*, *94*, 17,543–17,559, 1989.

Richards, M. A., and B. H. Hager, Geoid anomalies in a dynamic Earth, *J. Geophys. Res.*, *89*, 5987–6002, 1984.

Rubincam, D. R., Postglacial rebound observed by LAGEOS and the effective viscosity of the lower mantle, *J. Geophys. Res.*, *89*, 1077–1087, 1984.

Sakai, K., and W. R. Peltier, A simple model of the Atlantic thermohaline circulation: Internal and forced variability with paleoclimatological implications, *J. Geophys. Res.*, *100*, 13,455–13,479, 1995.

Sakai, K., and W. R. Peltier, A multibasin reduced model of the global thermohaline circulation: Paleoceanographic analyses of the origins of ice-age climate variability, *J. Geophys. Res.*, *101*, 22,535–22,562, 1996.

Sakai, K., and W. R. Peltier, Dansgaard-Oeschger oscillations in a coupled atmosphere-ocean climate model, *J. Clim.*, *10*, 949–970, 1997.

Sauramo, M., Land uplift with hinge lines in Fennoscandia, *Ann. Acad. Sci. Fenn.*, *Ser. A*, *344*, 1–25, 1958.

Seidelman, P. L., 1980 IAU theory of nutation: The final report of the IAU working group on nutation, *Celest. Mech*, *27*, 79–106, 1982.

Shackleton, N. J., Oxygen isotope analyses and Pleistocene temperatures re-addressed, *Nature*, *215*, 15–17, 1967.

Shackleton, N. J., Oxygen isotopes, ice volume and sea level, *Quat. Sci. Rev.*, *6*, 183–190, 1987.

Shackleton, N. J., A. Berger, and W. R. Peltier, An alternative astronomical calibration of the lower Pleistocene timescale based upon ODP Site 677, *Trans. R. Soc. Edinburgh Earth Sci.*, *81*, 251–261, 1990.

Simons, M., and B. H. Hager, Localization of the gravity field and the signature of glacial rebound, *Nature*, *390*, 500–504, 1997.

Stephenson, E. R., and L. V. Morrison, Long term fluctuations in the Earth's rotation: 700 B.C. to A.D. 1990, *Philos. Trans. R. Soc. London*, *Ser. A*, *351*, 165–202, 1995.

Stuiver, M., and P. J. Reimer, Extended ^{14}C data base and revised calib. 3.0 ^{14}C age calibration program, *Radiocarbon*, *35*, 215–230, 1993.

Stuiver, M., B. Kromer, B. Becker, and C. W. Ferguson, Radiocarbon age calibration back to 13,300 years BP and the ^{14}C age matching of the German oak and US bristle cone pine chronologies, *Radiocarbon*, *28*, 969–979, 1986.

Sykes, M. V., R. Greenberg, S. F. Dermott, P. D. Nicholson, J. A. Burns, and T. N. Gautier, Dust bands in the asteroid belt, in *Asteroids II*, edited by R. P. Binzel, T. Gehrels, and M. Shapley, pp. 336–367, Univ. of Ariz. Press, Tucson, 1989.

Tarantola, A., and B. Valette, Inverse problems = quest for information, *J. Geophys.*, *50*, 159–170, 1982a.

Tarantola, A., and B. Valette, Generalized nonlinear inverse problems solved using the least squares criterion, *Rev. Geophys.*, *20*, 219–232, 1982b.

Tarasov, L., and W. R. Peltier, A high-resolution model of the 100 kyr ice-age cycle, *Ann. Glaciol.*, *25*, 58–65, 1997a.

Tarasov, L., and W. R. Peltier, Terminating the 100 kyr ice age cycle, *J. Geophys. Res.*, *102*, 21,665–21,693, 1997b.

Tarasov, L., and W. R. Peltier, The influence of ice sheet thermomechanics in a theory of the 100 kyr ice-age cycle, *J. Geophys. Res.*, in press, 1998.

Thompson, D. J., Quadratic inverse spectrum estimates: Applications to Paleoclimatology, *Philos. Trans. R. Soc. London*, *Ser. A*, *332*, 539–597, 1990.

Thorsteinsson, T., J. Kipfstuhl, and H. Miller, Textures and fabrics in the GRIP ice core, *J. Geophys. Res.*, *102*, 26,583–26,599, 1997.

Tushingham, A. M., and W. R. Peltier, ICE-3G: A new global model of late Pleistocene deglaciation based upon geophysical predictions of post-glacial relative sea level change, *J. Geophys. Res.*, *96*, 4497–4523, 1991.

Tushingham, A. M., and W. R. Peltier, Validation of the ICE-3G model of Würm-Wisconsin deglaciation using a global data base of relative sea level histories, *J. Geophys. Res.*, *97*, 3285–3304, 1992.

Vermeersen, L. L. A., R. Sabadini, and G. Spada, Analytical visco-elastic relaxation models, *Geophys. Res. Lett.*, *23*, 697–700, 1996.

Vincente, R. O., and S. Yumi, Co-ordinates of the pole (1899–1968) returned to the conventional international origin, *Publ. Int. Latit. Obs. Mizusawa*, *7*, 41–50, 1969.

Vincente, R. O., and S. Yumi, Revised values (1941–1961) of the co-ordinates of the pole referred to the CIO, *Publ. Int. Latit. Obs. Mizusawa*, *7*, 109–112, 1970.

Wakahama, G., On the plastic deformation of single crystal of ice, paper presented at International Conference on Low Temperature Science, Sapporo, Japan, 1966.

Walcott, R. I., Structure of the Earth from glacio-isostatic rebound, *Annu. Rev. Earth Planet. Sci.*, *1*, 15–37, 1973.

Walcott, R. I., Rheological modes and observational data of glacio-isostatic rebound, in *Earth Rheology, Isostasy and Eustacy*, edited by N.-A. Mörner, pp. 3–10, John Wiley, New York, 1980.

Weertman, J., Creep laws for the mantle of the Earth, *Philos. Trans. R. Soc. London*, *Ser. A*, *334*, 110–125, 1978.

Wolf, D., Note on estimates of the glacial-isostatic decay spectrum for Fennoscandia, *Geophys. J. Int.*, *127*, 801–805, 1996.

Wu, P., The response of a Maxwell Earth to applied surface loads: Glacial isostatic adjustment, M.Sc. thesis, Dep. of Phys., Univ. of Toronto, Toronto, Ont., Canada, 1978.

Wu, P., and W. R. Peltier, Viscous gravitational relaxation, *Geophys. J. R. Astron. Soc.*, *70*, 435–485, 1982.

Wu, P., and W. R. Peltier, Pleistocene deglaciation and the Earth's rotation: A new analysis, *Geophys. J. R. Astron. Soc.*, *76*, 202–242, 1984.

Yoder, C. F., J. G. Williams, J. O. Dickey, B. E. Schutz, R. J. Eanes, and B. D. Tapley, Secular variation of the Earth's gravitational harmonic J_2 coefficient from LAGEOS and non-tidal acceleration of Earth rotation, *Nature*, *303*, 757–762, 1983.

W. R. Peltier, Department of Physics, University of Toronto, 60 St. George Street, Toronto, Ontario, Canada M5S 1A7. (peltier@atmosp.physics.utoronto.ca)